Institut de Physique de l'Université de Neuchâtel (Suisse)

# Exciton condensation in $1T$-$TiSe_2$: A photoemission study and its theoretical model

Thèse
présentée à la Faculté des Sciences
de l'Université de Neuchâtel
pour l'obtention du grade de Docteur ès Sciences par

**Claude Monney**

soutenue le 22 septembre 2009
en présence du directeur de thèse
Prof. Philipp Aebi
et des rapporteurs
Prof. Hans Beck, Université de Neuchâtel
Prof. Manfred Sigrist, ETHZ
Dr. Felix Baumberger, University of St-Andrews

Neuchâtel, 15 octobre 2009

Université de Neuchâtel

FACULTE DES SCIENCES
Secrétariat-Décanat de la faculté
- Rue Emile-Argand 11
- CP 158
- CH-2009 Neuchâtel

# IMPRIMATUR POUR LA THESE

# Exciton condensation in 1*T*-$TiSe_2$: A photoemission study and its theoretical model

**Claude MONNEY**

---

UNIVERSITE DE NEUCHATEL

FACULTE DES SCIENCES

La Faculté des sciences de l'Université de Neuchâtel,
sur le rapport des membres du jury

MM. P. Aebi (directeur de thèse, Université de Neuchâtel et Université de Fribourg),
H. Beck (Université de Neuchâtel),
F. Baumberger (University of St. Andrews, UK)
et M. Sigrist (ETH Zürich)

autorise l'impression de la présente thèse.

Neuchâtel, le 8 octobre 2009

Le doyen :
F. Kessler

UNIVERSITE DE NEUCHATEL
FACULTE DES SCIENCES
Secrétariat - décanat de la faculté
Rue Emile-Argand 11 - CP 158
CH-2009 Neuchâtel
felix Kessler

## Keywords

Angle-resolved photoemission spectroscopy, transition metal dichalcogenides, quasi two-dimensional systems, exciton condensate phase, spectral function, strongly correlated electron system.

## Mots clés

Spectroscopie de photoémission résolue en angle, dichalcogénures de métaux de transition, système quasi bidimensionnel, phase de condensat d'excitons, fonction spectrale, système d'électrons fortement corrélés.

# *Abstract*

In this thesis, the question of the origin of the charge density wave phase transition appearing in the transition metal dichalcogenide $1T$-$TiSe_2$ is addressed by the comparison of new angle-resolved photoemission spectroscopy data with a theoretical model called the exciton condensate phase. Both these experimental and theoretical aspects are here developed in details. Photoemission intensity maps generated by the spectral function calculated in this model are compared with the experimental data and the very good agreement provides a strong support for the realisation of such a phase in $1T$-$TiSe_2$.

Photoemission data, recorder over a wide temperature range, allow to extract the detailed temperature behaviour of the order parameter characterising this exotic phase. A typical mean field behaviour is evidenced below the critical temperature of the transition and strong electron-hole fluctuations are observed above this temperature. Moreover, an important chemical potential shift is revealed in this analysis. The order parameter is also computed by means of the gap equation provided by the model and is compared to the experimental curve.

A dramatic renormalisation of the conduction band is evidenced for the first time in the low temperature measurements. This effect together with the onset of the exciton condensate phase and the resulting chemical potential shift is used to compute the corresponding resistivity of $1T$-$TiSe_2$, leading its first comprehensive understanding.

Finally, the electron-phonon coupling is investigated in a tight-binding formalism to address the question of the origin of the periodic lattice distortion which has been observed in $1T$-$TiSe_2$. It is shown that the new periodic potential generated by the exciton condensate is capable of producing atomic displacements of the same order of magnitude than what is experimentally observed.

# Preface

The content of this thesis is based on research carried out in the Electron Spectroscopy Group of Prof. Philipp Aebi at the Institut de physique, Université de Neuchâtel, and at the Département de physique, Université de Fribourg, during the period 2005-2009. This work was supported by the Swiss National Science Foundation (SNF) through Division II and the National Center of Competence in Research (NCCR) Materials with Novel Electronic Properties (MaNEP).

The thesis consists of eight chapters. Chapter 1 is a general introduction to the thesis. Chapter 2 describes the photoemission technique and its relation to many-body theory. Chapters 3, 4, 5, 6, 7 are based on articles, which are either published, submitted or not submitted yet. Supplementary material has been added to comment these articles, to introduce new theoretical methods and to elaborate further discussions. Therefore, in the table of contents, there is often a section "Comments" appearing. Nonetheless, each of these chapters mostly stands on its own and can be read independently, although the whole thesis has been written with a certain continuity. However, for sequential reading, this leads inevitably to some redundancies. Chapter 8 is a general conclusion to the thesis, offering also some perspectives for future work. Appendix A presents a completely independent work, with an unpublished article. Articles included in this thesis are

H. Cercellier C. Monney, F. Clerc, C. Battaglia, L. Despont, M. G. Garnier, H. Beck, P. Aebi, L. Patthey, H. Berger, L. Forró,
**Evidence for an excitonic insulator phase in 1$T$-$TiSe_2$**,
published in Physical Review Letters
Phys. Rev. Lett. **99**, 146403 (2007) ..... page 44

C. Monney, H. Cercellier, F. Clerc, C. Battaglia, E.F. Schwier, C. Didiot, M. G. Garnier, H. Beck, P. Aebi, H. Berger, L. Forró, L. Patthey,
**Spontaneous exciton condensation in 1$T$-$TiSe_2$: a BCS-like approach**,
published in Physical Review B
Phys. Rev. B **79**, 045116 (2009) ..... page 52

C. Monney, H. Cercellier, C. Battaglia, E.F. Schwier, C. Didiot, M. G. Garnier, H. Beck, P. Aebi,
**Temperature dependence of the excitonic insulator phase model in 1$T$-$TiSe_2$**,
Accepted for publication in Physica B
DOI 10.1016/j.physb.2009.07.047 ..... page 79

C. Monney, H. Cercellier, E.F. Schwier, C. Battaglia, N. Martiotti, C. Didiot, M. G. Garnier, H. Beck, J. Marcus, P. Aebi,
**A photoemission study of the temperature dependence of the exciton condensate phase of 1$T$-$TiSe_2$**,
to be submitted ..... page 86

# Contents

# Abbreviations

| | |
|---|---|
| **ARPES** | Angle-resolved photoemission spectroscopy |
| **CDW** | Charge density wave |
| **CEM** | Constant energy map |
| **DFT** | Density functional theory |
| **FSM** | Fermi surface map |
| **LCAO** | Linear combination of atomic orbitals |
| **LDA** | Local density approximation |
| **LEED** | Low energy electron diffraction |
| **PLD** | Periodic lattice distortion |
| **STM** | Scanning tunneling microscopy |
| **TMDC** | Transition metal dichalcogenides |
| **UHV** | Ultra high vacuum |
| **UPS** | Ultraviolet photoemission spectroscopy |
| **XPD** | X-ray photoemission diffraction |
| **XPS** | X-ray photoemission spectroscopy |

# Chapter 1

# Introduction

This thesis basically aims at improving the physical understanding of $1\,T$-$TiSe_2$, which is a novel synthetic material. It is concerned with fundamental research in the field of condensed matter physics, whose primary purpose is to create knowledge, without any direct practical use in mind.

Condensed matter physics studies the properties of matter in the liquid or solid phases, both macroscopically and microscopically, and it represents a very active field of research in physics. In opposition to matter in gas phases, condensed matter involves particles in extremely large numbers, where interactions cannot be neglected. Let us consider copper for instance. This is a very common material, widely used for electrical assembly. However, even if every interaction between its particles was known, so that classical equations of motion could be written for the entire system, it would be hopeless to calculate the trajectory of each particle to predict the properties of this material. The main reason is that 1 $cm^3$ of copper contains already about $10^{23}$ particles. Even with the most powerful computers available today, such a task would require too much time. In fact, already three particles in interaction can be a problem for those looking for an exact solution ...

The ambition of condensed matter physics is then to make possible the mathematical treatment of such a large number of particles. Namely, the goal is to extract from this multitude of particles and interactions, the relevant minimal parameters that will allow to build a simple model, which can be reasonably handled and is capable of predicting and reproducing the essential properties of that material. A close dialog between theoretical and experimental physics is crucial to establish a coherent model and verify its accuracy. Ultimately, the model permits a microscopic understanding of the physics at play in the system investigated.

In condensed matter physics, and especially in the domain of solid state, a common classification is to separate the properties of a system into those relative to the atomic structure and to the electronic structure. The former is generally characterized by the dispersions of phonons, which are the quantized lattice vibrations, and the latter by the electronic dispersions, which represent the discrete states where the electrons can live in the solid. This description of matter is meaningful, since the macroscopic properties of condensed matter originate in the low energy excitations of phonons and electrons. Photoemission is therefore a privileged experimental technique, as it measures directly the elementary electronic excitation of condensed matter.

Pioneered in the early 1960s, photoemission has been stimulated by the Nobel prize of 1981 awarded to K. Siegbahn "for his contribution to the development of high-resolution electron spectroscopy", allowing to perform chemical analysis of samples by means of core-electron spectroscopy [1]. In the last twenty years, photoemission benefited from an impressive development in instrumentation, resulting in a huge improvement of the energy resolution (and of the momentum resolution too), from about $\sim 100$ meV in the 1980s to less than 1 meV in the last few years. Such an energy resolution is highly profitable, since it permits to resolve fine structures in the photoemission spectra, which can be related to the coupling between the electron excited by photoemission and any collective modes in the solid like phonons, excitons, plasmons and a superconducting state. This gives photoemission the possibility to probe indirectly subtle phenomena in the solid, which can be understood within the framework of many-body theory.

In this thesis, we study a particular material, $1T$-$TiSe_2$, using the photoemission technique as an experimental probe. This material is of a particular interest, because it undergoes a phase transition at the critical temperature $T_c$ of 200K. $1T$-$TiSe_2$ has also the advantage of being a simple layered material[a], made of only two atomic species, giving rise to a sober electronic band structure, which can be easily modelled. The two phases above and below $T_c$, namely a normal and a charge density wave phase, display clearly different macroscopic properties (like the resistivity), as well as specific spectroscopic signatures. In this work, we propose an exotic model, called the exciton condensate phase[b], based on purely electronic effects, for explaining the origin of the phase transition. A close dialog between photoemission and many-body theory has allowed to improve both the understanding of the material and of the model.

Chapter 2 presents the photoemission technique, both experimentally and theoretically. Within a few approximations, a simple formula is elaborated, providing a link, the spectral function, between photoemission and many-body theory. This chapter also summarizes some general aspects of many-body theory for illustrating what physical information is provided by the spectral function. Chapter 3 briefly introduces the concept of the Peierls transition, which is the prototype one-dimensional charge density wave transition. Several elements of the transition metal dichalcogenides family, which are candidates for a Peierls-like charge density wave transition, are then outlined, before a detailed overview of the properties of $1T$-$TiSe_2$ is given. In chapter 4, which is devoted to the exciton condensate phase, the BCS theory of superconductivity is presented first, for comparison with our model, as they share some similarities. Then the excitonic insulator phase model, which is a simplified one-dimensional version of our model, is introduced for pedagogical purposes. Afterwards, the exciton condensate phase, specific to $1T$-$TiSe_2$, is described in detail, at the mean-field level and at zero temperature. In chapter 5, the temperature dependence of the exciton condensate phase is studied, both theoretically and experimentally. This chapter is concluded by the resolution of the corresponding gap equation and the discussion of its results. In chapter 6, photoemission data revealing a dramatic renormalization of the electronic bands near the Fermi level are shown and discussed in connection with transport data. A comprehensive qualitative and quantitative understanding of the resistivity of $1T$-$TiSe_2$ is elaborated. Chapter 7 discusses the coupling of the exciton condensate to the underlying atomic lattice for

[a] It is therefore generally considered as a quasi-two dimensional compound, resulting in a reduced perpendicular dispersion and a natural predisposition to cleaving.

[b] A similar model, the excitonic insulator phase, has been already elaborated theoretically in the 1960s, although no particular material was known at that time as an experimental realization of this phase [2, 3].

giving a quantitative explanation of the observed periodic lattice distortion. This analysis is made within a tight-binding formalism based on DFT calculations. Finally, in appendix A, an unfinished work on the strongly correlated material $Na_xCoO_2$ (which is not related to the rest of this thesis) is discussed, together with the XPD technique, used for obtaining the corresponding results. This work has not been published, since it appeared later on that the studied crystals were of a poor quality, casting doubts on this analysis.

# Chapter 2

# The photoemission technique

## 2.1 Basics of photoemission

Photoemission is a powerful technique allowing to map in reciprocal space the low energy electronic excitations of the probed system. Under specific conditions, it turns out that such a mapping corresponds to the electronic bandstructure of the system under investigation. However, this ideal case is often not met and thus the interpretation of the photoemission data becomes more complex and requires a deeper knowledge of the photoemission process. The goal of this chapter is to provide the reader with a quick introduction to the photoemission technique and to explain what physical information can be extracted. The interested reader is invited to look further into the rich literature on the subject [4, 5, 6, 7].

Photoemission originates in the photoelectric effect. Discovered by H. Hertz in 1885, it is based on the fact that when light is illuminating matter, it can be instantaneously converted into energy and eject electrons from matter, called photoelectrons [8]. It was only 20 years later, in 1905, that A. Einstein gave a full understanding of this phenomenon by introducing the quantized nature of light, the photons [9]. As this thesis is concerned with matter in the solid state, and particularly with crystal lattices, we will focus now on such systems. Knowing the energy of the impinging photon and measuring the kinetic energy of the outgoing photoelectron allow us to infer the energy of the photoelectron when being in the solid. As we will see later in this chapter, this task can be formidably difficult. Usually, to ease the understanding of the photoemission process, we separate it in three processes depicted in Fig. 2.1. In a first step, an electron, living in an inital Bloch state $\phi_i$ of the solid, absorbs an incoming photon and jumps into an empty final Bloch state $\phi_f$ of the solid, leaving a hole behind it. This is the optical transition in the solid. Then, this electron, called now the photoelectron, has to reach the surface, in order to escape from the solid and enter in the detector. This is the second process. Finally, the photoelectron will cross the surface, a process which can be viewed as refraction, due to the wave-like nature of electrons. This is the third step of this model of photoemission. After that, the photoelectron can freely propagate in vacuum to the detector. While this model, called the three-step model, gives a simple and intuitive description of photoemission, it leaves nonetheless disturbing open questions. In particular, how can the photoelectron travel to the surface after the optical transition, as it is described by a usual Bloch state of an infinite crystal? In other words, how can this Bloch state $\phi_f$ transform itself into a state propagating towards

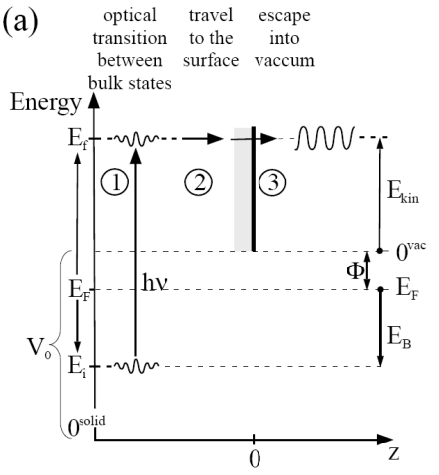


FIGURE 2.1: Simplified decomposition of the photoemission process into three steps (from reference [5]). In step 1, the optical transition takes place. An electron is emitted from an occupied Bloch state at energy $E_i$ and promoted to an unoccupied Bloch state at an energy $E_f$. Then, in step 2, it travels to the surface. Finally, in step 3, it crosses the surface in a way similar to classical refraction, due to its wave-like property. It can then escape into vacuum to reach the detector.

the surface in the solid and then in a free electron final state propagating towards the detector in the vacuum? The answer is given by the one-step model, which describes the whole photoemission process at once [10, 11, 12]. The final state after the absorption of the incoming photon is then a complicated wave function displaying a decaying tail in the solid, which has a finite amplitude where the optical transition takes place, and displaying a free electron like behaviour in vacuum. Thus it considers the situation of a semi-infinite crystal and fully takes into account the presence of its surface (a single Bloch states is not sufficient for such a description). Such a state is often called an inverse LEED state. In a LEED experiment, electrons are shot on a crystal where they are scattered after having penetrated into it. Reversing the time dependence of such a state produces a good candidate for a photoemission final state.

A photoemission experiment provides particularly useful information thanks to the conservation laws of energy and momentum. The first one allows us to relate the measured kinetic energy of the photoelectron to its binding energy in the solid and the second one to determine partially its momentum in the solid. However, the interaction of the electron with its neighbors severely complicates the energy conservation by adding different contributions, giving rise to extra features (discrete or continuous) in the excitation spectrum of the solid. Two classes of such features are usually distinguished: the intrinsic and the extrinsic spectrum. The intrinsic spectrum is generated during the optical transition of the electron. Part of the energy of the incoming photon will be directly given to other entities (like electron-hole excitations, phonons, ...) in the solid through their coupling to the electron. The extrinsic spectrum is generated during the transport of the photoelectron to the surface. It corresponds to inelastic scattering events.

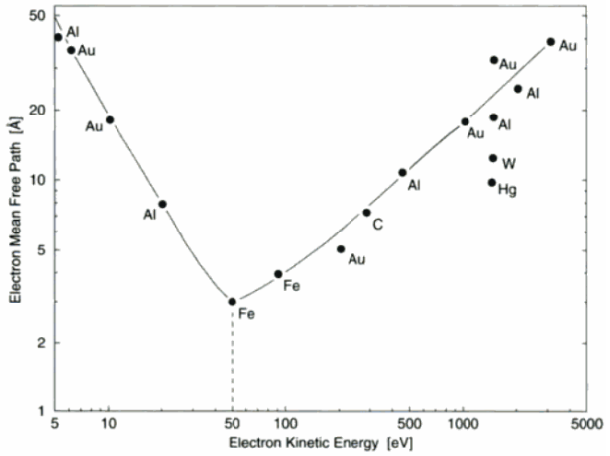


FIGURE 2.2: Inelastic mean free path for the electron as a function of its kinetic energy. Experimental data have been collected for various metals, emphasizing the universality of this curve (from reference [5]).

## 2.2 Experimental setup for measuring photoemission

Photoemission is a photon-in electron-out technique. As electrons strongly react with matter, it imposes constraints on the experimental setup. First of all, their inelastic mean free path vary between 8 Å and 20 Å, for an electron kinetic energy of 20 to 1000 eV (typical energies used in photoemission), as shown in Fig. 2.2. It means that the photoelectrons escaping the material come from a very thin layer beneath the surface and that this surface must therefore be atomically clean. UHV, which corresponds to a pressure in the low $10^{-10}$ mbar, is then required as the optimal environment for preparing and keeping a clean surface throughout the data acquisition process. Obtaining UHV is demanding as it requires a very efficient pumping installation and puts constrains on the choice of materials that can be used within the setup.

Apart from the UHV system, a conventional photoemission experiment contains three main components: a photon source, a manipulator holding the sample and an electron analyzer (photoelectron detector). A schematic picture of the situation is given in Fig. 2.3.

Different photon sources are commercially available, providing light at different energies $h\nu$. Standard laboratory equipments consist of an ultraviolet lamp ($h\nu = 21.2$ eV), based on a helium plasma, and x-ray tubes, often having anodes in magnesium ($h\nu = 1253.6$ eV), aluminium ($h\nu = 1486.6$ eV). The choice of the source depends in general on which region of the electronic structure we are interested in, since core levels require high energy photons to be excited and the valence band is usually probed with low photon energies[a]. This leads to the so-called XPS or UPS regimes respectively. We will essentially focus on the UPS regime in this thesis, though the basic theory for the XPS regime is not much different. Recently, laser-based photoemission experienced a very intense and fast development, resulting in very efficient laboratory equipments [15, 16]. Tunable photon energies for photoemission are available at synchrotron light sources, ranging from the low ultraviolet regime at 15 eV to the hard x-ray regime at $\sim$ 10

[a]Currently, high photon energies are more and more used for probing the valence band, since at these energies the bulk sensitivity is enhanced, according to Fig. 2.2 [13, 14].

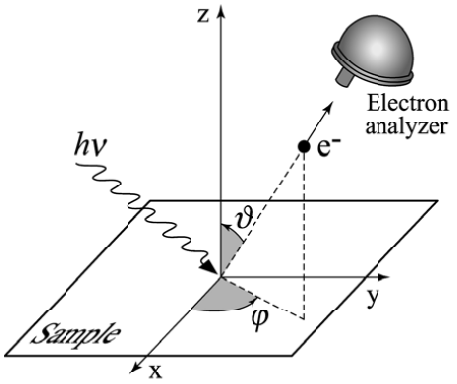


FIGURE 2.3: Schematic description of a photoemission experiment (from reference [4]). Incoming light of energy $h\nu$ excites an electron from the sample, which can then be detected by an electron analyzer. The direction of the outgoing photoelectron is usually parametrized by the polar angle $\theta$ and azimuthal angle $\phi$.

keV. For photoemission, the photon source needs to be as monochromatized as possible, in order to increase the overall energy resolution of the experiment. A source with a high intensity is also crucial, since it will allow the user to get a good statistics in a limited time, avoiding contamination of the surface of the sample. Other features can be useful, like the possibility to change the light polarization to discriminate between optical transition in the solid, as well as the control of the beam spot size to illuminate different parts of the sample.

The manipulator holds the sample in front of the light source and of the analyzer. For performing angle-resolved photoemission, it basically involves two angular degrees of freedom, the azimuthal and polar angles, as depicted in Fig. 2.3. They offer the possibility of rotating the sample with respect to the analyzer, allowing to scan the reciprocal space as it will be demonstrated below. Therefore their angular resolution is directly related to the resolution in wave vector $\vec{k}$ in reciprocal space. Another essential feature of the manipulator is its ability to cool the sample down to very low temperatures. High temperature prevents the realization of exotic ground states like superconductivity or CDW phases and ruins the energy resolution of the setup. The low temperature limit reached by the manipulator is therefore a domain of constant development. Stabilizing the sample to intermediate temperatures is also important, as it permits studying accurately phase transitions as we will see later in this work.

The analyzer consists generally of electrostatic lenses, which focus and accelerate the photoelectrons to two concentric hemispheres, where they are discriminated with respect to their kinetic energies, before entering into the detector. Modern detectors are made of a two-dimensional array of channeltrons (the multi-channel plate), which offers the possibility to measure simultaneously over a certain energy and $\vec{k}$ range.

## 2.3 The theory of photoemission

In this section, we describe mathematically the process of photoemission within a second quantization formalism. Reasonable approximations are introduced to get simple formulas which will be used further in this thesis.

We start with the Fermi golden rule where the interaction of the solid with light is represented by the perturbation $V_{int}$. For incoming light (with photons of energy $\hbar\omega$) of relatively low intensity and within the Coulomb gauge, the interaction of an electron of mass $m$ and charge $-e$ with light is introduced by the minimal subsitution

$$\frac{1}{2m}(\vec{p}-e\vec{A})^2 = \frac{p^2}{2m} + \frac{(eA)^2}{2m} - \frac{\vec{p}\cdot e\vec{A} + e\vec{A}\cdot\vec{p}}{2m} \cong \frac{p^2}{2m} - \frac{e\vec{A}\cdot\vec{p}}{m}.$$

To obtain this last approximation, we neglect the $A^2$ term due to the low intensity of light and we use the relation $[\vec{p},\vec{A}] = -i\hbar\nabla\cdot\vec{A} = 0$ in the Coulomb gauge. Therefore, the interaction is $V_{int} = -\vec{A}\cdot\vec{p}e/m$, so that the transition probability (per unit time) between an initial state $\psi_i^{(N)}$ having a total energy $E_i^{(N)}$ and a final state $\psi_f^{(N)}$ having a total energy $E_f^{(N)}$ is given by

$$P_{fi} \propto |\langle\psi_f^{(N)}|V_{int}|\psi_i^{(N)}\rangle|^2\delta(E_f^{(N)} - E_i^{(N)} - \hbar\omega).$$

Here, $\psi_i^{(N)}$ and $\psi_f^{(N)}$ are $N$-electron (in interaction) wave functions. This formula deals here only with the optical transition within the solid.

In the second quantization, the one-particle operator for interaction with light $V_{int}$ is written like

$$V_{int} = \sum_{\mu,\nu,\vec{k},\vec{k}'} M_{\nu\mu}(\vec{k},\vec{k}')c_\nu^\dagger(\vec{k})c_\mu(\vec{k}')$$

where the matrix elements of the optical transition are defined by

$$M_{\nu\mu}(\vec{k},\vec{k}') = \langle\phi_\nu^{\vec{k}}|V_{int}|\phi_\mu^{\vec{k}\,'}\rangle.$$

The fermionic operators $c_\mu(\vec{k})^\dagger$ and $c_\mu(\vec{k})$ create and annihilate respectively an electron described by a Bloch wave $\phi_\mu^{\vec{k}}(\vec{r}) = u_{\mu\vec{k}}(\vec{r})\exp(i\vec{k}\cdot\vec{r})$, in a band labelled $\mu$, with wave vector $\vec{k}$ and energy $\varepsilon_{\mu\vec{k}}$. For a monochromatic light wave of wave vector $\vec{q}$, having a spatial dependence given by $\vec{A}(\vec{r}) = \vec{A}_0\exp(\vec{q}\cdot\vec{r})$, the matrix elements directly translate into

$$\begin{aligned} M_{\nu\mu}(\vec{k},\vec{k}') &= \frac{\hbar e}{im}\int d^3r\; u^*_{\nu\vec{k}}(\vec{r})\mathrm{e}^{-i\vec{k}\cdot\vec{r}}\vec{A}_0\mathrm{e}^{i\vec{q}\cdot\vec{r}}\cdot\vec{\nabla}u_{\mu\vec{k}'}(\vec{r})\mathrm{e}^{i\vec{k}'\cdot\vec{r}} \\ &= \frac{\hbar e}{im}\int d^3r\;\mathrm{e}^{-i(\vec{k}-\vec{k}'-\vec{q})\cdot\vec{r}}u^*_{\nu\vec{k}}(\vec{r})\vec{A}_0\cdot(\vec{\nabla}+i\vec{k}')u_{\mu\vec{k}'}(\vec{r}). \end{aligned}$$

Here, the integration runs over the whole space. We now use the translational symmetry of the Bravais lattice and the relation $u_{\mu\vec{k}}(\vec{r}+\vec{R}) = u_{\mu\vec{k}}(\vec{r})$ for a Bravais lattice vector $\vec{R}$

$$
\begin{aligned}
M_{\nu\mu}(\vec{k},\vec{k}') &= \frac{\hbar e}{im}\sum_{\vec{R}}\int_{UC} d^3r\, \mathrm{e}^{-i(\vec{k}-\vec{k}'-\vec{q})\cdot(\vec{r}+\vec{R})} u^*_{\nu\vec{k}}(\vec{r})\vec{A}_0\cdot(\vec{\nabla}+i\vec{k}')u_{\mu\vec{k}'}(\vec{r}) \\
&= \frac{\hbar e}{im}\underbrace{\sum_{\vec{R}}\mathrm{e}^{-i(\vec{k}-\vec{k}'-\vec{q})\cdot\vec{R}}}_{=N\delta_{\vec{k}-\vec{k}'-\vec{q},\vec{G}}}\int_{UC} d^3r\, \mathrm{e}^{-i(\vec{k}-\vec{k}'-\vec{q})\cdot\vec{r}} u^*_{\nu\vec{k}}(\vec{r})\vec{A}_0\cdot(\vec{\nabla}+i\vec{k}')u_{\mu\vec{k}'}(\vec{r}) \\
&= N\delta_{\vec{k}-\vec{k}'-\vec{q},\vec{G}}\frac{\hbar e}{im}\int d^3r\, \mathrm{e}^{-i\vec{G}\cdot\vec{r}} u^*_{\nu\vec{k}}(\vec{r})\vec{A}_0\cdot(\vec{\nabla}+i\vec{k}')u_{\mu\vec{k}'}(\vec{r}) \\
&= N\delta_{\vec{k}-\vec{k}'-\vec{q},\vec{G}}\,\tilde{M}_{\nu\mu}(\vec{k},\vec{k}'),
\end{aligned}
$$

where $N$ is the number of unit cells in the system. The notation UC indicates that the integration runs now over the unit cell only (the integration has been expanded to the whole space in the last equation due to the identity $\exp(\vec{G}\cdot\vec{R})=1$). The delta function here is responsible for momentum conservation, where the participation of the lattice has been introduced explicitly through the reciprocal wave vector $\vec{G}$.

To go on further with this theoretical description, we make use of the sudden approximation. It states that, after the transition, the photoelectron of momentum $\vec{k}_f$ has a sufficiently high energy $\varepsilon_{\alpha\vec{k}}$ such that it immediately decouples from the remaining $(N-1)$ electron system, described by the wave function $\psi^{(N-1)}_{f,s}$. However, we admit that this remaining system can be left in different excited states labelled $s$, which will eventually relax in a $(N-1)$ electron ground state, giving rise to satellites in the photoemission spectrum. The final system composed of the $(N-1)$ remaining electrons and the photoelectron has an energy $E^{(N)}_{f,s}\cong E^{(N-1)}_{f,s}+\varepsilon_{\alpha\vec{k}}$. We can thus write $|\psi^{(N)}_f\rangle \simeq \sum_s c^\dagger_\alpha(\vec{k}_f)|\psi^{(N-1)}_{f,s}\rangle$ and the photoemission transition probability in the solid becomes

$$
\begin{aligned}
P_{fi} &\propto \sum_{s,\alpha}\sum_{\mu,\nu,\vec{k},\vec{G}} |\tilde{M}_{\nu\mu}(\vec{k},\vec{k}-\vec{q}-\vec{G})|^2 |\langle\psi^{(N-1)}_{f,s}|c_\alpha(\vec{k}_f)c^\dagger_\nu(\vec{k})c_\mu(\vec{k}-\vec{q}-\vec{G})|\psi^{(N)}_i\rangle|^2 \\
&\quad\times\delta(E^{(N)}_{f,s}-E^{(N)}_i-\hbar\omega) \\
&\propto \sum_{\mu,\nu,\vec{G}} |\tilde{M}_{\nu\mu}(\vec{k}_f,\vec{k}_f-\vec{q}-\vec{G})|^2 \sum_s |\langle\psi^{(N-1)}_{f,s}|c_\mu(\vec{k}_f-\vec{q}-\vec{G})|\psi^{(N)}_i\rangle|^2 \\
&\quad\times\delta(E^{(N)}_{f,s}-E^{(N)}_i-\hbar\omega).
\end{aligned}
$$

To obtain the second equation, we used the commutation relation for the fermionic operators $[c_\alpha(\vec{k}_f),c^\dagger_\nu(\vec{k})]=\delta_{\vec{k}_f,\vec{k}}\,\delta_{\alpha,\nu}$, together with the fact that $c_\alpha(\vec{k}_f)|\psi^{(N)}_i\rangle=0$, since $c_\alpha(\vec{k}_f)$ tries to annihilate an electron with an energy much above $E_F$ (due to the excitation energy $\hbar\omega$), which is not possible in the initial system $\psi^{(N)}_i$. We are thus able to explicitly write out the one-electron states $\phi^{\vec{k}}_\nu$ and $\phi^{\vec{k}'}_\mu$ directly involved in the optical transition. As this transition happens in the solid, the wave vector $\vec{k}$ is a good quantum number.

We now work out the $\delta-$function imposing energy conservation to relate the measured photoelectron kinetic energy $\varepsilon_{kin}$ to that of excitations of the inital state. As a consequence of the sudden approximation, $E^{(N)}_f\simeq E^{(N-1)}_f+\varepsilon_{\nu\vec{k}}$. Then, using the definition

of the chemical potential, $\mu = E^{(N)} - E^{(N-1)}$, (which is independent of the number of particles $N$ if $N$ is large enough) and introducing the energy of the many-body excitation in the solid $\varepsilon_s = E_f^{(N)} - E_i^{(N)}$ (it can be seen as the "binding energy" of the excitation) of a system left in the excited state $s$, we can rewrite the argument of the $\delta-$function like $\delta(E_{f,s}^{(N)} - E_i^{(N)} - \hbar\omega) = \delta(\varepsilon_{kin} + \varepsilon_s - \hbar\omega)$, where we have also defined the kinetic energy of the photoelectron (in the solid) by $\varepsilon_{kin} = \varepsilon_{\nu\vec{k}} - \mu$.

The photoemission intensity, resulting from the optical transition in the solid, is proportional to the transition probability $P_{fi}$ and is a function of the photoelectron kinetic energy $\varepsilon_{kin}$ and momentum $\vec{k}_f$, which are the measured observables (strictly speaking, $\vec{k}_f$ is not completely observed, see below) in a standard photoemission setup. Multiplying the result by the Fermi-Dirac distribution $N_F$ to ensure that photoemission probes only occupied states (this last step can be demonstrated more formally, see for instance reference [17]), we obtain

$$\begin{aligned} I(\varepsilon_{kin}, \vec{k}_f) \quad \propto \quad & \sum_{\mu,\nu,\vec{G}} |M_{\nu\mu}(\vec{k}_f, \vec{k}_f - \vec{q} - \vec{G})|^2 N_F(\hbar\omega - \varepsilon_{kin}) \\ & \times \sum_s |\langle \psi_{f,s}^{(N-1)} | c_\mu(\vec{k}_f - \vec{q} - \vec{G}) | \psi_i^{(N)} \rangle|^2 \delta(\varepsilon_{kin} + \varepsilon_s - \hbar\omega). \end{aligned}$$

This formula describes the first step of photoemission, namely the optical transition in the solid within the sudden approximation.

We will neglect the second step of the photoemission process, since the extrinsic spectrum generated by the transport of the photoelectron to the surface often results in the production of a background which does not affect too much the measured spectrum in valence band photoemission (the excitation energy being small). This is at least the case for the photoemission data presented in this work. The third step of photoemission, the refraction through the surface, has more consequences on the measurement. First of all, the presence of surface breaks the translational symmetry of the crystal, impeding the use of $\vec{k}$ as a good quantum number. However, as one knows from classical refraction, the wave vector parallel to the surface $\vec{k}_\parallel$ is still conserved, allowing us to relate the polar and azimuthal angles of the sample relatively to the detector (see Fig. 2.3) to the position of the measurement in reciprocal space

$$\begin{aligned} k_{\parallel,i}^x &= \sqrt{\frac{2m}{\hbar}} \sqrt{\varepsilon_{kin}^{vac}} \sin\theta \cos\phi, \\ k_{\parallel,i}^y &= \sqrt{\frac{2m}{\hbar}} \sqrt{\varepsilon_{kin}^{vac}} \sin\theta \sin\phi. \end{aligned}$$

The kinetic energy of the photoelectron in vacuum $\varepsilon_{kin}^{vac}$ differs from $\varepsilon_{kin}$ by the work function $\Phi$, which is the energy to pay to extract the photoelectron from the solid, so that $\varepsilon_{kin}^{vac} = \varepsilon_{kin} - \Phi$. As mentionned above, momentum conservation is not fulfilled in the whole photoemission experiment. In particular, the component of the photoelectron wave vector perpendicular to the surface $k_\perp$ is not conserved. A simple way to overcome this problem is to assume that the photoelectron final state in the solid is well described by a free electron state. This extra relation allows then to fully compute its wave vector $\vec{k}$ in the solid, thanks to energy conservation, and to perform for instance band mapping of the studied system in the case of negligible correlations [18]. However, this free electron final state model is a simplistic approximation. We can get a first insight on

the consequences of such a failure by considering a correct photoemission final state as in the one-step model. This inverse LEED state takes into account the semi-infiniteness of the crystal near its surface. The corresponding wave function must then display a finite (but non-negligible) oscillatory tail decaying into the crystal and a free electron-like behaviour in vacuum [19, 20]. The finite tail of the wave function in the crystal can be described as a linear combination of Bloch waves. As a consequence, from the viewpoint of the three-step model, a measured inverse LEED state will be able to couple to many different initial Bloch states with different $k_\perp$ (but all with the same $\vec{k}_\parallel$). The recorded spectrum will be the result of the sum of different initial states. This effect is sometimes called $k_\perp$ integration and leads to a broadening of the spectral features, blurring the fine structures in the recorded spectra [21]. Fortunately, this effect is limited for quasi-two-dimensional systems where the $k_\perp$ dispersion is small, as is the case generally for TMDCs.

## 2.4 A short introduction to many-body physics

### 2.4.1 Green's function and the spectral function at zero temperature

In this section, we introduce the concept of Green's functions as a tool to describe many-body theory and we relate them to photoemission via their spectral representation. This will enable us to interpret photoemission data in the framework of the well established many-body theory of solid state. This theory within the Green's function formalism is a standard topic of condensed matter text books [22, 23].

This formalism is built on the interaction representation, which is an alternative to the Heisenberg and Schroedinger representations, and where both the operators and the wave functions depend on time. We consider a $N$-particle Hamiltonian separable in two parts

$$H = H_0 + V,$$

where $H_0$ is the unperturbed part of the Hamiltonian $H$, while $V$ is a weak interaction. This is very important, as it will permit us to treat this interaction in a perturbation scheme. In this representation, the time evolution of operators is governed by the unperturbed part $H_0$

$$\hat{O} = \mathrm{e}^{iH_0t} O \mathrm{e}^{-iH_0t}$$

We will use the caret $\hat{O}$ to denote an operator $O$ considered within this representation.

At zero temperature, the Green's function describing an electron of wave vector $\vec{k}$ is defined as

$$G(\vec{k},t,t') = -i\langle|Tc(\vec{k},t)c^\dagger(\vec{k},t')|\rangle = -i\langle\psi_0|Tc(\vec{k},t)c^\dagger(\vec{k},t')|\psi_0\rangle \tag{2.1}$$

where $c(\vec{k},t)$ and $c^\dagger(\vec{k},t)$ are annihilation and creation operators at time $t$ for an electron of wave vector $\vec{k}$. $T$ is the time-ordering operator. We neglect any spin dependent interaction and thus do not consider the spin degree of freedom. The average notation $\langle\psi_0|...|\psi_0\rangle$ stands for a zero-temperature average over the exact ground state $\psi_0$ of the $N$-particle system. In most of the cases, this exact ground states is complicated and is unknown, as well as the Green's function $G(\vec{k},t,t')$. Usually, only the unperturbed

Green's function $G_0(\vec{k},t,t')$

$$G_0(\vec{k},t,t') = -i\langle|Tc(\vec{k},t)c^\dagger(\vec{k},t')|\rangle_0 = -i\langle\phi_0|Tc(\vec{k},t)c^\dagger(\vec{k},t')|\phi_0\rangle,$$

is known. It is defined in terms of the exact ground state $\phi_0$ of the non-interacting system, related to the unperturbed Hamiltonian $H_0$. Our goal will be to find an equation relating $G(\vec{k},t,t')$ to $G_0(\vec{k},t,t')$ in a perturbation scheme based on the weak interaction $V$.

For most purpose, we will work with Green's function in frequency $\omega$ rather than in time $t$. A simple Fourier transform allows the conversion.

Let us assume that we are able to calculate the Green's function $G(\vec{k},\omega)$ describing the system in interaction. We want now to find a simple expression relating this Green's function to photoemission. For this purpose, another way to see the Green's function is to express it in terms of its spectral function $A(\vec{k},\omega)$, which can be shown to decompose into two components $A = A^+ + A^-$. The Green's function then reads

$$G(\vec{k},\omega) = \int d\omega' \left[\frac{A^+(\vec{k},\omega')}{\omega-\omega'-\mu+i\eta} + \frac{A^-(\vec{k},\omega')}{\omega+\omega'-\mu-i\eta}\right]$$

($\eta$ is an infinitesimally small positive quantity). The spectral functions $A^+, A^-$ can be shown to be

$$\begin{aligned} A^+(\vec{k},\omega) &= \sum_n |\langle\psi_n^{(N+1)}|c^\dagger(\vec{k})|\psi_0\rangle|^2\delta(\omega-\varepsilon_n), \\ A^-(\vec{k},\omega) &= \sum_n |\langle\psi_n^{(N-1)}|c(\vec{k})|\psi_0\rangle|^2\delta(\omega-\varepsilon_n). \end{aligned} \tag{2.2}$$

$\psi_n^{(N)}$ describes the $n$-th eigenstate of the $N$-particle Hamiltonian $H$ and $\varepsilon_n = E_n - E_0$ (independent of $N$) is the excitation energy between this state and the ground state (the chemical potential appearing above is $\mu = E_0^{(N+1)} - E_0^{(N)}$).

At this point, we need to introduce another Green's function, the retarded Green's function $G^{ret}$

$$G^{ret}(\vec{k},t-t') = -i\theta(t-t')\langle|c(\vec{k},t)c^\dagger(\vec{k},t') + c^\dagger(\vec{k},t')c(\vec{k},t)|\rangle,$$

which is more closely related to the experiment. Due to the $\theta-$function, it operates only for $t > t'$ and this makes it causal. It is important, since the retarded Green's function is the one which is measured in experiment. This can be shown more formally in the context of correlation functions. Its spectral decomposition is then slightly different than that of the previous Green's function, namely

$$G^{ret}(\vec{k},\omega) = \int d\omega' \left[\frac{A^+(\vec{k},\omega')}{\omega-\omega'-\mu+i\eta} + \frac{A^-(\vec{k},\omega')}{\omega+\omega'-\mu+i\eta}\right].$$

We can also write a simpler formula for the relation between the spectral function and its associated Green's function with help of the Sokhotsky formula

$$\lim_{\eta\to 0}\frac{1}{x-x_0+i\eta} = \mathcal{P}\frac{1}{x-x_0} - i\pi\delta(x-x_0) \tag{2.3}$$

($\mathcal{P}$ denotes the principal part), so that

$$\mathrm{Im}\, G^{ret}(\vec{k},\omega) = \begin{cases} -\pi A^{+}(\vec{k},\omega-\mu), & \omega > \mu, \\ -\pi A^{-}(\vec{k},-\omega+\mu), & \omega < \mu. \end{cases}$$

Equation 2.2 is essential, since, by comparison with our Fermi golden rule for photoemission (equation 2.1), it relates the photoemission intensity to the many-body physics of the system under investigation. Therefore, the photoemission intensity for a photoelectron kinetic energy $\varepsilon_{kin}$ and a wave vector $\vec{k}$, considering only the optical transition in the solid, takes the form

$$I(\varepsilon_{kin},\vec{k}) = \sum_{\nu,\mu,\vec{G}} I^{(0)}_{\nu\mu}(\vec{k},\vec{G}) N_F(\hbar\omega-\varepsilon_{kin}) A(\vec{k}-\vec{q}-\vec{G},\hbar\omega-\varepsilon_{kin}). \tag{2.4}$$

Here $I^{(0)}_{\nu\mu} \propto |M_{\nu\mu}(\vec{k},\vec{k}-\vec{q}-\vec{G})|^2$ contains the matrix elements of the optical transition, which depend on the wave function of the final state. The Fermi-Dirac distribution $N_F$ ensures that photoemission probes only occupied states. The spectral function $A^{\pm}(\vec{k},\omega) = -\mathrm{Im}\, G^{ret}(\vec{k},\omega)$ contains most of the physical information on the investigated system. In particular, it represents the response of the system when excited by light, i.e. how the system reacts when a hole is suddenly created[b]. This information is carried by the photoelectron which we collect and measure in a photoemission experiment. It gives rise to the intrinsic spectrum, which contains the low energy excitations of the system [4].

### 2.4.2 The case of non-interacting electrons in a band

To illustrate this section and give a basis for the discussion of the self-energy, we consider now non-interacting electrons living in a partially filled band, with a chemical potential $\mu$. The corresponding Hamiltonian reads

$$H = \sum_{\vec{k}} (\varepsilon(\vec{k})-\mu) c^{\dagger}(\vec{k}) c(\vec{k})$$

where $\varepsilon(\vec{k}) = \hbar^2 k^2/2m_b$ is the electronic dispersion of free-electrons of band mass $m_b$. This means that the interaction is null, $V = 0$, so that the ground state of $H$ is the same than that of $H_0$, $\psi_0 \equiv \phi_0$.

To calculate the Green's function of this system, we need first the equation of motion of $c(\vec{k},t)$,

$$i\partial_t c(\vec{k},t) = [c(\vec{k},t), H] = (\varepsilon(\vec{k})-\mu) c(\vec{k},t)$$

so that

$$\begin{aligned} \partial_t G_0(\vec{k},t) &= -i\partial_t \langle |T c(\vec{k},t) c^{\dagger}(\vec{k},0)| \rangle \\ &= -i\delta(t) \langle |\{c(\vec{k},t), c^{\dagger}(\vec{k},0)\}| \rangle - i\langle |T\partial_t c(\vec{k},t) c^{\dagger}(\vec{k},0)| \rangle \\ &= -i\delta(t) + (-i)^2 (\varepsilon(\vec{k})-\mu) \langle |T c(\vec{k},t) c^{\dagger}(\vec{k},0)| \rangle \\ &= -i\delta(t) - i(\varepsilon(\vec{k})-\mu) G_0(\vec{k},t). \end{aligned}$$

[b] In fact, this is true only for $\omega < \mu$ and the spectral function appearing in equation 2.4 is then $A^{-}$. For $\omega > \mu$, we must use $A^{+}$, which is related to inverse photoemission.

The $\delta-$function here appears from the derivative with respect to $t$ of the Heaviside function $\theta(t)$ stemming from the $T$ operator. Isolating $G$ and doing a Fourier transform into frequency space leads to

$$G_0(\vec{k},\omega) = \frac{1}{\omega - (\varepsilon(\vec{k}) - \mu) + i\eta_{\vec{k}}} = G_0^R(\vec{k},\omega). \tag{2.5}$$

This non-interacting Green's function turns out to be the same as its retarded version (in that particular case). The infinitesimal element $\eta_{\vec{k}} := \eta\,\mathrm{sign}(\varepsilon(\vec{k}) - \mu)$ is introduced here rather artificially. In other ways to derive this result (see reference [22] for instance), this element is essential for ensuring a good convergence in the Fourier transform. It plays an important role now to compute the associated spectral function with help of the Sokhotsky formula 2.3

$$A_0(\vec{k},\omega) = -\frac{1}{\pi}\mathrm{Im}[G_0^R(\vec{k},\omega)] = \delta(\omega - (\varepsilon(\vec{k}) - \mu)).$$

The resulting spectrum consists of $\delta-$functions, which will be broadened in relatively sharp Gaussians by the experimental resolution, dispersing according to $\varepsilon(\vec{k})$. This tells us that, if we neglect the influence of matrix elements (and in the approximation that the optical transition dominates the photoemission process), the low energy excitations of the system consist only in the band dispersion of the electrons. The $\delta-$functions being infinitely narrow, these excitations have an infinite lifetime. This is the logic consequence of the simple Hamiltonian considered here where no scattering mechanism was allowed. In order to improve this situation and to describe more realistic situation, the interaction should be considered appropriately. This is the goal of the next section.

### 2.4.3 The self-energy

To get more insight in the physics of realistic systems, interaction must be explicitly added to the non-interacting case studied in the previous section. As mentionned above, this interaction is treated perturbatively. We will quickly summarize results of the many-body theory to reach the definition of the self-energy. The interested reader is strongly advised to look at the rich literature in the domain to get a deeper understanding of this theory [22, 24].

In a first step, we write down an expression telling us how the exact ground state of the $N$-particle system $\psi_0$ can be obtained from the ground state $\phi_0$ of the non-interacting system

$$\psi_0(t=0) = S(0,-\infty)\phi_0. \tag{2.6}$$

The $S$-matrix appearing here is closely related to the usual evolution operator $U(t) = \mathrm{e}^{iH_0t}\mathrm{e}^{-iHt}$. In that sense, $S(0,-\infty)$ can be viewed as the operator transforming slowly $\phi_0$ into $\psi_0$ by switching on adiabatically the interaction. In the definition of the Green's function in equation 2.1, we can do the replacement $|\rangle = S(0,-\infty)|\rangle_0$. Long calculations lead to the expression

$$G(\vec{k},t-t') = \sum_{n=0}(-i)^{n+1}\int_{-\infty}^{+\infty}dt_1\cdots\int_{-\infty}^{+\infty}dt_n\langle|T\hat{c}(\vec{k},t)\hat{c}^\dagger(\vec{k},t')\hat{V}(t_1)\hat{V}(t_2)\cdots\hat{V}(t_n)|\rangle_0$$

(different connected) (2.7)

which shows explicitly the perturbation expansion with a sum over the different orders $n$. On the right hand side, all the operators in the average appear in the interaction representation. At each order $n$, these operators can be paired two-by-two in different manners and factorized thanks to Wick's theorem. Each factorized pair looks like $\langle|T\hat{c}(\vec{k},t)\hat{c}^\dagger(\vec{k},t')|\rangle_0$ and thus translates into an unperturbed Green's function. Therefore, each order produces a certain number of factorizations involving different unperturbed Green's function related to each other by interactions $\hat{V}$. These complicated mathematical objects can be represented graphically with the Feynman diagrams. The comment "different connected" to equation 2.7 means that only diagrams which cannot be seperated in different pieces without cutting any part and which have not been already encountered previously must be taken into account in the summation.

In a third step, it can be seen that two categories of Feynman diagrams exist: reducible and irreducible diagrams. Reducible diagrams are those that can be separated into irreducible ones. Then, all possible combinations of reducible diagrams can be generated by an iterative scheme which is called the Dyson equation which for a Green's function $G$ takes the form

$$G(\vec{k},\omega) = G_0(\vec{k},\omega) + G_0(\vec{k},\omega)\Sigma(\vec{k},\omega)G(\vec{k},\omega). \tag{2.8}$$

The new object introduced here, $\Sigma$, is called the (irreducible) self-energy. It is generally a complex function. It contains all the possible irreducible diagrams generated in the perturbation expansion. These different elements arise from the different interactions considered in the model. The Dyson equation 2.8 can be rewritten like

$$G(\vec{k},\omega) = \frac{G_0(\vec{k},\omega)}{1 - G_0(\vec{k},\omega)\Sigma(\vec{k},\omega)}$$

which corresponds formally to summing all the contributions appearing in the iterative process summarized by equation 2.8. Introducing our previous result $G_0$ for non-interacting electrons in a partially filled band (2.5) leads to an essential formula

$$G(\vec{k},\omega) = \frac{1}{\omega - (\varepsilon(\vec{k}) - \mu) - \Sigma(\vec{k},\omega)}. \tag{2.9}$$

This result tells us that the self-energy $\Sigma$ induces a correction which modifies the non-interacting band dispersion $\varepsilon(\vec{k})$ in view of the interactions in the system. More specifically, the real part of the self-energy renormalizes the non-interacting dispersion $\tilde{\varepsilon}(\vec{k},\omega) = \varepsilon(\vec{k}) - \mathrm{Re}\Sigma(\vec{k},\omega)$. Concerning the imaginary part of the self-energy $\Sigma$, we recall the definition of the Green's function and derive a simple example to give a feeling about its signification. In the case of an empty band (of dispersion $\varepsilon(\vec{k})$), the Green's function takes the form

$$G(\vec{k},t) = -i\langle c(\vec{k},t)c^\dagger(\vec{k},0)\rangle = -i\underbrace{\langle 0|\mathrm{e}^{iHt}c(\vec{k})}_{=\langle\psi_2(t)|}\underbrace{\mathrm{e}^{-iHt}c^\dagger(\vec{k})|0\rangle}_{=|\psi_1(t)\rangle}.$$

It can be understood as the projection of an initial state $|\psi_1(t)\rangle = \mathrm{e}^{-iHt}c^\dagger(\vec{k})|0\rangle$ where a particle is created at time $t = 0$ in the ground state and which evolves until time $t$ on a final state $|\psi_2(t)\rangle = c^\dagger(\vec{k})\mathrm{e}^{-iHt}|0\rangle$ where the ground state evolves first until time $t$ when a particle is created. A large overlap between $\psi_1(t)$ and $\psi_2(t)$ means that the time at which the particle is created does not change much. In other words, it means that this excitation of the ground state $|0\rangle$ is stable. Now we assume that the excitation is not

stable for some reason. This appears through an imaginary term in the energy of the excitation

$$\begin{aligned} G(\vec{k},t) &= -i\langle c(\vec{k},t)c^\dagger(\vec{k},0)\rangle = -i\langle 0|\mathrm{e}^{iHt}c(\vec{k})\mathrm{e}^{-iHt}c^\dagger(\vec{k})|0\rangle \\ &= -i\langle 0|\mathrm{e}^{i0t}c(\vec{k})\mathrm{e}^{-i(\varepsilon(\vec{k})-i\Gamma)t}c^\dagger(\vec{k})|0\rangle = -i\mathrm{e}^{-i(\varepsilon(\vec{k})-i\Gamma)t}\underbrace{\langle 0|c(\vec{k})c^\dagger(\vec{k})|0\rangle}_{=1} \end{aligned}$$

which can be directly Fourier transformed in frequency

$$G(\vec{k},\omega) = \frac{1}{\omega - \varepsilon(\vec{k}) + i\Gamma}.$$

By comparison with the Green's function 2.9, it directly emphasizes the link between the imaginary part of the self-energy and the dissipative channels in the model Hamiltonian, like phonon or impurity scattering or electron-electron scattering.

The signature of the self-energy in the spectral function is readily obtained by taking the imaginary part of the corresponding retarded Green's function (the retarded Green's function also obeys to a Dyson equation like 2.8, implying a retarded self-energy)

$$A(\vec{k},\omega) = -\frac{1}{\pi}\mathrm{Im}\, G^R(\vec{k},\omega) = -\frac{1}{\pi}\frac{\mathrm{Im}\,\Sigma^R(\vec{k},\omega)}{[\omega - (\varepsilon(\vec{k}) - \mathrm{Re}\,\Sigma^R(\vec{k},\omega) - \mu)]^2 - [\mathrm{Im}\,\Sigma^R(\vec{k},\omega)]^2}. \tag{2.10}$$

It represents a Lorentzian, whose width is given by the imaginary part of the self-energy, and whose position is the renormalized energy $\tilde{\varepsilon}(\vec{k},\omega)$. This important result makes explicit the spectroscopic signature of a given model whose physics is encapsulated in the self-energy $\Sigma^R$. This relation is useful in both directions. It allows to interpret the dispersions extracted from photoemission data in the framework of many-body physics [25, 26, 27] and also to predict the spectra specific to a particular model [28, 29].

### 2.4.4 Finite temperature Green's functions

Until now, Green's functions were calculated at zero temperature. However, real experiments are always done at finite temperature and, in the particular case of $1T$-$TiSe_2$, where the critical temperature of the transition is as high as $T_c \simeq 200$K, temperature effects cannot be neglected. Therefore, in this section, we give a very short summary of the finite temperature Green's function formalism and of the Matsubara technique used to compute these Green's functions.

To consider the effect of temperature, one generally couples the investigated system to a bath of other particles having an average energy related to temperature. Formally, the average computed in the previous section, $\langle\psi_0|...|\psi_0\rangle$, used in the definition of the Green's function 2.1, can be generalized to

$$\langle c(\vec{k},t)c^\dagger(\vec{k},t')\rangle := \frac{\mathrm{Tr}\ \mathrm{e}^{-\beta K}c(\vec{k},t)c^\dagger(\vec{k},t')}{\mathrm{Tr}\ \mathrm{e}^{-\beta K}}, \tag{2.11}$$

where the trace Tr denotes a summation over all possible states of the system. These states are weighted by the thermal factor $\mathrm{e}^{-\beta K}$ ($1/\beta = k_B T$), computed in the grand canonical ensemble with help of $K = H - \mu N$. The time evolution is also governed by

this potential

$$O(t) = \mathrm{e}^{iKt} O \mathrm{e}^{-iKt},$$

so that a perturbation expansion on $V$ (remember that $H = H_0 + V$) would be really cumbersome and would mix powers of $V$ and $H_0$. However, such an expansion involves terms from $\mathrm{e}^{-\beta K}$ and from $\mathrm{e}^{-iKt}$. Therefore, considering $\beta$ like the imaginary part of a complex time could unify both terms. The method of Matsubara does exactly the converse, since it treats time as the imaginary part of a complex temperature $\tau$, so that only one $S$-matrix expansion is necessary, provided that $t \mapsto -i\tau$.

In that context, finite temperature Green's functions will be defined like

$$G(\vec{k}, \tau) = -\langle |T c(\vec{k}, \tau) c^\dagger(\vec{k}, 0)| \rangle, \tag{2.12}$$

with the average $\langle ... \rangle$ given by equation 2.11 and the imaginary time evolution governed by

$$O(\tau) = \mathrm{e}^{K\tau} O \mathrm{e}^{-K\tau}.$$

Compared to the definition 2.1, we see that the imaginary unit $i$ disappeared. Together with the symbol $\tau$, this information tells us that we are working at finite temperature. The Fourier transform of this complex temperature $\tau$ into frequency space is done according to

$$G(\vec{k}, i\omega_n) = \int_0^\beta d\tau \, G(\vec{k}, \tau) \, \mathrm{e}^{i\omega_n \tau}. \tag{2.13}$$

The imaginary frequencies appearing here are called the Matsubara frequencies and their value depends on the type of particle investigated,

$$\omega_n = \begin{cases} 2n\pi/\beta & \text{for bosons,} \\ (2n+1)\pi/\beta & \text{for fermions.} \end{cases}$$

These relations come from the fact that Green's functions defined with an imaginary time are periodic function of periodicity $\beta$.

An important relation, which we give here without any proof, permits to relate the finite temperature Green's function to the retarded Green's function,

$$G_{ret}(\vec{k}, \omega) = G(\vec{k}, i\omega_n \mapsto \omega + i\eta). \tag{2.14}$$

Such a conversion is also valid for self-energies.

### 2.4.5 Calculations at finite temperature

In many instances, we will obtain Green's functions in frequency space, where (time) differential equations simplify to algebraic equations. In that cases, the information on temperature is hidden in these peculiar Matsubara frequencies. Going back to time space will allow us to retrieve this information. This is formally done with an inverse Fourier transform

$$G(\vec{k}, \tau) = \frac{1}{\beta} \sum_{i\omega_n} G(\vec{k}, i\omega_n) \, \mathrm{e}^{-i\omega_n \tau}. \tag{2.15}$$

To illustrate the utility of such a formula, we consider again the case of non-interacting electrons in a band. The calculations are very similar to what has been already done in

section 2.4.2. The derivative of the annihilation operator reads

$$\partial_\tau c(\vec{k},\tau) = [c(\vec{k},\tau), H] = (\varepsilon(\vec{k}) - \mu)c(\vec{k},\tau).$$

Note that the imaginary unit $i$ does not appear here, since we are working in imaginary time. Inserting this in the non-interacting Green's function leads to

$$\partial_\tau G_0(\vec{k},\tau) = -\delta(\tau) - (\varepsilon(\vec{k}) - \mu)G_0(\vec{k},\tau),$$

so that Fourier transforming this expression with definition 2.13 and isolating $G_0(\vec{k}, i\omega_n)$ results in

$$G_0(\vec{k}, i\omega_n) = \frac{1}{i\omega_n - (\varepsilon(\vec{k}) - \mu)}.$$

As we will see later when discussing BCS theory in section 4.1, we will have to evaluate zero time Green's functions, like $G(\vec{k}, \tau = 0)$. This is done using relation 2.15

$$G(\vec{k}, \tau = 0) = \frac{1}{\beta}\sum_{i\omega_n} G(\vec{k}, i\omega_n). \tag{2.16}$$

The key point here is to realize that for fermions, the Matsubara frequencies $i\omega_n = i(2\pi + 1)n/\beta$ are the poles of the Fermi distribution $n_F(z)$. Therefore, the elements summed in equation 2.16 are the residues of $G(\vec{k}, z)N_F(z)$ coming from the Fermi distribution (up to a factor $-1/\beta$). This allows us to use the residue theorem on this expression and to write

$$I = \lim_{R\to\infty}\int \frac{dz}{2\pi i} G(\vec{k}, z)N_F(z) = -\frac{1}{\beta}\sum_{i\omega_n} G(\vec{k}, i\omega_n) + \sum_\alpha Res\left[G(\vec{k}, z_\alpha)\right] N_F(z_\alpha).$$

Here $z_\alpha$ are the poles of $G(\vec{k}, z)$, where the residues $Res[...]$ of $G(\vec{k}, z)$ are evaluated. The contour integration $I$, which is done on a large circle of radius $R$, vanishes for $R \to \infty$, so that

$$\frac{1}{\beta}\sum_{i\omega_n} G(\vec{k}, i\omega_n) = \sum_\alpha Res\left[G(\vec{k}, z_\alpha)\right] N_F(z_\alpha).$$

In our case of non-interacting electrons in a band, the Green's function has only one pole at $z_1 = \varepsilon(\vec{k}) - \mu$, giving rise to a unit residue $Res\left[G(\vec{k}, z_1)\right] = 1$. The final result is then

$$G(\vec{k}, \tau = 0) = N_F(\varepsilon(\vec{k}) - \mu).$$

This result could have been directly obtained by taking the limit $\tau \to 0$ with $\tau < 0$ (this is a convention [22]) of the Green's function

$$G(\vec{k}, \tau = 0^-) = \langle c^\dagger(\vec{k}, 0)c(\vec{k}, 0)\rangle = N_F(\varepsilon(\vec{k}) - \mu).$$

# Chapter 3

# Transition metal dichalcogenides

## 3.1 Principles of the CDW: the Peierls transition

The collective phenomenon of a CDW is widely discussed in the condensed matter community. In a first approach, one generally associates the occurence of a CDW to the particular case of a Peierls transition [30]. This Peierls scenario is a good pedagogical starting point to understand a possible origin of a CDW.

One considers a one-dimensonal lattice of spacing $a$, such that its electronic structure consists of a half-filled free-electron-like band. In that case, the Fermi wave vector is $k_F = \pm\pi/2a$. This situation is depicted in Fig. 3.1 (left). Then, working in the quasi-free electron model (where the interaction of electrons with the underlying lattice is weak), the basic idea of the Peierls transition comes from the observation that if, for some reason, the system doubles its lattice periodicity, gaps will open around $k_F$. This will lower the near-$k_F$ occupied electronic branch, allowing the system to gain electronic energy. However, in practice, to double the lattice periodicity, ions should shift a little bit to dimerize, generating a lattice elastic energy cost, which should be balanced by the electronic energy gain to make this scenario profitable for the system. This model Peierls transition is notably characterized by a gap opening at $E_F$. Consequently, it is a

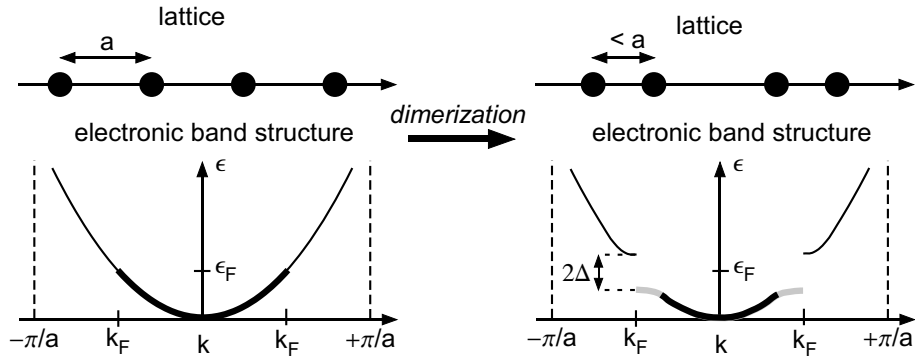


FIGURE 3.1: Cartoon pictures of the Peierls transition in a one-dimensional chain of atoms. On the left, the atomic arrangement and the corresponding electronic band structure before the transition. On the right, the atomic arrangement and the corresponding electronic band structure after the transition.

metal-insulator transition. The corresponding atomic and electronic structure after this transition is shown in Fig. 3.1 (right).

A simple theoretical approach to this problem is given by linear response theory applied to a free electron gas. The main results are given here, but more details can be found elsewhere [23, 31]. One considers the effect of an external (space dependent) field $F_{ext}$ which couples to an observable $O(\vec{r})$ of the system through a term like

$$V_{ext} = \int d\vec{r} F_{ext}(\vec{r}) O(\vec{r}).$$

This interaction can be treated perturbatively, in a manner similar to the interaction $\hat{V}_{ext}$ in the Green's function expansion of equation 2.7. In that sense, one assumes that this interaction term $V$ is switched on adiabatically at $t = -\infty$. Then, to linear order in $F_{ext}$, the expectation value of the observable $\langle O \rangle$ reads

$$\langle O \rangle = \lim_{\eta \to 0} \left( -\frac{i}{\hbar} \right) \int d\vec{r}\,' F_{ext}(\vec{r}) \int_{-\infty}^{0} dt' \mathrm{e}^{\eta t'} \langle |[O(\vec{r}, t), O(\vec{r}\,', t')]| \rangle_0 \tag{3.1}$$

where $O(\vec{r}, t)$ is the time evolved operator $O(\vec{r})$ in the Heisenberg picture. In equation 3.1, the averaged quantity on the right hand side is identified as a correlation function, also called general (linear) susceptibility,

$$\chi(\vec{r}, \vec{r}\,', t, t') := -\frac{i}{\hbar} \theta(t - t') \langle |[O(\vec{r}, t), O(\vec{r}\,', t')]| \rangle_0.$$

Replacing back into equation 3.1 and extending the time integral to absorb the $\theta$-function, one gets

$$\langle O \rangle = \lim_{\eta \to 0} \int d\vec{r}\,' F_{ext}(\vec{r}) \int_{-\infty}^{+\infty} dt' \mathrm{e}^{-\eta |t'|} \chi(\vec{r}, \vec{r}\,', t, t').$$

Therefore, the general susceptibility is a measure of how strong a given observable of a system will respond to an external perturbation. It contains all the many-body physics of that system.

As a particular case, we consider a many-electron system coupled to an external electrostatic potential, $F_{ext} = \phi_{ext}$, and study its influence on the charge density $O(\vec{r}) = \rho(\vec{r})$. $\chi$ represents then the electronic susceptibility and is a density-density correlation function. If we neglect the interaction between electrons (and define $|\rangle_0$ as the filled Fermi sea), it can be shown that the static electronic susceptibility in reciprocal space takes the form

$$\chi^{(0)}(\vec{q}, \omega = 0) = \sum_{\vec{k}} \frac{N_F(\varepsilon(\vec{k})) - N_F(\varepsilon(\vec{k} + \vec{q}))}{\varepsilon(\vec{k}) - \varepsilon(\vec{k} + \vec{q})}. \tag{3.2}$$

This is a very interesting formula, since we already guess that something spectacular may happen when the denominator in the sum cancels. This can be the case for well-chosen values of $\vec{q}$. As mentionned above, $\chi^0$ is a density-density correlation function (for non-interacting electrons). It follows that poles of such a correlation function represent stable (electron-hole) excitations of the system. At $\omega = 0$, these excitations enter in competition with the ground state. If these poles develop at $\vec{q} \neq 0$, the corresponding

excitations form a static and periodic charge modulation, the CDW, which breaks the translational symmetry of the inital ground state. To get a more precise idea of this effect and to draw a link with the Peierls transition sketched above, we restrict ourselves to a one-dimensional electron gas and perform the summation over $\vec{k}$, leading to

$$\chi^{(0)}(q, \omega = 0) = -\frac{e^2 m}{\pi \hbar^2 q} \ln \left| \frac{q + 2k_F}{q - 2k_F} \right|.$$

This simple result confirms our previous hypothesis. When $q = 2k_F$, the susceptibility diverges, so that, at this wave vector, the response of the charge density to $V_{ext}$ becomes infinitely large. This means that an infinitesimal external perturbation of the system will give rise to a drastic rearrangement of the charge density, but at a particular wave vector $q = 2k_F$. This corresponds therefore in turn to a CDW of period $\lambda = 2\pi/q = \pi/k_F$.

The condition $q = 2k_F$ in the CDW mechanism brings up an important remark. It means that the topology of the Fermi surface (defined as the set of all wave vector $k_F$) is intimately related to a possible unstability of the charge density towards a CDW. However, the preceding argument was developed in one-dimension. Generalization can be reached by integrating equation 3.2 in higher dimensions. It turns out that in two dimensions already, the divergency of the charge susceptibility disappears. However, the form of the sum in equation 3.2 still implies that the states near the Fermi surface dominate its result. Therefore, if a high number of states near $E_F$ fulfill $\varepsilon(\vec{k_F}) \approx \varepsilon(\vec{k_F} + \vec{q}_0)$ for the same $\vec{q}_0$ wave vector, the static susceptibility may display a maximum at $\vec{q}_0$. In other words, this happens when large segments of the Fermi surface are parallel and connected by a single wave vector $\vec{q}_0$. This condition is called *nesting*. In general, the lower is the dimension of the system, the more important the nesting is.

Examples of a quasi-one-dimensonial system exhibiting a CDW transition and a Fermi surface topology compatible with excellent nesting conditions are for instance $NbSe_3$ [32] or $(TaSe_4)_2I$ [33]. In quasi-two-dimensional systems, $CeTe_3$ presents a complicated Fermi surface which offers parts favorable for nesting [34]. As a consequence, only those bands involved in nesting are gapped at $E_F$. The TMDC family offers numerous examples of layered compounds with a CDW transitions [35, 36, 37]. However, for some members of this family, the explanation of the occurence of the CDW phase with the nesting scenario is not always obvious. A detailed introduction to the TMDCs will be given below.

It is worth mentionning here a recent work by M.D. Johannes and I.I. Mazin [38]. In this work, they notify that a large misconception about the origin (and the definition) of CDWs spread over the scientific community. In their opinion, a "CDW" term is reserved for a Peierls-like instability that occurs due to a divergence in the real part of the electronic susceptibility (the static electronic susceptibility derived above is purely real). In fact, this electronic instability, leading to a CDW, would appear even without any structural distortion. Of course, in real materials, a PLD always develops in parallel to the CDW, due to the interaction between the lattice and the electrons. They show that even for a prototypical one-dimensional system, the divergency of the real part of the susceptibility is fragile with respect to temperature, imperfect nesting or scattering. These realistic effects transform the divergency into a simple peak.

Their work supports the idea that Fermi surface nesting is at least not strong enough to generate a CDW. In the worst case, it would play a minor role and we should pay more

attention to the electron-phonon interaction as a possible origin of the CDW. In that sense, no true distinction would exist between a CDW and a structural phase transition.

This study casts doubts on the conventional idea of nesting as a possible origin to CDWs. However this criticism will probably initiate a debate which should lead to a better understanding of nesting.

## 3.2 Collective phenomena in the TMDC family

TMDCs are layered compounds of chemical composition $MX_2$. $M$ stands for a transition metal, which is an element having an incomplete $d$ sub-shell (group 3 to 10 of the periodic table of the elements), and $X$ stands for a chalcogen (element of the group 16), usually S, Se or Te. They consist of $X-M-X$ layers, weakly bound together by Van der Waals interactions and they belong to different polytypes denominated $1T$, $2H$, $3R$, $4H_a$, $4H_b$ or $6R$, where the figure describes the number of such layers per unit cell [39]. $T$, $H$ and $R$ refer to the symmetry of the unit cell, namely trigonal, hexagonal or rhombohedral, respectively. The $1T$ and the $2H$ polytypes will be discussed in more details below. The weak coupling between $MX_2$ layers brings up two advantages for photoemission. First, it is easy to cleave the sample in vacuum to obtain a clean surface for photoemission. Secondly, it implies that the dispersion in $k_z$ direction, perpendicular to the surface, is weak, so that the system can be considered quasi-two dimensional. Therefore it is less important to do excitation energy dependent measurements (to span the $k_z$-direction) and the $k_z$-broadening due to the complicated form of the photoemission final state is limited (remember the discussion at the end of section 2.3).

Usually, in solid state physics, reduced dimensionality generates complex phase diagrams with non-Fermi liquid ground states. One can understand this by noticing that the lower the dimensions of the system are, the less possibilities the particles have to avoid each other, and therefore the stronger are the correlation effects. We can also appeal to the concept of nesting developed previously (section 3.1). With reduced dimensionality, nesting possibilities are larger, enhancing the electronic susceptibility so that the response of the system to instabilities is increased. To illustrate this discussion, we refer to different studies of TMDCs where CDW and superconductivity phases have been discovered.

**$1T$-$TaSe_2$.** $1T$-$TaSe_2$ exhibits an incommensurate ($\sqrt{13}\times\sqrt{13}$) CDW at high temperature, while at low temperature the CDW locks into a commensurate $\sqrt{13}\times\sqrt{13}$-R13.9° [40]. No clear mechanism has been proposed for its origin, but both the electron-electron and the electron-phonon interactions are thought to be important components of the CDW driving force [41].

**$1T$-$TaS_2$.** Similarly to $1T$-$TaSe_2$ , $1T$-$TaS_2$ displays an incommensurate ($\sqrt{13}\times\sqrt{13}$) CDW at high temperature and a commensurate $\sqrt{13}\times\sqrt{13}$-R13.9° at low temperature [40]. However, the situation is slightly more complicated, since the system transits through a quasi-commensurate phase at intermediate temperatures. The origin of its CDW is not clear yet and a Mott transition has been put forward to explain the low temperature commensurate phase which is accompanied by an increase in the resistivity [42]. The observation of broad dispersive features below $E_F$ and the absence of clear quasi-particles at $E_F$ in the commensurate phase incited Clerc *et al.* to propose a polaron-based phase at low temperature instead of nesting [43, 44].

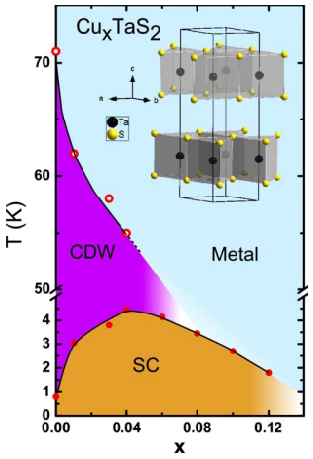


FIGURE 3.2: Phase diagram of $2H$-$TaS_2$ under intercalation of Cu [46].

**$2H$-$TaS_2$.** The $2H$ polytype of $TaS_2$ also undergoes a CDW transition below 70K, but it additionnally exhibits superconductivity below 1K (see the corresponding phase diagram in Fig. 3.2). This competition between CDW and superconductivity is a very motivating playground for both experimental and theoretical physics. TMDCs are in general very favorable to intercalation of foreign atoms in their Van der Waals gap, which opens new opportunities for studying CDW phase. Wagner *et al.* have studied $TaS_2$ intercalated with Cu up to 12%. They saw that intercalation of Cu progressively kills the CDW phase, but enhances superconductivity whose critical temperature increases up to 4K at $x \simeq 4\%$.

**$2H$-$TaSe_2$.** Borisenko *et al.* explored in details the Fermi surface of $2H$-$TaSe_2$ [45]. This material undergoes first an incommensurate CDW phase transition at 122K and then a commensurate $(3 \times 3)$ CDW transition at 90K. They were able to evidence a significant nesting of the Fermi surface which is in agreement with the observed CDW.

**$1T$-$NbTe_2$.** Finally Battaglia *et al.* investigated the case of $NbTe_2$, which stabilizes in a monoclinically distorted version of the trigonal $1T$ polytype, that can be interpreted as a $(3\times1)$ CDW [36]. Below $\sim 0.6$K, it enters into a superconductivity phase. A comparison of the Fermi surface measured with ARPES and calculated with DFT evidences the possibility of a nesting instability at the correct wave vector, which is related to a singularity in the RPA susceptibility. This scenario is supported by ab initio phonon calculations that display imaginary modes at the same wave vector. This study therefore concludes that Fermi surface nesting and electron-phonon coupling play a key role in the CDW of $NbTe_2$.

This short review of selected TMDCs emphasizes that demonstrating the role of nesting in the instability of a system towards a CDW phase is subtle and seldom completely achieved. As mentionned above, nesting in two dimensions is generally imperfect and probably only plays an intermediate role. It is then often necessary to look for other mechanisms which can act in addition to nesting or not. Nonetheless, ARPES turns out to be the most adequate technique to investigate the Fermi surface of TMDCs and to reveal or rule out the possibility of nesting. It is also an excellent tool for evidencing a CDW as it probes the electronic degrees of freedom.

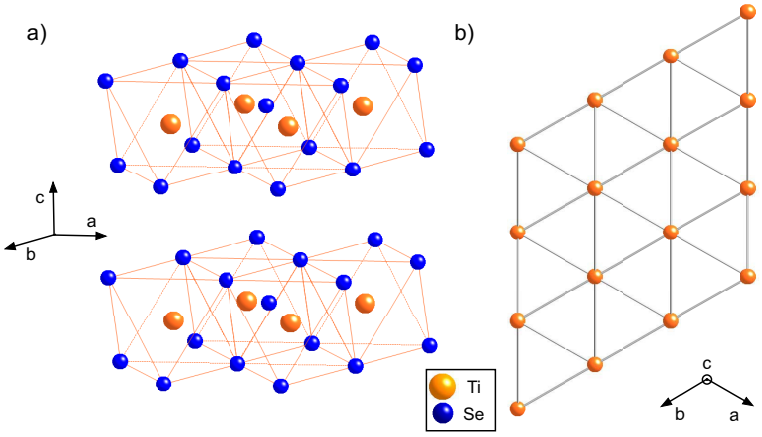


FIGURE 3.3: Structure of $1T$-$TiSe_2$. (a) It consists of Se-Ti-Se layers where Ti is in octahedral coordination with Se. (b) The Ti atoms form a triangular lattice in the $a-b$ plane.

**$1T$-$TiSe_2$.** One particular TMDC has not been discussed above. It crystallizes in the $1T$ polytype and develops a CDW with intense spectral weight with a high transition temperature. This system, $1T$-$TiSe_2$, is the central topic of this thesis.

## 3.3 The particular case of $1T$-$TiSe_2$

### 3.3.1 Description of the system

In this section, we will summarize the main information about $TiSe_2$ which is available in the literature. This will of course not be exhaustive, as this system has been much studied since 1960. It regained interest in 2005 when Morosan *et al.* discovered superconductivity in its Cu intercalated version [47].

**Atomic structure.** $1T$-$TiSe_2$ is a TMDC of the $1T$ polytype, having one Se-Ti-Se layer per unit cell where the Ti atom is in octahedral coordination with the neighbouring Se atoms (Fig. 3.3 (a)). The Ti atoms form a triangular lattice in the $a-b$ plane. At room temperature, it crystallizes into the $P\bar{3}m1$ space group, displaying a trigonal symmetry, with unit cell parameters $a = b = 3.54$Å and $c = 6.001$Å. It has a threefold symmetry around the $c$-axis.

$TiSe_2$ is particularly interesting because it undergoes a phase transition towards a commensurate $(2 \times 2 \times 2)$ CDW phase at $T_c \cong 200$K. The CDW phase is accompanied by a PLD which is schematically depicted in Fig. 3.4 (a) and has been observed by analyzing neutron diffraction measurements on the basis of symmetry arguments [48]. The displacements of the atoms are rather small, Ti atoms being shifted by 0.083 Å and Se atoms by 0.028 Å (at 77K). Fig. 3.4 (b) shows the temperature evolution of a superlattice spot intensity, which attests to the onset of the PLD at $T_c$. It follows a mean-field curve, with a zero-intensity above $T_c$, meaning that (nearly) no fluctuations take place in this regime. Holt *et al.* performed x-ray thermal diffuse scattering to investigate the behaviour of the phonon mode $(L_1^-)$ involved in the PLD around $T_c$ [49]. They clearly evidenced a phonon mode softening at $T_c$ (Fig. 3.4 (c)), which confirms that the lattice strongly reacts at the CDW phase transition.

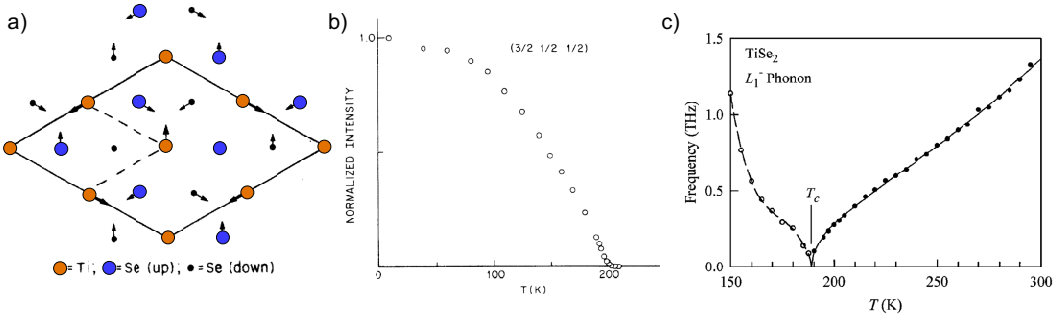


FIGURE 3.4: (a) Schematic view of the PLD affecting $1T$-$TiSe_2$ below $T_c$. (b) Intensity of the superlattice superspot at $(3/2, 1/2, 1/2)$ as a function of temperature (from neutron diffraction measurements) [48]. (c) Temperature dependence of the frequency of the $L_1^-$ phonon mode deduced from x-ray thermal diffuse scattering [49].

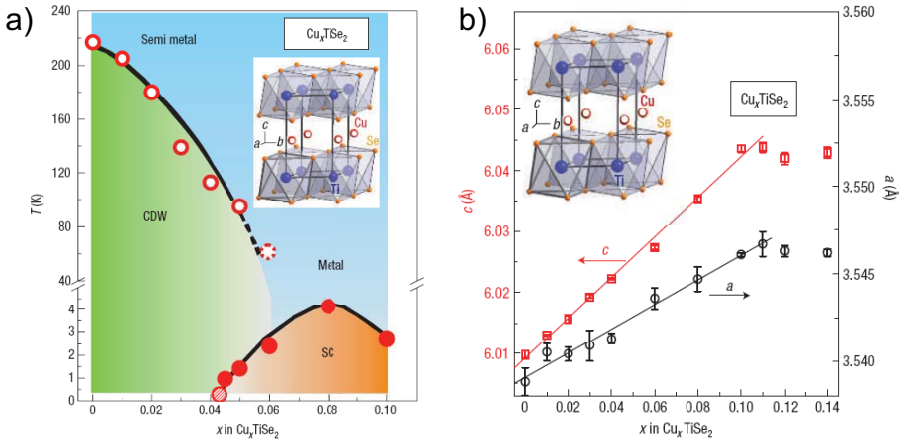


FIGURE 3.5: (a) Phase diagram of $TiSe_2$ intercalated with low amounts of Cu. (b) Lattice parameters expansion as a function of Cu doping $x$ [47].

Due to its layered structure and to the weak forces binding the different layers, $TiSe_2$ turns out to be an excellent candidate for intercalation in the Van der Waals gap. Many different works treated this subject with different doping elements like Ni [50], Fe [51], Cr, Mn [52], Rb [53], Ag [54], the most interesting being that of Morosan *et al.* who discovered a superconductive dome (at $T_c = 4.15$K) with about 8% of Cu [47]. They built a phase diagram which is reproduced in Fig. 3.5 (a). It emphasizes the possible competition between the CDW and the superconductivity phases. Fig. 3.5 (b) shows the lattice parameters evolution upon Cu doping. It indicates a systematic expansion until 11%, which is the limit of solubility of Cu reached in this work.

**Transport**. The CDW transition has a strong signature in the transport properties of $TiSe_2$ [55]. Fig. 3.6 (a) shows the electrical resistivity and the Hall resistance as a function of temperature. The room temperature value of the resistivity of $TiSe_2$ is that of a semiconductor or a semimetal. Upon decreasing the temperature, the resistivity increases strongly above $T_c$, reaches a maximum below $T_c$, at $\sim$ 160K, and then falls again. A kink in the curve appears at $T_c$. The sign of the Hall resistance $R_H$, inversely proportional to the charge carrier density, is important, as it gives information on their nature. Above $T_c$, $R_H > 0$ and the transport is dominated by holes. $R_H$ changes its sign at $T_c$ so that at low temperature electrons become the dominant charge carriers.

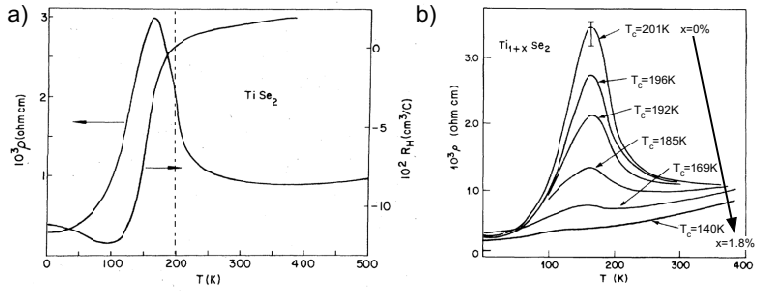


FIGURE 3.6: (a) Electrical resistivity and Hall resistance in the $a-b$ planes for $TiSe_2$ [48]. (b) Electrical resistivity as a function of the overdoping of Ti with the corresponding critical temperature $T_c$ [55].

In chapter 6, we will present a more detailed analysis of this subject in the framework of the exciton condensate phase model.

As emphasized by Di Salvo *et al.*, the preparation of the $1T$-$TiSe_2$ samples is delicate. They noticed that the temperature during the growth of the samples had a strong influence on the critical temperature of the CDW transition [55]. To quantify this effect, they performed a systematic study and found out that it was due to deviations from the ideal stoichiometry. They concluded that the higher the growth temperature, the higher the amount of excess Ti atoms $x$ in $Ti_{1+x}Se_2$. This excess doping, which is probably situated in the Van der Waals gap of the sample, lowers the critical temperature of the transition. This result is depicted in Fig. 3.6 (b).

**Calculated electronic structure**. This information allows us to perform calculations to get an idea about the ground state band structure of the system. Fig. 3.7 (b) shows the band structure of $1T$-$TiSe_2$ calculated in DFT within LDA with the program Wien2k (see section B.2 for a short introduction to DFT) [56]. The $\Gamma MLA$ $\vec{k}$-path along which DFT has been performed is indicated in the Brillouin zone of Fig. 3.7 (a), together with other characteristic high symmetry points. Looking at the near-$E_F$ situation, we see that DFT predicts a metallic configuration for $TiSe_2$, since the overlap between the bands at $\Gamma$ and those at $L$ is $\sim 0.5$ eV. From a band character analysis, we learn that the bands at $\Gamma$ are Se4$p$-derived, while the band at $L$ is Ti3$d$-derived. They will mostly be refered to as valence and conduction bands in this thesis. A schematic Fermi surface which corresponds to this situation is represented in Fig. 3.7 (c). It consists of a hole pocket in its center ($\Gamma$) and two groups of three symmetry equivalent electron pockets at $L$ and $L'$.

**Measured electronic structure**. Since the year 2000, many different high-resolution ARPES studies have been carried out on $1T$-$TiSe_2$. In these studies, a central issue is the nature of the $TiSe_2$ gap at room temperature. Pillo *et al.* focussed on the position of the conduction band [57], which is a delicate problem since this band is very close to $E_F$. From their analysis, the conduction band turned out to be above $E_F$, at 10 meV at room temperature. Relying on "old" ARPES results of Anderson *et al.* who derived a valence band maximum at 15 meV [58], they inferred a semimetallic configuration for $TiSe_2$. This allowed them to appeal to the excitonic insulator phase as the driving force of the CDW. We will come back on this exotic phase extensively in chapter 4. A study performed two years later with synchrotron light has been published by Kidd [59]. They resolved the topmost valence band at a binding energy of $-30$ meV and the conduction band at about 10 meV above $E_F$, in the unoccupied states. They obtained therefore a

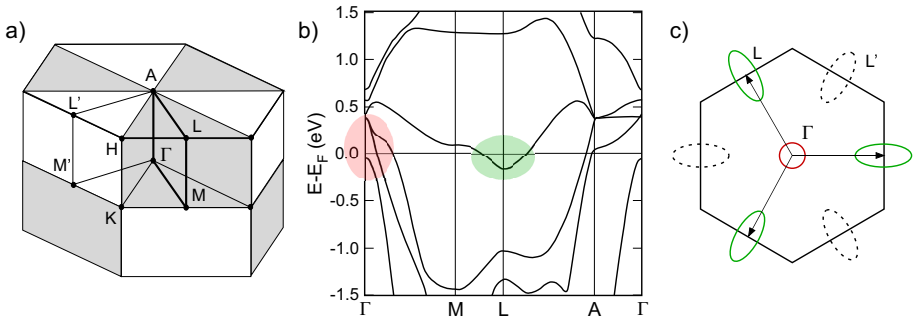


FIGURE 3.7: (a) Brillouin zone of the trigonal space group $P\bar{3}m1$. (b) Band structure of $1T$-$TiSe_2$ along high symmetry directions, calculated in DFT within LDA. (c) Schematic Fermi surface corresponding to this band structure.

positive gap of about $\sim 40$ meV, leading to a semiconducting configuration. To model their measurements, they built an effective Hamiltonian containing three Ti3*d*-derived conduction bands and two Se4*p*-derived valence bands coupled together by an electron-hole interaction. A crystal-field splitting term was also introduced to lift the degeneracy between their symmetry-related conduction bands. This model Hamiltonian was used to fit the low temperature experimental dispersions and allowed them to support a mechanism mixing an excitonic insulator phase (due to the electron-hole coupling) and a Jahn-Teller distortion (due to the crystal-field splitting) for the origin of the CDW phase. At the same time, Rossnagel *et al.* performed ARPES measurements over a wide range of temperature, from 300K to 100K [60]. From the leading edges of the valence and conduction bands, they evidenced shifts as a function of temperature of about $\sim 60$ meV and $\sim 30$ meV respectively. Using a simple two-band Drude-like model for conduction, they were able to explain qualitatively the Hall resistance and the increase of the resistivity (see Fig. 3.6). From their results, they favoured the Jahn-Teller mechanism, by comparison with the calculation of Motizuki *et al.* based on a microscopic model for such a mechanism [61]. We will come back to this discussion in chapter 7. However they could not unambiguously distinguish between a semimetallic or semiconducting configuration at room temperature. Finally, Rasch *et al.* found recently a smart way of by-passing the problem of determining the position of a band in the unoccupied states [62]. They adsorbed $H_2O$ on the surface of a $TiSe_2$ sample, causing this way a distinct band bending which shifted the band structure into the occupied states. With this technique, they were able to infer a gap of 150 meV, evidencing a clear semiconducting configuration. This result is quite surprising since it is in quantitative disagreement with all the previous studies, implying band extrema that are more than 50 meV away from $E_F$.

According to DFT, which is a theory involving an effective single-particle Hamiltonian, the overlap between the valence and conduction bands is so large, that this system is predicted to be a metal in its ground state (at $T = 0$K). As we know from chapter 2, ARPES investigates the low energy excitation spectrum of a system. However, in such a comparison between DFT and ARPES, one usually hopes that the correlations are not too strong such that the measured spectra do not differ too much from the ground state of the system.

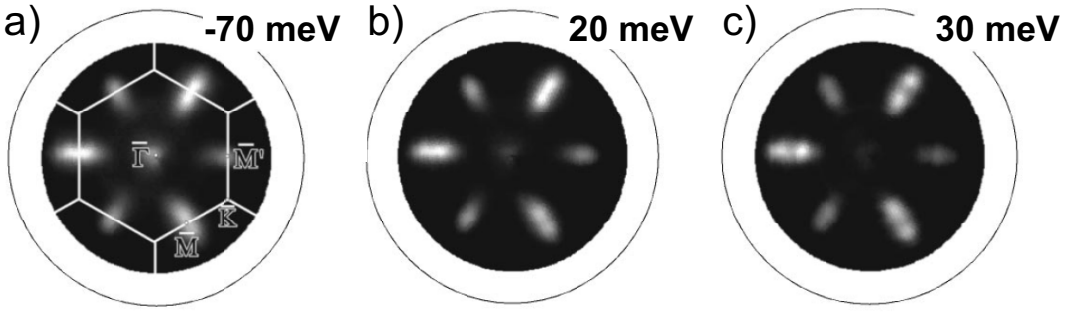


FIGURE 3.8: Constant energy surface mappings of $1T$-$TiSe_2$ taken at room temperature at binding energies of (a) -70 meV, (b) 20 meV and (c) 30 meV [57].

### 3.3.2 Origin of the CDW

From the previous paragraph, it emerges that different scenarios have been proposed for the origin of the CDW phase of $1T$-$TiSe_2$. In this section, we will enumerate them and describe them in more details.

**Fermi surface nesting**. After the first studies on $TiSe_2$, nesting was proposed as the driving force of the CDW transition, although the shape of its Fermi surface was not exactly known [48]. With their early DFT calculations, Zunger and Freeman also subscribed to this idea. However, as we will see later, DFT alone fails to reproduce the room temperature band structure of $TiSe_2$. Furthermore, looking at the constant energy surface mappings of Pillo *et al.* reproduced in Fig. 3.8, we immediately see that the nesting possibilities in the vicinity of the Fermi level are very tiny, due to the different shapes of the hole and electron pockets.

**Phonon mode softening**. Stimulated by the high lattice polarizability of $TiSe_2$ inferred from optical data, White and Lucovsky suggested that the CDW transition may occur by a coupling of the electronic degrees of freedom to a soft phonon mode [63]. This transition can be seen as an antiferroelectric transition. However, the origin of this soft phonon mode stays unclear.

**Band Jahn-Teller effect**. On the basis of band structure calculations, Hugues pointed out that, when going from an octahedral to a trigonal coordination (for Ti atoms with respect to Se atoms), the lowest $d$-band is lowered in energy [64]. Looking carefully at the PLD depicted in Fig. 3.4 (a), we see that the local coordination of Ti atoms tends towards trigonal. Hugues noticed that this PLD is in fact an antiferroelectric distortion. Furthermore this scenario depends strongly on the partial occupation of the lowest $d$-band, since the electronic energy gained by the lowering of these occupied states would be balanced by the elastic energy cost of the lattice distortion.

**Excitonic insulator phase**. The excitonic insulator phase as the origin of the CDW phase in $1T$-$TiSe_2$ relies on the electron-hole coupling between bands separated by an indirect gap or overlap. This will be the main subject of this thesis and it will be introduced in details in chapter 4. It has a purely electronic origin and the PLD is rather a consequence of it (see chapter 7 for this discussion).

# Chapter 4

# The exciton condensate phase

In 1961, Mott considered a system of two bands separated by a gap and predicted that the number of free carriers would not vary continuously as one compresses such a system to decrease its gap [65]. He noticed that at a low carrier density, the Coulomb force between electrons excited accross the gap and holes left behind would create bound states of electrons and holes, called excitons, which would not participate in the free carrier density. As the number of free carriers increases with the decreasing gap, the screening of the Coulomb force intensifies so that at some point it would not lead to electron-hole bound states anymore and the free carrier density would jump to a higher value.

Two years later, Knox considered the role of the Coulomb interaction in particular and remarked that, if the exciton binding energy $E_B$ exceeded the indirect band gap $E_G$, then the conventional insulating ground state would be unstable against the formation of excitons and a transition to a new phase would result [66]. More quantitatively, the system must fulfill the condition

$$E_B = \frac{\mu}{m_0} \frac{13.6\,\mathrm{eV}}{\epsilon_r^2} > E_G, \tag{4.1}$$

where $1/\mu = 1/m_e + 1/m_h$ is the reduced mass of the exciton, formed by an electron of mass $m_e$ and a hole of mass $m_h$ ($m_0$ is the bare electron mass). $\epsilon_r$ is the relative dielectric constant of the material hosting the excitons. The corresponding phase diagram for this excitonic insulator phase is represented in Fig. 4.1. At zero temperature, this exotic phase appears on the semiconductor side, if $E_G < E_B$. From the semimetallic side, the situation is different. Indeed, the more semimetallic the system is, the higher the density of electrons at $E_F$, leading to a better screening of the Coulomb interaction, so that the binding of electrons and holes will be less efficient. Of course, temperature plays an important role, as it destroys excitons when it overcomes their binding energy.

A few years later, different papers went further into this problem. In their seminal work, Keldysh and Kopaev studied a band structure consisting of one valence band and one conduction band seperated by an indirect gap $E_G$ [3]. They focussed on the case of a balanced semimetal, $E_G < 0$, where the valence and conduction bands are isotropic and of same effective mass. Then, they considered the instability of the ground state (with no interaction) towards pairing of electrons from the conduction band and holes from the valence band through a screened Coulomb interaction. They realized that the

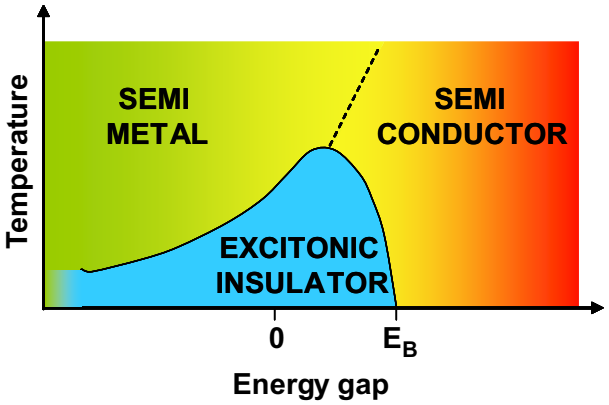


FIGURE 4.1: The temperature vs size of the gap $E_G$ phase diagram of the excitonic insulator phase (derived from reference [2]).

energy spectrum of this system is the same than that of a superconductor. Indeed, their technical treatment of this problem was very similar to that of BCS superconductors. They could also show that the electrons and holes are paired in singlet states. However, they emphasized that this transition transforms a semimetal at high temperature into a semiconductor at low temperature. Furthermore, contrarily to BCS superconductors, they found that the size of the gap is inversely proportional to the electron density.

At the same time, Jérome *et al.* addressed a similar situation, but generalized to systems with a positive (semiconductor) or negative (semimetal) gap $E_G$ and with valence and conduction bands of different effective masses [2]. They arrived at similar conclusions concerning the new ground state, which they named the excitonic insulator phase, and they evidenced its new long-range order characterized by the wave vector $\vec{w}$, being the distance between the extrema of the valence and conduction bands. In their paper, Jérome *et al.* also studied the general response of the excitonic insulator phase, from which collective modes, response to a static magnetic field and conductivity were calculated.

Zittartz generalized further the discussion of the excitonic insulator phase to the case of anisotropic bands [67] and also to the presence of normal impurities [68]. He showed that the anisotropy leads to qualitatively new features for a semimetallic region and that strong anisotropy of the bands involved in the pairing tends to destabilize the excitonic insulator phase. Zittartz also arrived at the conclusion that impurities have a pair breaking effect for excitons, similarly to the effect of magnetic impurities in BCS superconductivity.

We emphasize that there is here an essential difference between this type of exciton condensate, which forms spontaneously in a semimetallic or semiconducting material, and the more usual case of excitons created in semiconductors with larger gaps. Indeed, in the latter case, these excitons do not form spontaneously. Due to the larger gap size, electrons and holes have a very low density and the rare excitons decay rapidly (depending on the nature of the gap) as electrons and holes tend to recombine. To create a large population of excitons, the system must be optically pumped (by lasers). It is then challenging to meet the necessary conditions for observing a condensate of such optically pumped excitons [69, 70].

Our goal in this chapter is to use the Hamiltonian of the excitonic insulator phase and a few assumptions related to this phase to compute the corresponding spectral function. With this spectral function, we will be able to calculate photoemission intensity maps, which are the spectroscopic signature of the excitonic insulator phase. Then, we will rely on comparisons with experimental data to give support to this phase as the origin of the CDW phase of $1T$-$TiSe_2$. The formalism used in these calculations is very similar to that of the BCS theory. Therefore, as an introduction to the excitonic insulator phase, we will first recall some results of the BCS theory and compute its spectral function.

## 4.1 A short introduction to BCS superconductivity

The BCS theory of superconductivity was formulated by Bardeen, Cooper and Schrieffer to describe the superconducting properties of weak superconductors [71]. It is based on an effective attractive electron-electron interaction mediated by phonons, that allows electrons to bind together in pairs called Cooper pairs. To understand the origin of this attractive force, we have to consider the screening of the Coulomb interaction coming both from electron-hole pairs (which are no excitons, as they are no bound states!) and from interactions with phonons. The former appears naturally when considering the second-order contributions to the self-energy of interacting electrons, among other contributions. Such an electron-hole pair excitation, often referred to as a polarization bubble, is mathematically symbolized by $\Pi_0(\vec{k},\vec{\omega})$. One approximation, called the Random Phase Approximation, consists of considering only polarization bubbles, and simple combinations of them in series, for the self-energy. This development in series of the self-energy contribution allows to write down a Dyson-like equation (remember equation 2.8) for the effective interaction hidden in the self-energy (detailed calculations can be found in references [22, 23])

$$V_{RPA}(\vec{k},\omega) = V(\vec{k}) - \frac{1}{\hbar}V(\vec{k})\Pi_0(\vec{k},\omega)V_{RPA}(\vec{k},\omega).$$

The screened Coulomb interaction in the RPA $V_{RPA}$ can be directly extracted

$$V_{RPA}(\vec{k},\omega) = \frac{V(\vec{k})}{1+\frac{1}{\hbar}V(\vec{k})\Pi_0(\vec{k},\omega)} = \frac{V(\vec{k})}{\varepsilon_{RPA}(\vec{k},\omega)},$$

where a RPA dielectric function $\varepsilon_{RPA}$ has been defined. Note that $V_{RPA}$ is frequency dependent, meaning that the interaction is not instantaneous. The self-energy generated by all RPA diagrams contains also other contributions. These are obtained by mixing Coulomb and electron-phonon interaction together in the same diagrams, with polarization bubbles inbetween, in all possible combinations in series. We give here the final result for the effective screened Coulomb interaction

$$V_{eff}(\vec{k},\omega) = V_{RPA}(\vec{k},\omega)\frac{1}{1-\frac{\tilde{\omega}^2(\vec{k},\omega)}{\omega_{\vec{k}}^2}+i\eta}. \tag{4.2}$$

Here $\tilde{\omega}(\vec{k},\omega) = \omega_{\vec{k}}/\varepsilon_{RPA}(\vec{k},\omega)$ are phonon frequencies $\omega_q$ renormalized within the RPA (coming from a Dyson-like expansion of the phonon Green's function in interaction with electrons).

Equation 4.2 is of central importance in the origin of BCS superconductivity for simple metals. It says that if the renormalized phonon frequencies $\tilde{\omega}$ are sufficiently enhanced to surpass the bare frequencies $\omega$, the effective interaction between electrons $V_{eff}$ becomes attractive! This allows then to anticipate the formation of bound pairs of electrons with opposite momenta and spins, $(\vec{k},\downarrow)$ and $(-\vec{k},\uparrow)$. To tackle this problem, we adopt now the strategy developed in Mahan's book [22], which is a weak coupling approach. The Hamiltonian considered here has the form

$$H = \sum_{\vec{p}\sigma} \xi_p c^\dagger_{\vec{p}\sigma} c_{\vec{p}\sigma} + \frac{1}{2v} \sum_{\vec{q}\vec{p}\vec{p}\,'} \sum_{\sigma\sigma'} V(q) c^\dagger_{\vec{p}+\vec{q},\sigma} c^\dagger_{\vec{p}\,'-\vec{q},\sigma'} c_{\vec{p}\,',\sigma'} c_{\vec{p},\sigma}. \tag{4.3}$$

with a simplified interaction

$$V(q) = \begin{cases} -V_0 & \text{for } |\xi_q| \leq \omega_D, \\ 0 & \text{otherwise,} \end{cases} \tag{4.4}$$

It is designed to model the effective screened Coulomb interaction 4.2, with an attractive constant part up to the Debye frequency of the solid $\omega_D$. Working at finite temperature, we introduce three Green's functions in imaginary time, namely

$$\begin{aligned} G(\vec{p},\tau-\tau') &= -\langle |T_\tau c_{\vec{p},\sigma}(\tau) c^\dagger_{\vec{p},\sigma}(\tau)| \rangle, \\ F(\vec{p},\tau-\tau') &= -\langle |T_\tau c_{-\vec{p},\downarrow}(\tau) c_{\vec{p},\uparrow}(\tau)| \rangle, \\ F^\dagger(\vec{p},\tau-\tau') &= \langle |T_\tau c^\dagger_{\vec{p},\uparrow}(\tau) c^\dagger_{-\vec{p},\downarrow}(\tau)| \rangle. \end{aligned} \tag{4.5}$$

While $G$ is a standard Green's function, $F$ and $F^\dagger$ are called anomalous Green's function. This strange denomination comes from the fact that the ket $|\rangle$ operated by two creation or annihilation operators does not have the same number of particle than the bra $\langle|$. Therefore, in the normal state, these anomalous Green's functions are identically zero. However, this is allowed in the BCS ground state, provided that we are working in the grand canonical ensemble.

Having the Hamiltonian, we can use the same technique as that illustrated for the non-interacting electrons in a band, in section 2.4.2, to derive the analytical form of these Green's functions. We thus compute the equation of motion of our creation and annihilation operators. For instance we find

$$\frac{\partial}{\partial\tau} c_{\vec{p},\sigma}(\tau) = [H, c_{\vec{p},\sigma}] = -\xi_p c_{\vec{p}\sigma} - \frac{1}{v} \sum_{\vec{q}\vec{p}\,'\sigma'} V(q) c^\dagger_{\vec{p}\,'-\vec{q},\sigma'}(\tau) c_{\vec{p}\,',\sigma'}(\tau) c_{\vec{p}-\vec{q},\sigma}(\tau).$$

It permits to compute the $\tau$-derivative of the Green's function $G$

$$\begin{aligned} \frac{\partial}{\partial\tau} G(\vec{p},\tau-\tau') = -\delta(\tau-\tau') &- \xi_p G(\vec{p},\tau-\tau') \\ &+ \frac{1}{v} \sum_{\vec{q}\vec{p}\,'\sigma'} V(q) \langle |T_\tau c^\dagger_{\vec{p}\,'-\vec{q},\sigma'}(\tau) c_{\vec{p}\,',\sigma'}(\tau) c_{\vec{p}-\vec{q},\sigma}(\tau) c_{\vec{p},\sigma}(\tau')^\dagger| \rangle. \end{aligned}$$

Thanks to Wick's theorem, the four operator term $\langle c^\dagger c c c^\dagger \rangle$ can be factorized into pairs which will be related to Green's functions. In the normal state, only terms like $\langle c^\dagger c \rangle \langle c c^\dagger \rangle$ are allowed. However, in the superconducting state, also terms like $\langle cc \rangle \langle c^\dagger c^\dagger \rangle$ have to be considered, as they are related to anomalous Green's functions, so that the four operator

average becomes

$$\frac{1}{v}\sum_{\vec{q}\vec{p}'\sigma'} V(q)\langle|T_\tau \quad c^\dagger_{\vec{p}'-\vec{q},\sigma'}(\tau) \quad c_{\vec{p}',\sigma'}(\tau)c_{\vec{p}-\vec{q},\sigma}(\tau)c_{\vec{p},\sigma}(\tau')^\dagger|\rangle$$
$$= \qquad \frac{1}{v}\sum_{\vec{q}} V(q)\left[G(\vec{p},\tau-\tau')n_{\vec{p}-\vec{q}} - F(\vec{p}-\vec{q},0)F^\dagger(\vec{p},\tau-\tau')\right]$$

(as a simplification, pairings involving a zero momentum interaction have been neglected, on the basis that $V(\vec{q}=0)\approx 0$ at large distances). The first term in the right hand side is an exchange term, which is assumed not to differ too much between the normal and the superconducting states. Consequently it will be neglected. The second term in the right hand side is important and contains an expression that we define now as the gap function

$$\Delta(\vec{p}) = -\frac{1}{v}\sum_{\vec{q}} V(q)F(\vec{p}-\vec{q},\tau=0). \tag{4.6}$$

It is assumed here to be real, i.e. $\Delta(\vec{p})^\dagger = \Delta(\vec{p})$ (this can be shown [22]). Its meaning will become clearer below. It can also be seen as an order parameter characterizing the BCS superconductive state. We can rewrite the equation of motion for the normal Green's function

$$\left(-\frac{\partial}{\partial\tau} - \xi_p\right)G(\vec{p},\tau-\tau') + \Delta(\vec{p})F^\dagger(\vec{p},\tau-\tau') = \delta(\tau-\tau'). \tag{4.7}$$

In this equation, $F^\dagger$ and $G$ are unknowns ($\Delta$ is a parameter here). Other relations between these two Green's functions are needed to build a closed system of equations which can be solved to get $F^\dagger$ and $G$. Therefore we look for the equation of motion of $F^\dagger$. It is done in the same manner as that of $G$ and provides us with

$$\left(-\frac{\partial}{\partial\tau} + \xi_p\right)F^\dagger(\vec{p},\tau-\tau') + \Delta(\vec{p})G(\vec{p},\tau-\tau') = 0 \tag{4.8}$$

(here the self-energy has been neglected too). We now convert the (imaginary) time $\tau$ into Matsubara frequencies $ip_n$ with help of Fourier transform (see equation 2.13), so that the differential equations 4.7 and 4.8 become algebraic equations

$$\begin{aligned}(ip_n - \xi_p)\,G(\vec{p},ip_n) + \Delta(\vec{p})F^\dagger(\vec{p},ip_n) &= 1\\ (ip_n + \xi_p)\,F^\dagger(\vec{p},ip_n) + \Delta(\vec{p})G(\vec{p},ip_n) &= 0\end{aligned}$$

which can be easily solved

$$\begin{aligned}G(\vec{p},ip_n) &= -\frac{ip_n+\xi_p}{p_n^2+\xi_p^2+\Delta(\vec{p})^2},\\ F^\dagger(\vec{p},ip_n) &= \frac{\Delta(\vec{p})}{p_n^2+\xi_p^2+\Delta(\vec{p})^2} = F(\vec{p},ip_n).\end{aligned} \tag{4.9}$$

We immediately see that when $\Delta = 0$, the anomalous Green's functions vanish, as required by our derivation. We can now use the knowledge of the many-body theory to exploit these Green's functions. Their poles are the renormalized dispersions, namely $E_p = \sqrt{\xi_p^2 + \Delta(\vec{p})^2}$, corresponding to the excitation energy of the system. It allows us

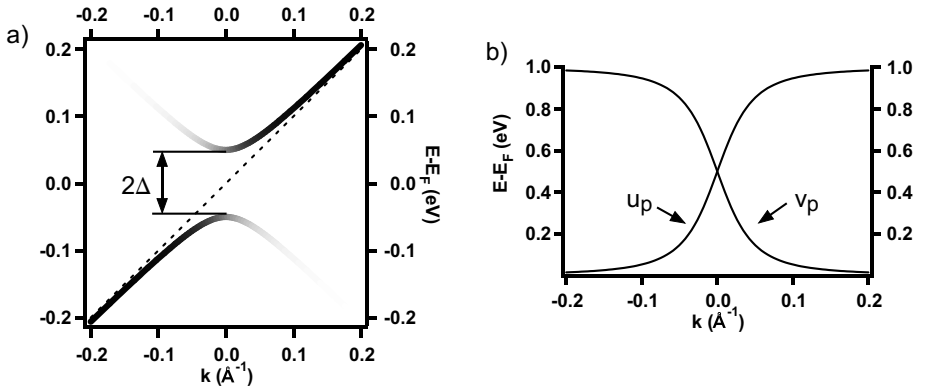


FIGURE 4.2: (a) Renormalized bands coming from a bare linear dispersion (dashed line) obtained from the BCS spectral function 4.10 for $\Delta = 0.05$ eV. Their spectral weights (given by $u_p^2$ and $v_p^2$) superimposed to the dispersions in greyscale, are plotted in (b).

to rewrite these Green's functions in an expanded form

$$\begin{aligned} G(\vec{p}, ip_n) &= \frac{u_p^2}{ip_n - E_p} + \frac{v_p^2}{ip_n + E_p}, \\ F^\dagger(\vec{p}, ip_n) &= -u_p v_p \left( \frac{1}{ip_n - E_p} - \frac{1}{ip_n + E_p} \right) = F(\vec{p}, ip_n). \end{aligned}$$

where the coherence factors $u_p^2 := (1 + \xi_p/E_p)/2$ and $v_p^2 := (1 - \xi_p/E_p)/2$ have been introduced. Now the analytical continuation $ip_n \to \omega + i\eta$ (see equation 2.14) can be easily performed to obtain the (real frequency) retarded Green's function which can be used in turn to compute the spectral function

$$A(\vec{p}, \omega) = -\frac{1}{\pi} \mathrm{Im}\, G^{ret}(\vec{p}, \omega) = u_p^2 \delta(\omega - E_p) + v_p^2 \delta(\omega + E_p). \tag{4.10}$$

According to our (simplified) expression for photoemission (equation 2.4), this spectral function gives the spectroscopic signature of a BCS superconductor. Fig. 4.2 (a) displays the renormalization of a linear dispersion $\xi \propto k$ (dashed line) in the BCS superconductive phase for an order parameter fixed to $\Delta = 0.05$ eV, as seen by photoemission. Near $E_F$, a gap opens, which has a magnitude of $2\Delta$. This explains why the order parameter $\Delta$ is also called the gap function. It separates the linear dispersion into two curved dispersions, carrying spectral weights corresponding to $u_p^2$ and $v_p^2$. These spectral weight functions are displayed in Fig. 4.2 (b), their sum being normalized to one. The high spectral weight is distributed on the parts of the renormalized dispersions which are the closer to the non-renormalized ones. The gap measured in photoemission is twice the BCS gap function, $E_g = 2\Delta$. The reason behind this is that we cannot excite just one electron from the BCS ground state (where all electrons are bound into pairs) when destroying a Cooper pair, but we must excite two electrons, paying therefore at least $2\Delta$.

As an illustration of this discussion of the BCS spectral function 4.10, we refer to a recent article which proposes a direct application of these results in photoemission [72]. The authors analyze data taken on high-temperature superconductors and extract the spectral weight carried by the measured bands, which compares well to the theory.

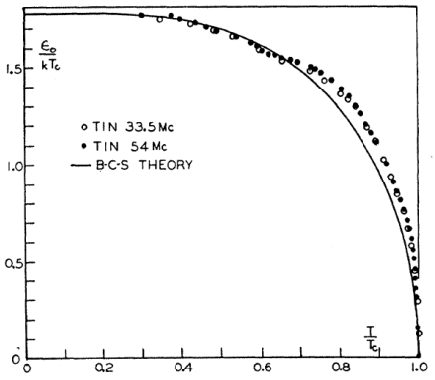


FIGURE 4.3: BCS gap as a function of temperature for tin. Dots are values coming from ultrasonic attenuation measurements (at 2 different frequencies for the acoustic waves). $\varepsilon_0 = 1.75\ k_B T_c$, with $T_c = 3.5$K [73]. The continuous line represents the theoretical prediction.

In the analysis above, we chose a particular value of the order parameter to illustrate the theory. However, this order parameter obeys to the gap equation 4.6. On its right hand side appears the time dependent anomalous Green's function $F^\dagger$ which can be computed by Fourier transforming equation 4.9

$$F^\dagger(\vec{p}, \tau = 0) = \frac{1}{\beta} \sum_{ip_n} F^\dagger(\vec{p}, ip_n) = \frac{1}{\beta} \sum_{ip_n} \frac{\Delta(\vec{p})}{p_n^2 + \xi_p^2 + \Delta(\vec{p})^2}.$$

This is computed in the usual fashion for Matsubara frequency summations (remember section 2.4.5). The result for $F^\dagger$ is

$$F^\dagger(\vec{p}, \tau = 0) = \frac{\Delta}{2E_p} \tanh\left(\frac{\beta E_p}{2}\right).$$

Inserting it into the gap equation 4.6 brings an integral equation for the order parameter

$$\Delta(\vec{p}) = -\frac{1}{v} \sum_{\vec{q}} V(q) \frac{\Delta(\vec{p} - \vec{q})}{2E_{\vec{p}-\vec{q}}} \tanh\left(\frac{\beta E_{\vec{p}-\vec{q}}}{2}\right). \tag{4.11}$$

It turns out that the right hand side is $\vec{p}$ -independent (due to the particular form of the interaction 4.4), meaning that the order parameter is $\vec{p}$ -independent too. This one-dimensional integral equation can be solved numerically. A comparison of this theoretical prediction with the gap measured in tin is displayed in Fig. 4.3 and shows an excellent agreement [73].

## 4.2 The excitonic insulator phase: a 1D model

As a first approach to the specific case of $1T$-$TiSe_2$, we consider the one-dimensional model studied in the thesis of F. Clerc (for that reason, we will give only the main results) [31]. It is a simplified version of what will be presented in the next section, mainly because it involves only one electron pocket separated by a wave vector $\vec{w}$. The

starting one-electron Hamiltonian has the form

$$H_0 = \sum_{\vec{k}} \varepsilon_v(\vec{k}) a^\dagger(\vec{k}) a(\vec{k}) + \sum_{\vec{k}} \varepsilon_c(\vec{k} + \vec{w}) b^\dagger(\vec{k}) b(\vec{k})$$

containing the dispersions of the valence band $\varepsilon_v$ which has its maximum at $\Gamma$ and the conduction band $\varepsilon_c$ which has its minimum at $M$

$$\varepsilon_v(\vec{k}) = \varepsilon_v^0 + \frac{\hbar^2 k^2}{2m_v},$$
$$\varepsilon_c(\vec{k}) = \varepsilon_c^0 + \frac{\hbar^2(\vec{k} - \vec{w})^2}{2m_c}.$$

In practice, these dispersions should be extracted from photoemission data taken at room temperature. The gap between these two bands is then $E_G = \varepsilon_c^0 - \varepsilon_v^0$. The distance between the two extrema is $\vec{w} = \Gamma M$, called the spanning vector. The fermionic operators $a^\dagger(\vec{k})$ and $b^\dagger(\vec{k})$ create electrons in the valence band with wave vector $\vec{k}$ and in the conduction band with wave vector $\vec{k} + \vec{w}$ respectively. Thanks to electron-hole symmetry, $a$ can be thought as an operator creating a hole in the valence band. In practice, these dispersions are obtained by fitting the room temperature photoemission data.

We now introduce the interaction between these two bands

$$V = \sum_{\vec{q},\vec{k},\vec{k}\,'} a^\dagger(\vec{k} + \vec{q}) b^\dagger(\vec{k}\,' - \vec{q}) V_c(\vec{q}) b(\vec{k}\,') a(\vec{k})$$

with $V_c$ the Coulomb potential. The total Hamiltonian $H = H_0 + V$ is then formally treated by a perturbation expansion on $V$, in a way similar to BCS theory (see section 4.1). However, we make a few simplifications with respect to BCS theory. First we neglect the spin degrees of freedom (as mentionned above, the electrons and holes form singlet bound states). Then, in this section we will work at the mean-field level, that is, at the lowest order in the expansion. Finally we focus onto the condensate phase (low temperature phase) and thus we introduce only zero temperature normal Green's functions

$$\begin{aligned} G_v(\vec{p}, t - t') &= -i\langle|T_t a(\vec{p}, t) a^\dagger(\vec{p}, t')|\rangle, \\ G_c(\vec{p}, t - t') &= -i\langle|T_t b(\vec{p}, t) b^\dagger(\vec{p}, t')|\rangle, \end{aligned}$$

for the valence and the conduction band respectively. Then, we also introduce anomalous Green's function

$$\begin{aligned} F(\vec{p}, t - t') &= -i\langle|T_t b(\vec{p}, t) a^\dagger(\vec{p}, t')|\rangle, \\ F^+(\vec{p}, t - t') &= -i\langle|T_t a(\vec{p}, t) b^\dagger(\vec{p}, t')|\rangle, \end{aligned}$$

which should be zero above $T_c$ and non-zero in the condensate phase, below $T_c$. They are indeed closely related to excitons, since $b(t)a^\dagger(t')$ creates a hole in the conduction band at time $t'$ and creates an electron in the valence band at time $t$.

This problem is solved using the same strategy than what was done in section 4.1. We first calculate the equation of motion for the annihilation operators $a$ and $b$ and then use these relations to compute the equation of motion for the Green's functions. For

example, in the case of the valence band, we find

$$\begin{aligned}\left[-i\frac{\partial}{\partial t}-\varepsilon_v(\vec{p})\right]G_v(\vec{p},t-t') &= \delta(t-t') \\ -i\sum_{\vec{k},\vec{q}} & V_c(\vec{q}) \quad \langle|T_t a(\vec{p}+\vec{q},t)b^\dagger(\vec{k},t)b(\vec{k}-\vec{q},t)a^\dagger(\vec{p},t')|\rangle.\end{aligned}$$

Again, the factorization of the average involving four creation/annihilation operators is made using Wick's theorem. It lets appear three different combinations among which one is trivially zero and one is a Hartree term. As the dispersions are obtained from the experiment, we consider that they already contain the Hartree correction and that such a term changes negligibly with temperature (such an assumption was already done in the BCS theory), compared to excitonic effects. The remaining term (keeping only the possibility $\vec{k}=\vec{p}+\vec{q}$) leads to

$$\begin{aligned}\left[-i\frac{\partial}{\partial t}-\varepsilon_v(\vec{p})\right]G_v(\vec{p},t-t') &= \delta(t-t') \\ -i\sum_{\vec{q}} & V_c(\vec{q}) \quad \langle|T_t a(\vec{p}+\vec{q},t)b^\dagger(\vec{p}+\vec{q},t)|\rangle\langle|b(\vec{p},t)a^\dagger(\vec{p},t')|\rangle\end{aligned} \tag{4.12}$$

where we recognize the anomalous Green's function $F$ in the right hand side. By analogy with BCS superconductivity, we also introduce here an order parameter $\Delta$ obeying to

$$\Delta(\vec{p})=\sum_{\vec{q}} V_c(\vec{q})\underbrace{\langle|a(\vec{p}+\vec{q},t)b^\dagger(\vec{p}+\vec{q},t)|\rangle}_{=iF^\dagger(\vec{p}+\vec{q},t=0)} \tag{4.13}$$

which allows us to rewrite equation 4.12 like

$$\left[-i\frac{\partial}{\partial t}-\varepsilon_v(\vec{p})\right]G_v(\vec{p},t-t')=\delta(t-t')-\Delta(\vec{p})F(\vec{p},t).$$

This differential equation is then Fourier transformed in frequency space to get an algebraic equation

$$\left[z-\varepsilon_v(\vec{p})\right]G_v(\vec{p},z)=1-\Delta(\vec{p})F(\vec{p},z). \tag{4.14}$$

Applying the same procedure to the anomalous Green's function $F$, we obtain

$$\left[z-\varepsilon_c(\vec{p}+\vec{w})\right]F(\vec{p},z)=-\Delta(\vec{p})G_v(\vec{p},z) \tag{4.15}$$

and thus a closed set of equations for $G_v$. Equations 4.14 and 4.15 can be easily solved and the resulting expression for the valence band Green's function is

$$G_v(\vec{p},z)=\frac{z-\varepsilon_c(\vec{p}+\vec{w})}{(z-\varepsilon_v(\vec{p}))(z-\varepsilon_c(\vec{p}+\vec{w}))-|\Delta(\vec{p})|^2}=\frac{1}{z-\varepsilon_v(\vec{p})-\frac{|\Delta(\vec{p})|^2}{z-\varepsilon_c(\vec{p}+\vec{w})}}. \tag{4.16}$$

This particular form of $G_v$ emphasizes immediately the role of the self-energy

$$\Sigma_v(\vec{p},z)=\frac{|\Delta(\vec{p})|^2}{z-\varepsilon_c(\vec{p}+\vec{w})}.$$

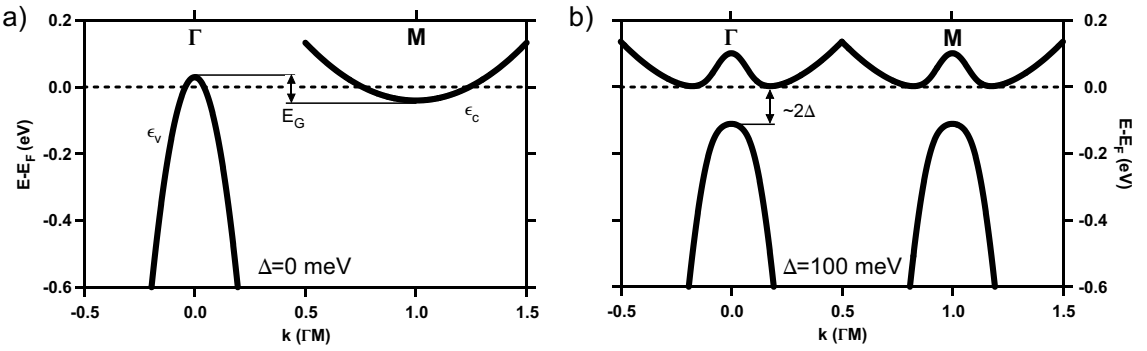


FIGURE 4.4: (a) Dispersions in the normal phase ($\Delta = 0$ meV) for a semimetallic configuration. (b) Renormalized dispersions in the excitonic insulator phase, calculated for an order parameter $\Delta = 100$ meV.

This self-energy involves the conduction band (around its minimum) and is purely real. In comparison to the electron gas, this result is not surprising since we considered only the lowest order of the expansion in $V$ [22].

The Green's function for the conduction band is obtained analogously to that of the valence band. It reads

$$G_c(\vec{p}, z) = \frac{z - \varepsilon_v(\vec{p} - \vec{w})}{(z - \varepsilon_c(\vec{p}))(z - \varepsilon_v(\vec{p} - \vec{w})) - |\Delta(\vec{p})|^2} = \frac{1}{z - \varepsilon_c(\vec{p}) - \frac{|\Delta(\vec{p})|^2}{z - \varepsilon_v(\vec{p} - \vec{w})}}. \tag{4.17}$$

Both the valence 4.16 and the conduction 4.17 Green's functions have the same denominator (up to a shift of $\vec{w}$)

$$D(\vec{p}, z) = (z - \varepsilon_c(\vec{p} + \vec{w}))(z - \varepsilon_v(\vec{p})) - |\Delta(\vec{p})|^2 \tag{4.18}$$

and its roots are the renormalized dispersions in the condensate phase at $T < T_c$, namely

$$z_\pm(\vec{p}) = \frac{1}{2}\left(\varepsilon_v(\vec{p}) + \varepsilon_c(\vec{p} + \vec{w})\right) \pm \frac{1}{2}\sqrt{(\varepsilon_v(\vec{p}) - \varepsilon_c(\vec{p} + \vec{w})^2) + 4|\Delta(\vec{p})|^2}. \tag{4.19}$$

With these roots, the Green's functions can be decomposed into simple fractions (involving only first order poles) and their spectral function can be computed according to equation 2.4 so that

$$\begin{aligned} A_v(\vec{p}, z) &= u_v^2(\vec{p})\delta(z - z_+(\vec{p})) + v_v^2(\vec{p})\delta(z - z_-(\vec{p})) \\ A_c(\vec{p}, z) &= u_c^2(\vec{p})\delta(z - z_+(\vec{p})) + v_c^2(\vec{p})\delta(z - z_-(\vec{p})) \end{aligned}$$

with the coherence factors being

$$\begin{aligned} u_v^2(\vec{p}) &= \frac{z_+(\vec{p}) - \varepsilon_c(\vec{p} + \vec{w})}{z_+(\vec{p}) - z_-(\vec{p})}, \qquad v_v^2(\vec{p}) = \frac{z_-(\vec{p}) - \varepsilon_c(\vec{p} + \vec{w})}{z_-(\vec{p}) - z_+(\vec{p})}, \\ u_c^2(\vec{p}) &= \frac{z_+(\vec{p}) - \varepsilon_v(\vec{p} - \vec{w})}{z_+(\vec{p}) - z_-(\vec{p})}, \qquad v_c^2(\vec{p}) = \frac{z_-(\vec{p}) - \varepsilon_v(\vec{p} - \vec{w})}{z_-(\vec{p}) - z_+(\vec{p})} \end{aligned} \tag{4.20}$$

(satisfying $u_v^2 + v_v^2 = 1$ and $u_c^2 + v_c^2 = 1$). The spectral functions of the valence and conduction bands 4.20 have a similar form to that of a BCS superconductor 4.10. The renormalized dispersions $z_\pm$ represent also a band structure gapped at $E_F$.

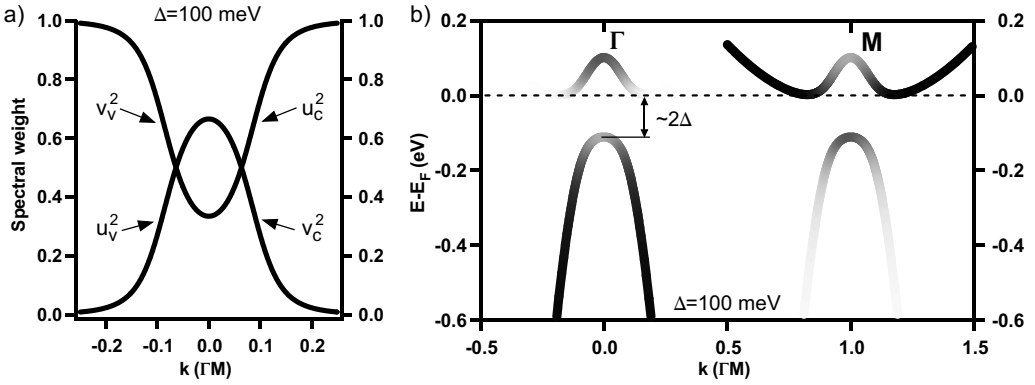


FIGURE 4.5: (a) Spectral weights of the renormalized valence and conduction bands in the excitonic insulator phase, calculated for $\Delta = 100$ meV. (b) Renormalized dispersions of Fig. 4.4 (a) with their respective spectral weights.

In Fig. 4.4 (a), we plot the dispersions[a] in the normal phase (i.e. with $\Delta = 0$ meV) for a semimetal, with $E_G = -0.07$ eV (band parameters are chosen in agreement with the generalized case which will be presented in section 4.3[b]) along $\Gamma M$. Fig. 4.4 (b) presents the renormalized dispersions calculated with the roots $z_\pm(\vec{k})$ of equation 4.19 in the excitonic insulator phase with $\Delta = 100$ meV. Many different features should be emphasized.

- In the excitonic insulator phase, the dispersions at $\Gamma$ are identical to those at $M$ [c]. This is the manifestation of the CDW associated to this exotic phase.
- Similarly to the BCS theory, a gap opens at $E_F$. However, as we will see later with the generalized case of section 4.3, this particularity is not intrinsic to the theory but specific to the initial band structure. The gap always opens at the crossing of the valence and conduction bands. This causes the system to become insulating in the low temperature phase.
- The light holes of the valence band disappear, as this band shifts to higher binding energies. The conduction band disperses now above $E_F$, displaying a non-trivial shape, since, around $M$, it deviates from its initial parabolic shape and follows now the top of the former valence band. This can be seen as hybridization between these two bands.

To get a complete view of the spectroscopic signature of the excitonic insulator phase, we must add the spectral weights to the dispersions of Fig. 4.4 (a). It turns out that the four different coherence factors 4.20, which are nothing else than the spectral weights seen in photoemission, reduce to only two different ones, since $u_v^2(\vec{p}) = v_c^2(\vec{p})$ and $v_v^2(\vec{p}) = u_c^2(\vec{p})$. They are plotted in Fig. 4.5 (a), for $\Delta = 100$ meV. We see graphically that they obey to the sum rules $u_v^2 + v_v^2 = 1$ and $u_c^2 + v_c^2 = 1$. Fig. 4.5 (b) shows the renormalized dispersions with their respective spectral weights, for $\Delta = 100$ meV. We note the following changes with respect to the previous picture in Fig.4.4 (b).

[a] We will distinguish between the dispersion, where only the energy as a function of the wave vector $\vec{k}$ is considered, and the band, which is a dispersion carrying a spectral weight.

[b] $\varepsilon_v^0 = 0.03$ eV, $\varepsilon_c^0 = -0.04$ eV, $m_v = -0.23 m_e$ and $m_c = 5.5 m_e$.

[c] This stems from the fact that all the Green's functions have the same denominator 4.18.

- The band structure at Γ is not identical to that at $M$ anymore. The spectral weight distributions break this equivalency, so that the CDW appears only partially to photoemission.
- Due to the equalities $u_v^2 + v_v^2 = 1$ and $u_c^2 + v_c^2 = 1$ and to the sum rules seen above, the spectral weight lost in the valence band at Γ is totally transferred into its backfolded version at $M$ and vice versa for the conduction band at $M$ and its backfolded version at Γ.

In the examples above, we have considered the order parameter $\Delta$ as a parameter, independent of the wave vector $\vec{p}$. However, from its definition 4.13, we see that it can be calculated with the anomalous Green's function $F(\vec{p}, \tau = 0)$. Knowing the valence band Green's function $G_a$ and using equation 4.15, this anomalous Green's function can be also determined. It involves the renormalized dispersions $z_\pm$ which are functions of $\Delta$. Therefore, we would get an integral equation for the order parameter, in a similar way (but more complicated) to the BCS order parameter (see equation 4.11). However, we will not study $\Delta$ for the simple case of the one-dimensional excitonic insulator phase, as it will be done later for the generalized case (see section 5.5).

To conclude this section, we comment on the similarities and differences between the Peierls transition and the excitonic insulator phase transition. Formally, it has been shown by Rice and Gartstein that the half-filled Peierls insulator is in fact an excitonic insulator [74]. They emphasized that the order parameter describing these two kinds of transitions obeys to the same gap equation and that the corresponding Hamiltonians are the same. However an essential difference between these two models of the CDW transition lies in the origin of the pairing interaction. In the case of the Peierls transition, it is an electron-lattice interaction. For the excitonic insulator phase transition, it is the Coulomb interaction. This is very important, because this latter transition is very unlikely in a half-filled band. The high charge carrier density in the neighbourhood of the Fermi level would induce a strong screening of the Coulomb interaction, very unfavorable to the exciton formation.

## 4.3 The exciton condensate phase: a 3D generalization for 1*T*-$TiSe_2$

In this section, we study the case of the three dimensional excitonic insulator phase. In comparison to the one-dimensional case developed in the previous section, we have the following differences.

- We now consider three symmetry equivalent conduction bands near the Fermi surface, located at $L$ and separated from Γ by the (spanning) wave vectors $\vec{w}_i$ ($i = 1, 2, 3$) (see Fig. 4.10 (a)).
- The valence and conduction bands disperse now in three dimensions. In particular, the conduction bands are anisotropic.

Looking at the schematic Fermi surface of Fig. 3.7 (c), the reader may be surprised that we do not consider also the electron pockets centered at $L'$. This choice is motivated by

following reason. We look for a minimal model, which reproduces well the experiment without comprising too many parameters and without requiring too much computational effort. Indeed, to be fully consistent with DFT calculations, we should not only include the two symmetry inequivalent conduction bands (at $L$ and $L'$) but also the three valence bands dispersing at $\Gamma$. This would result in a complicated Hamiltonian with many interactions and many parameters to characterize them (like the spin-orbit coupling for the valence bands or a crystal field interaction for the conduction bands [59]), whose values could be hard to motivate afterwards.

To follow the chronology of the publication of our results, we first insert the article published in Physical Review Letters in 2007.

## 4.4 Evidence for an excitonic insulator phase in 1*T*-$TiSe_2$

H. Cercellier C. Monney, F. Clerc, C. Battaglia, L. Despont, M. G. Garnier, H. Beck, P. Aebi,

*Institut de Physique, Université de Neuchâtel, CH-2000 Neuchâtel, Switzerland*

L. Patthey,

*Swiss Light Source, Paul Scherrer Institute, CH-5232 Villigen, Switzerland*

H. Berger, L. Forró

*Institut de Physique de la Matière Complexe, EPFL, CH-1015 Lausanne, Switzerland*

Published in Physical Review Letters **99**, 146403 (2007)

We present a new high-resolution angle-resolved photoemission study of 1*T*-$TiSe_2$ in both, its room-temperature, normal phase and its low-temperature, charge-density wave phase. At low temperature the photoemission spectra are strongly modified, with large band renormalisations at high-symmetry points of the Brillouin zone and a very large transfer of spectral weight to backfolded bands. A calculation of the theoretical spectral function for an excitonic insulator phase reproduces the experimental features with very good agreement. This gives strong evidence in favour of the excitonic insulator scenario as a driving force for the charge-density wave transition in 1*T*-$TiSe_2$.

Transition-metal dichalcogenides (TMDC's) are layered compounds exhibiting a variety of interesting physical properties, mainly due to their reduced dimensionality [75]. One of the most frequent characteristics is a ground state exhibiting a charge-density wave (CDW), with its origin arising from a particular topology of the Fermi surface and/or a strong electron-phonon coupling [44]. Among the TMDC's 1*T*-$TiSe_2$ shows a commensurate 2×2×2 structural distortion below 202 K, accompanied by the softening of a zone boundary phonon and with changes in the transport properties [48, 49]. In spite of many experimental and theoretical studies, the driving force for the transition remains controversial. Several angle-resolved photoelectron spectroscopy (ARPES) studies suggested either the onset of an excitonic insulator phase [57, 59] or a band Jahn-Teller effect [60]. Furthermore, $TiSe_2$ has recently attracted strong interest due to the observation of superconductivity when intercalated with Cu [47]. In systems showing exotic properties, such as Kondo systems for example [76], the calculation of the spectral function has often been a necessary and decisive step for the interpretation of the ARPES data and the determination of the ground state of the systems. In the case of 1*T*-$TiSe_2$, such a calculation for an excitonic insulator phase lacked so far.

In this letter we present a high-resolution ARPES study of 1*T*-$TiSe_2$, together with calculations of the excitonic insulator phase theoretical spectral function for this compound. We find that the experimental ARPES spectra show strong band renormalisations with a very large transfer of spectral weight into backfolded bands in the low-temperature phase. The spectral function calculated for the excitonic insulator phase is in strikingly

good agreement with the experiments, giving strong evidence for the excitonic origin of the transition.

The excitonic insulator model was first introduced in the sixties, for a semi-conductor or a semi-metal with a very small indirect gap $E_G$ [2, 77, 78, 79]. Thermal excitations lead to the formation of holes in the valence band and electrons in the conduction band. For low free carrier densities, the weak screening of the electron-hole Coulomb interaction leads to the formation of stable electron-hole bound states, called excitons. If the exciton binding energy $E_B$ is larger than the gap energy $E_G$, the system becomes unstable upon formation of excitons. This instability can drive a transition to a coherent ground state of condensed excitons, with a periodicity given by the spanning vector $\mathbf{w}$ that connects the valence band maximum to the conduction band minimum. In the particular case of $TiSe_2$, there are three vectors ($\mathbf{w}_i$, $i = 1, 2, 3$) connecting the Se 4p-derived valence band maximum at the $\Gamma$ point to the three symmetry-equivalent Ti 3d-derived conduction band minima at the $L$ points of the Brillouin zone (BZ) (see inset of fig. 4.6b)).

Our calculations are based on the BCS-like model of Jérome, Rice and Kohn [2], adapted for multiple $\mathbf{w}_i$. The band dispersions for the normal phase have been chosen of the form

$$\begin{aligned} \epsilon_v(\mathbf{k}) &= \epsilon_v^0 + \hbar^2 \frac{k_x^2 + k_y^2}{2m_v} + t_v \cos(\frac{2\pi k_z}{c}) \\ \epsilon_c^i(\mathbf{k}, \mathbf{w}_i) &= \epsilon_c^0 + \hbar^2 \Big( \frac{(k_x - w_{ix})^2}{2m_c^x} + \frac{(k_y - w_{iy})^2}{2m_c^y} \Big) \\ &\quad + t_c \cos\Big( \frac{2\pi(k_z - w_{iz})}{c} \Big) \end{aligned} \tag{4.21}$$

for the valence ($\epsilon_v$) and the three conduction ($\epsilon_c^i$) bands respectively, with $c$ the lattice parameter perpendicular to the surface in the normal (1×1×1) phase, $t_v$ and $t_c$ the amplitudes of the respective dispersions perpendicular to the surface and $m_v$, $m_c$ the effective masses.

Within this model one-electron Green's functions were calculated for the excitonic insulator phase. For the valence band, one obtains

$$G_v(\mathbf{k}, z) = \Big( z - \epsilon_v(\mathbf{k}) - \sum_{\mathbf{w}_i} \frac{|\Delta|^2(\mathbf{k}, \mathbf{w}_i)}{z - \epsilon_c(\mathbf{k} + \mathbf{w}_i)} \Big)^{-1} . \tag{4.22}$$

This is a generalized form of the equations of Ref. [2] for an arbitrary number of $\mathbf{w}_i$. The order parameter $\Delta$ is related to the number of excitons in the condensed state at a given temperature. For the conduction band, the Green's functions $G_c^i$ corresponding to each spanning vector $\mathbf{w}_i$ is:

$$\begin{aligned} G_c^i(\mathbf{k} + \mathbf{w_i}, z) &= \Big( z - \epsilon_c(\mathbf{k} + \mathbf{w_i}) \\ &- \frac{|\Delta|^2(\mathbf{k}, \mathbf{w}_i)}{z - \epsilon_v(\mathbf{k}) - \sum_{j \neq i} \frac{|\Delta|^2(\mathbf{k}, \mathbf{w_j})}{z - \epsilon_c(\mathbf{k} + \mathbf{w_j})}} \Big)^{-1} \end{aligned} \tag{4.23}$$

This model and the derivation of the Green's functions will be further described in a forthcoming paper [80].

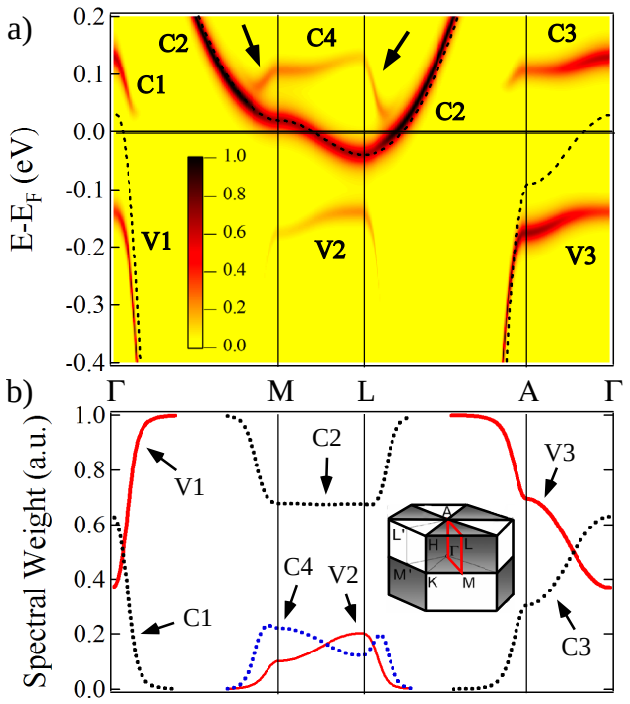


FIGURE 4.6: (color online): a) Theoretical spectral function of the excitonic insulator in a $1T$ structure, calculated for the band structure described in the text and an order parameter $\Delta$=0.075 eV. The V1-V3 (resp. C1-C4) branches refer to the valence (resp. conduction) band. Dashed lines correspond to the normal phase ($\Delta$=0). The path in reciprocal space is shown in red in the inset. b) Spectral weight of the different bands. Inset : bulk Brillouin zone of $1T$-$TiSe_2$.

The parameters for equations 4.21 were derived from photon energy dependent ARPES measurements carried out at the Swiss Light Source on the SIS beamline, using a Scienta SES-2002 spectrometer with an overall energy resolution better than 10 meV, and an angular resolution better than 0.5°. The fit to the data gives for the Se 4p valence band maximum +30 ± 10 meV, and for the Ti 3d conduction band a minimum -40 ± 5 meV with respect to the Fermi energy $E_F$ [d], yielding a semimetallic band structure with a negative gap (*i.e.* an overlap) $E_G$=-70 ± 15 meV for the normal phase of $TiSe_2$, in agreement with the literature [58].

The spectral function calculated along several high-symmetry directions of the BZ is shown in fig. 4.6a), for a zero order parameter (dashed lines) and for an order parameter $\Delta$=0.075 eV. This value has been chosen for best agreement with experiment. The color scale shows the spectral weight carried by each band. For presentation purposes the $\delta$-like peaks of the spectral function have been broadened by adding a constant 30 meV imaginary part to the self-energy. In the normal phase (dashed lines), as previously described we consider a semimetal with a 70 meV overlap, with bands carrying unity spectral weight. In the excitonic phase, the band structure is strongly modified. The first observation is the appearance of new bands (labeled C1, V2, C3 and C4), backfolded with the spanning vector $\mathbf{w} = \Gamma L$. The C1, C3 and V2 branches are the backfolded replicas of branches C4 and V3 respectively. In this new phase the $\Gamma$ and $L$ points are

[d] The fit parameters are : $\epsilon_v^0$=-0.03±0.005 eV, $m_v$=-0.23±0.02 $m_e$, where $m_e$ is the free electron mass, $t_v$=0.06±0.005 eV ; $\epsilon_c^0$=-0.01±0.0025 eV, $m_c^x$=5.5±0.2 $m_e$, $m_c^y$=2.2±0.1 $m_e$, $t_c$=0.03±0.0025 eV

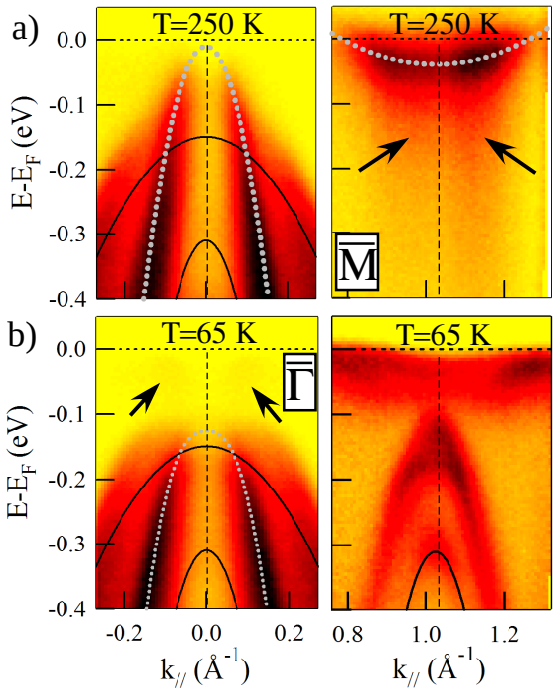


FIGURE 4.7: (color online): ARPES spectra of $1T$-$TiSe_2$ for a) above and b) below the CDW transition temperature. Thick dotted lines are parabolic fits to the bands in the normal phase and thin dotted lines are guides to the eye for the CDW phase. Fine lines follow the dispersion of the 4p sidebands (see text).

now equivalent (in the sense that the poles of the Green's functions are the same, but not the spectral weight), which means that the excitonic state has a 2×2×2 periodicity of purely electronic origin, as expected from theoretical considerations [2, 77]. Another effect of exciton condensation is the partial opening of a gap in the excitation spectrum. This results in a flattening of the valence band near Γ in the Γ$M$ direction (V1 branch) and in the $A\Gamma$ direction (V3 branch), and also an upward bend of the conduction band near $L$ and $M$ (C4 branch). It is interesting to notice that the splitting of the conduction band in two contributions (C2 and C4) near $M$ and $L$ results from the backfolding of the $L$ points onto each other, according to the new periodicity of the excitonic state (see fig. 8 in ref. [81]). The spectral weight carried by the bands is shown in fig. 4.6b). The largest variations occur near the Γ, $A$, $L$ and $M$ points, where the band extrema in the normal phase are close enough for excitons to be created. Away from these points, the spectral weight decreases in the backfolded bands (C1, V2, C3 and C4) and increases in the others. The intensity of the V1 branch, for example, decreases by 60% when approaching Γ, whereas the backfolded C1 branch shows the opposite behaviour. Such a large transfer of spectral weight into the backfolded bands is a very uncommon and striking feature. Indeed, in most compounds with competing potentials (CDW systems, vicinal surfaces,...), the backfolded bands carry an extremely small spectral weight [33, 36, 82]. In these systems the backfolding results mainly from the influence of the modified lattice on the electron gas, and the weight transfer is related to the strength of the new crystal potential component. Here, the case of the excitonic insulator is completely different, as the backfolding is an intrinsic property of the excitonic state. The large transfer of spectral weight is then a purely electronic effect, and turns out to be a characteristic feature of the excitonic insulator phase.

Fig. 4.7 shows ARPES spectra recorded at a photon energy h$\nu$=31 eV as a function of temperature. At this photon energy, the normal emission spectra correspond to states located close to the Γ point. For the sake of simplicity the description is in terms of the surface BZ high-symmetry points $\bar{\Gamma}$ and $\bar{M}$. The 250 K spectra exhibit the three Se 4p-derived bands at $\bar{\Gamma}$ and the Ti 3d-derived band at $\bar{M}$ widely described in the literature [57, 59, 60]. The thick dotted lines (white) are fits by equation 4.21, giving for the topmost 4p band an apparent maximum energy of -20 ± 10 meV, and for the Ti 3d a minimum energy of -40 ± 5 meV at this temperature. We speak here of an apparent maximum energy for the valence band, as the system appears already affected by excitonic fluctuations. Indeed, on the 250 K spectrum at $\bar{\Gamma}$, the intensity is low near normal emission. This reduced intensity and the residual intensity at $\bar{M}$ around 150 meV binding energy (arrows) may arise from exciton fluctuations (see reduction of spectral weight near Γ in the V1 branch in fig. 1b). Matrix elements appear to play a minor role as the intensity variation only depends very slightly on photon energy and polarization, and is also observed in the second Brillouin zone. In the 65 K data (fig. 4.7b)), the topmost 4p band flattens near $\bar{\Gamma}$ and shifts to higher binding energy by about 100 meV (thin white, dotted line). This shift is accompanied by a larger decrease of the spectral weight near the top of the band. The two other bands (fine black lines) are only slightly shifted. Intuitively this can be understood by the fact that these bands are further away from $E_F$ and therefore less involved by the interaction. In the $\bar{M}$ spectrum strong backfolded valence bands can be seen, and the conduction band shows significant intensity variations, with a maximum intensity located about 0.25 $Å^{-1}$ from $\bar{M}$. This observation is in agreement with Kidd *et al.* [59], although in their case the conduction band was unoccupied in the normal phase. This difference is due to a slight Ti overdoping of our samples [48]. In our case, the 2×2 CDW was found to appear at 180 ± 10 K from scanning tunneling microscopy measurements, indicating a Ti doping of less than 1 %. However, a 40 meV binding energy for the conduction band is still consistent with the excitonic insulator scenario, as the exciton binding energy is expected to be close to that value. [57, 59].

Spectral functions calculated for the same $k_{//}$ as the data of fig. 4.7 are shown in fig. 4.8. Only the Γ and $L$ points are shown, as the excitonic effects are more important near these points. For comparison with fig. 4.7 we refer to the projection of these points on the surface BZ $\bar{\Gamma}$ and $\bar{M}$. The effect of temperature was taken into account via the order parameter and the Fermi function. In order to understand the detailed behaviour of the ARPES spectra, a three band model would be necessary. However, considering only the topmost valence band allows to reproduce the essential features of the ARPES data. Indeed, the behavior of this band is extremely well reproduced by the calculation. In the 250 K calculation an effective order parameter of 25 meV was used to account for the fluctuation effects. This allows to reproduce the intensity loss near $\bar{\Gamma}$ and the appearance of spectral weight at $\bar{M}$ (arrows). In the 65 K calculation the valence band is flattened near $\bar{\Gamma}$, and the spectral weight at this point is reduced to 39 %, close to the experimental value of 35 %. The agreement is very satisfying, considering that the calculation takes into account only the lowest excitonic state.

In the near-$\bar{M}$ spectral function, the backfolded valence band is strongly present in the 65 K calculation. The conduction band maximum intensity is located away from $\bar{M}$ as in the experiment. It is important to notice that the ARPES spectra show no significant shift of the conduction band related to atomic displacements in the distorted phase [59, 60, 83]. Such atomic displacements, in terms of a band Jahn-Teller effect, were suggested as a driving force for the transition. However, the key point is that, although

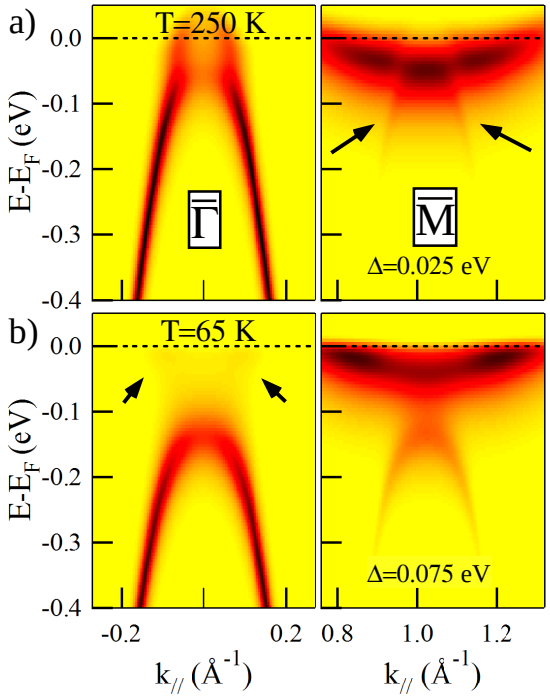


FIGURE 4.8: (color online): Theoretical spectral function of $1T$-$TiSe_2$ in the vicinity of $\Gamma$ and $L$. a) above and b) below the CDW transition temperature (see text). For comparison with fig. 4.7 we refer to the projection of these points on the surface BZ $\bar{\Gamma}$ and $\bar{M}$.

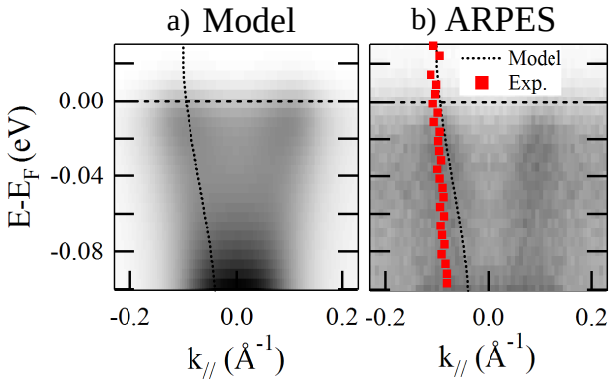


FIGURE 4.9: (color online): Near-$E_F$ spectral function in the vicinity of the $\Gamma$ point. The theoretical data correspond to fig. 4.8b and the ARPES to fig. 4.7b (see arrows on these figures).

the lattice distortion may shift the conduction band, the very small atomic displacements ($\approx$ 0.02 Å[48]) in $1T$-$TiSe_2$ are expected to lead to a negligable spectral weight in the backfolded bands [33]. As an example, $1T$-$TaS_2$, another CDW compound known for very large atomic displacements [84] (of order $>$ 0.1 Å) introduces hardly detectable backfolding of spectral weight in ARPES. Clearly, an electronic origin is necessary for obtaining such strong backfolding in the presence of such small atomic displacements. Therefore, our results allow to rule out a Jahn-Teller effect as the driving force for the transition of $TiSe_2$.

Furthermore, the ARPES spectra also show evidence for the backfolded conduction band at the $\bar{\Gamma}$ point. Fig. 4.9 shows spectra around the Fermi energy, taken from the data of fig. 4.7b and 4.8b (arrows). In the ARPES data two slightly dispersive peaks clearly cross the Fermi level. The experimental dispersion of these peaks (red squares) is well reproduced in the calculation (dotted lines). These features turn out to be the populated tail of the backfolded conduction band, whose centroid is located just above the Fermi level. To our knowledge no evidence for the backfolding of the conduction band had been put forward so far.

In summary, by comparing ARPES spectra of $1\,T$-$TiSe_2$ to theoretical predictions for an excitonic insulator, we have shown that the $2\times2\times2$ periodicity induced by the exciton condensate results in a very large transfer of spectral weight into backfolded bands. This effect, clearly evidenced by photoemission, turns out to be a characteristic feature of the excitonic insulator phase, thus giving strong evidence for the existence of this phase in $1\,T$-$TiSe_2$ and its prominent role in the CDW transition.

Skillfull technical assistance was provided by the workshop and electric engineering team. This work was supported by the Fonds National Suisse pour la Recherche Scientifique through Div. II and MaNEP.

## 4.5 Comments to "Evidence for an excitonic insulator phase in 1*T*-$TiSe_2$"

In this article, the three-dimensional dispersions of the valence and conduction band have been introduced. Their parameters have been extracted from excitation energy dependent measurements [e]. The resulting electronic configuration is that of a semimetal in the *normal phase* and this is an essential point. Indeed, looking at the ARPES spectra of Fig. 4.7 (a), it seems that the valence band seen in photoemission at $\Gamma$ and at room temperature is not crossing $E_F$. However, as discussed in this article, obvious traces of the CDW phase are already present at room temperature, like the large loss of spectral weight exactly at $\Gamma$ or the high spectral weight at $\bar{M}$ below the conduction band. These are interpreted as the signature for strong fluctuations at temperatures above the excitonic phase. Therefore, to obtain the dispersions in the normal phase, we had to go beyond these fluctuation effects. As we will see later, in the excitonic insulator phase, the valence band top is flattened and it is shifted to higher binding energy, but its parts away from its maximum are less affected. Therefore, we can reconstruct its shape in the normal phase by extrapolating its parabolic dispersions from its high binding energy parts. This way, we inferred a *normal phase* valence band maximum of $\epsilon_v^0 = 0.030 \pm 0.005$ eV, despite the electon-hole fluctuations already present at room temperature.

Together with a conduction band minimum in the occupied states, at $\epsilon_c^0 = -0.04$ eV, this yields a negative gap $E_G = -0.07$ eV. This semimetallic situation is highly favorable to exciton formation, in the sense that the condition 4.1 is trivially fulfilled. Of course, in that case, screening may be a problem, since a semimetal has a higher charge carrier density than a semiconductor. This issue will be discussed in section 5.5. Formally, in the band configuration revealed by this photoemission study, we calculate that the exciton binding energy is $E_B \simeq 0.01$ eV[f], which translates into an exciton radius of $a_{exc} \sim 40$Å. We are then in the case of weakly bound excitons, called Mott-Wannier excitons.

The next article presents the detailed calculations which lead to the Green's functions 4.22 and 4.23. These were used in turn to obtain the corresponding spectral functions which generated the photoemission intensity maps of Fig. 4.8.

[e] Carried out at the Swiss Light Source synchrotron

[f] For 1*T*-$TiSe_2$, an exact value of $\epsilon_r$ is difficult to obtain. We rather use $\epsilon_\infty = 19$ from the optical study of Li *et al.*.

## 4.6 Spontaneous exciton condensation in 1*T*-$TiSe_2$: BCS-like approach

C. Monney, H. Cercellier, F. Clerc, C. Battaglia, E.F. Schwier, C. Didiot, M. G. Garnier, H. Beck, P. Aebi,

*Institut de Physique, Université de Neuchâtel, CH-2000 Neuchâtel, Switzerland*

H. Berger and L. Forró

*Institut de Physique de la Matière Complexe, EPFL, CH-1015 Lausanne, Switzerland*

L. Patthey,

*Swiss Light Source, Paul Scherrer Institute, CH-5232 Villigen, Switzerland*

Published in Physical Review B **79**, 045116 (2009)

Recently we found strong evidence in favor of a BCS-like condensation of excitons in 1*T*-$TiSe_2$ [Phys. Rev. Lett. **99**, 146403 (2007)]. Theoretical photoemission intensity maps have been generated by the spectral function calculated within the exciton condensate phase model and set against experimental angle-resolved photoemission spectroscopy data. The scope of this article is to present the detailed calculations in the framework of this model. They represent an extension of the original excitonic insulator phase model of Jérome *et al.* [Phys. Rev. **158**, 462 (1967)] to three dimensional and anisotropic band dispersions. A detailed analysis of its properties and comparison with experiment is presented. Finally, the disagreement with density functional theory is discussed.

### 4.6.1 Introduction

In the early 1960s, a new insulating phase was predicted to possibly exist at low temperature in solids having small energy gaps. Jérome *et al.*[2] published an extended study of this phase developing a BCS-like theory of its ground state. However, at that time an experimental realization of this phase was missing.

The excitonic insulator phase may occur in a semi-metallic or semiconducting system exhibiting a small (negative respectively positive) gap. Indeed, for a low carrier density, the Coulomb interaction is weakly screened, allowing therefore bound states of holes and electrons, called excitons, to build up in the system. If the binding energy $E_B$ of such pairs is larger than the gap $E_G$, the energy to create an exciton becomes negative, so that the ground state of the normal phase becomes unstable with respect to the spontaneous formation of excitons. According to Jérome *et al.*[2], at low temperature, these excitons may condense into a macroscopic coherent state in a manner similar to Cooper pairs in conventional BCS superconductors. Kohn[77] argued that exciton condensation may lead to the formation of charge density waves (CDW) of purely electronic origin (neglecting any lattice distortion), characterized by an order parameter.

$1\,T$-$TiSe_2$ is a layered transition-metal dichalcogenide exhibiting a commensurate (2x2x2) CDW[48] accompanied by a periodic lattice distortion below the transition temperature of $T_c \cong 200$ K. The origin of its CDW phase was controversial for a long time. Different scenarios have been proposed [63, 85], the best candidates being a band Jahn-Teller effect [64] and the excitonic insulator phase. Angle-resolved photoemission spectroscopy (ARPES) studies, evidencing directly the CDW, gave support to the former[59, 60] or the latter mechanism[57]. In 2006, superconductivity has been discovered in $TiSe_2$ upon Cu intercalation, providing a renewed interest in this system[47]. Furthermore superconductivity also occurs for the pure compound under pressure [86]. Recently, we presented ARPES data on $1\,T$-$TiSe_2$[87]. Theoretical photoemission intensity maps generated by the spectral function computed within the exciton condensate phase model gave strong evidence for exciton condensation in this material. To our knowledge, $1\,T$-$TiSe_2$ is the only presently known candidate for a low temperature phase transition to the exciton condensate state without the influence of any external parameters other than temperature. Indeed, as pressure is increased above 6 kbar on $TmSe_{0.45}Te_{0.55}$ samples (allowing to control the gap size and thus the energy necessary to create excitons), a transition to an insulating phase happens, whose origin can also be explained with exciton condensation[88]. In this context Bronold and Fehske proposed an effective model for calculating the phase boundary of a pressure-induced excitonic insulator, in the spirit of a crossover from a Bose-Einstein to a BCS condensate[79].

In this work, we adhere to the previously motivated mechanism of the exciton condensate phase for the origin of the CDW. We present the theory from which we compute the spectral function used to describe photoemission on $TiSe_2$ and provide further support for the exciton condensate phase scenario. In section 4.6.2, we extend the model worked out by Jérome *et al.*[2] for one dimension to three dimensional and anisotropic band dispersions. The Green's functions of the different bands are derived here. Section 4.6.4 first introduces the spectral function and its relation to photoemission. Then spectral weights and positions of the different bands are analyzed within this model. These theoretical results are compared to ARPES data of $TiSe_2$. Finally, the chemical potential and discrepancies with density functional theory (DFT) are discussed before we conclude in section 4.6.5.

### 4.6.2 The exciton condensate model

In this section, we present the model from which the spectral function describing photoemission on $TiSe_2$ has been computed. Jérome, Rice and Kohn [2] have already treated in detail the case of a one-dimensional excitonic insulator. In their work, they consider a single valence band and a single conduction band, both isotropic. However, for comparison with real experiment on the electronic structure of $TiSe_2$ an extension of the model to three dimensions with anisotropic band dispersions is required.

### 4.6.3 Description of the model

The Hamiltonian of the model is composed of a one-electron part $H_0$ and a Coulomb interaction part $W$. The one-electron part contains the dispersions of a single valence

band $\epsilon_v(\vec{k})$ and of three conduction bands $\epsilon_c^i(\vec{k})$ $(i = 1, 2, 3)$

$$H_0 = \sum_{\vec{k}} \epsilon_v(\vec{k}) a^\dagger(\vec{k}) a(\vec{k}) + \sum_{\vec{k},i} \epsilon_c^i(\vec{k} + \vec{w}_i) b_i^\dagger(\vec{k}) b_i(\vec{k}).$$

Here $a^\dagger(\vec{k})$ and $b_i^\dagger(\vec{k})$ are operators creating electrons with wave vector $\vec{k}$ in the valence band and with wave vector $\vec{k} + \vec{w}_i$ in the conduction band labelled $i$, respectively. In the case of $TiSe_2$, we consider the valence band (mainly of Se 4p character) giving rise to a hole pocket centered at Γ and three conduction bands (mainly of Ti 3d character), equivalent by symmetry, giving rise to electron pockets centered at the different L points of the Brillouin zone (BZ) (see Fig. 4.10 for a sketch of high symmetry points in the BZ). The Γ point is separated from the $L$ points by the three spanning vectors $\vec{w}_i = \Gamma L$. The band dispersions have been chosen of the form (previous expressions[87] were restricted to the $k_x-$axis)

$$\begin{aligned}
\epsilon_v(\vec{k}) &= \hbar^2 \frac{k_x^2 + k_y^2}{2m_v} + t_v \cos\left(\frac{2\pi k_z}{2k_{\Gamma A}}\right) + \epsilon_v^0, \\
\epsilon_c^i(\vec{k}) &= \frac{\hbar^2}{2m_L}\left((\vec{k} - \vec{w}_i)\cdot \vec{e}_{i\|}\right)^2 + \frac{\hbar^2}{2m_S}\left((\vec{k} - \vec{w}_i)\cdot \vec{e}_{i\perp}\right)^2 + t_c \cos\left(\frac{2\pi(k_z - w_{iz})}{2k_{\Gamma A}}\right) + \epsilon_c^0,
\end{aligned}$$

which describe well the bands near their extrema as they are measured in ARPES[87]. The unit vectors $\vec{e}_{i\|}$ and $\vec{e}_{i\perp}$, pointing along and perpendicular to the long axis of the ellipses, respectively, form a local in-plane basis for the electron pockets at the different $L$ points. Thus, $\vec{e}_{i\|} = \vec{w}_{i\|}/||w_{i\|}||$ where $\vec{w}_{i\|} = (w_{ix}, w_{iy}, 0)$ and $\vec{e}_{i\perp} = \vec{w}_{i\perp}/||w_{i\perp}||$ where we used the vector product $\vec{w}_{i\perp} = (0, 0, 1) \times \vec{w}_i$. The $m_v$, $m_L$ and $m_S$ are the effective masses of the valence band holes and of the conduction band electrons along the long and short axis of the electron pockets, respectively. The hopping parameters $t_v$ and $t_c$ represent the amplitudes of the dispersions perpendicular to the surface and $k_{\Gamma A}$ is the distance in reciprocal space between Γ and the A point. Parameters $\epsilon_v^0$ and $\epsilon_c^0$ are the band extrema of the bands.

The interaction part $W$ contains only the direct Coulomb interaction between electrons in the valence and the conduction bands

$$W = \sum_{\vec{q},i} \rho_a(\vec{q}) V_c(\vec{q}) \rho_{b,i}^\dagger(\vec{q}, \vec{w}_i)$$

where we have introduced partial electron density operators

$$\rho_a(\vec{q}) = \sum_{\vec{k}} a^\dagger(\vec{k} + \vec{q}) a(\vec{k}), \;\; \rho_{b,i}(\vec{q}, \vec{w}_i) = \sum_{\vec{k}} b_i^\dagger(\vec{k} + \vec{q}) b_i(\vec{k}).$$

The above sums run over the first BZ. Finally the Coulomb potential reads

$$V_c(\vec{q}) = \frac{4\pi e^2}{\epsilon(\vec{q}) q^2},$$

with $\epsilon$ being the dielectric function of the material.

In fact for $1T$-$TiSe_2$ there are three ($4p$-derived and Se related valence) bands at Γ near the Fermi energy. However, within a minimal model, we include only the highest lying valence band (as the valence band) in the calculations. Finally, the chemical potential

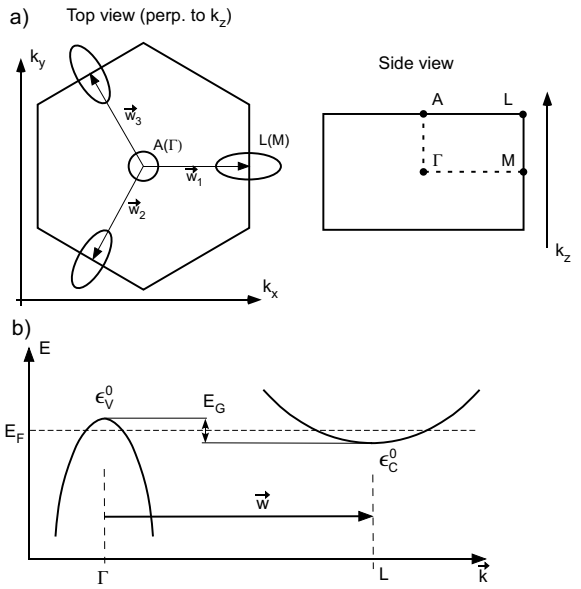


FIGURE 4.10: Schematic picture of the $1T$-$TiSe_2$ bands considered in this model (near the Fermi energy $E_F$). (a) Top view of the BZ (perpendicular to $k_z$). The Fermi surface has a hole pocket at $\Gamma$ and three symmetry equivalent electron pockets at $L$, separated from $\Gamma$ by the spanning vectors $\vec{w}_i$, $i = 1, 2, 3$. The side view of the BZ helps to situate the high symmetry points. (b) Schematic cut along the $\Gamma L$ direction, showing the dispersions of the valence band (at $\Gamma$) and one conduction band (at $L$).

is not explicitly included in the model but it will be nonetheless discussed at the end of section 4.6.4.

#### 4.6.3.1 Exciton physics

In this paragraph, we introduce the formulation of the exciton physics in a similar way to Babichenko and Kiselev [89]. The aim of this discussion is to give a better insight into the concept of the excitons. We start from the field operator $\psi_a(\vec{r}) = \sum_{\vec{k}} \mathrm{e}^{i\vec{k}\cdot\vec{r}} a(\vec{k})$ which creates a hole in the valence band at position $\vec{r}$ and $\psi^\dagger_{b_i}(\vec{r}) = \sum_{\vec{k}} \mathrm{e}^{-i(\vec{k}+\vec{w}_i)\cdot\vec{r}} b^\dagger_i(\vec{k})$ which creates an electron in the conduction band $i$ at position $\vec{r}$. From these two entities, we construct the exciton creation operator

$$A^\dagger(\vec{r}, \vec{r}\,', \vec{w}_i) \quad = \quad \psi^\dagger_{b_i}(\vec{r})\psi_a(\vec{r}') = \sum_{\vec{k}_1, \vec{k}_2} \mathrm{e}^{-i(\vec{k}_1+\vec{w}_i)\cdot\vec{r}} \mathrm{e}^{i\vec{k}_2\cdot\vec{r}'} b^\dagger_i(\vec{k}_1) a(\vec{k}_2).$$

It is more appropriate to describe the exciton in terms of relative $\vec{u}$ and center of mass $\vec{R}$ coordinates. Due to the anisotropy of the electron pockets at $L$, we need to distinguish the in-plane coordinates parallel and perpendicular to the long axis of the ellipses, $\vec{w}_{i\parallel}$. For simplicity, we admit that $\vec{w}_{i\parallel}$ is parallel to the $x$-axis (for the other ellipses it is possible to generalize the following arguments using the $\vec{e}_{i\parallel}$ and $\vec{e}_{i\perp}$ unit vectors). Then we write $\vec{u} = \vec{r} - \vec{r}\,'$ and $R_\alpha = m'_\alpha r'_\alpha / M_\alpha + m_\alpha r_\alpha / M_\alpha$ with $M_\alpha = m'_\alpha + m_\alpha$ for $\alpha = x, y$. In terms of the previously defined masses we have $m'_\alpha = m_v$, since the hole pocket at $\Gamma$ is isotropic, and $m_x = m_L$ and $m_y = m_S$. Then, the exciton creation operator may be

redefined as

$$A^\dagger(\vec{R},\vec{u},\vec{w}_i) \;=\; \sum_{\vec{Q},\vec{p}} \mathrm{e}^{-i(\vec{Q}+\vec{w}_i)\cdot\vec{R}}\; \mathrm{e}^{-i\vec{p}\cdot\vec{u}-i\sum_\alpha \frac{m'_\alpha}{M_\alpha} w_{i\alpha}u_\alpha} b_i^\dagger\left(p_\alpha+\frac{m_\alpha}{M_\alpha}Q_\alpha\right) a\left(p_\alpha-\frac{m'_\alpha}{M_\alpha}Q_\alpha\right)$$

using the notation $a(k_\alpha)$ instead of $a((k_x,k_y)) \equiv a(\vec{k})$. The center of mass momentum $\vec{Q}=\vec{k}_1-\vec{k}_2$ and the relative momentum $p_\alpha = m_\alpha k_{1,\alpha}/M_\alpha + m'_\alpha k_{2,\alpha}/M_\alpha$ arise naturally.

At this point, we can expand the operator $b^\dagger a$ in terms of the exciton creation operator $A^\dagger$ in reciprocal space

$$b_i^\dagger\left(p_\alpha+\frac{m_\alpha}{M_\alpha}Q_\alpha\right) a\left(p_\alpha-\frac{m'_\alpha}{M_\alpha}Q_\alpha\right) = \sum_\lambda \phi^*_\lambda(\vec{p},\vec{w}_i) A^\dagger_\lambda(\vec{Q},\vec{w}_i) \tag{4.24}$$

where the coefficients appearing on the right hand side are the eigenfunctions of the hydrogen atom. In other words, the operator $A^\dagger_\lambda(\vec{Q},\vec{w}_i)$ creates an exciton having a center of mass momentum $\vec{Q}$. The electron-hole bound state is described by the hydrogen state $\phi_\lambda$ having the energy $E_\lambda = \mu e^4/8\epsilon^2\lambda^2$, $\epsilon$ being the dielectric constant and $1/\mu = \sum_\alpha 1/2\mu_\alpha$ being the reduced mass with $1/\mu_\alpha = 1/m_\alpha + 1/m'_\alpha$. According to Babichenko and Kiselev [89] (and generalizing to anisotropic conduction bands), this hydrogen state obeys to

$$\left(\sum_\alpha \frac{p_\alpha^2}{2\mu_\alpha} + E_\lambda\right)\phi^*_\lambda(\vec{p},\vec{w}_i) = \sum_{\vec{p}'} V_c(\vec{p}-\vec{p}')\phi^*_\lambda(\vec{p}',\vec{w}_i).$$

Due to orthogonality of the hydrogen wave functions, the relation (4.24) can be inverted to

$$A^\dagger_\lambda(\vec{Q},\vec{w}_i) = \sum_{\vec{p}} \quad \phi^*_\lambda(\vec{p},\vec{w}_i) \quad b_i^\dagger\left(p_\alpha+\frac{m_\alpha}{M_\alpha}Q_\alpha\right) a\left(p_\alpha-\frac{m'_\alpha}{M_\alpha}Q_\alpha\right)$$

which is the Fourier transform of the exciton creation operator. We now compute the equations of motion for annihilation operators.

#### 4.6.3.2 Equations of motion for the Green's functions

With the help of the Hamilonian $H = H_0 + W$, we compute the equation of motion for our electron annihilation operators

$$\begin{aligned} i\frac{\partial}{\partial t}a(\vec{p},t) &= [a(\vec{p},t),H] = \epsilon_v(\vec{p})a(\vec{p},t) + \sum_{\vec{q},\vec{k},i} V_c(\vec{q})a(\vec{p}+\vec{q},t)b_i^\dagger(\vec{k},t)b_i(\vec{k}-\vec{q},t), \\ i\frac{\partial}{\partial t}b_i(\vec{p},t) &= [b_i(\vec{p},t),H] = \epsilon_c^i(\vec{p}+\vec{w}_i)b_i(\vec{p},t) + \sum_{\vec{q},\vec{k}} V_c(\vec{q})a^\dagger(\vec{k}+\vec{q},t)a(\vec{k},t)b_i(\vec{p}+\vec{q},t). \end{aligned} \tag{4.25}$$

We now introduce Green's functions for the valence and the conduction bands

$$\begin{aligned} G_v(\vec{k},t,t') &= (-i)\langle Ta(\vec{k},t)a^\dagger(\vec{k},t')\rangle, \\ G_c^i(\vec{k},t,t') &= (-i)\langle Tb_i(\vec{k},t)b_i^\dagger(\vec{k},t'),\rangle \end{aligned}$$

where we used the time ordering operator $T$. Their equations of motion are derived directly from equations (4.25)

$$\begin{aligned}\left(i\frac{\partial}{\partial t}-\epsilon_v(\vec{p})\right)G_v(\vec{p},t,t') &= \delta(t-t')\\ &- i\sum_{\vec{q},\vec{k},i}V_c(\vec{q})\langle Ta(\vec{p}+\vec{q},t)b_i^\dagger(\vec{k},t)b_i(\vec{k}-\vec{q},t)a^\dagger(\vec{p},t')\rangle,\\ \left(i\frac{\partial}{\partial t}-\epsilon_c^i(\vec{p}+\vec{w}_i)\right)G_c^i(\vec{p},t,t') &= \delta(t-t')\\ &- i\sum_{\vec{q},\vec{k}}V_c(\vec{q})\langle Ta^\dagger(\vec{k}+\vec{q},t)a(\vec{k},t)b_i(\vec{p}+\vec{q},t)b_i^\dagger(\vec{p},t')\rangle.\end{aligned}$$

Using Wick's theorem we simplify the four-operator averages $\langle ...\rangle$ by neglecting correlations, i.e. keeping only the lowest order terms. The calculation is similar for both Green's functions. We get three two-operator contributions, namely

$$\begin{aligned}\langle Ta(\vec{p}+\vec{q},t)b_i^\dagger(\vec{k},t)b_i(\vec{k}-\vec{q},t)a^\dagger(\vec{p},t')\rangle = \langle a(\vec{p}+\vec{q},t)b_i^\dagger(\vec{k},t)\rangle\langle Tb_i(\vec{k}-\vec{q},t)a^\dagger(\vec{p},t')\rangle\\ -\langle a(\vec{p}+\vec{q},t)b_i(\vec{k}-\vec{q},t)\rangle\langle Tb_i^\dagger(\vec{k},t)a^\dagger(\vec{p},t')\rangle - \langle Ta(\vec{p}+\vec{q},t)a^\dagger(\vec{p},t')\rangle\langle b_i(\vec{k}-\vec{q},t)b_i^\dagger(\vec{k},t)\rangle,\end{aligned}$$

out of which only the first one remains (the second one is zero and the last one is a Hartree term which we consider as already included in the measured dispersions) so that the corresponding equations of motion become

$$\begin{aligned}\left(i\frac{\partial}{\partial t}-\epsilon_v(\vec{p})\right)G_v(\vec{p},t,t') &\approx \delta(t-t')\\ &+ i\sum_{\vec{q},\vec{k},i}V_c(\vec{q})\langle b_i^\dagger(\vec{k},t)a(\vec{p}+\vec{q},t)\rangle\langle Tb_i(\vec{k}-\vec{q},t)a^\dagger(\vec{p},t')\rangle,\\ \left(i\frac{\partial}{\partial t}-\epsilon_c^i(\vec{p}+\vec{w}_i)\right)G_c^i(\vec{p},t,t') &\approx \delta(t-t')\\ &- i\sum_{\vec{q},\vec{k}}V_c(\vec{q})\langle b_i(\vec{p}+\vec{q},t)a^\dagger(\vec{k}+\vec{q},t)\rangle\langle Ta(\vec{k},t)b_i^\dagger(\vec{p},t')\rangle.\end{aligned} \tag{4.26}$$

At this point, to go further we need to introduce the concept of the condensate phase.

#### 4.6.3.3 Condensate phase

When the energy gap is smaller than the exciton binding energy, the energy necessary to create an exciton becomes negative and the normal ground state becomes unstable towards the spontaneous formation of excitons. Once temperature is low enough, these excitons may condense into a macroscopic coherent state analogous to that of Cooper pairs in the BCS theory of superconductivity.

The first average on the right hand side of equations (4.26), for $\vec{k}=\vec{p}+\vec{q}$, can be expressed by the exciton creation operator (equation (4.24))

$$\langle b_i^\dagger(\vec{p}+\vec{q},t)a(\vec{p}+\vec{q},t)\rangle = \sum_\lambda \phi_\lambda^*(0,\vec{w}_i)\langle A_\lambda^\dagger(\vec{p}+\vec{q},\vec{w}_i)\rangle \approx \phi_0^*(0,\vec{w}_i)\langle A_0^\dagger(\vec{p}+\vec{q},\vec{w}_i)\rangle.$$

At sufficiently low temperature, only the lowest lying excitonic level is populated.

By analogy with the BCS theory, we can identify the average in this last equation with anomalous Green's functions, after appropriate variable substitutions. These new functions are defined as follows

$$\begin{aligned} F_i(\vec{k},t,t') &= (-i)\langle T b_i(\vec{k},t)a^\dagger(\vec{k},t')\rangle, \\ F_i^\dagger(\vec{k},t,t') &= (-i)\langle T a(\vec{k},t)b_i^\dagger(\vec{k},t')\rangle. \end{aligned} \tag{4.27}$$

They describe the scattering of a valence electron into the conduction band or inversely. Pushing further the analogy, we introduce the order parameter $\Delta_i$ describing the condensate

$$\begin{aligned} \Delta_i(\vec{p}) &= -i\sum_{\vec{q}} V_c(\vec{q})F_i^\dagger(\vec{p}+\vec{q},t,t)\rangle = \sum_{\vec{q}} V_c(\vec{q})\langle b_i^\dagger(\vec{p}+\vec{q},t)a(\vec{p}+\vec{q},t)\rangle \\ &\approx \sum_{\vec{q}} V_c(\vec{q})\phi_0^*(0,\vec{w}_i)\langle A_0^\dagger(\vec{p}+\vec{q},\vec{w}_i)\rangle \end{aligned} \tag{4.28}$$

(here the anomalous Green's function definition (4.27) and equation (4.24) have been used). It quantifies the intensity of exciton formation between the valence band and the conduction band labelled $i$. Moreover, it characterizes the state of the system in the sense that, when the order parameter is different than zero, exciton condensation drives the system into the CDW phase (see section 4.6.4 for further discussion).

#### 4.6.3.4 The Green's function of the valence band

With the help of these new elements, we can go back to equation (4.26). In the particular case of the Green's function of the valence band, we obtain

$$\left(i\frac{\partial}{\partial t} - \epsilon_v(\vec{p})\right) G_v(\vec{p},t,t') = \delta(t-t') - \sum_i \Delta_i(\vec{p}+\vec{q})F_i(\vec{p},t,t'). \tag{4.29}$$

In order to solve this equation for $G_v$, we need to find a similar expression for the anomalous Green's function by computing its equation of motion. This procedure results in the following relation

$$\left(i\frac{\partial}{\partial t} - \epsilon_c^i(\vec{p}+\vec{w}_i)\right) F_i(\vec{p},t,t') = -\Delta_i(\vec{p})G_v(\vec{p},t,t') \tag{4.30}$$

where we have again identified the order parameter.

Converting the time-dependence into a (imaginary) frequency $z$ dependence with a Fourier transform allows us to solve the system of equations given by (4.29) and (4.30) for the Green's function of the valence band

$$G_v(\vec{p},z) = \left(z - \epsilon_v(\vec{p}) - \sum_i \frac{|\Delta_i(\vec{p})|^2}{z-\epsilon_c^i(\vec{p}+\vec{w}_i)}\right)^{-1}. \tag{4.31}$$

#### 4.6.3.5 The Green's function of the conduction band

Calculating the Green's function of the conduction band involves a treatment similar to that of the valence band. From equation (4.26) and with definitions (4.27) and (4.28) we get

$$\left(i\frac{\partial}{\partial t} - \epsilon_c^i(\vec{p}+\vec{w}_i)\right) G_c^i(\vec{p},t,t') = \delta(t-t') - \Delta_i^*(\vec{p})F_i^\dagger(\vec{p},t,t'). \tag{4.32}$$

The equation of motion of $F^\dagger$ is obtained with help of equation (4.25) and Wick's theorem

$$\begin{aligned}\left(i\frac{\partial}{\partial t} - \epsilon_a(\vec{p})\right) F_i^\dagger(\vec{p},t,t') &= -i\sum_{\vec{k},\vec{q},j} V_c(\vec{q})\langle Ta(\vec{p}+\vec{q},t)b_j^\dagger(\vec{k},t)b_j(\vec{k}-\vec{q},t)b_i^\dagger(\vec{p},t')\rangle \\ &\approx -i\sum_{\vec{q},j} V_c(\vec{q})\langle a(\vec{p}+\vec{q},t)b_j^\dagger(\vec{p}+\vec{q},t)\rangle\langle Tb_j(\vec{p},t)b_i^\dagger(\vec{p},t')\rangle.\end{aligned} \tag{4.33}$$

The averages on the right hand side bring into play three $b$ operators and present an off-diagonal term mixing $b_i$ with $b_j^\dagger$ operators. When $j=i$, the last average lets appear the Green's function $G_b^i$ while $i \neq j$ terms involve new Green's functions representing the scattering of an electron from one conduction band to another one (usually called multivalley scattering)

$$H_{ij}(\vec{k},t,t') = (-i)\langle Tb_i(\vec{k},t)b_j^\dagger(\vec{k},t')\rangle.$$

Their equation of motion reads

$$\left(i\frac{\partial}{\partial t} - \epsilon_c^i(\vec{p}+\vec{w}_i)\right) H_{ij}(\vec{k},t,t') = -\Delta_i^*(\vec{p})F_j^\dagger(\vec{p},t,t'). \tag{4.34}$$

Thus, with the help of the definition of the order parameter $\Delta$, replacing this last definition into (4.33) results in

$$\left(i\frac{\partial}{\partial t} - \epsilon_a(\vec{p})\right) F_i^\dagger(\vec{p},t,t') = -\Delta_i(\vec{p})G_c^i(\vec{p},t,t') - \sum_{j\neq i}\Delta_j(\vec{p})H_{ji}(\vec{p},t,t'). \tag{4.35}$$

Equations (4.32), (4.34) and (4.35) together build a system of equations which can be solved with respect to $G_c^i$, providing us with the following expression after a Fourier transform to frequency space

$$G_c^i(\vec{p}+\vec{w}_i,z) = \left(z - \epsilon_c^i(\vec{p}+\vec{w}_i) - \frac{|\Delta_i(\vec{p})|^2}{(z-\epsilon_v(\vec{p})) - \sum_{j\neq i}\frac{|\Delta_j(\vec{p})|^2}{z-\epsilon_c^j(\vec{p}+\vec{w}_j)}}\right)^{-1}. \tag{4.36}$$

The Green's functions of the valence band (4.31) and of the conduction bands (4.36) have been already written in our previous paper[87] without the mathematical derivation developed here in details.

### 4.6.4 Results and discussions

#### 4.6.4.1 The spectral function

In the context of photoemission, the spectral function $A(\vec{p},\Omega)$ plays a central role. It is directly proportional to the imaginary part of the Green's function and in the case of one-electron Green's functions as defined in section 4.6.2, it describes the one-electron removal spectrum.

For the exciton condensate model, we distinguish the spectral function of the valence band

$$A_v(\vec{p},\Omega) \;=\; -\frac{1}{\pi}\mathrm{Im}[G_v(\vec{p},\Omega+i\delta)]$$

($\delta$ is here an infinitesimal real quantity) and that of the conduction band

$$A_c^i(\vec{p}+\vec{w}_i,\Omega) \;=\; -\frac{1}{\pi}\mathrm{Im}[G_c^i(\vec{p},\Omega+i\delta)].$$

To simplify further calculations, we rewrite the Green's functions (equation (4.31) and (4.36)) in the following forms

$$G_v(\vec{p},z) \;=\; \frac{1}{\mathcal{D}(\vec{p},z)}\cdot\prod_i(z-\epsilon_c^i(\vec{p}+\vec{w}_i)), \tag{4.37}$$

$$\begin{aligned} G_c^i(\vec{p},z) \;=\; & \frac{1}{\mathcal{D}(\vec{p},z)}\cdot\Big((z-\epsilon_v(\vec{p}))\prod_{j\neq i}(z-\epsilon_c^j(\vec{p}+\vec{w}_j)) \\ & -\sum_{m,j\neq i}|\Delta_j(\vec{p})|^2|\varepsilon_{ijm}|(z-\epsilon_c^m(\vec{p}+\vec{w}_j))\Big) \end{aligned} \tag{4.38}$$

($\varepsilon_{ijm}$ is the permutation symbol). The denominator $\mathcal{D}$, common to all Green's functions, is

$$\begin{aligned} \mathcal{D}(\vec{p},z) \;&=\; (z-\epsilon_v(\vec{p}))\prod_i(z-\epsilon_c^i(\vec{p}+\vec{w}_i)) - \sum_i|\Delta_i(\vec{p})|^2\prod_{j\neq i}(z-\epsilon_c^j(\vec{p}+\vec{w}_j)) \\ &=\; \prod_{\alpha=1}^{4}(z-\Omega_\alpha(\vec{p})) \end{aligned} \tag{4.39}$$

(here the index $\alpha$ refers to the four zeros of the denominator $\mathcal{D}$, while the other indices refer to the three conduction bands). In the last line, the denominator is factorized in terms involving its four (real) zeros $\Omega_\alpha(\vec{p})$ (which are implicitly functions of the order parameter $\Delta$). These zeros can be calculated exactly. However their analytical forms are too long to be written here.

This allows us to break apart the Green's functions (4.37) and (4.38) into rational expressions with minimal denominators, so that we can use Sokhotsky's formula

$$\frac{1}{x-x_0+i\epsilon} = \mathcal{P}\frac{1}{x-x_0} - i\pi\delta(x-x_0)$$

($\mathcal{P}$ denotes the principal part) and write the spectral functions in rather simple forms

$$\begin{aligned} A_v(\vec{p},\Omega) &= \sum_{\alpha=1}^{4} P_\alpha^v(\vec{p})\,\delta(\Omega-\Omega_\alpha(\vec{p})), \\ A_c^i(\vec{p}+\vec{w}_i,\Omega) &= \sum_{\alpha=1}^{4} P_\alpha^{c_i}(\vec{p})\,\delta(\Omega-\Omega_\alpha(\vec{p})), \end{aligned}$$

where the weights $P_\alpha(\vec{p})$ (which are also implicitly functions of the order parameter $\Delta$) associated to the poles $\Omega_\alpha$ are

$$\begin{aligned} P_\alpha^v(\vec{p}) &= \frac{\prod_i(\Omega_\alpha-\epsilon_c^i(\vec{p}+\vec{w}_i))}{\prod_{\beta\neq\alpha}(\Omega_\alpha-\Omega_\beta)}, \\ P_\alpha^{c_i}(\vec{p}) &= \frac{(\Omega_\alpha-\epsilon_v(\vec{p}))\prod_{n\neq i}(\Omega_\alpha-\epsilon_c^n(\vec{p}+\vec{w}_n))}{\prod_{\beta\neq\alpha}(\Omega_\alpha-\Omega_\beta)} \\ &\quad -\frac{\sum_{m,n\neq i}|\Delta_n(\vec{p})|^2|\epsilon_{inm}|(\Omega_\alpha-\epsilon_c^m(\vec{p}+\vec{w}_n))}{\prod_{\beta\neq\alpha}(\Omega_\alpha-\Omega_\beta)}. \end{aligned}$$

Until now, to ensure the generality of the theory, we always kept the $\vec{k}$-dependence of the order parameter $\Delta(\vec{k})$. However, in the practical analysis which will follow, we will use a $\vec{k}$-independent order parameter estimated from experiment.

#### 4.6.4.2 The spectral function and photoemission

Within the sudden approximation, the contributions to the photoemission intensity are the spectral function, the matrix elements and the Fermi-Dirac distribution. In this paper we concentrate on the spectral function, being well established in the previous subsection.

We now choose to fix the parameters that describe the band dispersions. They will take the values [g] determined from our previous ARPES study[87] on samples exhibiting a slight Ti overdoping ($\leq 1\%$). The case of an ideal compound (without overdoping), in relation to DFT calculations, will be discussed in section 4.6.4.4. The dispersions and the spectral weight curves presented below will be calculated along the high symmetry directions $\Gamma M$ and $AL$ only, which coincide with the long axis of the electron pocket ellipsis. This choice is motivated by the fact that the experimental intensity maps of section 4.6.4.3 were also measured in these directions and that the most important effects of the exciton condensate are visible along $\Gamma M$ and $AL$. From the spectral functions, we can derive a first important information. The zeros of their denominator $\mathcal{D}$ are the poles of the Green's functions and therefore represent the renormalized electronic band positions in the system. Noting that a zero order parameter $\Delta$ in equation (4.39) results in band positions that are not renormalized, one realizes that $\Delta$ is a good indicator of the strength of this renormalization. Moreover, since this denominator is the same for both the valence and the conduction bands, we see that the valence band at $\Gamma$ is backfolded at $L$ and that the conduction bands at $L$ are backfolded at $\Gamma$ (as expected from the electron-hole coupling). This is a first indication of the CDW phase in the

[g] The fit parameters are : $\epsilon_v^0$=-0.03±0.005 eV, $m_v$=-0.23±0.02 $m_e$, where $m_e$ is the free electron mass, $t_v$=0.06±0.005 eV ; $\epsilon_c^0$=-0.01±0.0025 eV, $m_c^x$=5.5±0.2 $m_e$, $m_c^y$=2.2±0.1 $m_e$, $t_c$=0.03±0.0025 eV.

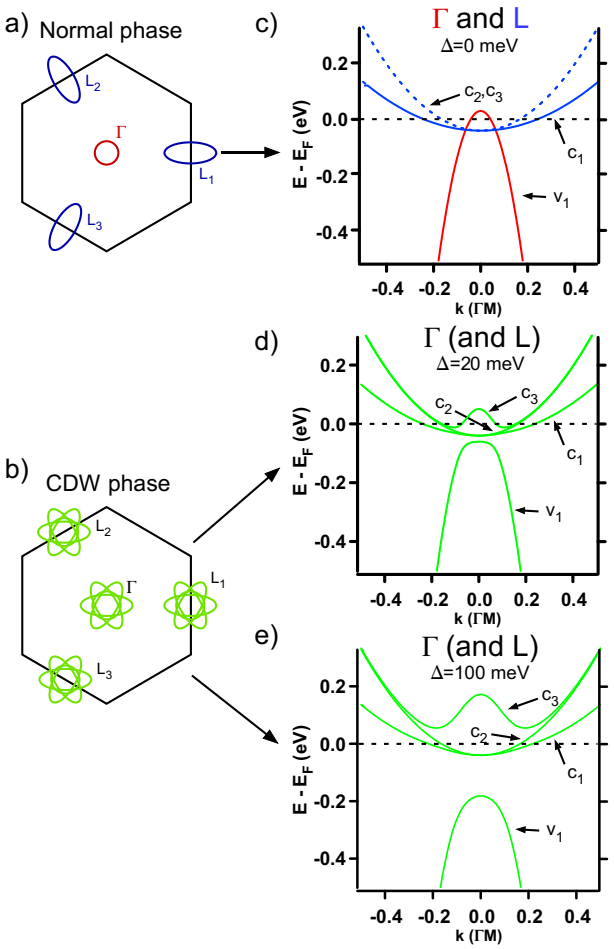


FIGURE 4.11: Schematic picture of the band positions in the model (near $E_F$) in the normal phase and in the CDW phase. Wave vectors are expressed in a multiple of $\Gamma M$. (a) In the normal phase ($\Delta = 0$ meV), the Fermi surface composed of the valence band at $\Gamma$ (in red) and three symmetry equivalent conduction bands at $L$ (in blue). (b) In the CDW phase ($\Delta \neq 0$ meV), $\Gamma$ becomes equivalent to $L$. The electron pockets at $L$, backfolded to $\Gamma$, produce "flower"-like Fermi surfaces at each newly equivalent high symmetry point. (c) Dispersions calculated parallel to $\Gamma M$ (see Fig. 1(a)) around $\Gamma$ and parallel to $AL_1$ around the three $L$-points in the normal phase plotted on the same graph (the minima of the different conduction bands $c_1, c_2, c_3$ have been displaced from the $L$-points to $\Gamma$ on the graph). (d),(e) Dispersions around $\Gamma$ and along $\Gamma M$ in the CDW phase for $\Delta = 20$ meV respectively $\Delta = 100$. In the CDW phase, $\Gamma$ and $L$ become equivalent concerning the dispersions.

system. The situation for the band positions (not considering their spectral weight) is illustrated in Fig. 4.11. Part (a) depicts a cut through the Fermi surface (FS) (around the $\Gamma$ and L points) in the normal phase, composed of the valence band hole pocket (red) and three (symmetry equivalent) electron pockets (blue). In the CDW phase, which is characterized by an order parameter $\Delta \neq 0$ meV, this FS changes into that of Fig. 4.11 (b). Via the electron-hole coupling the $L$-points become equivalent to $\Gamma$ (not yet considering the spectral weights) and all three conduction bands are backfolded onto the valence band. In parallel, in Fig. 4.11 (c), (d) and (e) we show the associated dispersions. The labels $v_1, c_1, c_2, c_3$ refer to the four different poles of the Green's functions, being identified as the valence band ($v_1$) and the three symmetry equivalent conduction bands ($c_1$,$c_2$,$c_3$). To facilitate the comparison, in the normal phase, we superimpose the valence

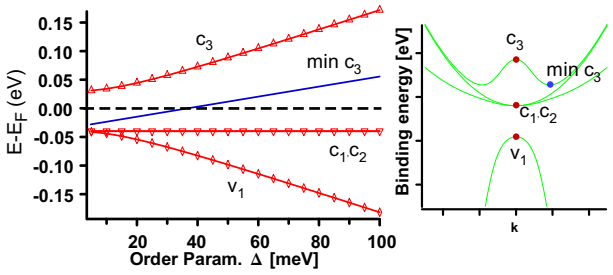


FIGURE 4.12: Extrema of the renormalized bands as a function of the order parameter $\Delta$ (left). Position of these extrema on the band dispersions (right).

band ($v_1$ located at $\Gamma$, red continuous line) and the conduction bands (blue continuous line for $c_1$ and blue dashed line for $c_2, c_3$, normally located at the $L$-points but shifted here to $\Gamma$). For the CDW phase, we distinguish two cases, one with a low value of the order parameter (Fig. 4.11 (d), $\Delta = 20$ meV) and one with a high value of the order parameter (Fig. 4.11 (e), $\Delta = 100$ meV). These values are reasonable in comparison with experiment and help to understand how the CDW transition sets in. Once the order parameter increases to a non-zero value, there is a strong change in the band dispersions. The valence band $v_1$ and the conduction band $c_3$ split, opening a gap between them. As the order parameter increases to $\Delta = 100$ meV, $v_1$ and $c_3$ repell each other further, while $c_1$ and $c_2$ stay at their original positions.

We now turn to the discussion of the extrema of the bands. Fig. 4.12 presents the band extrema as a function of the order parameter $\Delta$. We see that, except for small values of the order parameter, they display a linear behaviour (this can be shown analytically from the denominator in equation (4.39) for $\vec{k}$ exactly at $\Gamma$ and $L$ where the three original conduction bands have the same energy). Among the three conduction bands, only one ($c_3$) shifts away from the Fermi energy. Its two minima (blue line) also increase linearly. Compared to the conduction band $c_3$, the valence band maximum ($v_1$) follows the inverse behaviour, thereby opening a gap below $E_F$.

It is important to realize that when considering three conduction bands instead of one, the system remains in a semimetallic state at low temperature rather than evolving into an insulating state, since the gap opens below the Fermi energy. Therefore, strictly speaking, the denomination excitonic insulator phase in this context is misleading and we rather adopted the expression exciton condensate phase.

Besides the position of the bands the spectral function contains an additional crucial information, namely, the spectral weight (SW) carried by each band in the process of one-electron removal probed by photoemission. It is related to the numerator of the spectral function. We now add this feature to the previous figure and obtain Fig. 4.13, where the SW of the bands is indicated in gray scale. The evolution from the normal state (Fig. 4.13(a)) to the CDW state with an order parameter of 20 meV (Fig. 4.13(b)) and 100 meV (Fig. 4.13(c)) is shown.

We immediately see (Fig. 4.13) that, with respect to the SW, the backfolding is in fact incomplete even at a large value of the order parameter. In the CDW phase with an order parameter of $\Delta = 100$ meV (Fig. 4.13(c)), at $\Gamma$, the original valence band looses SW in favor of the backfolded conduction band ($c_3$). At $L$, the situation is different. Two backfolded bands appear now, a symmetry equivalent conduction band ($c_3$) and the valence band ($v_1$), taking their SW from the original conduction band ($c_1$). The dashed

lines indicate a conduction band ($c_1$) backfolded to $\Gamma$, which has a negligibly small SW (see below).

In Fig. 4.14, we focus on the SW of the bands at $\Gamma$ and $L$ (SW of the conduction band $c_2$ is not represented here since it is exactly 0 for every $k$ along the $\Gamma M$ and $AL$ directions). Graphs 4.14(a) and (b) display the SW of the valence band ($v_1$) at $\Gamma$ and $L$, respectively, for different values of the order parameter $\Delta$. Graphs 4.14(c), (d) and 4.14(e), (f) show the SW for bands $c_3$ and $c_1$, respectively. These graphs allow to quantify the observations made above. At $\Gamma$, the original valence band gives 60% (4.14(c)) of its SW to the backfolded conduction band, keeping 40% (4.14(a))for itself. At $L$, the situation is more complicated, since three bands ($v_1$, $c_1$, $c_3$) share now the SW. The original conduction band ($c_1$) keeps a minimum of 67% of SW (4.14(f)), while the other two backfolded bands ($c_3$ and $v_1$) divide among themselves the remaining 33% (4.14(b),(d)). At $\Gamma$, the backfolded conduction band ($c_1$) has a small non-zero SW as shown in Graph 4.14(e) (it is less than 1% for the values of the order parameter considered here).

We also present the graphs for $\Delta = 20$ meV. We see that there is a large SW loss (more than 80% at $\vec{k} = \vec{0}$ Å$^{-1}$) in the valence band, even larger than that for $\Delta = 100$ meV (Fig. 4.14(a)). What happens can be seen as follows. Going back to Fig. 4.13, if we observe the graphs (a), (b) and (c) close to $\Gamma$ (i.e., the left panels) as a function of $\Delta$, we see that at $\Delta = 20$ meV the shape of the valence band tries to stay the same as for $\Delta = 0$ meV. This is achieved by a reduced SW of $v_1$ and an increased SW of $c_3$. At $\Delta = 100$ meV the dispersions are sufficiently different from the non-renormalized ones to carry more SW. In other words, for small values of the order parameter, the SW will be distributed along the parts of the dispersions corresponding mainly to the non-renormalized ones. A similar situation happens at $L$, as can be seen in Fig. 4.13 between bands $v_1$, $c_1$ and $c_3$. But this time, the original band (in the normal phase) is the conduction band $c_1$, so that for small values of the order parameter, its SW is shared between $v_1$, $c_1$ and $c_3$.

It should be noted that from photoemission data it is difficult to extract information concerning (thermally occupied) states above the Fermi energy (set to 0 eV here), so that SW of band $c_3$ is hardly measured in experiment[87].

#### 4.6.4.3 Comparison with experiment

The purpose of this section is to make a link with our previous paper. Therefore we further analyze experimental ARPES intensity maps[87] in the light of the discussions of section 4.6.4.2(calculated intensity maps are not reproduced hereafter, see[87] for more details). The data were collected at the Swiss Light Source with a photon energy of 31 eV on $TiSe_2$ samples. At this photon energy, the normal emission spectra correspond to states located close to the $\Gamma$ point, but not exactly. Therefore we will use the surface notation $\bar{\Gamma}$ for these measured intensity maps.

Fig. 4.15 presents comparisons between the theoretical (left) and experimental (right) electronic structures at $\Gamma$ and $\bar{\Gamma}$ respectively. The experimental intensity maps at $T =$ 250K (Fig. 4.15 (a)) and $T = 65$K (Fig. 4.15 (b)) are compared to calculated bands with $\Delta = 25$ meV and $\Delta = 75$ meV, respectively. These values for the order parameter in the RT and low temperature phases respectively have been chosen to ensure the best

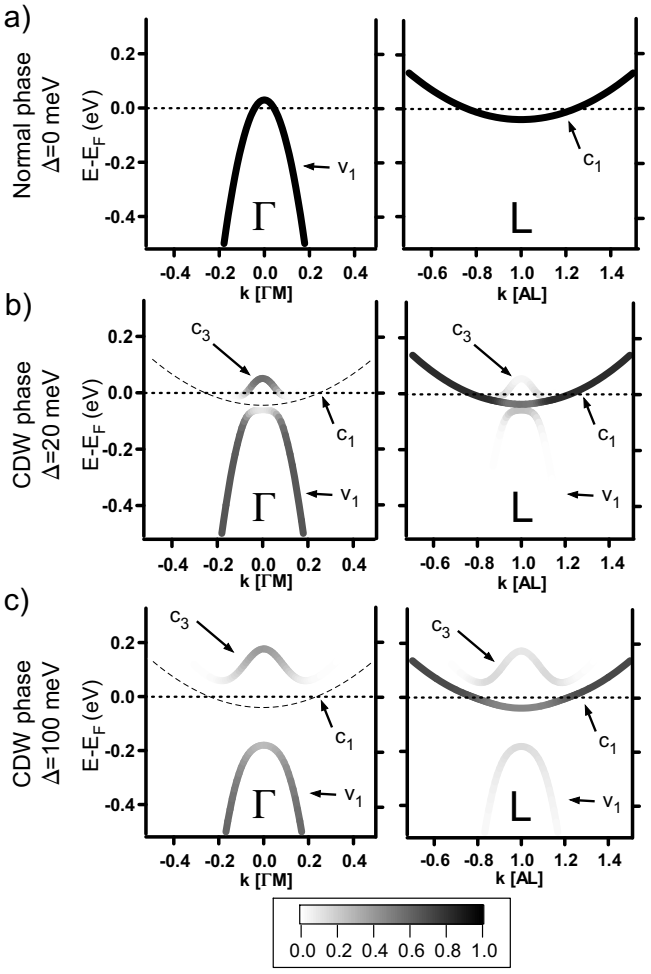


FIGURE 4.13: Band dispersions with their corresponding spectral weight at Γ and $L$, along Γ$M$ and $AL$ directions, respectively. Graph (a) describe the normal phase ($\Delta = 0$ meV), (b) the CDW phase with moderate excitonic effects ($\Delta = 20$ meV) and (c) the CDW phase with strong excitonic effects ($\Delta = 100$ meV). The dashed lines indicate a band ($c_1$) having a small non-zero SW (see text).

visual agreement between calculated and measured intensity maps[87]. This gives thus an estimation of the size of the order parameter describing the exciton condensate in $TiSe_2$. At $T = 250$K on the experimental side (Fig. 4.15, right), the situation is more complicated than in our model. Indeed, there are three Se4$p$-derived valence bands, out of which two (black lines), are not considered in our model. The dashed white line corresponds to the valence band $v_1$ of the model, which suffers already SW loss at $T = 250$K. It flattens at its maximum and deviates from the parabolic shape of the normal phase dispersion (this is clear from an energy distribution curve taken at $k_{\|} = 0$ Å$^{-1}$, not shown here). On the theoretical side (Fig. 4.15 (a), left), the dispersion reproduces well the experiment when considering an order parameter of $\Delta = 25$ meV. However, at this temperature, the system should be in the normal phase. Nevertheless, as in high temperature superconductors, above the critical temperature, we expect fluctuations to persist well above $T_c$ in the exciton condensate phase[90, 91]. Thus, this non-zero order parameter above $T_c$ may be understood in terms of fluctuations. According to the left graph of Fig. 4.15 (a), the bottom of the backfolded conduction band $c_3$ appears just below $E_F$. In parallel, the experiment shows small humps in momentum distribution

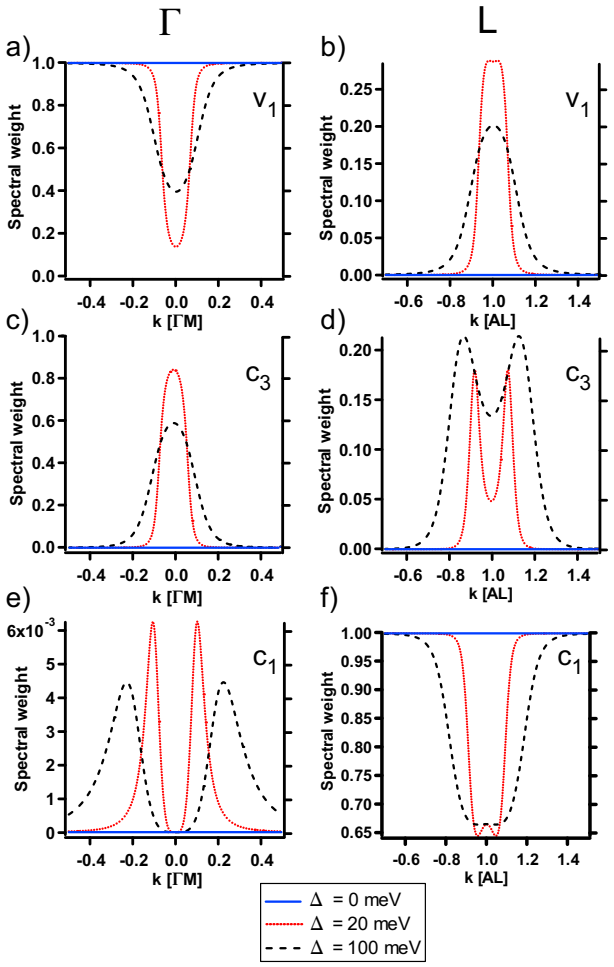


FIGURE 4.14: Spectral weights of the bands at Γ and $L$, along Γ$M$ and $AL$ directions, respectively, for Δ values of 0, 20 and 100 meV. Graphs (a) and (b) describe the valence band ($v_1$) at Γ and its backfolded version at $L$, respectively. Graphs (c) and (d) describe the conduction band $c_3$ at Γ (where it follows the top of the original valence band) and $L$ respectively. Graphs (e) and (f) describe the conduction band $c_1$ at Γ and $L$, respectively (where it is the original conduction band).

curves near $E_F$ (not seen in the false colour map here). These can be attributed to $c_3$, considering that the Fermi distribution will weaken the SW of this band on the theoretical dispersion. At $T$ = 65K (Fig. 4.15 (b), right), the valence band in the experimental intensity map shifts to higher binding energies, in agreement with the theoretical dispersions calculated for an order parameter Δ = 75 meV (Fig. 4.15 (b), left). Moreover, on the experimental map, some intensity emerges just below $E_F$ (not seen in the false colour map, see Ref.[87]), revealing a dispersive band. Altough it does not appear directly in the corresponding calculation using $\delta$-peaks, it is reproduced if a finite 30 meV line broadening (lifetime) is introduced. In other words, this dispersive intensity comes from the combined tails of the maximum of the valence band $v_1$ (located in the occupied states) and of the minima of the backfolded conduction band $c_3$ (located in the unoccupied states).

Fig. 4.16 presents comparisons between the theoretical and experimental electronic structures at the Brillouin zone boundary. The experimental intensity maps at $T$ = 250K (Fig. 4.16 (a)) and $T$ = 65K (Fig. 4.16 (b)) are compared to calculated bands with

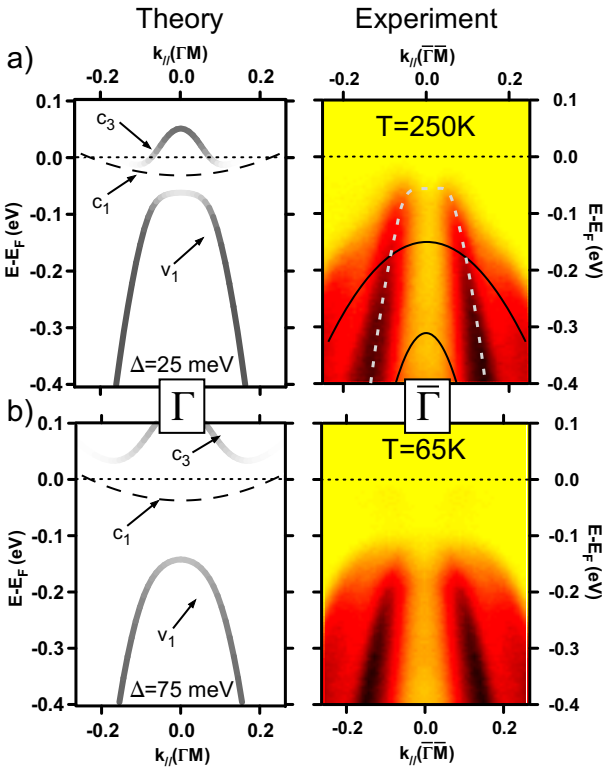


FIGURE 4.15: Comparisons between theoretical and experimental ($h\nu = 31$ eV) electronic structures at $\Gamma$ and $\bar{\Gamma}$ respectively (see text for explanations of this notation). (a) The theoretical bands have been calculated for $\Delta = 25$ meV and the experimental intensity maps are taken at $T = 250$K. The continuous black lines highlight the Se4$p$-derived bands not considered in the model, while the dashed white line indicates the valence band corresponding to $v_1$. (b) The theoretical bands have been calculated for $\Delta = 75$ meV and the experimental intensity maps are taken at $T = 65$K. The dashed black lines indicate the backfolded conduction band $c_1$ which carries a small non-zero SW (Fig. 4.14 (e)).

$\Delta = 25$ meV and $\Delta = 75$ meV, respectively. At a photon energy of 31 eV, initial states between $M$ and $L$ are probed (in a free electron final state picture, we are not probing the BZ exactly at $L$). Therefore, we will use the $\bar{M}$ notation for the measured intensity maps below. Substantial changes (explained by excitonic effects) in the spectra are evident. At $T = 250$K (Fig. 4.16 (a)), on the experimental side (right), the conduction band, highlighted by the dashed white line, is well described by the theoretical band $c_1$ (left). It also exhibits a decrease of intensity at its bottom, as predicted by our model (see Fig. 4.14 (f)). Moreover it looks like a band having a large width and some surprisingly high intensity persists far from its centroid, even at binding energies of about 300 meV. These features can be well explained by the theoretical bands (Fig. 4.16, left) at $\Delta = 25$ meV. Due to the finite width of real bands, the conduction band $c_1$ merges with its close (backfolded) neighbours $v_1$ or $c_3$ (depending on the position along $AL$), resulting in a band broadening. The residual intensity at high binding energies is explained with the populated branches of the backfolded valence band $v_1$ (see Fig. 4.14 (b)). Indeed, looking carefully at the lower part of the experimental map (Fig. 4.16 (a), right), one sees that the residual intensity is larger away from $\bar{M}$ (this is confirmed by momentum distribution curves, not shown here). At $T = 65$K (Fig. 4.16 (b)), on the experimental side (right), a strong signature of the CDW appears. The valence band is backfolded at $\bar{M}$ with a high SW. In fact, even a second Se4$p$-derived valence band (indicated by the

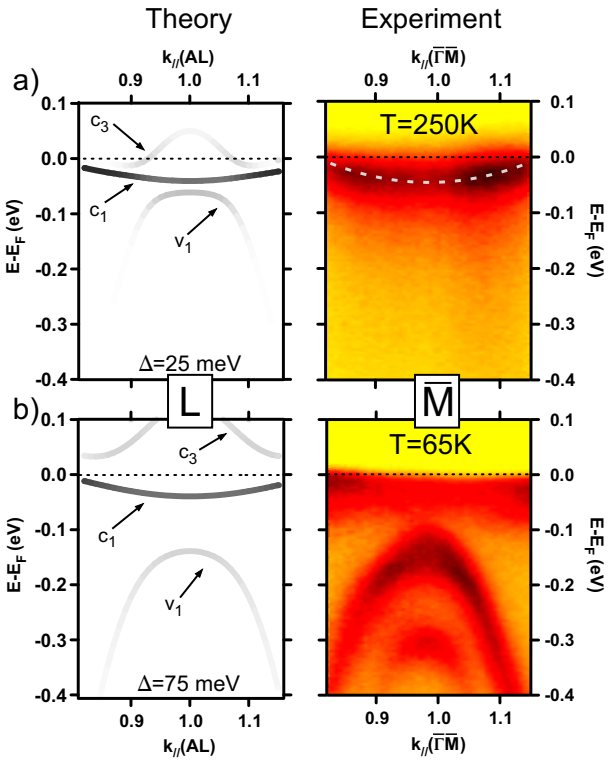


FIGURE 4.16: Comparisons between theoretical and experimental ($h\nu = 31$ eV) electronic structures at the Brillouin zone boundary (see text). (a) The theoretical bands have been calculated for $\Delta = 25$ meV and the experimental intensity maps are taken at $T = 250$K. The dashed white line indicates the conduction band corresponding to $c_1$. (b) The theoretical bands have been calculated for $\Delta = 75$ meV and the experimental intensity maps are taken at $T = 65$K.

lowest lying black line in the right graph of Fig. 4.15 (a)) participates to the backfolding at $\bar{M}$. On the theoretical side, this situation (considering only the topmost Se4*p*-derived valence band) is reproduced with an order parameter of $\Delta = 75$ meV. The backfolded valence band $v_1$ is well separated from the conduction band $c_1$, as in the experiment. It can be clearly seen in the corresponding experimental intensity map that the conduction band $c_1$ does not shift with an increasing order parameter (see Fig. 4.12) and looses more SW at its bottom (see Fig. 4.14 (f)). The backfolded conduction band $c_3$ is too far away from $E_F$ in the unoccupied states to be measured by ARPES. In the model, at $L$, the intensity of the backfolded valence band $v_1$ is lower than that of the conduction band $c_1$ for high values of the order parameter, corresponding to a well settled CDW phase (see Fig. 4.14 (b) and (f)). In the ARPES measurements presented here, this intensity relation is reversed, as can be seen on the right graph of Fig. 4.16 (b). The precise reason for this matter remains unclear. It can be due to the fact that we consider only the topmost valence band in our model. Indeed, a second backfolded valence band appears at $\bar{M}$ in the low temperature measurements (Fig. 4.16 (b), right). Moreover, we have noticed that this intensity relation between the original and backfolded bands can change from one sample to another, or even depends on the quality of the cleaved surface. Further investigations are needed to understand this issue.

#### 4.6.4.4 Further discussions

In the model described in section 4.6.2, the chemical potential was not explicitly calculated since it was defined as the zero energy of the dispersions. To verify whether the chemical potential shifts when the system enters in the CDW phase, we have computed the electronic density for the renormalized bands, taking into account their dispersion over the whole BZ. Due to the parabolic approximation of the band dispersions around their extrema, we only took into account electrons having an energy up to 0.5 eV below $E_F$. If we keep the chemical potential at $\mu = 0$ eV, a decrease of about 35% of the electronic density results between the normal phase and the CDW phase with an order parameter $\Delta = 75$ meV. This discrepancy is reduced to zero if we shift the chemical potential by $+60$ meV. This result can be understood with the SW transfers depicted on Fig. 4.13. At $\Gamma$, when going from the normal to the CDW phase (from Fig. 4.13 (a) to (c)) we loose 13% of the SW of the normal phase (integration of the SWs of Fig. 4.14 (a) and (c)) accounting for the Fermi distribution. At $L$ (from Fig. 4.13 (a) to (c)), after the CDW transition, we loose 40% of SW in the conduction band and we acquire 18% of SW in the backfolded valence band (integration of the SWs of Fig. 4.14 (b), (d) and (f)). Thus, considering only the high symmetry directions for illustrative purposes, this results in the 35% of SW missing when going from the normal to the CDW phase, which can be recovered by slightly raising the chemical potential (which affects mostly the conduction band $c_1$).

This shift would be measurable in photoemission. For having a detailed knowledge of the chemical potential, one needs to perform precise ARPES measurements over a wide range of temperatures. However, this is beyond the scope of this article and will be studied in the future.

In previous ARPES data[87], we extracted (from RT measurements) an overlap between the valence and conduction bands in the normal phase of 70 meV. DFT calculations within local density approximation agree on the semimetallic nature of $TiSe_2$ but the size of the overlap varies from 200 meV[85] to 800 meV[92]. According to our ARPES data, the position of the minimum of the conduction band has been determined to -40 meV. The position of the maximum of the valence band has been evaluated at 30 meV. To ensure charge neutrality in the system, that is, an equal number of holes in the valence band and electrons in the conduction bands, our valence band should have its maximum at about 380 meV (this comes from a calculation similar to that done above for the chemical potential shift), provided that the maximum of the conduction bands remains at -40 meV. This results in an overlap of 420 meV which is of the same order of magnitude than DFT. As shown by Di Salvo *et al.*[48], deviation from the optimal conditions of sample growth provokes an excess of Ti atoms which in turn decreases the transition temperature $T_c$ of the system. In our case, an excess of about 1% of Ti can explain the slightly lower $T_c$ we observe in our samples[87]. A simple calculation shows that a valence band having its maximum at 30 meV is then reasonable provided that these excess Ti atoms give their $3d$ electrons to fill this band. The assumption according to which doping electrons go preferentially to the valence band is actually supported by the fact that excess atoms reside in the Van der Waals gap where they build bonds with the neighbouring Se atoms[93, 94]. Fig. 4.17 illustrates the alternative case of an ideal (non-doped) system with an overlap of 420 meV, in the CDW phase with moderate excitonic effects. Dispersions of this ideal compound are plotted with the corresponding SWs for $\Delta = 20$ meV. This has to be compared with Fig. 4.13(b) describing the similar situation for the overdoped system. At $\Gamma$, the situation is very different above $E_F$. In the

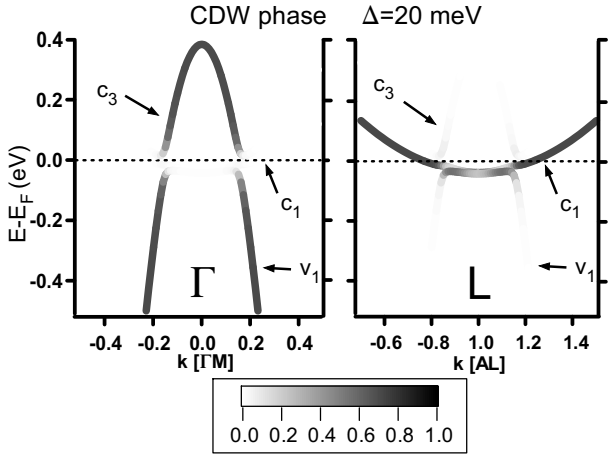


FIGURE 4.17: Band dispersions of the ideal (non doped) system (see text) with their corresponding spectral weight at Γ and $L$, along Γ$M$ and $AL$ directions, respectively. An order parameter of $\Delta = 20$ meV has been used, describing a CDW phase with moderate excitonic effects.

ideal system, the backfolded conduction band $c_3$ follows the top of the original valence band with a high SW. However, this band is located in the unoccupied states, being thus nearly invisible to photoemission. In the occupied states, the valence band $v_1$ is much more similar to its equivalent in the overdoped system, the main difference being the radius of the valence band parabola near $E_F$. At $L$, the original conduction band $c_1$ of the ideal compound suffers more from excitonic effects than in the overdoped one, but the backfolded valence band $v_1$ is so close to it that its SW compensates for that lost by $c_1$. At $L$, $c_3$ has a very low SW, but is in any case in the unoccupied states.

In summary, we have compared the cases of an ideal system, having an equal number of holes and electrons, and of an overdoped system, displaying a large difference in their normal phase electronic structure near $E_F$. However, once excitonic effects are switched on (similar to those identified in the experiment at room temperature already), this difference nearly vanishes. From the considerations described above, it turns out that the best criterium to distinguish between these two cases is the radius of the valence band parabola at Γ near $E_F$ and at room temperature. Looking at Fig. 4.15 (a) (right) indicates clearly that this radius is much smaller in the experiment than in the ideal system (Fig. 4.17), supporting the idea that our samples are slightly overdoped.

### 4.6.5 Conclusions

Recently intensity maps calculated within the exciton condensate phase model have been compared with ARPES data of $1T$-$TiSe_2$. Strikingly good agreement gave strong evidence for exciton condensation as the driving force of the CDW transition[87]. In the present paper, we have presented the theory of the excitonic insulator model generalized to the three dimensional case of $1T$-$TiSe_2$ with anisotropic band dispersion. From the Green's functions of the valence and conduction bands, we computed the corresponding spectral functions needed to generate photoemission intensity maps. The mathematical treatment is similar to BCS theory and the deduced order parameter in the low temperature phase describes the intensity of condensating electron-hole pairs (excitons). These pairs are created by the electron-hole interaction between the valence band at Γ

and the conduction bands at $L$. As a natural consequence of the non-zero momentum of the excitons, this produces band backfoldings between $\Gamma$ and $L$ which thus tend to be equivalent as the order parameter increases. It must be emphasized that the CDW produced by this model is of purely electronic origin and that the spectral weights transferred between the original and backfolded bands are large (see reference[87] for a more complete discussion of this subject). While no real gap opens at the Fermi energy, it is notably shown that the valence band (original and backfolded) is shifted in a quasi-linear manner to higher binding energies as the order parameter increases. Such a behaviour could offer a direct way to extract the temperature dependence of the excitonic order parameter. Further investigations of the model are in progress, notably to tackle the important question of the origin of the very small lattice distortion observed by Di Salvo *et al.*[48] (involving ion displacements of hundredths of angströms). Preliminary calculations, based on the electron-lattice coupling in the tight binding formalism of Yoshida and Motizuki[95], indicate that the exciton condensate corresponding to an order parameter of the order of $\Delta = 100$ meV, produces forces on the ions of the right order of magnitude. Finally, the present paper treats only the low temperature condensation phase of the exciton condensate. However, room temperature measurements indicate that strong excitonic fluctuations prevail far above $T_c$, reminding the behaviour of the pseudo-gap in high temperature superconductors above the critical temperature. Their theoretical and experimental study promises an interesting extension of this work.

Skillfull technical assistance was provided by the workshop and electric engineering team. This work was supported by the Fonds National Suisse pour la Recherche Scientifique through Div. II and MaNEP.

## 4.7 Comments to "Spontaneous exciton condensation in 1*T*-$TiSe_2$: a BCS-like approach"

### 4.7.1 An effective Hamiltonian: another point of view

This article contains the detailed calculation of the three-dimensional system, that has been done using many body theory within the Green's function formalism, at zero temperature. Therefore, the perturbation expansion of the electron-hole interaction was performed at lowest order only, corresponding to a mean-field approximation. The goal was here to describe in detail the condensate phase at $T < T_c$, which was used in the previous article 4.4 to emphasize the very good agreement of our model with the experiment.

As we can see in section 4.6.2, the calculations for the three-dimensional exciton condensate phase are heavier than those developed in section 4.2. In particular, a new type of Green's function, $H_{ij}(\vec{k}, t, t')$, representing the scattering of electrons between the different electron pockets at $L$, had to be introduced. It is instructive to build the matrix form of an effective Hamiltonian $\hat{H}_{eff}$ including the valence $\epsilon_v$ and the conduction bands $\epsilon_c^i$ with an effective one-body interaction between them symbolized by the parameter $\delta$

$$\begin{pmatrix} \epsilon_v & \delta & \delta & \delta \\ \delta^* & \epsilon_c^1 & 0 & 0 \\ \delta^* & 0 & \epsilon_c^2 & 0 \\ \delta^* & 0 & 0 & \epsilon_c^3 \end{pmatrix}. \tag{4.40}$$

This suggests that any Hamiltonian having this matrix form, that is, any Hamiltonian where only the valence and the conduction bands are coupled together, can lead to the photoemission intensity maps calculated previously. In particular, an effective electron-phonon mediated interaction, like for the band Jahn-Teller mechanism, would lead to a similar Hamiltonian [59]. However, specificities of the electron-hole interaction will be emphasized in the forthcoming chapters, as for instance the high value of the corresponding order parameter, steming from the strength of the electon-hole interaction (see chapter 5), or the small ionic displacements involved in the PLD (see chapter 7).

Diagonalizing the Hamiltonian 4.40 is done by finding the roots of the secular determinant $||z - \hat{H}_{eff}|| = 0$. The determinant of the inverse of a matrix is the inverse of the determinant of that matrix. Therefore, this is equivalent to finding the roots of the matrix

$$(z\mathbf{1} - \hat{H}_{eff})^{-1} = \hat{G}.$$

Interestingly, it turns out that $\hat{G}$ is the matrix formed by all the different Green's functions we have encountered in section 4.6,

$$\hat{G} = \begin{pmatrix} G_v & F_1 & F_2 & F_2 \\ F_1^\dagger & G_c^1 & H_{12} & H_{13} \\ F_2^\dagger & H_{21} & G_c^2 & H_{23} \\ F_3^\dagger & H_{31} & H_{32} & G_c^3 \end{pmatrix}.$$

The matrix form 4.40 suggests that we are studying the dynamics of an effective Hamiltonian where the valence and conduction bands only are coupled with an effective one-body

interaction of the form $V_{eff} \sim V_0\, b_i^\dagger a$. This could be viewed as a kind of hybridization $V_0 = \langle\psi_b|V_{eff}|\psi_a\rangle$ between the valence and conduction bands (corresponding to eigenstates of wave functions $\psi_a$ and $\psi_b$ respectively). However, in our case, as can be seen in Fig. 4.10 (c) for instance, the valence and conduction bands do not cross each other, so that no hybridization can take place between them. Their extrema are located at different position in reciprocal space, which is the reason why their coupling leads to a CDW phase.

### 4.7.2 Differences between the one-dimensional and the three-dimensional models

In the three-dimensional model, all the three conduction bands located at $L$ are coupled to the valence band at $\Gamma$ via the electron-hole coupling. As a consequence, the corresponding band structure in the CDW phase is more complicated than that of the one-dimensional case. Instead of the two bands at $\Gamma$ and at $M$ (see Fig. 4.4) for the latter model, we have now four bands at $\Gamma$ (see Fig. 4.11 (e)), among which the original valence ($v_1$) band and three backfolded conduction bands ($c_1, c_2, c_3$). At $L$, the original conduction band ($c_1$) is accompanied by two backfolded (from the other symmetry equivalent $L$ points) conduction bands ($c_2, c_3$) and the backfolded valence band ($v_1$). Here it should be emphasized that, although the notation $c_1, c_2, c_3$ refers, in the normal phase, to the conduction bands located at the different $L$ points ($L_1, L_2, L_3$ in Fig. 4.11 (a)), they refer, in the CDW phase, (together with $v_1$) to the different poles of the denominator of equation 4.39 and a simple connection with the different $L$ points cannot be made anymore (due to hybridisation).

An essential difference between the two models is that, within the three-dimensional case, the CDW gap does not affect the whole Fermi surface, but, as can be seen on Fig. 4.13, the original conduction band ($c_1$) remains visible at $L$, since it carries a non-negligible spectral weight in the CDW phase. This effect of partial Fermi surface gapping due to a CDW phase has already been observed in different materials and it has been related to the fact that only the states involved in the formation of the CDW shift from $E_F$ and open a gap [34, 45, 96]. However, in our case, the situation is different. Both the valence and the conduction bands, which are the main contributions to the Fermi surface, are involved in the process at the origin of the CDW.

- In the one-dimensional case, this is equivalent to a system of two levels in interaction, whose energy spectrum at $L$ is depicted in Fig. 4.18 (a). Here both levels move away from each other as the interaction ($\Delta$) increases, opening a gap between them.
- In the three-dimensional case, this is equivalent to four levels in interaction and their behaviour at $L$ as the interaction increases, depicted in Fig. 4.18 (b), is more complicated. Two levels move away from each other ($v_1$ and $c_3$), opening a gap between them, but the two other levels ($c_1$ and $c_2$) stay at their original position. The situation is slightly different when adding the spectral weights. The original conduction band ($c_1$) carries most of the spectral weight, while the other one ($c_2$) can be neglected (see Fig. 4.13 and the corresponding discussion). This makes the crucial difference between these two models. As a consequence, exciton condensation in the three-dimensional model does not lead to a semimetal-semiconductor transition (if the conduction band in the normal phase crosses $E_F$),

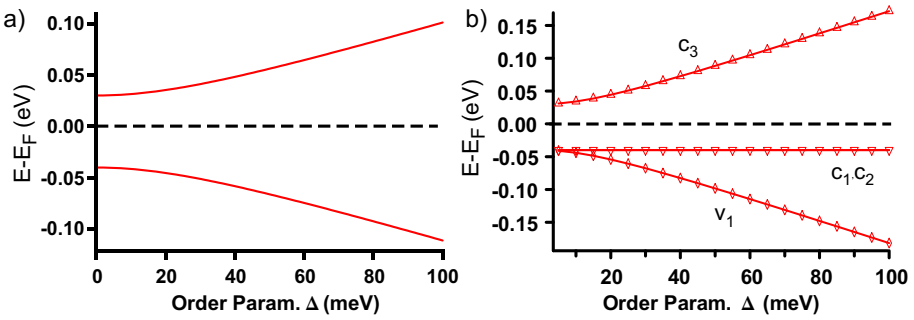


FIGURE 4.18: (a) Positions of the bands for the one-dimensional model at $M$ as a function of the order parameter. (b) Positions of the bands for the three-dimensional model at $L$ as a function of the order parameter.

since occupied states always exist at $E_F$. Therefore, we called the low temperature phase the exciton condensate phase, rather than the excitonic insulator phase (which remains valid for the one-dimensional model).

This difference allows us also to discriminate between the two models and to answer the question whether it is necessary to consider the coupling of the valence band to three conduction bands. First of all, theoretically it would be difficult to argue in favour of a single valence-conduction band coupling, especially in view of the threefold symmetry of the system. Then, from measurements taken along the $\bar{\Gamma}\bar{M}$ direction, it is clear[h] that the original conduction band keeps its initial parabolic shape (like curve $c_1$ in Fig. 4.11 (e)), rather than exhibiting the upturn characteristic of the top of the valence band (like in Fig. 4.4 (b)).

Finally, in the case of the (one-dimensional) excitonic insulator phase, we have noticed that the spectral weight loss in the valence band at $\Gamma$ was transferred to its backfolded replica at $M$. Due to the higher number of bands implied in the (three-dimensional) exciton condensate phase, the situation is different. It turns out that the spectral weight lost by the valence band at $\Gamma$ is exactly shared by its three backfolded replica, at the three symmetry-equivalent $L$ points.

### 4.7.3 Discussion of the chemical potential

In our excitonic models, we do not include the chemical potential $\mu$ in our Hamiltonian to ensure a self-consistent conservation of the occupied states. Nonetheless, we discussed its evolution in the CDW phase in section 4.6.4.4.

Similarly to what is done in physics textbooks, any change of the chemical potential can be determined by requiring that the electronic density $n$ is constant with respect to any temperature or phase change

$$n = \int \frac{d\vec{k}}{4\pi^3} \int d\omega A(\vec{k},\omega) N_F(\omega-\mu) = \int \frac{d\vec{k}}{4\pi^3} N_F(\varepsilon(\vec{k})-\mu), \tag{4.41}$$

for the case where the spectral function $A(\vec{k},\omega) = \delta(\omega - \varepsilon(\vec{k}))$ describes a dispersion $\varepsilon(\vec{k})$ having a zero width (a delta function). Here we explicitly wrote the chemical potential

[h] This is not really the case with the measurements of Fig. 4.16 (a) (right), but data presented in chapter 6 are much more conclusive on this point.

in the Fermi distribution. In the case of the exciton condensate phase, we have to deal with four different dispersions having different spectral weights, which depend on whether they are evaluated at $\Gamma$ or $L$. Therefore equation 4.41 becomes

$$n = n_\Gamma + n_L = \sum_{\alpha=1}^{4} \int \frac{d\vec{k}}{4\pi^3} P_\alpha^v(\vec{k}) N_F(\Omega_\alpha(\vec{k}) - \mu) + \frac{3}{2} \sum_{\alpha=1}^{4} \int \frac{d\vec{k}}{4\pi^3} P_\alpha^c(\vec{k}) N_F(\Omega_\alpha(\vec{k}) - \mu). \tag{4.42}$$

It is important to perform this integral over the *normal phase* Brillouin zone. The factor 3/2 accounts for the fact that the electrons pockets at $L$ appear three times but must be divided by two due to the Brillouin zone boundary.

This formula allowed us to compute in section 4.6.4.4 the chemical potential shift of +60 meV (i.e. a shift of the bands into the occupied states) when the system, starting from the normal state ($\Delta = 0$ meV), enters into the CDW state with $\Delta = 100$ meV.

Appendix A gives more details about the numerical routine used for these calculations.

# Chapter 5

# Temperature dependence of the exciton condensate phase

## 5.1 Introduction

In chapter 4, we have introduced the exciton condensate phase model, which is a three-dimensional version of the original excitonic insulator phase adapted to the band dispersions of 1$T$-$TiSe_2$. Based on this model, we were able to compute the corresponding spectral functions, for the valence and the conduction bands. These spectral functions were then used to compute photoemission intensity maps which were compared with experimental ones. Once the parameters of the valence and conduction bands are fixed (by fits to experimental data taken at room temperature), the only remaining free parameter in the model is the order parameter. In section 4.4, it was determined qualitatively, by ensuring the best visual agreement of calculated photoemission intensity maps with those measured at 250K and 65K (Fig. 4.7 and 4.8 respectively).

In this chapter, in section 5.2, we first present a theoretical study of the effect of temperature in the exciton condensate model. In a first step, a simple way to introduce such

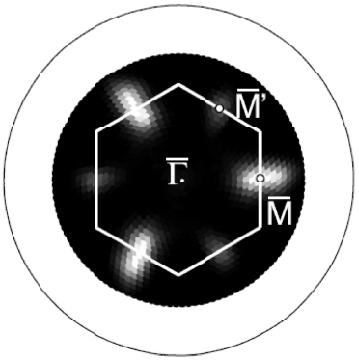


FIGURE 5.1: Fermi surface mapping of $TiSe_2$ ($h\nu$=21.2 eV) in the $\bar{\Gamma}\bar{M}\bar{K}$ plane, with the corresponding surface projected (along the (0001)) direction Brillouin zone, in grayscale (white indicates high intensity).

effects in our model (derived at zero-temperature), is to focus onto the temperature dependence of the order parameter. For that purpose, we have chosen a BCS-like form $\Delta(T) = \Delta_0 \cdot \sqrt{1 - (T/T_c)^2}$.

In section 5.3, in a second step, we present photoemission measurements taken at different temperatures. As shown in Fig. 5.1, the main contribution to the Fermi surface comes from the conduction bands at $\bar{M}$. Therefore we focus on these bands in our study. They are analyzed within the framework of the exciton condensate phase model to extract not only the temperature dependence of the order parameter, but also of the chemical potential.

Finally, in section 5.5, we compute the order parameter of the exciton condensate phase model, using the gap equation 4.28 derived previously, and comment on its dependence on the band parameters and on the screening of the Coulomb interaction.

## 5.2 Temperature dependence of the excitonic insulator phase model in 1*T*-$TiSe_2$

C. Monney[a], H. Cercellier[b], C. Battaglia[a], E.F. Schwier[a], C. Didiot[a], M. G. Garnier[a], H. Beck[a] and P. Aebi[a],

[a] *Institut de Physique, Université de Neuchâtel, CH-2000 Neuchâtel, Switzerland*
[b] *Institut Néel, CNRS, F-38042 Grenoble, France*

Accepted for publication in Physica B

**Abstract**

Recently, detailed calculations of the excitonic insulator phase model adapted to the case of 1*T*-$TiSe_2$ have been presented. Through the spectral function theoretical photoemission intensity maps can be generated which are in very good agreement with experiment [Phys. Rev. Lett. **99**, (2007) 146403]. In this model, excitons condensate in a BCS-like manner and give rise to a charge density wave, characterized by an order parameter. Here, we assume an analytical form of the order parameter, allowing to perform temperature dependent calculations. The influence of this order parameter on the electronic spectral function, to be observed in photoemission spectra, is discussed. The resulting chemical potential shift and an estimation of the resistivity are also shown.

*Key words:* photoemission, strongly correlated electrons, calculated intensity maps, exciton condensate
*PACS:* 1.45.Lr, 71.27.+a, 79.60.Bm, 71.35.Lk

### 5.2.1 Introduction

The transition metal dichalcogenide 1*T*-$TiSe_2$ is a layered compound exhibiting a commensurate (2x2x2) charge density wave (CDW) at low temperature[48]. In transport measurements, its signature is a strong anomaly in the resistivity, peaking slightly below the transition temperature $T_c = 200$K. The CDW is accompanied by a periodic lattice distortion involving small atomic displacements. At the same time, a zone boundary phonon softens, being a central ingredient to conventional theories of structural transitions[49]. High resolution angle-resolved photoemission spectroscopy (ARPES) measurements brought a deeper insight into the electronic properties of 1*T*-$TiSe_2$ by clearly revealing the appearance of new backfolded bands, characterisitc of a new periodicity in the system[57, 59, 60].

The origin of the CDW can hardly be explained by the usual nesting mechanism[85], because there are notably no large parallel Fermi surface portions[38]. Currently, the best candidates are a band Jahn-Teller effect[64] and the excitonic insulator phase. Recently, the latter scenario has been strongly supported by comparison of ARPES data with theoretical photoemission intensity maps [87]. These calculations are based

on the excitonic insulator phase model [2, 77], which has been adapted to the particular case of $1T$-$TiSe_2$[80]. The excitonic insulator phase may occur in a semimetallic or semiconducting system exhibiting a small (negative respectively positive) gap. Indeed, for a low carrier density, the Coulomb interaction is weakly screened, allowing therefore bound states of holes and electrons, called excitons, to build up in the system. If the binding energy $E_B$ of such pairs is larger than the gap $E_G$, the energy to create an exciton becomes negative, so that the ground state of the normal phase becomes unstable with respect to the spontaneous formation of excitons. At low temperature, these excitons may condense into a macroscopic coherent state in a manner similar to Cooper pairs in conventional BCS superconductors. Exciton condensation may lead to the formation of CDW of purely electronic origin (not initiated by a lattice distortion), characterized by an order parameter $\Delta$. To our knowledge, $1T$-$TiSe_2$ is the only presently known candidate for a low temperature phase transition to the excitonic insulator state without the influence of any external parameters other than temperature. Indeed, as pressure is increased above 6 kbar on $TmSe_{0.45}Te_{0.55}$ ( controlling the gap size and thus the energy necessary to create excitons), a transition to an insulating phase happens, whose origin can also be explained with exciton condensation [88]. In this context Bronold and Fehske proposed an effective model for calculating the phase boundary of a pressure-induced excitonic insulator, in the spirit of a crossover from a Bose-Einstein to a BCS condensate [79].

Here, we study the temperature dependence of the excitonic insulator phase. This is achieved by choosing a simple analytical form for its order parameter and inserting it into the results of our previous calculations [80].

### 5.2.2 Results and Discussion

The electronic structure of $1T$-$TiSe_2$ near the Fermi energy $E_F$ is composed of three Se4$p$-derived valence bands at the $\Gamma$ point (center of Brillouin zone) and three Ti3$d$-derived conduction bands distributed among the three symmetry equivalent $L$ points (zone boundary). There is a slight overlap of $\sim$ 70 meV, such that $1T$-$TiSe_2$ has a semimetallic character. This issue is still controversial among the ARPES community, but a recent infrared study confirmed the semimetallicity [97]. In an ionic picture, Ti [Ar]$3d^2 4s^2$ gives all its valence electrons to the two neighbouring Se [Ar]$3d^{10} 4s^2 4p^4$, leaving a system with an empty $d^0$ shell. In our model, we consider only the topmost valence band (the other two do not cross the Fermi energy and play a minor role) and the three conduction bands. The valence band and the three symmetry equivalent conduction bands give rise to a hole pocket at $\Gamma$ and electron pockets at $L$ (see Fig. 5.2(a)). Their band dispersions, $\epsilon_v$ for the valence band and $\epsilon_c^i$ $(i = 1, 2, 3)$ for the conduction bands, have been approximated by a parabolic form which describes them well near their extrema, in agreement with ARPES experiment [87].

Our Hamiltonian is composed of a one-electron part $H_0$, containing the one-electron energies, and a Coulomb interaction part $W$, which represents the electron-hole interaction between the valence and the conduction bands. Below $T_c$, this interaction allows electron-hole pairs, i.e. excitons, to form a condensate described by the order parameter $\Delta$. The calculated Green's functions $G_v$ and $G_c$ describing the bandstructure at $\Gamma$ and

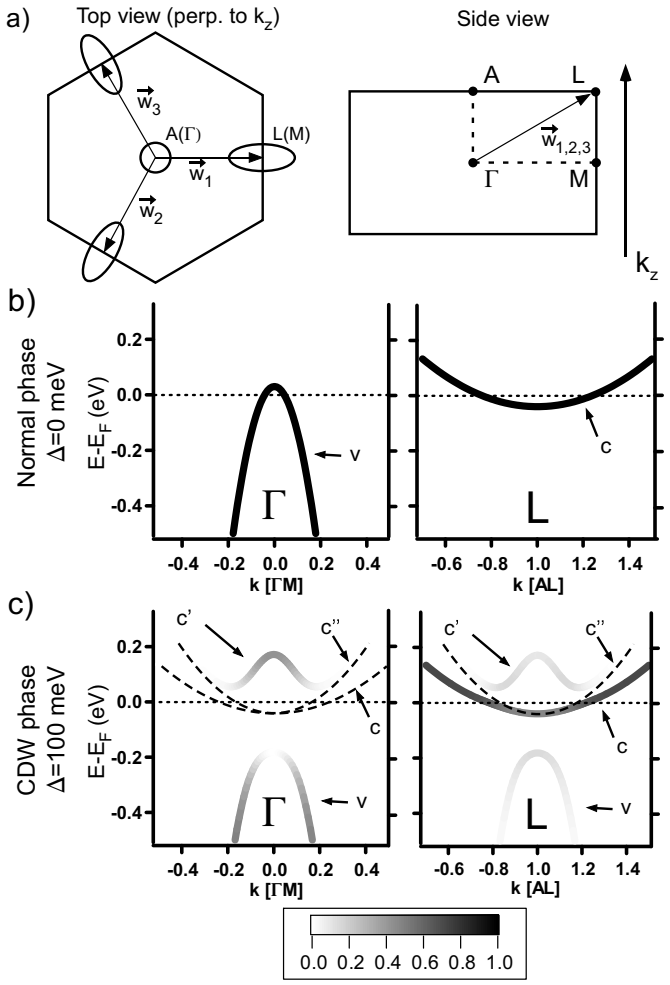


FIGURE 5.2: (a) On the left, schematic picture of the Fermi surface (in the plane perpendicular to $k_z$) considered in the model, placed on the Brillouin zone of $1\,T$-$TiSe_2$. On the right, side view of the Brillouin zone showing high symmetry points. Graphs (b) and (c) show band dispersions with their spectral weight (photoemission spectra) calculated with the spectral function at $\Gamma$ and $L$ along the high symmetry direction $\Gamma M$ and $AL$ (long axis of the electron pockets) for an order parameter $\Delta = 0$ meV and $\Delta = 100$ meV respectively. The spectral weight carried by the band is indicated in grayscale. In Graphs (c), the thin dashed lines indicate the position of bands having negligibly small spectral weight.

$L$ respectively have the following forms [80]

$$
\begin{aligned}
G_v(\vec{p},z) &= \prod_i (z-\epsilon_c^i(\vec{p}+\vec{w}_i))\cdot\frac{1}{\mathcal{D}(\vec{p},z)},\\
G_c^i(\vec{p},z) &= \left((z-\epsilon_v(\vec{p}))\prod_{j\neq i}(z-\epsilon_c^j(\vec{p}+\vec{w}_j)) - |\Delta|^2\sum_{m,j\neq i}|\varepsilon_{ijm}|(z-\epsilon_c^m(\vec{p}+\vec{w}_j))\right)\\
&\quad\cdot\frac{1}{\mathcal{D}(\vec{p},z)}
\end{aligned}
$$

($\varepsilon_{ijm}$ is the permutation symbol). The vectors $\vec{w}_i$, called spanning vectors, correspond to the distance between $\Gamma$ and the $L$ points. The denominator $\mathcal{D}$, common to both

Green's functions, is

$$\mathcal{D}(\vec{p},z) \;=\; (z-\epsilon_v(\vec{p}))\prod_i (z-\epsilon_c^i(\vec{p}+\vec{w}_i)) - |\Delta|^2 \sum_i \prod_{j\neq i} (z-\epsilon_c^j(\vec{p}+\vec{w}_j)).$$

The zeroes of this denominator give the renormalized band dispersions, which depends on the order parameter $\Delta$. They are common to $\Gamma$ and $L$, i.e., for $G_v$ and $G_c$, as one expects for a CDW characterized in our case by the spanning vectors $\vec{w}_i$. The spectral function, $A(\vec{p},\Omega) = -\mathrm{Im}[G(\vec{p},\Omega+i\delta)]/\pi$, describes the one-electron spectrum, essential for our purposes. It provides us with the spectral weight (SW) carried by the dispersions in the process of photoemission. Fig. 5.2(b) and (c) present calculated photoemission spectra at $\Gamma$ and $L$ along the high symmetry direction $\Gamma M$ and $AL$ (long axis of the electron pockets) for an order parameter $\Delta = 0$ meV (normal phase) and $\Delta = 100$ meV (CDW phase) respectively. The SW of the dispersions is indicated in grayscale. On Fig. 5.2 (c), the bands indicated by the thin dashed lines have a negligibly small SW, so that they do not appear on these grayscale graphs. We immediately see that the similarity of the bands at $\Gamma$ and $L$ is only approximate. At $\Gamma$, as the order parameter increases, the lower part of the valence band $v$ shifts to higher binding energies, while its top $c'$ shifts above $E_F$, opening thereby a gap. Some SW is then tranferred from $v$ to $c'$. At $L$, with an increasing order parameter, the conduction band $c$ does not move but looses SW in favor of the backfolded valence band $v$ and the new band $c'$ (which are the same as those appearing at $\Gamma$).

In order to introduce temperature effects in the model in a simple way, we now choose a particular form for the order parameter $\Delta(T) = \Delta_0 \cdot \sqrt{1-(T/T_c)^2}$ where $\Delta_0$ is its value at $T = 0$K. This function is drawn in Fig. 5.3(a) for $\Delta_0 = 100$ meV and $T_c = 200$K. It is similar to a BCS order parameter, displaying a steep decrease at $T_c$ and a saturation for $T \to 0$K. Introducing this order parameter into the denominator of $\mathcal{D}$ and calculating its zeros provides us with the curves of Fig. 5.3 (b). They show the temperature dependence of the band positions at $\Gamma$ and $L$. Below the transition temperature, the backfolded valence band $v$ and conduction band $c'$ shift away from their normal phase positions, exhibiting a behaviour very similar to the shape of the order parameter. At the same time, the conduction band $c$ and a symmetry equivalent version $c''$ stay at their inital position. Considering also SWs and broadening the $\delta$-like peaks with a finite width of 30 meV (for presentation purposes), Fig. 5.3 (c) displays over a wide temperature range spectra at $L$ (not equivalent to $\Gamma$ due to the SWs), where the excitonic effects are the most spectacular. Here, below $E_F$, one sees that the evolution of the backfolded valence band $v$ is characteristic of the temperature dependence of the order parameter (as the backfolded conduction band $c'$, which is however not accessible to photoemission, since the states are unoccupied). These calculated spectra highlight how the real (experimental) temperature behaviour of the order parameter can be extracted from ARPES data. One sees that the situation is particularly delicate when the order parameter is small, since the peak of the backfolded valence band $v$ merges with the peak of the conduction band (see arrow on Fig. 5.3 (c)).

From the condition of conservation of occupied electronic states (weighted with the SW), one can also compute the temperature dependence of the chemical potential $\mu$. Technically, we only take into account states down to $-1.0$ eV, due to the parabolic approximation of the bands around their extrema. Then, we compute the number of occupied electronic states $n_{\mathrm{occ}}$ at $T = 300$K (taking into account the SW of the dispersions)

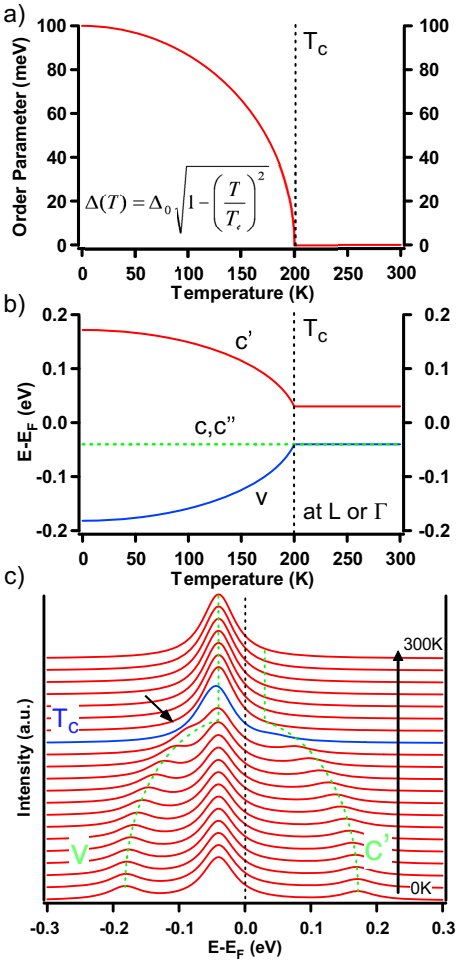


FIGURE 5.3: (a) BCS-like temperature dependence chosen for the order parameter. (b) Position of the bands at Γ and $L$ as a function of a temperature (for the above order parameter). (c) Evolution of the broadened spectra (see text) at $L$ under the effect of temperature.

for getting a reference value. Then, decreasing the temperature gradually (and possibly increasing the order parameter), we adapt the chemical potential so that the number of occupied electronic states remains constant $n_{\mathrm{occ}}(T < 300\mathrm{K}) = n_{\mathrm{occ}}(T = 300\mathrm{K})$. This has been done for two differents cases. First we fix $\Delta_0 = 0$ meV, which means that we look at a normal system, exhibiting no transition. Then we fix $\Delta_0 = 100$ meV, as before, for the excitonic insulator system. Fig. 5.4 (a) shows the behavior of the chemical potential. One sees that without excitonic effects, a system having the modelized configuration of $1T$-$TiSe_2$ undergoes already a chemical potential shift of about 12 meV over the range of 300K due to the change in the thermal occupation of electronic states. If an excitonic phase transition with $\Delta_0 = 100$ meV sets in, a drastic change happens around $T_c$ and the chemical potential shift increases up to nearly 60 meV. Such a large effect should be visible in ARPES, but it must be emphasized that this holds only for the simplified $1T$-$TiSe_2$electronic bandstructure of this model (in particular without considering the other Se4$p$-derived valence bands).

Knowing the band dispersions around $E_F$ and their shift due to the combined effect of the chemical potential and the order parameter, it is also possible to estimate the free

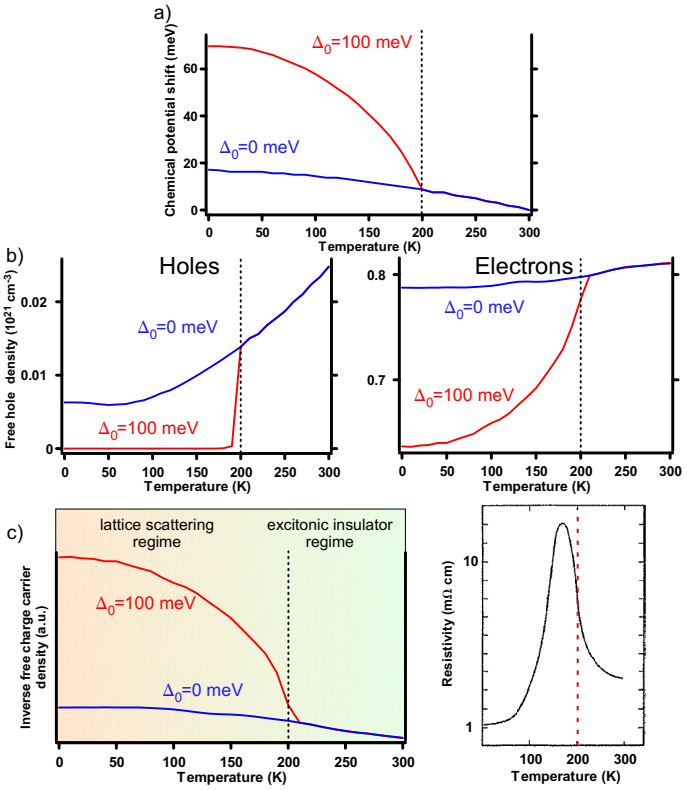


FIGURE 5.4: Compared behaviours for the cases of a simple semi-metallic system (i.e. $\Delta_0 = 0$ meV, in blue) and an excitonic insulator (i.e. $\Delta_0 = 100$ meV, in red). (a) Temperature dependence of the chemical potential. (b) Temperature depence of the free hole (left) and electron (right) density. (c) Left graph: inverse free carrier density approximating the resistivity (see text for explanation concerning the two regimes). Right graph: the measured inplane resistivity of $1T$-$TiSe_2$[57]

carrier density $n = n_{\text{hole}} + n_{\text{electron}}$ in the system, composed of holes in the valence band and electrons in the conduction bands. In Fig. 5.4 (b) (left), in comparison with the normal metal ($\Delta_0 = 0$ meV), the excitonic insulator ($\Delta_0 = 100$ meV) displays a strong free hole density decrease below $T_c$. This can be explained with Fig. 5.2 (b) and (c). As the order parameter increases from a zero value, a gap opens at $\Gamma$ and $\mu$ remains in the conduction band so that the hole contribution to conduction vanishes. In Fig. 5.4 (b) (right), the free electron density of the excitonic insulator displays also a strong decrease below $T_c$. Indeed, at $L$, the bottom of the conduction band $c$ looses SW, reducing the free electron carrier density. In parallel, the chemical potential moves upward in the conduction band (this shift is nonetheless smaller than the gap produced by the order parameter), making available new states in the conduction band $c$ with higher SW than those at its bottom. However, this is not sufficient to counterbalance the previous effect.

In transport measurements, the CDW has a strong signature, raising the resistivity $\rho$ below $T_c$ as in an insulator. Having now an approximate behaviour of the free charge carrier density as a function of temperature, we can also estimate the resistivity in the Drude theory by $\rho = m/ne^2\tau$, with $\tau$ the relaxation time and $m$ the effective mass. Fig. 5.4 (c) shows $1/n$, one ingredient of $\rho$, again for $\Delta_0 = 0$ meV and $\Delta_0 = 100$ meV. In comparison to the normal system ($\Delta_0 = 0$ meV) which displays a nearly constant $1/n$, the excitonic insulator ($\Delta_0 = 100$ meV) exhibits a strong increase of $1/n$ below $T_c$, as

expected. Compared to the measured inplane resistivity shown in Fig. 5.4 (c) (right), one sees a relatively good qualitative agreement above 170K (indicated as the excitonic insulator regime in Fig. 5.4 (c)). At low temperature, our crude estimation of the resistivity, $\rho \propto 1/n$, does not take into account the scattering by the lattice represented by the relaxation time $\tau$ in the Drude theory. Indeed, for low temperatures, $\tau$ increases as a power of $T$, compensating thereby the decreasing $n$. This generally happens well below the Debye temperature, evaluated as $\Theta_D \cong 200$K [50] (indicated as the lattice scattering regime in Fig. 5.4 (c)).

Of course, the order parameter of the excitonic insulator model could be computed directly in the framework of the model, since it obeys to a gap equation similar to that of BCS theory. The chemical potential would be obtained as well in a self-consistent way. Notwithstanding, such a computation is demanding and goes beyond the discussion of the present study.

### 5.2.3 Conclusions

The temperature dependence of the excitonic insulator phase model adapted to $1T$-$TiSe_2$ [80, 87] has been studied. This was done in a simple way by assuming a given temperature dependent order parameter. Then, photoemission spectra were calculated as a function of temperature, with the help of the spectral function derived from our model. They inform us about the signature of the order parameter in photoemission and indicate how its real (experimental) behaviour can be extracted from ARPES experiments. Moreover the upturn in the measured resistivity of $1T$-$TiSe_2$ was explained in terms of the excitonic transition.

### 5.2.4 Acknowledgments

This work was supported by the Fonds National Suisse pour la Recherche Scientifique through Div. II and MaNEP.

## 5.3 A photoemission study of the temperature dependence of the exciton condensate phase of $1T$-$TiSe_2$

C. Monney[1], H. Cercellier[2], E.F. Schwier[1], C. Battaglia[1], N. Martiotti[1], C. Didiot[1], M. G. Garnier[1], H. Beck[1], J. Marcus[2] and P. Aebi[1],

[1] *Institut de Physique, Université de Neuchâtel, CH-2000 Neuchâtel, Switzerland*

[2] *Institut Néel, CNRS-UJF, BP 166, 38042 Grenoble, France*

Not submitted yet

The charge density wave transition of $1T$-$TiSe_2$ is studied by angle-resolved photoemission measurements over a wide temperature range. An important chemical potential shift which strongly evolves with temperature is evidenced. Moreover, in the framework of the exciton condensate phase, the detailed temperature dependence of the associated order parameter is extracted. Having a mean-field-like behaviour at low temperature, it exhibits a non-zero value above the transition, interpreted as strong excitonic fluctuations, reminiscent of the pseudo-gap phase of high temperature superconductors. Integrated intensity around the Fermi level is found to display a trend similar to the measured resistivity and is discussed within the model.

### 5.3.1 Introduction

The transition metal dichalcogenides (TMDC) belong to a class of quasi two-dimensional compounds famous for their charge density wave (CDW) phases [31, 98]. Due to their layered structure, they can be easily intercalated by foreign atoms in their so-called Van der Waals gap, providing a chemical parameter for tuning new phenomena. In this way, for instance superconductivity can be enhanced or suppressed, sometimes in competition with CDW phases [47, 99].

Among the TMDCs, $1T$-$TiSe_2$ turns out to be an interesting and enigmatic material. At the critical temperature of $T_c \simeq 200$K, the system undergoes a second-order phase transition, characterized notably by a peaking resistivity [48] and a phonon softening at $T_c$ [49]. The electronic band structure and its elementary excitations can be determined by angle-resolved photoemission spectroscopy (ARPES). At room-temperature (RT), ARPES evidenced two main contributions near the Fermi energy $E_F$, namely a valence band (of Se4$p$ character) and conduction bands (of Ti3$d$ character), whose relative positions are still controversial [62, 87]. At low temperature (LT), intense backfolded bands, characteristic of the CDW, appear. The origin of the CDW is not completely settled yet and resists to conventional explanations. Indeed, $1T$-$TiSe_2$ Fermi surface (FS) topology does not favor nesting, since no large parallel portion of FS are present [85]. A band Jahn-Teller effect [64] has been proposed as an alternative mechanism, relying on the fact that at the transition a periodic lattice distortion (PLD) develops, which results in a tendency of the system to pass from the $1T$ (octhedral environnment of the transition atom) to the $2H$ (prismatic environnment) polytype. A third explanation, that is developed hereafter, is the exciton condensate phase.

This phase, originally denominated as the excitonic insulator phase, appeared in the mid-1960s as a theoretical prediction [2, 3]. In its simplest version, its basic ingredients are a single valence and a single conduction band, having a semimetallic or semiconductor configuration. Then, if the overlap or the gap between them is small enough, bound states of holes and electrons, called excitons, will condense in a macroscopic state and drive the system into a new ground state, provided the temperature is sufficiently low. The CDW arises naturally from the coupling between the valence and conduction bands, opening a gap between them at LT and transforming the semimetallic or semiconducting configuration into an insulating one. In other words, the presence of condensed excitons in the system creates the CDW as a purely electronic process. In the case of $1T$-$TiSe_2$, the situation is more complicated. Three symmetry equivalent conduction bands having their minima at the border of the Brillouin zone (BZ) (at the $L$ point, see Fig. 5.5) are coupled to the valence band having its maximum at the center of the BZ (the $\Gamma$ point). The main difference with the basic excitonic insulator phase is that one of the conduction bands is not shifted by the electron-hole coupling, providing states unperturbed by the transition and tempering the insulating character of the transition [80].

Among the recent ARPES studies on $1T$-$TiSe_2$, Pillo *et al.* inferred the existence of a small indirect gap and a conduction band in the unoccupied states and supported the exciton condensate phase scenario [57]. Kidd *et al.* also evidenced a small indirect gap with a conduction band in the unoccupied states. They relied on a combination of an electron-hole coupling and a Jahn-Teller effect as the origin of the CDW phase [59]. Rossnagel *et al.* deduced remarkable shifts of the valence and conduction bands in the temperature range of $100\text{K} \leq T \leq 300\text{K}$, but without being able to determine the nature of the gap [60]. On this basis, they also gave a simple qualitative explanation of the peak in the resistivity of $1T$-$TiSe_2$. In their conclusions, they rather endorse the Jahn-Teller effect. In our recent publications, we defend the thesis of the excitonic insulator phase as the origin of the CDW phase of $1T$-$TiSe_2$ [80, 87]. We inferred a small indirect overlap of the valence and conduction bands in the normal phase, i.e. in the absence of excitonic effects.

In this paper, we present high resolution ARPES measurements of $1T$-$TiSe_2$ aimed at the extraction of a detailed temperature dependence over a wide temperature range. It evidences strong shifts of the backfolded valence band and of the conduction bands, which we are able to relate to the combined effects of the order parameter characterizing the exciton condensate phase and of a chemical potential shift. Moreover, in photoemission spectra, relevant intensity features following closely the shape of the temperature dependent resistivity are found. They can be well reproduced within our exciton condensate model, provided we take into account the two temperature dependent components determined previously. Finally, at the lowest temperature achieved here, we identify for the first time a new contribution in the conduction band which we discuss in the framework of the exciton condensate phase.

### 5.3.2 Experiment

The photoemission intensity maps presented here were recorded using linear $p$-polarized HeI$\alpha$ radiation at 21.2 eV and using a Scienta SES-2002 spectrometer with an overall energy resolution better than 10 meV. A liquid helium cooled manipulator having an angular resolution of $0.1^\circ$ was used, with a temperature stability $< 5\text{K}$. $1T$-$TiSe_2$ samples

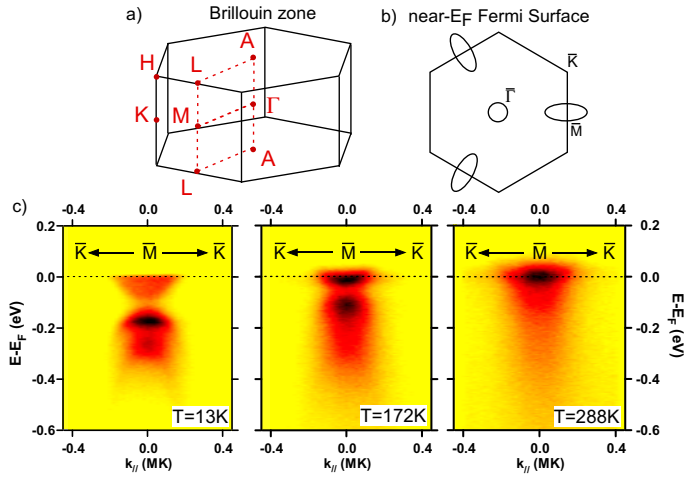


FIGURE 5.5: (a) Brillouin zone of $1T$-$TiSe_2$ with its high symmetry points. (b) Model Fermi surface of $1T$-$TiSe_2$ in the $\Gamma MK$ plane, with electron pockets at $L$ produced by the conduction band. At $\Gamma$, the valence band disperses near $E_F$ and only its tail provides some slight intensity below $E_F$. (c) Photoemission intensity maps, as false colour plots (dark colours represent strong intensity), measured along $\bar{\Gamma}\bar{K}$ (see text for an explanation of this notation) at three different temperatures corresponding, from left to right, to situations well below $T_c$, around $T_c$ and well above $T_c$ respectively.

were cleaved *in-situ*, in a base pressure in the low $10^{-11}$ mbar, ensuring a high longevity of the sample surface. Photoemission spectra were recorded from 13K to RT. At the end of the measurements, the sample was cooled again to 13K and comparable spectra were recorded again, confirming this situation. Reference spectra of polycrystalline gold evaporated on the same sampleholder as $1T$-$TiSe_2$ were recorded for determining the Fermi level position. At the excitation energy of 21.2 eV, at the border of the BZ, initial states close to the $L$ point are probed (see the BZ depicted in Fig. 5.5(a) for situating high symmetry points). We will then use the surface notation, $\bar{M}$, for such measurements. From resistivity measurements (not shown here) performed on this batch of samples, the critical temperature of the transition turns out to be $T_c \cong 180$K, which is less than that determined for stoichiometric samples and is probably due to some uncontrolled excess of Ti [48], which does not have a strong influence on the conclusions of the present study.

Fig. 5.5(b) presents the schematic *near-$E_F$* FS of $1T$-$TiSe_2$ (perpendicular to $k_z$) in the normal phase (i.e. in the absence of excitonic effects). We postpone the discussion of the semimetallic or semiconducting configuration near $E_F$ of $1T$-$TiSe_2$ and consider now the contributions in the neighbourhood of $E_F$. It consists of a hole pocket at $\Gamma$ and three symmetry equivalent electron pockets at $L$. As emphasized previously [87], at RT already strong excitonic fluctuations are present, opening a gap between the valence and conduction bands, so that the valence band shifts below $E_F$. Only the conduction bands remain in the neighbourhood of $E_F$. Therefore, to study the temperature dependence of the electronic structure of $1T$-$TiSe_2$, we focus on the situation at $\bar{M}$. At LT, the most prominent feature attesting of the CDW phase is seen at $\bar{M}$ in the form of the backfolded valence band. It is located well inside the occupied states, below the conduction band. Its maximum shifts to higher binding energies with decreasing temperature. Fig. 5.5 (c) shows photoemission intensity maps at the temperatures of 13K, 172K and 288K, corresponding to situations well below $T_c$, near $T_c$ and well above $T_c$, respectively. Well below $T_c$, the backfolded valence band is intense and clearly distinct from the conduction band. In fact, two contributions can be resolved at high binding energies attesting of

two backfolded valence bands. The conduction band provides some intensity just below $E_F$. This will be discussed in more details below, when showing energy distribution curves (EDC). Near $T_c$, the backfolded valence band is less intense and closer to the conduction band, which has gained intensity below $E_F$. Well above $T_c$, the backfolded valence band mixes up with the conduction band and only some residual intensity shows up below the conduction band, foretelling the CDW and the backfolded valence bands.

From each intensity map, the central EDC (situated at $\bar{M}$ exactly) is extracted, allowing to plot the waterfall of Fig. 5.6(a) (left). The blue EDC was measured at 180K, at $T_c$. The conduction band is clearly recognized just below $E_F$. At LT, a new peak develops below the conduction band and is identified as the valence band backfolded to $\bar{M}$. With decreasing temperature, it shifts to higher binding energies and becomes much more intense. This increase in spectral weight is mainly balanced by a decrease in spectral weight of the original valence band at $\bar{\Gamma}$ (not shown here, see reference [80] for a comprehensive discussion). Looking more carefully one sees that another peak also develops below this backfolded band, which can be identified with a second (spin orbit splitted) valence band backfolded from $\bar{\Gamma}$ to $\bar{M}$. Fig. 5.6(a) (right) shows a false color plot of this waterfall, emphasizing this way the temperature evolution of the position and intensity of the backfolded valence band. The vertical dotted line indicates $T_c$. To find a link with the particular behaviour of the resistivity of $1\,T$-$TiSe_2$, the intensity of the photoemission intensity maps (as those shown in Fig. 5.5(c)) is integrated in the vicinity of $E_F$ ($\pm$50 meV around $E_F$) and plotted as a function of temperature in Fig. 5.6(b). It is a crude approximation to the resistivity as it represents the electron density $n$ of the occupied states participating in the conductivity $\sigma$, according to the Drude formula. The inverse of this curve, in Fig. 5.6(c), represents then an approximation of the corresponding resistivity, as, according to the Drude formula, it can be related to the electron density $n$ participating to transport. It displays qualitatively the behaviour of the measured resistivity curve [48], with a sharp increase around $T_c$ and a decrease at lower temperatures. It should be noted that at RT the measured conductivity is dominated by holes, which stem from the valence band [48]. However their contribution to transport quickly vanishes as the valence band shifts to higher binding energies at lower temperatures. Our goal is now to understand the origin of this phenomenon and, knowing its basic ingredients, to reproduce it with the help of our model.

To get more information from the data of Fig. 5.6(a), fitting EDCs as a function of temperature is necessary. Fig. 5.7(a) displays the EDC at $\bar{M}$ for $T = 13$K, where the backfolded bands are clearly separated from the conduction band. Four contributions, labelled A to D, can be distinguished. Contribution $A$ and $B$, at about -260 meV and -170 meV respectively, are the Se4$p$ derived valence bands (two out of three), backfolded from $\bar{\Gamma}$ to $\bar{M}$. Contribution $C$, at about -60 meV, is the Ti3$d$ derived conduction band. The last one, contribution $D$, is close to $E_F$ and its origin is unclear. It is resolved here for the first time to our knowledge (similar measurements performed on other samples confirm this result). The splitting between contribution $C$ and $D$ is of the order of $\sim 60$ meV and as the temperature increases, contribution $D$ shifts into the unoccupied state and rapidly disappears to photoemission. Exactly at $L$, in our model [80], two conduction bands are degenerate (the original one and a backfolded one). A residual interaction, not accounted for in our minimal model (remember that the second backfolded valence band is not included in the model and could make the situation slightly more complicate), could lift this degeneracy, giving rise to this extra feature. It could be seen as a higher order interaction between the different conduction bands, mediated by the electron-hole interaction. This unknown contribution complicates the fitting procedure of the EDCs

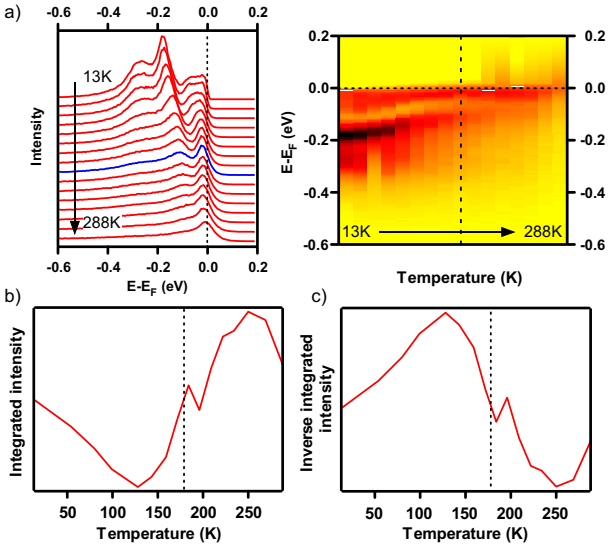


FIGURE 5.6: (color online) (a) Left: EDCs measured exactly at $\bar{M}$, as a function of temperature (for the blue EDC, $T = 180$K). Right: the corresponding false color plot, with the dashed line at $T = 180$K. (b) Integrated intensity around $E_F$ (over $\pm 50$ meV) for each measured photoemission intensity map, as a function of temperature. (c) Inverse integrated intensity.

at the lowest temperatures, where it only appears. Therefore, we adopt the following strategy. For EDCs at the lowest temperatures, we start by adjusting a Lorentzian to the contribution C alone (this approximation results in larger error bars) and subtract it from the EDC. Then, contributions A and B are fitted separately by two Lorentzians. At higher temperatures, the situation is simpler as fitting with three Lorentzians is possible in once for the whole EDC. Fitting is done in an iterative way, meaning that parameters of the previous fit (i.e. with a lower temperature) are used as an initial guess. Fig. 5.7(b) displays the position of contributions $A$, $B$ and $C$ as a function of the temperature, namely the two backfolded valence bands and the conduction band respectively. All three bands undergo a shift towards $E_F$ as the temperature increases, with the largest change below $T_c$. Moreover, at RT, the center of the conduction band at $\bar{M}$ (close to $L$) is at 18 meV above $E_F$, meaning the band lies in the unoccupied states at RT.

### 5.3.3 Discussion of the experimental data

We now adopt the exciton condensate phase mechanism as the origin of the CDW transition to go further in our analysis. In that framework, at LT, the CDW naturally appears from the condensation of excitons, which are bound pairs of holes from the valence band and electrons from the conduction bands. The non-zero center-of-mass momentum of the excitons, which is the distance between $\Gamma$ and $L$, gives rise to the CDW, as a purely electronic mechanism. This CDW phase is characterized by a non-zero order parameter $\Delta$, similar to that of the BCS theory (see reference [80] for a rigorous derivation). It has been shown that the order parameter $\Delta$ does not influence the position of the conduction band, provided the chemical potential is fixed. Therefore, in that model, any displacement of this band will testify of a chemical potential shift. Fig. 5.7 (c) shows the shift of the position of the conduction band (at $\bar{M}$) with respect

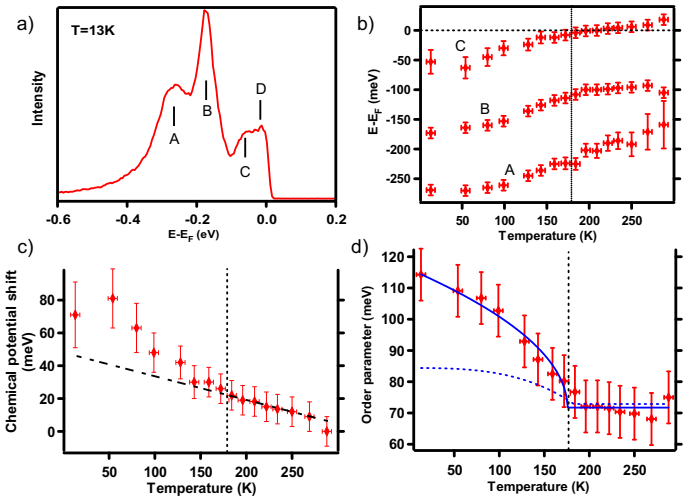


FIGURE 5.7: (a) EDC measured at $L$ and at $T = 13$K. A,B,C and D point out the different contributions assigned to different bands (see text). (b) Position of contributions A,B,C as a function of temperature, obtained by fitting EDCs, and with their error bars. (c) Chemical potential shift. The dotted-dashed line represents the extrapolation of a linear fit to the high temperature part. (d) Order parameter of the exciton condensate phase. The continuous (blue) line is a fit with a mean-field-like function. The dashed (blue) line is a similar fit, after subtraction of the chemical potential fit (see text for more details).

to its RT value as a function of temperature. The dashed-dotted line mimics a linear behaviour, revealing that this chemical potential shift is probably composed of two components. To get furter insight, we refer to a previous paper, where we addressed the question of the temperature dependence of the exciton condensate phase of $1T$-$TiSe_2$ by feeding the model with an order parameter having a given mean-field form [100]. In Fig. 3(a) of that study, it was shown that a semimetal like $1T$-$TiSe_2$ (with electron pockets at $L$ points partially in the occupied states), exhibits a quasi-linear chemical shift when no CDW transition takes place (if $\Delta = 0$ meV over the whole temperature range). Once an excitonic transition sets in, the chemical potential shift deviates from this quasi-linear behaviour at $T_c$ and increases even more. In Fig. 5.7(c) presented here, the measured chemical potential displays a similar trend, with less amplitude however.

In the exciton condensate model adapted to $1T$-$TiSe_2$, once $\Delta \neq 0$ meV, new bands, that are the direct manisfestation of the CDW, develop at high symmetry points. Calculated band dispersions in this framework, at $L$ and along the $LH$ direction, and for an order parameter of $\Delta = 100$ meV, are depicted in Fig. 5.8(a). Besides the original conduction band $c_1$, the valence band $v_1$ gets backfolded at $L$ as well as symmetry equivalent conduction bands $c_2$ and $c_3$. Their positions are complicated functions of $\Delta$. However, exactly at $L$, the situation simplifies drastically to

$$\begin{aligned} E_{v_1}(\Delta) &= E_{c_1} - \frac{E_G}{2} - \frac{1}{2}\sqrt{E_G^2 + 12\Delta^2}, \\ E_{c_3}(\Delta) &= E_{c_1} - \frac{E_G}{2} + \frac{1}{2}\sqrt{E_G^2 + 12\Delta^2}, \end{aligned} \tag{5.1}$$

with $E_{c_1} = 18$ meV, the position of the conduction band for $\Delta = 0$ meV, and $E_G := E_{c_1} - E_{v_1} = -12$ meV, the gap between the valence and conduction bands, which in our case is an overlap ($E_{v_1} = 30$ meV is the position of the valence band for $\Delta = 30$

meV [87]). These relationships are of great interest since they provide a simple way to extract the temperature dependence of the order parameter $\Delta(T)$ from the position of these backfolded bands. In our case, only $E_{v_1}$ is useful, since the band $c_3$ cannot be observed by photoemission. Inverting this relationship and inserting the temperature dependent position of the valence band of Fig. 5.7(b) result in the data points of Fig. 5.7(d). For comparison, they are superimposed on a mean-field-like order parameter of the form

$$\Delta(T) = \Delta_0 \sqrt{1 - \left(\frac{T}{\tilde{T}_c}\right)^{\alpha}} + \Delta_{\text{off}} \tag{5.2}$$

fitted to the experiment (continuous blue line), with $\alpha = 1$. One sees immediately that the critical temperature extracted from the ARPES data $\tilde{T}_c = 175$K is very similar to that determined from resistivity measurements $T_c = 180$K. For ensuring the best agreement with the data, an offset value for the order parameter $\Delta_{\text{off}} = 72$ meV has to be added above $T_c$. This feature can be understood as a simple way to model strong fluctuations of incoherent excitons above $T_c$. Looking at the right intensity plot of Fig. 5.5(c) measured at 288K, one sees indeed that some blur intensity remains at about 200 meV below the conduction band, foretelling the emergence of the backfolded valence band and confirming this hypothesis. Once the temperature decreases below $T_c$, the order parameter displays a clear increase in a mean-field fashion. This is a clear indication of the macroscopic condensation of coherent excitons. At the lowest temperature the order parameter reaches the value of $\Delta(T = 0\text{K}) \cong 120$ meV (extrapolated from $\Delta(T = 13\text{K}) = 116$ meV). One may argue that part of the shift of the valence band, which is used to derive the order parameter curve, is due to the chemical shift of the electronic band structure. Indeed, both effects affect each other and a global treatment of these effects should be applied. However such an approach implies a self-consistent numerical calculation of the gap equation and of the chemical potential. Due to the anisotropy and the multiplicity of the conduction bands (the three symmetry equivalent conduction bands at the $L$ points), it turns out to be more complicated than for a simple BCS case and thus goes beyond the scope of the present work. Nonetheless, we superimpose on Fig. 5.7(d) a fit (dashed blue line) to the measured order parameter obtained with the position of the backfolded valence band $E_{v_1}$ from which the chemical potential shift of Fig. 5.7(c) has been subtracted. It thus represents a lower limit for the order parameter.

With the analysis of our photoemission data in the framework of the exciton condensate phase, we revealed here two mechanisms at play in the $1T$-$TiSe_2$ system, as a function of temperature. To better understand their influence on the properties of this system, we insert them into our model, first separately and then together.

Fig. 5.8(b) depicts a photoemission intensity map generated by the spectral function calculated in this model [80]. An order parameter $\Delta = 100$ meV has been used in this particular case (corresponding to a CDW phase with strong excitonic effects). It has to be reminded that only the topmost valence band is considered in our model, meaning that only one backfolded valence band will appear at $L$. Moreover, as a consequence of the present study, the position of the conduction band at RT is taken to be $E_{c_1} = +20$ meV, instead of the $-40$ meV value considered in our previous publications. This discrepancy will be discussed in more details below. For comparison with Fig. 5.6(c), the intensity of such calculated photoemission intensity maps in the vicinity of $E_F$ ($\pm 50$ meV around $E_F$) is integrated and plotted as a function of temperature in Fig. 5.8(c). The dashed

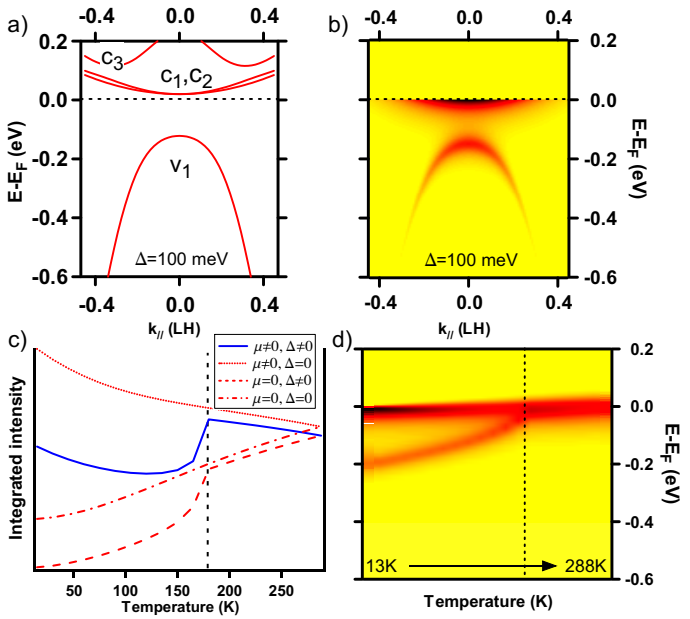


FIGURE 5.8: (a) Near $E_F$ dispersions around $L$ of $1\,T$-$TiSe_2$ calculated within the exciton condensate phase model for an order parameter $\Delta = 100$ meV. (b) Corresponding (calculated) photoemission intensity map (as a false color plot), where the spectral weight has been added to the dispersions. (c) Integrated intensity around $E_F$ (over $\pm 50$ meV) for each calculated photoemission intensity map, as a function of temperature. (d) False color plot made of the collection of calculated EDCs at different temperatures and at $L$ for the case of a non-zero chemical potential shift and a non-zero order parameter.

dotted (red) curve corresponds to the case of a system with an order parameter $\Delta(T) = 0$ meV and a chemical potential shift $\mu(T) = 0$ meV. The integrated intensity around $E_F$ shifts to smaller values as a consequence of the narrowing of the Fermi-Dirac distribution only. If excitonic effects are included ($\Delta_0 = 100$ meV, $\Delta_{\text{off}} = 20$ meV, $T_c = 175$K, see Eqn. (5.2)), one obtains the dashed (red) curve. Here, the loss of spectral weight in the conduction band, transferred to the backfolded valence band due to the CDW formation, induces an additional decrease of the integrated intensity below $T_c$. On the contrary, when a linear (with temperature) chemical potential shift, with an amplitude of 25 meV, is taken into account, the trend changes to the dotted (red) curve. Indeed, the chemical potential then shifts the conduction band into the occupied states, increasing this way the integrated intensity around $E_F$. In $1\,T$-$TiSe_2$, both effects compete against each other, so that the resulting behaviour is non-monotonic.

When combining these two effects, the integrated intensity (blue curve) shows the same behaviour than the measurements plotted in Fig. 5.6(b). It has to be noticed that the set of values ($\Delta_0 = 100$ meV, $\Delta_{\text{off}} = 20$ meV, $T_c = 175$K) giving the best agreement to our measurements is different from what can be inferred from experiment ($\Delta_0 = 48$ meV, $\Delta_{\text{off}} = 72$ meV, $T_c = 175$K). We attribute this discrepancy to the fact that our model does not reproduce all the features of the experiment and to the fact that the chemical potential and the order parameter influence each other and cannot simply be described separately (as explained above). In Fig. 5.8(d), the corresponding calculated EDCs (at $L$) are displayed in the same way as in Fig. 5.6(a) (right). It reproduces the main features of the experiment, namely the appearance of the backfolded valence band with a high intensity transferred from the conduction band, which shifts slowly into the

occupied states as the temperature decreases. However, the second backfolded valence is of course missing (not included in the model) and the intensity of the backfolded valence band is smaller than that of the original conduction band, in contrast to the experiment.

### 5.3.4 Further discussions

A delicate debate concerning $1T$-$TiSe_2$ is the configuration of the bands near $E_F$. In the present work, the conduction band at $\bar{M}$ (but very close to $L$) and at RT is observed to be above $E_F$, at $E_{c_1} = 18 \pm 10$ meV. This is in apparent contradiction with our previous work [87] (but in agreement with earlier ARPES studies [57, 59, 60]), where it has been measured below $E_F$, at $E_{c_1} = -40 \pm 5$ meV. A possible explanation lies in the uncontrolled excess of Ti in these samples [48]. In our recent work [80], in an attempt to reconcile density functional theory calculations (which predict a semimetallic configuration with a large overlap between the valence and conduction bands [92]) with the experiment, we argued that the electrons of the excess Ti atoms, which are probably situated in the van der Waals gap and are doping the adjacent $TiSe_2$ layers, would fill the hole pocket of the (Se4$p$) valence band, shifting it into the occupied states. However, this picture may be too simplistic and the doping electrons may eventually fill the conduction band and push it slightly below $E_F$. Then, a conduction band situated at $E_{c_1} = -40$ meV is simply the consequence of some excess Ti in the sample. Concerning the position of the valence band, the situation is delicate. Indeed, we have seen that at RT already, strong excitonic fluctuations are present, resulting in a situation similar to a CDW phase with $\Delta \neq 0$ meV, reminiscent to fluctuations in the pseudo-gap region of high temperature superconductors. In other words, according to our model, the position of the valence band at RT does not correspond to that of the valence band in the normal phase (i.e. with $\Delta = 0$ meV), since it is already shifted below the conduction band by excitonic fluctuations (see reference [80] for more details). From calculations performed within our model, only the top of the valence band is affected. Therefore, we fitted the branches of the valence band dispersion at RT with a parabola, as an extrapolation towards its *normal phase* dispersion [87]. A position of $E_v = 30$ meV for the valence band was determined, in contradiction to other ARPES studies, where it was measured at RT *with excitonic effects* (due to strong fluctuations).

An important question is now to see to which extent the position of the valence and conduction bands may change the conclusions of the present study. We used the temperature dependent position of the valence band backfolded to $\bar{M}$ to extract the temperature dependence of the order parameter of the exciton condensate phase. This operation was performed with the help of relationship (5.1), where the RT position of the conduction band $E_{c_1}$ and the gap $E_G = E_{c_1} - E_v$ are parameters. The former has been determined in this work. The latter, $E_G$, depends also on the RT position of the valence band $E_v$ which was determined in a previous work (see above), yielding an overlap of $E_G = -12$ meV and thus a semimetallic configuration. To test the influence of $E_v$ on this result, we also considered a semiconducting configuration, with the conduction band at the same position ($E_{c_1} = 18$ meV) but a valence band completely in the occupied states at $E_v = -30$ meV and calculated the corresponding order parameter. The resulting fit (also done with the equation (5.2)) is very similar, but the curve is shifted to lower energy values by 19 meV. It turns out in fact that the shift of the order parameter curve varies almost linearly with the size of the gap $E_G$ (and that its shape hardly changes).

A non-trivial issue is to know how to interpret the order parameter obtained from the measurements (Fig. 5.7(d)) which clearly consists of two regimes. Below $T_c$, it increases in a mean-field fashion, which we understand as a macroscopic condensation of excitons. However, mean-field theory predicts a zero value for the order parameter above $T_c$, while we get a finite value. This comes from the fact that a contribution from the backfolded valence bands (which is not negligible as can be seen in the EDCs of Fig. 5.6(a)) was necessary to fit the EDCs above $T_c$. We then interpret this finite order parameter above $T_c$ as the signature of strong excitonic fluctuations, in a manner similar to the phase fluctuations of the complex order parameter for high-temperature superconductors in the pseudo-gap phase [101]. If one leaves aside the data at the highest temperature, then it displays above $T_c$ a slow, quasi-linear decrease as the temperature increases. The transition from the fluctuating to the macroscopic condensation regime is now discussed. Three different possible cases can be compatible with our data. (i) In Fig. 5.7(d), we fit the experimental data with a function given by equation (5.2) (continuous line). This function describes a mean-field condensation starting at $T_c = 175$K, sitting on a constant background $\Delta_{\text{off}}$. In this case, incoherent excitons giving rise to fluctuations of the order parameter are present from RT to the lowest temperature (meaning that strong fluctuations produce above $T_c$ a pseudo-CDW phase throughout the whole sample, hiding the normal phase to photoemission) and below $T_c$ coherent excitons generated by the macroscopic condensation add themselves up to the incoherent ones. (ii) As another way to interpret the data of Fig. 5.7(d), one can imagine that at $T_c$ the macroscopic condensation suddenly converts all the incoherent excitons present above $T_c$ into coherent ones so that only coherent excitons exist below $T_c$. (iii) Finally, as an alternative to the second case, the conversion of incoherent excitons into coherent ones could be progressive, so that the macroscopic condensation would start at a critical temperature higher than what seems obvious in Fig. 5.7(d). In that sense, the nearly constant background of fluctuating excitons would hide the starting macroscopic condensation and the real critical temperature $T_c^*$ would be larger than what observed for the two other cases. Discriminating between these three scenarios is a difficult task, which requires a theoretical understanding of the fluctuation regime above $T_c$. This goes beyond the exciton condensate phase model we already investigated for $1T$-$TiSe_2$ [80] (where we studied the condensate phase below $T_c$). Recently, Ihle *et al.* studied the excitonic insulator phase within the extended Falicov-Kimball model, in order to understand the metal insulator transition of $TmSe_{0.45}Te_{0.55}$ [102]. They drew the corresponding phase diagram which strongly suggests a crossover from a BCS (weak coupling) to a Bose-Einstein condensate (BEC) (strong coupling) phase, which appears in the case of a semimetallic and a semiconducting configuration respectively. On the BEC side, above the critical temperature $T_c$ of the exciton condensation, they predict the existence of preformed excitons (which do not exist on the BCS side above $T_c$). In the context of our work, this gives a possible explanation to the existence of fluctuating excitons above $T_c$, provided that $1T$-$TiSe_2$ displays a semiconducting configuration, in contradiction to our conclusion that the valence band maximum is at $E_v = +30$ meV. The strength of the coupling can be then estimated with the well-known BCS relationship $2\Delta(T = 0\text{K})/k_B T_c = 12.5$ to 15.5. This value is the double of that of usual BCS systems, suggesting that a strong coupling is at play in $1T$-$TiSe_2$ to build excitons. This would not be surprising, since the pairing interaction is a weakly screened Coulomb interaction for excitons (rather than an overscreened one for Cooper pairs).

### 5.3.5 Conclusion

To summarize, we have performed angle-resolved photoemission measurements of $1T$-$TiSe_2$ between 13K and 288K. We focussed on the situation near $L$, where the conduction band represents the main contribution to the bandstructure near $E_F$. From its position obtained as a function of temperature, an important temperature dependent chemical potential shift is revealed. At LT, the valence band is backfolded from $\Gamma$ to $L$ as a direct manifestation of a transition towards a charge density wave phase. In the framework of the exciton condensate phase, its position is directly linked to the order parameter describing this phase. From our measurements, we are able to extract this temperature dependent order parameter. It shows a clear increase below the critical temperature $T_c$ of the transition, attesting of the exciton condensation in a mean-field manner. Most remarkably, it keeps a non-zero value above $T_c$, which we interpret as the signature of strong excitonic fluctuations. However, a theoretical study of the above-$T_c$ fluctuations, applied to the bandstructure of $1T$-$TiSe_2$, is still lacking. Finally, we integrated the near-$E_F$ spectral weight around $\bar{M}$ as a function of temperature. The inverse of the resulting curve exhibits a striking similarity to the anomalous resistivity of $1T$-$TiSe_2$. We are able to reproduce this behaviour qualitatively on the basis of our model, provided that a temperature dependent chemical potential shift is included in addition to excitonic effects.

We wish to acknowledge the support of our mechanical workshop and electronic engineering team. This project was supported by the Fonds National Suisse pour la Recherche Scientifique through Div. II and the National Center of Competence in Research "'Materials with Novel Electronic Properties"'.

## 5.4 Comment to "A photoemission study of the temperature dependence of the exciton condensate phase of 1*T*-$TiSe_2$"

This work represents a quantitative study of the CDW phase of 1*T*-$TiSe_2$, particularly in the framework of the exciton condensate phase. Such an approach is of course more delicate than the qualitative comparison shown in section 4.4, and it revealed different discrepancies with the model which we will comment in this section.

### 5.4.1 Position of the bands

As mentionned in section 3.3.1, the presence of the Van der Waals gap between $TiSe_2$ layers is favourable to intercalation. This can be advantageous, since intercalation of different species of atoms opens a new dimension in the phase diagram of $TiSe_2$. The disadvantage is that, in the case of the pristine sample, it allows for an uncontrolled excess of Ti atoms, which can easily settle in the Van der Waals gaps. As depicted in Fig. 3.6 (b), this excess of Ti, of the order of a few percents, suppresses the CDW transition and reduces its critical temperature. Such an amount of Ti atoms is difficult to detect and can, of course, change from sample to sample.

The samples we measured for the studies of section 4.4 and 4.6 were different from those leading to the results of section 5.3. In the former case, the extrema of the valence and conduction bands were determined as $\varepsilon_v^0 = 0.03$ eV and $\varepsilon_c^0 = -0.04$ eV respectively. In the latter case, these extrema were determined as $\varepsilon_v^0 = 0.03$ eV and $\varepsilon_c^0 = 0.02$ eV. The value for $\varepsilon_c^0 = 0.02$ eV turns out to be in better agreement with the existing literature [57, 59, 60]. As we know, due to the gap opened by the CDW, the main contributions to the Fermi surface at room temperature come from the conduction bands. Therefore, knowing the band structure, we can compute the electron density contained in the corresponding electron pockets, using formula 4.41. For $\varepsilon_c^0 = -0.04$ eV, we get $n_c^{el} = 3.6 \cdot 10^{-20}$ cm$^{-3}$ for one electron pocket. This can be easily converted into a Ti excess of 2% [a]. According to Di Salvo *et al.*, this would reduce the critical temperature of the transition below $T_c \simeq 140$K. This is certainly much lower than what is observed and should be considered rather like a lower limit. Indeed, for a conduction band slightly closer to $E_F$, at $\varepsilon_c^0 = -0.02$ eV, we get[b] $n_c^{el} = 1.2 \cdot 10^{-20}$ cm$^{-3}$, meaning $\sim$1.0% of Ti excess and $T_c \simeq 170$K. This is much more reasonable with respect to our photoemission results.

A conduction band minimum at $\varepsilon_c^0 = 0.02$ would mean a sample with a low Ti excess, about 0.5%. As a consequence, the critical temperature would be slightly lower than the optimal one, at about $T_c \simeq 190$K. This is above the critical temperature we obtained from the analysis of our photoemission data ($T_c \sim 180$K). There are different explanations for this discrepancies.

- As pointed out by Di Salvo *et al.*, traces of iodine, used in the crystal growth[c], may exist in weak concentration in $TiSe_2$ samples[55]. Iodine induces hole doping

[a] Knowing the main oxydation state of Ti (+4) and remembering that 6 half electron pockets participate to the Fermi surface of $TiSe_2$, leading to a 6/2 factor.

[b] Changes in the effective masses or the $k_z-$dispersion also affect this value.

[c] It has been confirmed by the persons producing the samples we measured.

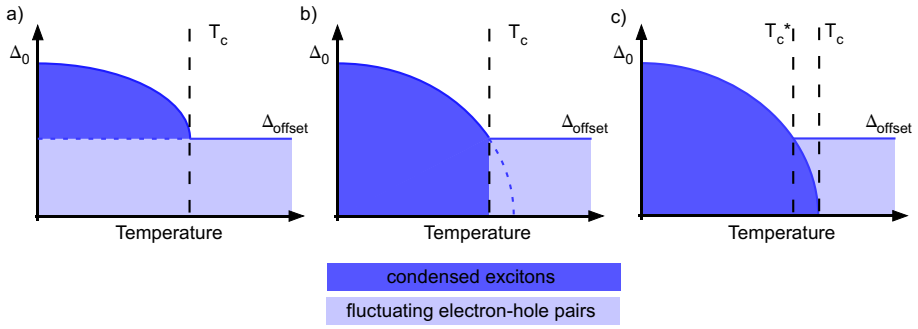


FIGURE 5.9: Different scenarios for interpreting the order parameter of $TiSe_2$ in the presence of fluctuations. (a) The mean-field order parameter sits on a constant fluctuation background. (b) At $T_c$, all the fluctuating electron-hole pairs existing above the transition are suddenly converted into condensed excitons. (c) Fluctuating electron-hole pairs are progressively converted to excitons, so that the real $T_c$ is hidden by them and only an apparent $T_c^*$ is seen.

in samples. These holes may compensate for Ti electron doping and therefore hide a larger Ti excess in the samples. This would mean that, in this case, the critical temperature is lower than expected and is consistent with our analysis. Then, CDW suppression would be mainly due to the disorder caused by the doping atoms.

- Another possibility is that the samples analyzed in the study of section 5.3 have indeed a low excess doping of Ti atoms so that the bulk critical temperature is near 200K. The value of $T_c \sim 180$K we inferred from our ARPES data is approximative. It comes from the fit to the order parameter data obtained from the shift of the valence band as a function of temperature (5.7 (d)). The strong fluctuation regime being poorly captured by our mean-field theory, the region above $T_c$ is difficult to interpret. We have discussed different scenarios in the conclusion of this work (section 5.3.4), which are summarized by the cartoons of Fig. 5.9. Graph (a) represents the situation we have considered in our analysis of Fig. 5.7 (d) with equation 5.2, where the order parameter "sits" on a background of fluctuations. Graphs (b) shows the case where electron-hole fluctuations exist only above $T_c$ and suddenly all condense together at $T_c$. In situation (c), electron-hole fluctuations, existing only above the apparent critical temperature $T_c*$, progressively condense until the observed critical temperature $T_c*$. Therefore, they hide the real $T_c$, which turns out to be larger than what we measure. This last scenario could explain why we observe a smaller $T_c$ than expected, but this is only a supposition and deserves a better theoretical understanding to be confirmed.

In section 4.6.4.4, we discussed the possibility of reconciliating the band structure predicted by DFT calculations with the dispersions obtained with photoemission. While such a hypothesis is reasonable, it comes out to be quite difficult to prove, since room temperature photoemission intensity maps are already affected by strong electron-hole fluctuations. Fig. 5.10 illustrates schematically this conjecture. Graph (a) shows a two-band compensated ($n_e = n_h$) semimetal, which corresponds to a DFT-like configuration[d]. For the band parameters of $TiSe_2$, the valence band maximum should be as

[d]DFT predicts a system with three valence bands 0.4 eV above $E_F$ and a conduction band at about 0.15 eV below $E_F$, as shown in Fig. 3.7 (b).

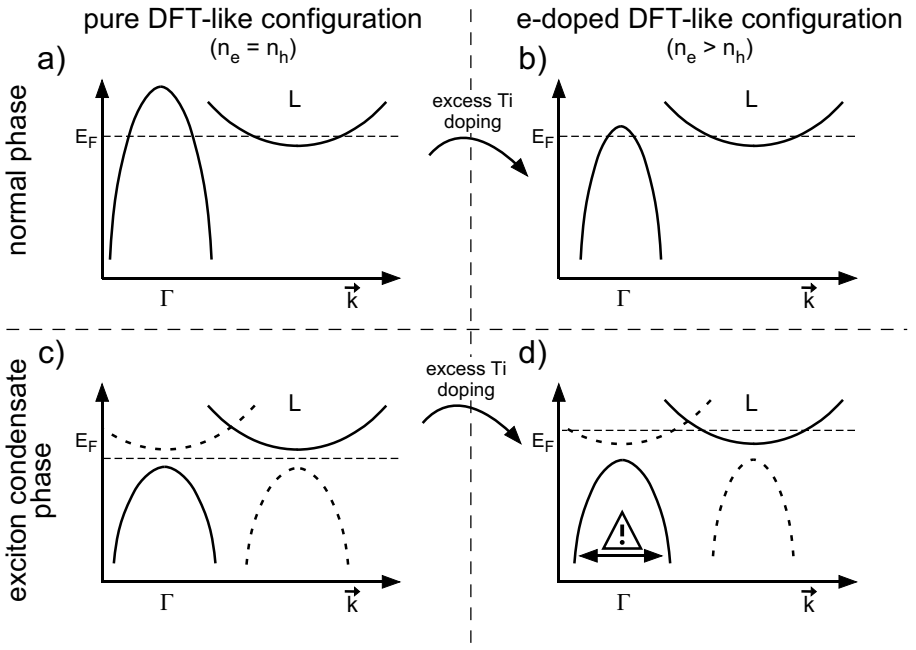


FIGURE 5.10: Schematic description of the evolution of the band structure of $TiSe_2$ under Ti excess doping and within the exciton condensate phase transition.

high as 0.38 eV, to compensate for a conduction band kept at -0.04 eV. In the model, doping and excitonic effects can be applied in two ways.

**Going from doping to excitons.** For 1% of Ti doping, in the normal phase, the valence band shifts into the occupied states (reasons for this choice have been given in section 4.6.4.4), leaving its maximum at 0.03 eV (graph (b)). This is the configuration we adopted in chapter 3. Then, in the exciton condensate phase, a gap opens between these two bands, shifting the valence band below $E_F$ (graph (d))[e].

**Going from excitons to doping.** We could also imagine this mechanism the other way around. Starting from the semimetallic configuration of graph (a), the system undergoes the exciton condensate phase transition, which opens the gap below the conduction band. The chemical potential then lies in the gap, since this is a compensated (semiconducting) system (graph (c)). Then, doping with Ti atoms will start to fill the conduction bands, raising the chemical potential by about 0.04 eV (graph (d)).

The final situations are not exactly the same. Indeed, for perfectly parabolic dispersions, the first mechanism ends up with a narrower valence band parabola than the second one (see discussion in section 4.6.4.4). However, it is very difficult to distinguish between these two scenarios, since three different valence bands cohabit at Γ (see for instance Fig. 4.7 (a) (left)).

In this context, it is worth discussing the recent work of Rasch *et al.* [62]. To solve the long-standing controversy of the position of the conduction band in $TiSe_2$, and thus of the nature of its gap, they use a particular surface effect. They evaporated $H_2O$ which adsorbed on a freshly cleaved $TiSe_2$ surface. The good detectability of all the principal

[e]This creates a negligible loss of holes which would raise the chemical potential a little bit.

features of $TiSe_2$ by photoemission on this modified surface lead the authors to assume that these water molecules adhered to the surface only through weak Van der Waals-like interactions (since $H_2O$ molecules are dipoles) without modifying the atomic structure. They observed that these dipoles weakly bound to the surface induced a band bending, which could not be prevented by the poor screening of the sample. For an amount of 160 kL[f] of $H_2O$ introduced in the vacuum chamber where the sample was, they obtained a band bending of $eV_{bend} \simeq 130$ meV into the unoccupied states. This allowed them to shift all the band structure so that the conduction band at $L$ appeared well below $E_F$ and to determine more easily the gap of the system, $E_{gap} = 150$ meV. This result points towards a semiconducting configuration, with a large gap. Knowing the gap size and the position of the top of the valence band for the clean sample, they could infer the position of the conduction band at $L$ at room temperature, $\varepsilon_c^0 = 80$ meV, for the sample without water molecules adsorbed. This is further away from $E_F$ than what we observed at room temperature ($\varepsilon_c^0 = 18$ meV) and what can be found in the literature [59, 60]. This discrepancy is surprising and casts doubt on the innocuousness of the adsorbed water on the band structure of $TiSe_2$. Indeed, one may think that the adsorbed molecules may have an influence on the near-surface structure and induce a relaxation[g].

### 5.4.2 Inhomogeneities due to Ti excess: the STM point of view

We have also performed STM measurements on freshly cleaved $TiSe_2$ samples, to visualize the topography of the surface on the atomic scale. Fig. 5.11 shows large scale topographic images, indicating a surface of good quality with a low density of defects. However, flat regions of different intensities reflect that the occupied density of states, integrated from -20 meV below $E_F$ to $E_F$, is varying with position. Regions of high density of states are interpreted as regions containing excess Ti atoms, located below the surface (probably in the first Van der Waals gap below the surface) [103], since electron doping mostly fills the conduction bands. Comparing the topographic image at 200K (a) with that at 77K (b), we see that at low temperature the $2 \times 2$ CDW can hardly develop itself in the doped regions. This is consistent with our hypothesis, since excess Ti suppresses the CDW, as we know from the work of Di Salvo *et al.* [48].

The influence of such inhomogeneities at the surface of $TiSe_2$ on our photoemission results is not clear yet. It probably results in the incoherent addition of photoemission intensities coming from such different regions, acting all like small samples of different doping concentrations. This can lead to wider features in the observed spectra. Such a scenario deserves deeper investigations.

[f] This corresponds to an exposure of the sample to a pressure of $H_2O$ of $10^{-5}$ mbar during 6 hours!

[g] Moreover, in their data, the peaks corresponding to the valence bands change as a function of the adsorbed water quantity, which may be even more obvious with a better resolution than their 40 meV.

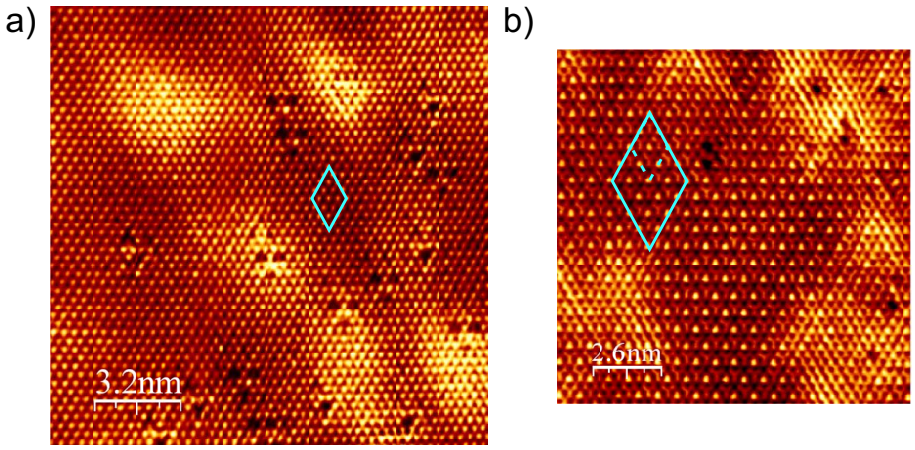


FIGURE 5.11: STM images from $TiSe_2$ (obtained with a current of 1.5 nA and a voltage of -20 mV) at (a) 200K and (b) 77K. Continuous blue lines delimitate areas containing 16 unit cells.

## 5.5 The order parameter in the model: self-consistent calculations

### 5.5.1 Analytical calculations

In section 5.2, to study the temperature dependence of the excitonic insulator model, we chose a particular form for the order parameter. This allowed us to infer the spectroscopic signature of the model as a function of temperature and also to compute the change of the charge carrier density as well as the chemical potential. This was a simplified approach. However, the model offers a more consistent way to obtain these temperature dependences through the gap equation 4.28, namely

$$\Delta_1(\vec{p}) = -i\sum_{\vec{q}} V_c(\vec{q})F_1^\dagger(\vec{p}+\vec{q}, t-t) = -i\sum_{\vec{q}} V_c(\vec{p}+\vec{q})F_1^\dagger(\vec{q}, t=0).$$

(we focus on the conduction band $i = 1$, but it turns out that by symmetry, $\Delta_1 = \Delta_2 = \Delta_3$). Here, the anomalous Green's function $F_1^\dagger$ is evaluated at zero temperature, as indicated by the real time $t = 0$. We can introduce the temperature effect by simply generalizing it to complex values, $\tau = 0$. Then, following the same strategy than what was done for the order parameter of the BCS theory (section 4.1), we have to perform the Matsubara frequency summation

$$F^\dagger(\vec{p}, \tau = 0) = \frac{1}{\beta}\sum_{i\omega_n} F(\vec{p}, i\omega_n). \tag{5.3}$$

At this point, we have to insert the exact form of $F_1^\dagger$. Knowing the conduction band Green's function, $F_1^\dagger(\vec{p}, \omega)$ is easily calculated from the Fourier transform of equation 4.32,

$$F_1^\dagger(\vec{p}, z) = \frac{-\Delta_1(\vec{p})(z-\epsilon_c^2(\vec{p}+\vec{w}_2))(z-\epsilon_c^3(\vec{p}+\vec{w}_3))}{(z-\Omega_1(\vec{p}))(z-\Omega_2(\vec{p}))(z-\Omega_3(\vec{p}))(z-\Omega_4(\vec{p}))} \tag{5.4}$$

($\Omega_\alpha(\vec{p})$ are the poles of the Green's functions). From the general method described in section 2.4.4, we know that the frequency summation of equation 5.3 is made of the residues of $F^\dagger(\vec{p},\omega)N_F(\omega)$ coming from the poles of the Fermi distribution $N_F$. It has to be equal to the residues coming from the anomalous Green's function

$$\frac{1}{\beta}\sum_{i\omega_n} F(\vec{p},i\omega_n) = -\sum_\alpha Res\left[F^\dagger(\vec{p},\omega_\alpha)\right] N_F(\omega_\alpha)$$

where $Res\left[f(\omega_\alpha)\right]$ is the residue of $f$ at $\omega_\alpha$. From equation 5.4, we see that these residues have to be evaluated at the poles $\Omega_\alpha$ of $F_1^\dagger$

$$\begin{aligned}\sum_\alpha Res\left[F^\dagger(\vec{p},\omega_\alpha)\right] \quad N_F(\omega_\alpha) \quad &= \\ - \quad \sum\nolimits_\alpha \quad & \frac{\Delta_1(\vec{p})(\Omega_\alpha(\vec{p})-\epsilon_c^2(\vec{p}+\vec{w}_2))(\Omega_\alpha(\vec{p})-\epsilon_c^3(\vec{p}+\vec{w}_3))}{\prod_{\mu\neq\alpha}(\Omega_\alpha(\vec{p})-\Omega_\mu(\vec{p}))} N_F(\Omega_\alpha)\end{aligned} \tag{5.5}$$

(the possibility of higher order poles has not been considered here for simplifying the notation, but they must be taken into account in the numerical evaluation). We appeal to the threefold symmetry of the system (and of the bare dispersions) to establish that $\Delta_1 = \Delta_2 = \Delta_3 = \Delta$. Using these last calculations, we can go back to the gap equation for our order parameter $\Delta$ and convert the sum into an integral

$$\begin{aligned}\Delta(\vec{p}) &= -\sum_{\vec{q}}\sum_\alpha V_c(\vec{p}+\vec{q}) Res\left[F_1^\dagger(\vec{q},\Omega_\alpha)\right] N_F(\Omega_\alpha) \\ &= -\frac{1}{2\pi^3}\sum_\alpha \int d\vec{q}\, V_c(\vec{p}+\vec{q}) Res\left[F_1^\dagger(\vec{q},\Omega_\alpha(\vec{q}))\right] N_F(\Omega_\alpha(\vec{q})).\end{aligned} \tag{5.6}$$

Here the order parameter appears also in the right hand side, when determining the poles $\Omega_\alpha$. This equation is therefore a complicated integral equation, involving a three dimensional integral, which cannot be simplified to lower dimensions, due to the anisotropy of the bare dispersions $\varepsilon_v$ and $\varepsilon_c^i$.

Until now, the Coulomb potential $V_c$ has not been defined exactly. To account for screening, we follow the Thomas-Fermi theory which tells us that the Coulomb potential can be written like

$$V_c(\vec{q}) = \frac{1}{\epsilon_0}\frac{e^2}{q^2+q_s^2},$$

where the parameter $q_s = 1/\lambda_s$ is related to the (Thomas-Fermi) screening length $\lambda_s$ (see for instance the chapter 17 in reference [104]). This is the only free parameter of our calculations of the order parameter. Indeed, the bare dispersions $\varepsilon_v$ and $\varepsilon_c^i$ are obtained from the experiment and determine strictly the anomalous Green's function $F^\dagger$.

### 5.5.2 Numerical calculations

In pratice, to simplify the numerical cost of the calculations, we compute the order parameter at $\vec{p}=0$, $\Delta(\vec{p}=0)$. Technical details are given in the appendix A.2. Fig. 5.12 shows calculations made with the band parameters of chapter 3 ($\varepsilon_v^0 = 0.03$ eV and

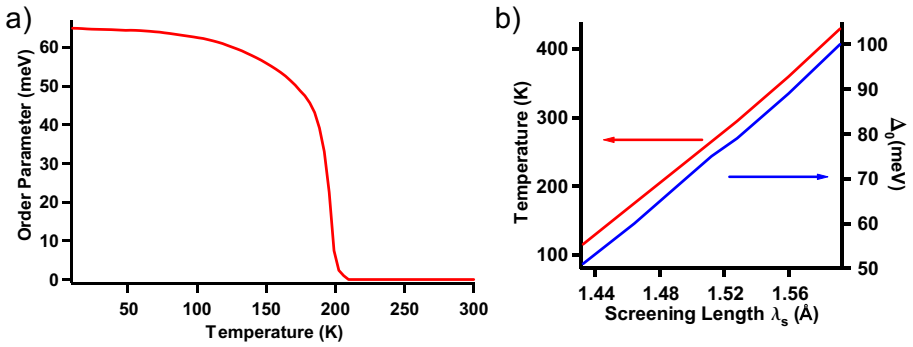


FIGURE 5.12: (a) Calculated order parameter for the model band structure of $1T$-$TiSe_2$, with a screening length $\lambda_s = 1.5$Å. (b) Critical temperature $T_c$ and zero temperature value $\Delta_0$ as a function of $\lambda_s$.

$\varepsilon_c^0 = -0.04$ eV). In graph (a), the order parameter curve is displayed for a screening length $\lambda_s = 1.5$Å. This value has been chosen to reproduce approximatively the critical temperature found experimentally, $T_c \sim 200$K. We see that its zero temperature value, $\Delta_0 = 65$ meV, is a reasonable value (in section 4.4, a value of 75 meV was chosen for the best visual comparison with experimental data measured at 65K). However, as we can see on graph (b), these two parameters, $T_c$ and $\Delta_0$, depend strongly on the screening length $\lambda_s$. With increasing $\lambda_s$, they both linearly increase. This emphasizes the significance of screening in the exciton condensate phase.

We then study the dependence of the shape of the order parameter curve on the position of the bands. Fig. 5.13 summarizes such an analysis, performed for $\lambda_s = 1.5$ Å. This approach is purely indicative, because the screening length is not calculated consistently with the electron density derived from the band structure.

**a)** Panel (a) shows the dependency of the critical temperature $T_c$, which turns out to be higher when the valence and the conduction bands are lying high above $E_F$. Such a result can be understood by analogy with the BCS theory. In this theory, working in the framework of thermodynamics, the condensation energy is defined as the difference between the internal energy of the normal state $U_n(T)$ and the energy of the superconducting state $U_s(T)$, which can be related to the zero value of the order parameter [105]

$$U_s(0) - U_n(0) = -\frac{1}{2}N(0)\Delta^2(0) = -\frac{1}{2}N(0)(1.76k_BT_c)^2. \tag{5.7}$$

Here, $N(0)$ is the density of states at $E_F$. We assume that a similar relation between the condensation energy, which is the difference in energy between the normal and the CDW phase band structure, and the critical temperature holds for the exciton condensate phase. On the basis of the schematic band structure of Fig. 5.14, we see that the largest quantity of electronic energy is gained (shaded red area) when the original valence band[h] is above $E_F$, $\varepsilon_v > 0$ (graphs (a) and (b)). As, according to relation 5.7, $T_c$ is inversely proportional to $\sqrt{N(0)}$, $T_c$ will be higher when the conduction band is above $E_F$, $\varepsilon_c^i > 0$ (graph (a)). This comparison with the BCS theory helps us to figure out why the exciton condensate phase is more robust to temperature for original valence and conduction bands above $E_F$.

[h]The conduction band does not contribute much to the condensation energy, as it does not shift as a function of $\Delta$.

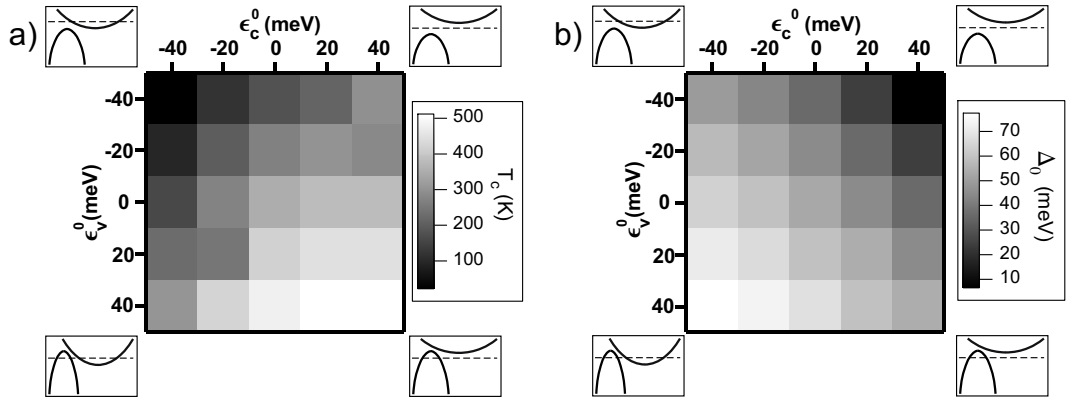


FIGURE 5.13: (a) Critical temperature $T_c$ and (b) zero temperature value of the order parameter $\Delta_0$ as a function of the extrema of the valence and conduction bands (with screening length $\lambda_s = 1.5$ Å). The small insets depict the band configuration corresponding to the extreme band parameters.

**b)** Fig. 5.13 (b) shows the dependence of the zero temperature value of the order parameter $\Delta_0$ on the band positions, telling us that $\Delta_0$ is maximal when the configuration is the most semimetallic. To interpret this result, we recall the exciton creation operator $A^\dagger$, introduced by equation 4.24, which is simply related to $b^\dagger a$ for zero center of mass momentum excitons in the lowest level $\lambda = 0$

$$b_i^\dagger(\vec{p})a(\vec{p}) \simeq \phi_0^*(\vec{p}, \vec{w}_i)A_\lambda^\dagger(0, \vec{w}_i).$$

Considering the gap equation 4.28 for a local potential $V_c(\vec{q}) \simeq V_0$, the order parameter can be linked to the operator $A^\dagger$

$$\Delta_i(0) \approx V_0 \langle A_0^\dagger(0, \vec{w}_i)\rangle \sum_{\vec{q}} \phi_0^*(\vec{q}, \vec{w}_i).$$

In this expression, where the temperature dependence is not explicitly worked out (it affects $A^\dagger$ in the right hand side), the principal dependence[i] on the band structure parameters is hidden in the ground state wave function $|\Psi\rangle$ in $\langle A_0^\dagger(0, \vec{w}_i)\rangle = \langle\Psi|A_0^\dagger(0, \vec{w}_i)|\Psi\rangle$. This term (and its complex conjugate) is indicative of the intensity of exciton formation and thus, the order parameter is proportional to it. The zero temperature value of the order parameter $\Delta_0$ is then a measure of the intensity of exciton formation at zero temperature.

A semimetallic configuration is most favourable to exciton formation, because it offers many possibilities to create such entities. Existing holes in the valence band can bind to electrons in the conduction bands, their respective density of states being larger for $\varepsilon_v^0 > 0$ eV and $\varepsilon_c^0 < 0$ eV. This corroborates the fact that $\Delta_0$ is high for such an electronic configuration.

### 5.5.3 Comparison with the experiment

An essential question is of course the comparison of the calculated data with the experimental data. In section 5.3, we extracted the behaviour of the order parameter for

[i]The exciton wave function $\phi_0$, which obeys a kind of Schroedinger equation (see section 4.6.3.1), mainly depends on the effective masses.

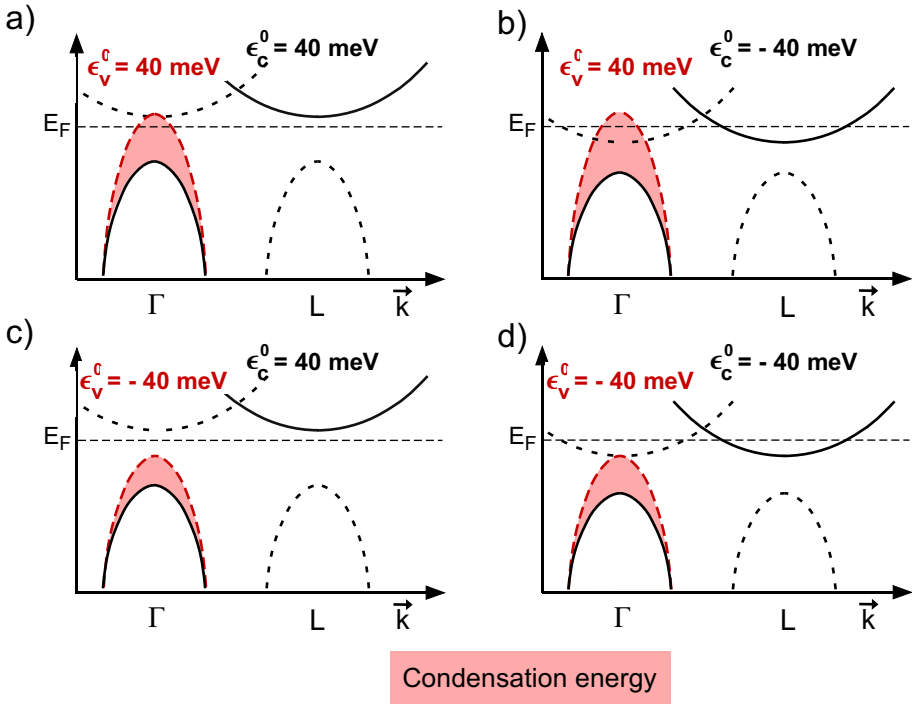


FIGURE 5.14: Schematic view of the CDW phase for two different positions of the valence and conduction bands. The dashed red line corresponds to the normal state valence band. The original bands in the CDW phase are depicted by continuous black lines and their backfolded version by dashed black lines. The shaded red area represents roughly the condensation energy $U_s(0) - U_n(0)$.

$1T$-$TiSe_2$. Fig. 5.7 (d) summarizes this results. Obviously, this does not compare well with a numerical curve like that of Fig. 5.12. First of all, our mean field approach does not reproduce the fluctuation contribution and yields thus a zero value for $\Delta$ above $T_c$. Then, below $T_c$, the calculated order parameter rises more quickly to a value which hardly changes afterwards, exhibiting saturation below 100K. In the experiment, the inferred order parameter displays a non-negligible increase down to 15K. We will now try to explain these discrepancies and the weakness of our numerical approach.

As we have seen in Fig. 5.12, the calculated order parameter depends strongly on the screening length of the Coulomb interaction $\lambda_s$. Until now, we considered $\lambda_s$ as a free parameter. However, it can be estimated in the case of a free electron gas from the electron density

$$q_s = \frac{2.95}{\sqrt{r_s/a_0}} \qquad \text{with} \qquad r_s = \left(\frac{3}{4\pi n}\right)^{1/3}.$$

The Bohr radius $a_0$ rescales the sphere radius of the average volume per conduction electron $r_s$. The screening length is a function of the conduction electron density $n$. This density has been evaluated by Li *et al.* from their optical measurements on $1T$-$TiSe_2$, $n \simeq 7.1{\cdot}10^{20}$ cm$^{-3}$ at room temperature, producing a screening length $\lambda_s = 1/q_s \simeq 1.2$Å. This value is smaller that what we used previously ($\lambda_s \simeq 1.5$Å which corresponds to $n \simeq 2.2 \cdot 10^{20}$ cm$^{-3}$).

These two problems are probably linked to each other. Indeed, the formation of the exciton condensate phase has a non-negligible consequence on the number of occupied

electronic states $n$, inducing a chemical shift up to $\sim 60$ meV for a chosen value $\Delta = 100$ meV. This should be incorporated in our calculation of $\Delta$. The screening length, which then depends on $n$, should also be determined. This results in a self-consistent calculation, where the order parameter $\Delta$, the chemical potential $\mu$, the electron density $n$ and the screening length $\lambda_s$ must be determined coherently. Such an self-consistent scheme is delicate and is beyond the scope of section 5.5. However, our simplified approach helped us to understand the strong influence of screening on the exciton condensate phase and to get a feeling about the interplay between the order parameter and the band structure.

# Chapter 6

# Anomalies at the Fermi surface of $1T$-$TiSe_2$ at low temperatures

## 6.1 Introduction

In the previous chapter, we have analyzed a detailed series of temperature dependent measurements of $1T$-$TiSe_2$. Guided by our theoretical study of calculated photoemission spectra for a given $\Delta(T)$, we focussed onto the situation at $\bar{M}$ and extracted the temperature evolution of the order parameter of the exciton condensate phase and of the chemical potential shift.

In this chapter, we focus again on the behaviour of the conduction band at low temperature, however with a broader view, and also on its overall dispersion. An impressive renormalization of the conduction band effective mass is unveiled, which develops only below 100K. We recall that at low temperature, the conduction band shifts into the occupied states and is the only contribution near the Fermi level. Therefore, this renormalization has a significant effect on the transport properties, which will be investigated and compared to the measured resistivity and will eventually permit to estimate the exciton density.

## 6.2 Dramatic effective mass renormalization in 1*T*-$TiSe_2$ induced by exciton condensation

C. Monney[1], H. Cercellier[2], E.F. Schwier[1], N. Mariotti[1], C. Didiot[1], M. G. Garnier[1], J. Marcus[2], H. Beck[1], P. Aebi[1],

[1] *Institut de Physique, Université de Neuchâtel, CH-2000 Neuchâtel, Switzerland*

[2] *Institut Néel, CNRS-UJF, BP 166, 38042 Grenoble, France*

Not submitted yet

We present angle-resolved photoemission spectroscopy data of 1*T*-$TiSe_2$ taken at temperatures ranging from 13K to 288K. These data evidence for the first time a dramatic renormalization of the conduction band below 100K. This can be explained qualitatively in the framework of the exciton condensate phase model, provided that the conduction electron pocket exhibits a pronounced anisotropy. This new phenomenon translates into an effective mass renormalization and can be directly related to the observed low temperature downturn of the resistivity. In other words, at low temperature, strengthening electron-electron interactions lead to a dramatic reduction of the effective mass of dominant charge carriers and thus to enhanced conductivity.

Quasi-two-dimensional materials offer an exciting playground for physics, as they usually display intriguing phase transitions related to their reduced dimensionality. The transition metal dichalcogenides (TMDC) belong to this class of materials due to their layered structure. They are famous for their charge density wave (CDW) phases [35, 98].

Among the family of the TMDCs, 1*T*-$TiSe_2$ is of particular interest. At the critical temperature of $T_c \simeq 200$K, the system undergoes a phase transition into a CDW phase [48]. At the transition, it displays strongly anomalous transport properties. In particular, the resistivity quickly increases at $T_c$, passing from a value describing a bad metallic state to an insulating one. Surprisingly, it falls back again to smaller values at lower temperatures. In the past years, different angle-resolved photoemission spectroscopy (ARPES) studies were carried out on 1*T*-$TiSe_2$[59, 60, 87]. They all evidenced two main contributions near the Fermi energy $E_F$, a Se-4*p* derived band at the center of the Brillouin zone (BZ) ($\Gamma$ point on figure 6.1 (a)), identified as a valence band in what follows, and a Ti-3*d* derived band at the border of the BZ ($L$ point), identified as a conduction band (see Fig. 6.1 (b) and (c)). As the temperature decreases below $T_c$, an intense backfolded valence band appears at $L$, direct evidence of the CDW. To answer the question of the origin of the phase transition in 1*T*-$TiSe_2$, different mechanisms have been proposed. While nesting can be clearly ruled out due to the inadequate topology of the Fermi surface [85], a band Jahn-Teller effect received more credit [64]. It relies on the fact that at the transition a periodic lattice distortion (PLD) develops and that the resulting electronic energy gain could be sufficient to overcome the elastic energy cost of the PLD [61]. However, the small atomic displacements ($\sim$0.08Å) associated to the PLD, in opposition to the high intensity in the backfolded valence band, casts doubts on this explanation. Indeed, it is well known that the intensity in the backfolded bands is proportional to the strength of the new potential of competing periodicity [33].

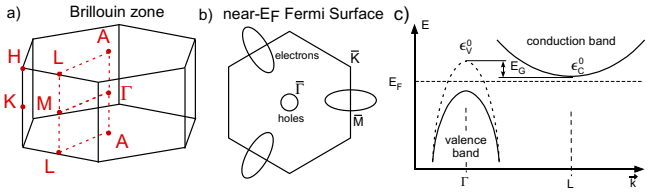


FIGURE 6.1: (a) Brillouin zone of $1T$-$TiSe_2$ with its high symmetry points. (b) Schematized near-$E_F$ constant energy surface of $1T$-$TiSe_2$ in the $\Gamma MK$ plane, with electron pockets at $L$ produced by the conduction band. (c) At $\Gamma$, the gap opening due to the exciton condensation shifts the valence band far below $E_F$ and only the conduction band provides some intensity at $E_F$.

In comparison, $1T$-$TaS_2$, another TMDC compound exhibiting a CDW phase, presents backfolded bands of low intensity [44, 106], although the associated PLD involves very large atomic displacements ($> 0.3$Å) [84] .

This matter of fact leads us to support a third mechanism, the exciton condensate phase. Originally denominated the excitonic insulator phase, it appeared in the mid-1960s as a theoretical prediction [2, 3]. Its basic ingredients are a valence and a conduction bands, having a semimetallic or semiconducting configuration. Then, bound states of holes and electrons, called excitons, can condense at low temperature into a macroscopic state, provided the gap is small and the screening of the Coulomb interaction is weak. This purely electronic effect naturally generates the CDW. An exciton is a neutral quasiparticle and as a consequence, condensation of such entities removes charge carriers from the system and results in the resistivity increase at the transition. This manifests itself in the band structure by a gap opening below the conduction band, which shifts the valence band away from $E_F$. However, all along the transition, the conduction band remains close to $E_F$, providing occupied states to transport so that the system never really becomes insulating (see Fig. 6.1 (c)). It explains also why the dominant carrier type available for transport changes from holes at high temperature to electrons at low temperature [60]. We calculated the spectral function of this model adapted to the particular case of $1T$-$TiSe_2$ [80]. ARPES measurements were compared to photoemission intensity maps generated with this spectral function and the very good agreement gave strong support to the exciton condensate phase as the origin of the CDW phase in $1T$-$TiSe_2$ [87]. Very recently, we analyzed temperature dependent ARPES data and extracted the evolution of the order parameter describing the exciton condensate phase, which follows a clear mean-field behaviour below $T_c$ [107]. An important chemical potential shift was also evidenced, which moves the bands into the occupied state by about 70 meV.

In this letter, we present ARPES measurements done at different meaningful temperatures on $1T$-$TiSe_2$. For the first time, a dramatic renormalization of the conduction band at low temperature is evidenced. Its origin is explained within the exciton condensate phase model. It is related to a strong reduction of the electron effective mass and brings a solid explanation of the resistivity downturn at low temperature.

The photoemission intensity maps presented here were recorded using linear $p$-polarized HeI$\alpha$ radiation at 21.2 eV and using a Scienta SES-2002 spectrometer with an overall energy resolution better than 10 meV. A liquid helium cooled manipulator having an angular resolution of $0.1°$ was used, with a temperature stability $< 5$K. $1T$-$TiSe_2$ samples were cleaved *in-situ*, in a base pressure in the low $10^{-11}$ mbar, ensuring a high lifetime of the sample surface. Photoemission spectra were recorded from 13K to 288K.

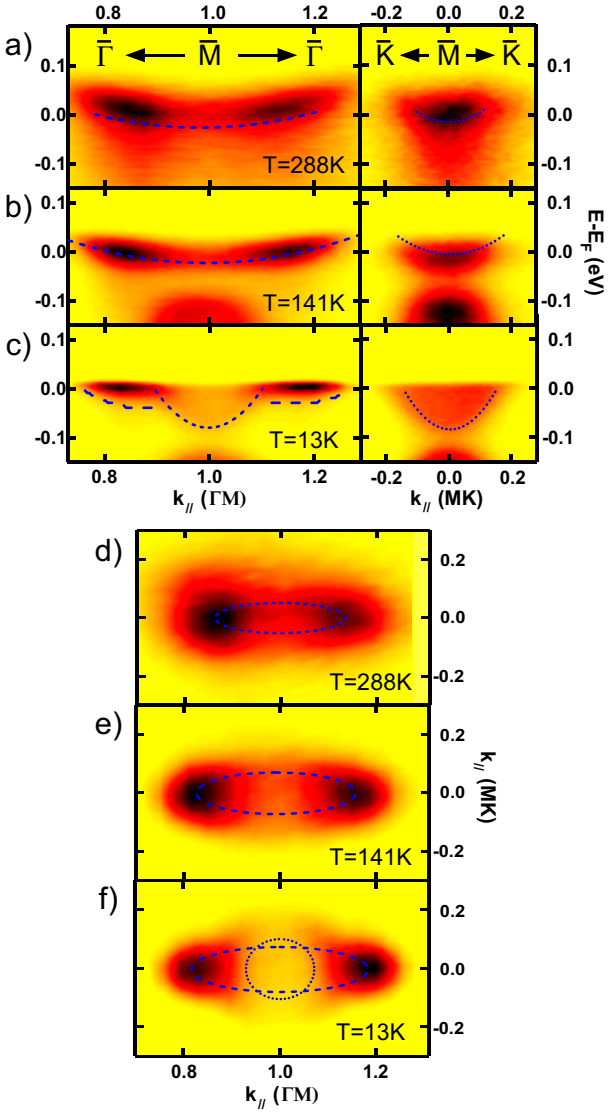


FIGURE 6.2: Photoemission intensity maps (in false colour plots where dark colours represent high intensity) of the electron pocket around $\bar{M}$. (a), (b), (c) Measurements along $\bar{\Gamma}\bar{M}$ (left panels) and $\bar{M}\bar{K}$ (right panels) at 288K, 141K and 13K respectively. (d), (e), (f) The corresponding "Fermi surfaces". Dashed and dotted lines represent fits of the high binding energy edge (see text).

At the end of the measurements, the sample was cooled again to 13K and comparable spectra were recorded again, confirming its stability. Reference spectra of polycrystalline gold evaporated on the same sampleholder were recorded for determining the Fermi level position. At the excitation energy of 21.2 eV, at the border of the BZ, initial states close to the $L$ point are probed (see the BZ depicted in Fig. 6.1(a) for situating high symmetry points). We will then use the surface notation $\bar{M}$ for such measurements. From resistivity measurements (not shown here) performed on this batch of samples, the critical temperature of the transition turns out to be $T_c \cong 180$K, which is less than that determined for stoichiometric samples and is probably due to some uncontrolled excess of Ti [48], which does not have a strong influence on the conclusions of the present study.

For 1 $T$-$TiSe_2$, in the neighbourhood of $E_F$, the main contribution is given by the electron

pocket at $\bar{M}$, the valence band lying below the Fermi energy $E_F$ (see Fig. 6.2). Fig. 6.2 presents photoemission intensity maps of this electron pocket taken at three different temperatures, along the high symmetry directions $\bar{\Gamma}\bar{M}$ and $\bar{M}\bar{K}$. Binding energy vs momentum carpets highlighting the behaviour of the dispersion of the conduction band at 288K, 141K and 13K are displayed in Fig. 6.2 (a), (b), (c) respectively. At 288K, the conduction band follows a clear wide parabolic dispersion along $\bar{\Gamma}\bar{M}$ (left panel), with a non-trivial spectral weight distribution. This peculiarity can be understood within the exciton condensate phase model [80]. Along $\bar{M}\bar{K}$ (right panel), the situation is more delicate due to a narrow near-$E_F$ dispersion. As the temperature decreases to 141K (Fig. 6.2 (b)), the conduction band gets flatter along $\bar{\Gamma}\bar{M}$ (left panel) and shifts slightly into the occupied states (see reference [107] for a study of the chemical potential shift). The top of the backfolded valence band is also clearly visible below a binding energy of $-0.1$ eV. The $\bar{M}\bar{K}$ photoemission intensity map (right panel) confirms the shift of the conduction band. At 13K (Fig. 6.2 (c)), a dramatic renormalization of the conduction band is visible. Along $\bar{\Gamma}\bar{M}$ (left panel), it has no more a simple parabolic shape and divides into different parts. Its branches closer to $E_F$ are now completely flat, while it displays a pronounced parabolic dispersion in the neighbourhood of its minimum, with a reduced intensity (relatively to the flat parts). The $\bar{M}\bar{K}$ carpet (right panel) evidences a clear shift of the conduction band minimum in the occupied states, with a surprisingly homogeneous spectral weight distribution. It turns out that this renormalization already appears at 88K (not shown here). Fig. 6.2 (d), (e), (f) display the corresponding "Fermi surfaces" at 288K, 141K and 13K respectively (one cannot really speak of a Fermi surface at 288K, since the conduction band lies above $E_F$). At 288K and 141K the "Fermi surface" consists of an electron pocket having an elliptical shape, with spectral weight loss at its center. At 13K, this electron pocket undergoes a strong distortion and deviates from its initial shape. All these features are very close to $E_F$ and follow unusual dispersions, so that fits of the energy distribution curves are not possible. Nonetheless, in order to extract approximatively the shape of these dispersions, we perform fits of their high binding energy edge (the opposite of the leading edge). The results are represented by dashed and dotted lines in Fig. 6.2. They especially emphasize the dramatic renormalization developing at 13K (Fig. 6.2 (c), left) and the features discussed above. In the "Fermi surface" (Fig. 6.2, (c),(d),(e)), these lines should be considered carefully. Only momentum distribution curves in the high symmetry directions ($\bar{\Gamma}\bar{M}$ and $\bar{M}\bar{K}$) were fitted to obtain the basic shapes of these "Fermi surface". Therefore, these lines are rather guides to the eyes. At 13K, on the basis of the two parts distinguished in the corresponding $\bar{\Gamma}\bar{M}$ carpet (Fig. 6.2 (c)), a circular and a narrow elliptic Fermi surface is combined to model the measurement. These fits of the high binding energy edges allow us to extract the effective mass of the

TABLE 6.1: Renormalized effective mass of the conduction band (in units of the bare electron mass) along the long axis $\tilde{m}_L$ and the short axis $\tilde{m}_S$ of its elliptic Fermi surface, as a function of temperature.

| | 13K | 81K | 141K | 288K |
|---|---|---|---|---|
| $\tilde{m}_L$ | 0.6 | 0.9 | 6.3 | 5.9 |
| $\tilde{m}_S$ | 0.4 | 0.5 | 1.0 | 0.9 |

conduction band near its minimum (at $\bar{M}$). Tab. 6.1 summarizes these results (including also data taken at 81K, not shown here). Both the renormalized effective mass along

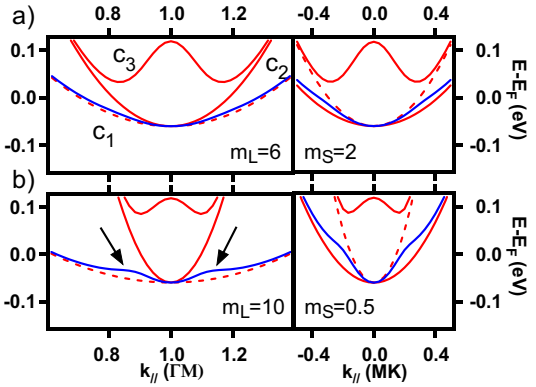


FIGURE 6.3: Renormalized band dispersions calculated within the exciton condensate phase model, around $L$. (a) The effective mass of the conduction band is fixed to $m_L = 6$ and to $m_S = 2$. (b) It is fixed to $m_L = 10$ and to $m_S = 0.5$. Continuous and dashed lines represent bands calculated with an order parameter $\Delta = 100$ meV and $\Delta = 0$ meV respectively. The blue line represents the original conduction band $c_1$.

the long axis ($\tilde{m}_L$) and the short axis ($\tilde{m}_S$) of its elliptic Fermi surface decrease as the temperature reduces. This renormalization is so strong that $\tilde{m}_L$ is reduced by about a factor 10 (and a factor 2 for $\tilde{m}_S$) from 288K to 13K.

The origin of the dramatic renormalization of the conduction band can be understood qualitatively in the framework of the exciton condensate phase model. This model and its spectroscopic signature in photoemission has been discussed already elsewhere to explain the origin of the CDW phase of $1T$-$TiSe_2$ [80]. When the order parameter $\Delta$ of this exotic phase increases to non-zero values, backfolded bands appear at $L$, giving rise to a complicated band structure. Fig. 6.3 depicts the situation near $E_F$. Continuous lines represent the original conduction band (blue) $c_1$ which cohabits with two symmetry equivalent backfolded conduction bands (red) $c_2$ and $c_3$, all calculated with an order parameter of $\Delta = 100$ meV. The dashed (red) line represents the bare ($\Delta = 0$ meV) original conduction band. In the CDW phase, the spectral weight is transferred from the original band $c_1$ to the backfolded bands $c_2$, $c_3$ (and also to the backfolded valence band which is not shown in Fig. 6.3, as it appears at higher binding energies), but mainly remains on the original band $c_1$. It turns out that the ratio of the bare effective masses $m_L/m_S$ (i.e. without excitonic effects, at $\Delta = 0$ meV) play an essential role in this dramatic renormalization. In Fig. 6.3 (a), where this ratio is 3 ($m_L = 6$, $m_S = 2$), the original conduction band $c_1$ does not differ much from the bare one near its minimum. In Fig. 6.3 (b), where this ratio is 20 ($m_L = 10$, $m_S = 0.5$), the original conduction band $c_1$ suffers from a strong renormalization near its minimum (arrows), along $\bar{\Gamma}\bar{M}$ (left panel). However, this does not happen in the vicinity of its minimum along $\bar{M}\bar{K}$ (right panel). This means that for a pronounced anisotropy of the electron pocket due to the conduction band, the dramatic renormalization near its minimum can be reproduced qualitatively by the exciton condensate model. Indeed the ratio $m_L/m_S$ must be increased to $\sim 10 - 20$ to produce a clear renormalization, while the experiment rather suggests a ratio $\sim 3$.

The dramatic renormalization of the conduction band unveiled in this work must clearly have a strong influence on the resistivity of $1T$-$TiSe_2$. Tab. 6.1, which quantifies approximatively this effect, shows that below 100K the effective mass of the conduction band is reduced by a factor $\sim$ 10. Fig. 6.4 recalls the behaviour of this resistivity,

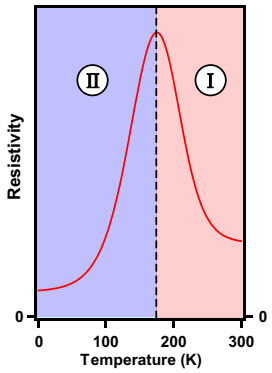


FIGURE 6.4: Schematic plot of the resistivity of $1T$-$TiSe_2$. Two regions are distinguished. Approximatively above $T_c \simeq 200$K (region I), exciton condensation opens a gap in the near-$E_F$ band structure. Below $T_c$ (region II), the dramatic mass renormalization enhances the conductivity.

where two regions are distinguished. Approximatively above $T_c$ (region I), the resistivity quickly increases. Rossnagel *et al.* already gave a phenomenological explanation of this behaviour with a two band model on the basis of ARPES data [60]. In the framework of the exciton condensate phase, a gap, already present in the RT band structure due to strong electron-hole fluctuations, increases strongly at $T_c$ and spectral weight is removed from the conduction band at the same time [80, 107]. Therefore, the number of charge carriers near $E_F$ available for transport is reduced. The resistivity increases. Then, below $T_c$, although the mechanism at work in region I still strengthens, different compensating effects enter into play. First, the chemical potential shifts the conduction band into the occupied states. Then, below 100K, the dramatic effective mass renormalization enhances conductivity. The resistivity decreases. Looking carefully at the photoemission intensity maps of Fig. 6.2, one sees that the spectral weight near the minimum of the conduction band, where the charge carriers are the lightest, diminishes as the temperature falls to 13K. One may then argue that this would suppress the influence of these light charge carrier on the resistivity. However, we have integrated the intensity near the minimum of the conduction band over $\pm 50$ meV and in fact it increases as the temperature decreases (due to the chemical potential shift).

In conclusion, with photoemission we have evidenced for the first time a dramatic renormalization in the band structure of $1T$-$TiSe_2$ at $T < 100$K. In this compound, the conduction band represents the main contribution near $E_F$. Below 100K, its effective mass progressively decreases by a factor 10 with respect to its room temperature value. In the framework of the exciton condensate phase model, we are able to reproduce qualitatively this phenomenon. It allows us to understand within this model not only the resistivity increase at $T_c$ in term of exciton condensation but also the resistivity downturn at lower temperatures with this dramatic effective mass renormalization. Therefore, at low temperature, strong electron-electron interactions, leading to exciton condensation, give rise to a substantial effective mass reduction of the dominant charge carriers and as a consequence to a strong conductivity enhancement. This is, to our knowledge, the first occurrence of such a phenomenon.

We wish to acknowledge the support of our mechanical workshop and electronic engineering team. This project was supported by the Fonds National Suisse pour la Recherche Scientifique through Div. II and the National Center of Competence in Research "'Materials with Novel Electronic Properties"'.

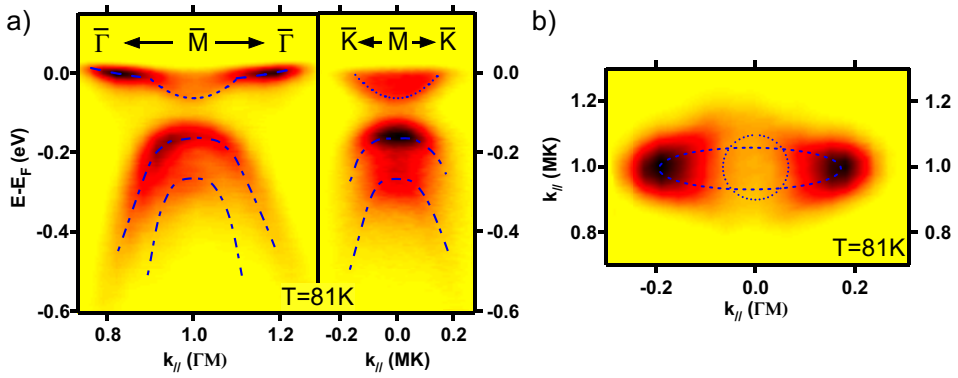


FIGURE 6.5: Photoemission measurements of the conduction band at 81K. (a) Dispersions of the conduction band measured along two high symmetry directions and (b) the corresponding (partial) Fermi surface mapping.

## 6.3 Comment to "Dramatic effective mass renormalization in 1*T*-$TiSe_2$ induced by exciton condensation"

In this paper, we have shown measurements of the Fermi surface and of the dispersion of the conduction band at 13K, 141K and 288K. To complete this set of data, we present similar measurements taken at 81K. Graph 6.5 (a) shows the dispersions along the high symmetry directions $\bar{\Gamma}\bar{M}$ and $\bar{M}\bar{K}$. This additional information is very interesting, because it tells us that the dramatic renormalization already starts around 90K and certainly increases progressively down to 13K, as it depends mainly on the amplitude of the order parameter, which increases as temperature decreases.

In the previous section, we focussed on CEMs taken at the Fermi energy and at different temperatures. It is also interesting to investigate such CEMs at higher binding energies. Fig. 6.6 shows CEMs measured at 13K and at different binding energies between $E_F$ and -0.4 eV, as sketeched in graph (g). As pointed out before, the Fermi surface (a) is apparently made of two contributions: an elongated ellipsis which corresponds to the original conduction band and a circular pocket which is due to the dramatic renormalization happening at low temperature. This distinction in two parts is clearer in graph (b), taken at a binding energy of -0.04 eV, where only the tails of the flat parts of the conduction band appear. At a binding energy of -0.11 eV (graph (c)), in the gap between the conduction band and the backfolded valence band, the CEM consists mainly of the circular part. At -0.17 eV below $E_F$ (graph (d)), the CEM cuts the top of the backfolded valence band. The original valence band is isotropic, so that its backfolded version at $L$ is also isotropic. At higher binding energy, in graphs (e) and (f), the CEMs are situated lower in the backfolded valence band, where they show a certain deviation from isotropy. This deviation comes from the fact that the spectral weight distribution (but not the dispersion) is anisotropic, due to the main contribution of the original conduction band in their calculation (see the formulas for the weights $P_\alpha$ in section 4.6.4.1). Moreover looking carefully at graphs (e) and (f), we see a second circular contribution inside the first one, which stems from the second backfolded valence band.

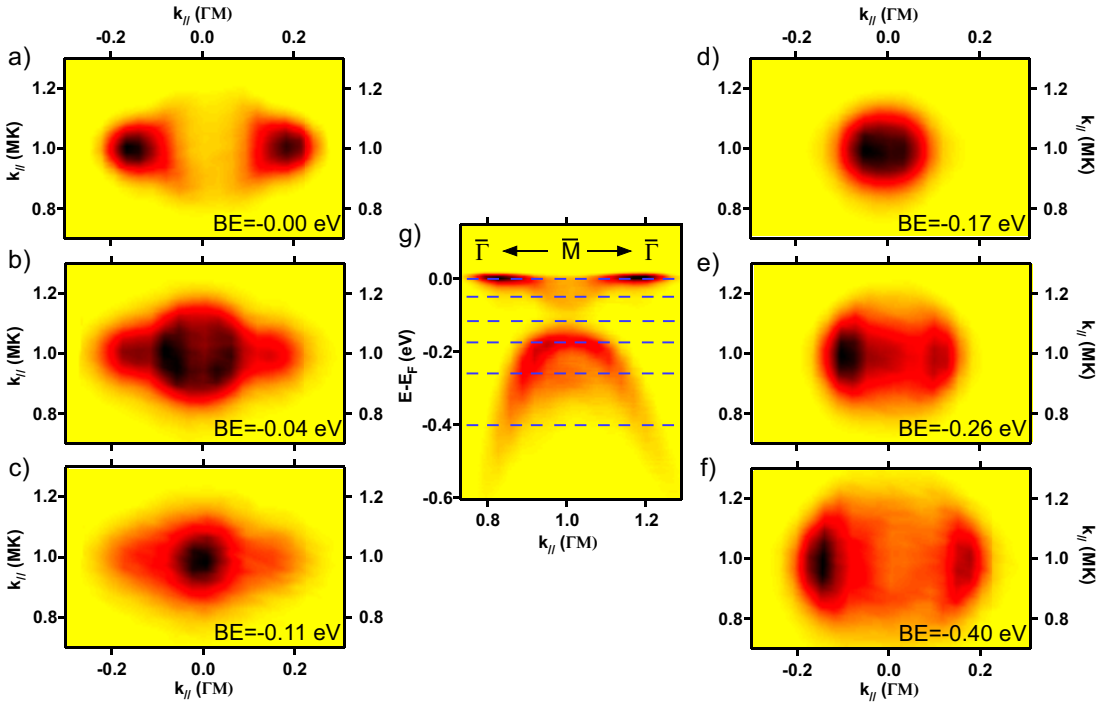


FIGURE 6.6: CEMs measured at 13K around $L$, at binding energies of (a) 0 eV, (b) -0.04 eV, (c) -0.11 eV, (d) -0.17 eV, (e) -0.26 eV and (f) -0.4 eV. (g) All these energies can be situated on the dispersions along the $\bar{\Gamma}\bar{M}$, with the help of the blue dashed lines. The colorscale of each CEM is independently normalized.

## 6.4 Impact on the transport properties

In this section, we recall the different effects in $1T$-$TiSe_2$ unveiled in this thesis and relate them to transport properties. We begin by summarizing them.

- In the exciton condensate phase, a gap opens below the conduction band and shifts the valence band into the occupied states, as a function of $\Delta(T)$, which has been determined in section 5.3.
- The chemical potential, which progressively shifts into the unoccupied states, has been determined in section 5.3 too.
- The integrated near-$E_F$ spectral weight around $\bar{M}$ (but only along $\bar{M}\bar{K}$) in our photoemission data displays a temperature dependence similar to that of the resistivity (section 5.3).
- Finally, in section 6.2, we have discovered a dramatic renormalization of the effective mass of the conduction band, which occurs only at low temperature.

### 6.4.1 Resistivity obtained by photoemission

We now want to use this information to predict transport data, in particular resistivity. The easiest way to compute resistivity is to use the Drude formula

$$\rho = \frac{m}{ne^2\tau}. \tag{6.1}$$

This describes the resistivity of metals arising from charge carriers of density $n$ and having an effective mass $m$, which undergo scattering with a relaxation time $\tau$. In the case of $1T$-$TiSe_2$, information about the contribution of holes cannot be easily obtained by means of photoemission, since the top of the valence band suffers a large spectral weight loss (and is not close enough to $E_F$ to infer the corresponding $k_F$). We therefore focus only on the contribution from electrons in the conduction bands, which we have measured and analyzed in details. Knowing the Drude formula, its parameters can be determined as follows.

- The relative charge carrier density $n$ (of electron type) is estimated with integrated photoemission intensity, in a way similar to what has been done in section 5.3. However, we integrate here the whole electron pocket over $\pm 50$ meV around $E_F$ rather than just a carpet along $\bar{M}\bar{K}$. The drawback is that we have only five temperature points of measurements. An interpolated curve of this (normalized) integrated intensity is shown in Fig. 6.7 (a), which represents of course only relative values for the charge carrier density. It is similar in shape to the curve of Fig. 5.6 (b), with a more pronounced minimum near 150K.

- The effective masses along the long axis $m_L$ and the short axis $m_S$ of the ellipsoidal electron pockets were estimated in section 6.2. Their interpolated temperature dependence is shown in Fig. 6.7 (b).

- In general, the relaxation rate can be estimated from ARPES data with the wave vector width $\Delta k$ of the conduction band at $E_F$ [108, 109]. However, in our case, at high temperature the centroid of the conduction does not cross $E_F$ and at low temperature, the unusual form of the conduction band makes such an analysis clearly difficult and inaccurate. Therefore we prefer using the relaxation rate obtained by Li *et al.* from optical data [97]. Fig. 6.7 (c) displays their (mathematically interpolated) result [a].

It may be questionable to use the Drude formula, which is established for simple metals, for the case of $1T$-$TiSe_2$, where the conduction band lies above $E_F$ at room temperature. However, a non-negligible intensity around $E_F$ is present at every temperatures and, in our crude approach, it is used as an indication of the charge carrier density $n$.

Using all these parameters, the resistivity as a function of temperature, calculated with formula 6.1, gives the calculated curve (red line) shown in Fig. 6.7 (d) , together with the measured one (blue line) [48]. It has to be emphasized that only relative values for the charge carrier density $n$ could be derived. Therefore, their absolute value is determined by ensuring a good agreement with the measured resistivity. This gives rise to a room temperature charge carrier (of electron type) density of $n_{el} \simeq 6.5 \cdot 10^{20}$ cm$^{-3}$, which is fortunately close to the value derived by Li *et al.*, $n = 7.1 \cdot 10^{20}$ cm$^{-3}$.

In view of the approximations used here (in particular that of the Drude formula), the agreement between the measured resistivity with that calculated with the help of photoemission and reflectivity data is very good. The calculated resistivity reproduces quite well the upturn at $T_c$ and also the downturn after $\sim$ 180K, although, at lower temperatures, it falls to values 100 times smaller than what is measured. This may be

[a] As a comparison, the relaxation rate at room and low temperatures has values similar to those of gold [104].

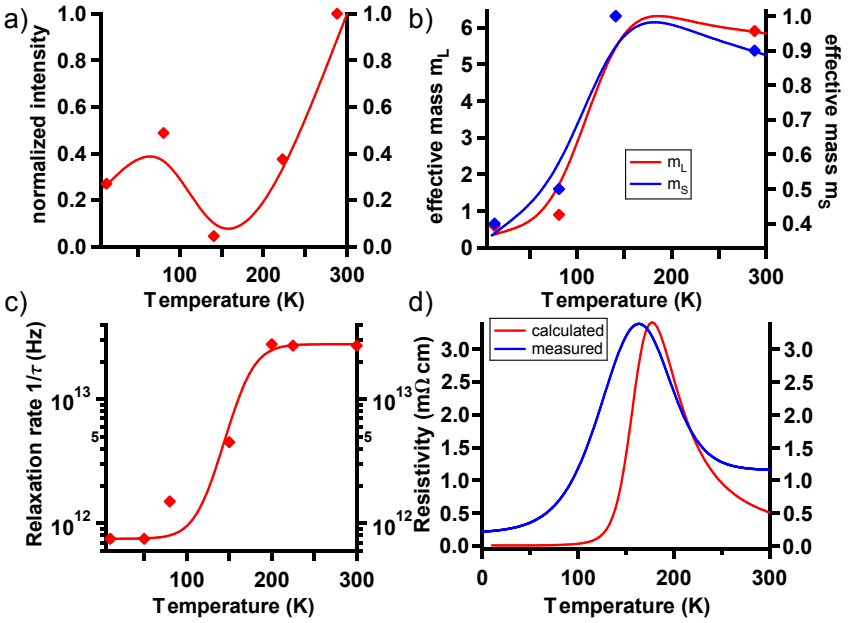


FIGURE 6.7: (a) Intensity of the conduction electron pockets integrated ±50 meV around $E_F$ and normalized. (b) Effective masses of the conduction band along the long axis $m_L$ and the short axis $m_S$ of the ellipsoidal pocket. (c) Relaxation rate obtained from reflectivity measurements [97]. (d) Resistivity calculated with the previous data, in comparison with the measured one [48]. All these curves have been interpolated and smoothed.

due to the fact that our approach neglects the contribution of phonons, which are known to be dominant at low temperature.

Having the different components of the resistivity, we are able to relate the upturn and the downturn of the calculated curve to a particular effect. As already shown before (see for instance section 5.2 and Fig. 5.4), the major changes happening around $T_c$ are due to the charge carrier density variation, represented by the normalized intensity of Fig. 6.7 (a). The strong decrease in this curve stems from the transfer of spectral weight from the original conduction band to backfolded bands at $L$[b], as a consequence of exciton condensation. At around $\sim$ 150K, the charge carrier density increases again. Moreover, it is widely amplified by the reduction of the relaxation rate and of the charge carrier effective mass. These two combined effects are at the origin of the low temperature resistivity downturn. The dramatic renormalization of the effective masses has been explained in section 6.2. The important decrease of the scattering rate below $T_c$ is certainly due to the shift of the hole pocket at $\Gamma$ away from $E_F$, since its disappearance removes one possible channel for scattering.

[b]In the model, the unit spectral weight of the original (conduction) band is distributed in the CDW phase among the other bands *at the same* $\vec{k}$*−point.*

### 6.4.2 Exciton densities

#### 6.4.2.1 Electron and hole densities

In the previous discussion, we focussed on the electron contribution to transport and calculated the resistivity after having obtained different parameters from our data and from literature. We will now work the other way around, using transport data from the literature to find the corresponding electron and hole densities and finally estimate the exciton density.

Di Salvo *et al.* measured the electrical and Hall resistivity of $1T$-$TiSe_2$ [55], which have already been shown in Fig. 3.6. According to them, in a two-band model for a semimetal with hole and electron densities $n_h$ and $n_e$ respectively, these resistivities obey to generalized Drude formulas

$$\begin{aligned} \rho &= \frac{1}{|e|}\frac{1}{(n_h\mu_h + n_e\mu_e)}, \\ R_H &= \frac{1}{|e|}\frac{n_h\mu_h^2 + n_e\mu_e^2}{(n_h\mu_h + n_e\mu_e)^2}, \end{aligned} \tag{6.2}$$

where $\mu_\alpha$ is the mobility of the $\alpha-$type charge carrier, defined as $\mu_\alpha = e\tau_\alpha/m_\alpha$. Making the assumption that $\tau_h = \tau_e$, we can directly compute $\mu_e$ and $\mu_h$ with the relaxation time and effective masses[c] used before. These mobilities are displayed in Fig. 6.8 (a) [d]. Using equations 6.2, it is then straightforward to obtain the electron and hole densities from the data of Di Salvo *et al.* [55]. Fig. 6.8 (b) shows the resulting curves. Both densities undergo a strong decrease from $\sim$ 250K to $\sim$ 120K. Below $\sim$ 120K, while the electron density remains more or less constant, the hole density increases again. This is surprising, because at this temperature, the valence band is far below $E_F$. This may be an artifact of our procedure since we analyze the resistivity purely from an electronic point of view. One knows that, at low temperature, the influence of the phonons should be considered and neglecting it may have such consequences.

Another peculiar fact is that, at room temperature, the electron and hole densities are far from being equal. Indeed, it is expected that, well above $T_c$ (where the excitonic fluctuations are negligible), the chemical potential ensures that for the charge carriers, $n_h = n_e$. Such a large discrepancy could point towards a Ti overdoped system (see discussion in section 5.4.1), although such a situation seems very unlikely with the data of Di Salvo *et al.*, since the authors paid much attention to carefully characterize and understand the presence of excess of Ti atoms [48]. A simpler explanation for this discrepancy could also stem from our assumption $\tau_e = \tau_h$. For example, increasing $\tau_h$ by 3 strongly reduces this discrepancy.

[c] For the holes, we keep $m_h = m_v = -0.23m_0$ ($m_0$ is the bare electron mass) over the whole temperature range.

[d] For comparison, at room temperature, typical electron and hole mobilities in Si are 1400 $cm^2/Vs$ and 500 $cm^2/Vs$ [110].

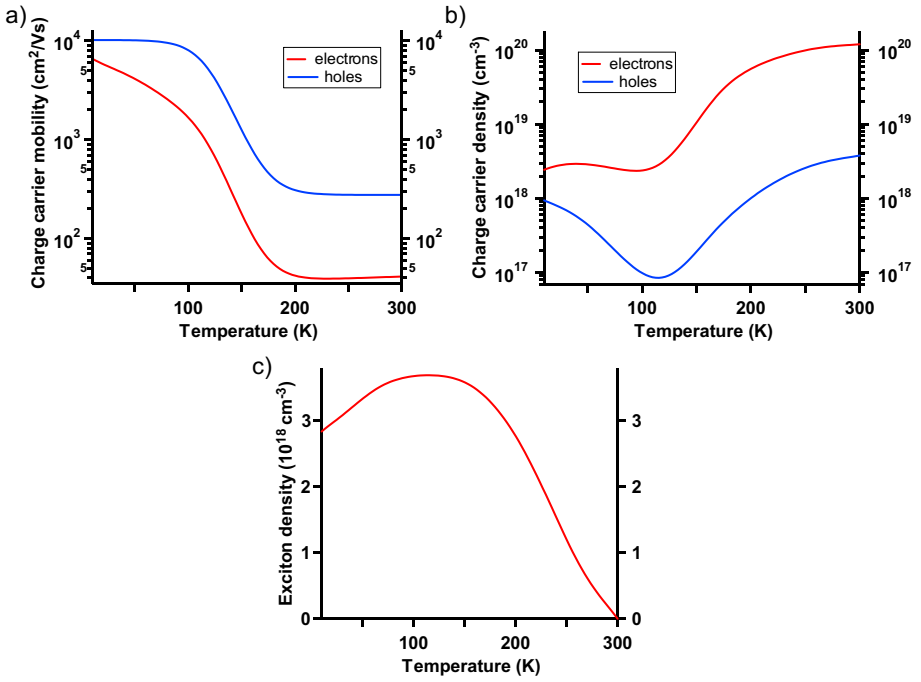


FIGURE 6.8: Data calculated from the electronic and Hall resistivities. Electron and hole (a) mobilities and (b) densities. (c) Exciton density.

#### 6.4.2.2 Exciton density

Finally, we want to estimate the exciton density in $1T$-$TiSe_2$ with this analysis of transport data. Then, from the electron and from the hole densities, which one is representative of the exciton density? Concerning the electron density, we know that the conduction band looses spectral weight in favour of the backfolded bands, as a direct consequence of exciton formation. However, it becomes partially occupied below $T_c$, as the chemical potential shifts into the unoccupied states, which is rather an indirect consequence of the excitons. These two effects result in a net loss of charge carriers of electron type (remember Fig. 5.4 (b)). Therefore it is difficult to distinguish between these two contributions. On the contrary, the disappearance of holes is mainly due to the exciton condensation, since it happens because of the large spectral weight loss at the maximum of the valence band and of its shift to higher binding energies due to the gap opening. In that sense, the reduction of the hole density attests to the formation of excitons. Fig. 6.8 (c) shows the exciton density, calculated from $n_{exc}(T) = |n_h(T) - n_h(T = 300\text{K})|$. This density increases from room temperature already and goes on faster below $\sim 250$K. This surprisingly precedes the critical temperature of the transition and may be due to the excitonic fluctuations above $T_c$. At about $\sim 120$K it saturates and reaches the value of $3.5 \cdot 10^{18}$ cm$^{-3}$. Below 120K, it decreases again, but this is certainly the consequence of the artifact mentionned above, since we consider only electronic degrees of freedom in our analysis of the resistivity. The maximum exciton density is about $\sim 1\%$ of the room temperature electron-type charge carrier density [e]. However, it is very similar to its low temperature value (at $\sim 100$K). It means that at low temperature, when exciton condensation fully develops, their density is comparable to the charge carrier density in the system, meaning that they certainly play a significant role. As discussed above, a

[e]This is rather a high value compared to BCS theory, since, for conventional superconductor like Pb, the density of Cooper pairs reaches hardly 0.1% [105, 111].

higher relaxation time for holes shifts the curves for the electron and hole densities and increases the exciton density, up to the $10^{19}$ cm$^{-3}$.

#### 6.4.2.3 Validity of the realisation of the exciton condensate

An exciton density $n_{exc}$ of $10^{18}$ to $10^{19}$ cm$^{-3}$ in the condensate is already a few order of magnitude larger than typical values in laser pumped semiconductors [69, 112]. At high density, excitons in a condensate may dissociate and create an electron-hole plasma, which turns out to be a metallic (liquid) phase of unbound electrons and holes [113]. The critical density $n_c$ at which such a transition happens can be calculated according to the formula [69, 114]

$$n_c(T) = (1.19)^2 \frac{\epsilon_r \epsilon_0 k_B T}{e^2 a_B^2},$$

($\epsilon_r$ is the relative dielectric constant of the material), which is derived from the condition that a too efficiently screened Coulomb interaction does not allow electron-hole bound states. For $1T$-$TiSe_2$, an exact value of $\epsilon_r$ is difficult to obtain. We rather use $\epsilon_\infty = 19$ from the optical study of Li *et al.* [97]. It leads to $n_c(200K) \simeq 2 \cdot 10^{18}$ cm$^{-3}$, which is very similar to the $n_{exc}$ determined here. This tells us that the exciton condensate in $1T$-$TiSe_2$ is very close to the electron-hole plasma regime and that a slight change of its bandstructure may lead to the disappearance of the exciton condensate phase. However, these numbers should be considered with care, as they are obtained by approximate methods.

In section 4.5, we have evaluated the exciton radius to $a_{exc} \sim 40$Å. Knowing the exciton density, it is interesting to estimate also their mean distance, by approximating the volume occupied by each exciton through a sphere, so that

$$\lambda_{exc} \simeq \left( \frac{3}{4\pi n_{exc}} \right)^{1/3} \simeq 30 \text{ to } 60\text{Å}.$$

This means that the exciton radius is comparable in size to the mean distance between excitons. This has the important consequence that the exciton wave functions are overlapping, enabling phase coherence to settle at the critical temperature $T_c$, similarly to the BCS theory of superconductivity.

# Chapter 7

# And what about the lattice?

Until now, in this thesis, we focussed on the electronic degrees of freedom and the onset of the CDW phase of $1T$-$TiSe_2$ below the transition temperature of $T_c = 200$K. We were able to reproduce very well the low temperature electronic structure measured by photoemission within the exciton condensate phase. However, despite this success, an important question remains. What happens with the underlying lattice? In Chapter 3, when introducing the $1T$-$TiSe_2$ system, we mentioned that below $T_c$ the CDW is accompanied by a PLD, whose structure has been determined by Di Salvo *et al.* with neutron diffraction [48] and which is depicted in Fig. 3.4. To summarize, this PLD involves a $(2 \times 2 \times 2)$ superlattice, which is characterized by the wave vectors $\vec{w}_1, \vec{w}_2, \vec{w}_3$.

In fact, this important issue has been already addressed in details by Motizuki and her coworkers. Based on a tight-binding fit to the first-principles band calculations of Zunger and Freeman [85], they calculated the wave vector dependent electronic susceptibility (including electron-phonon coupling) in the presence of a lattice distortion [95]. They found that this susceptibility has the highest value for a transverse phonon mode[a] of wave vector $\vec{w}_1$, meaning that the largest electronic energy would be saved for this mode. This is consistent with the observation of the $L_1^-$ phonon mode softening at $T_c$ [49]. In a further work, they calculated the electronic band structure as a function of the amplitude of the lattice distortion [61]. By minimizing the sum of the elastic and electronic energies, they found a distortion amplitude very close to the observed value. In summary, in their approach, Motizuki *et al.* support the Jahn-Teller mechanism, where the electronic energy gain caused by the CDW may be large enough to compensate the elastic energy cost of the lattice deformation.

Our approach in this chapter will be different. Having given much support to the exciton condensation at the origin of the CDW phase with photoemission, we now investigate whether the presence of this condensate is capable of generating the observed PLD. Similary to Motizuki and coworkers, our calculations will be done in a tight-binding formalism, based on our own DFT calculations. These two techniques are briefly introduced in appendix B.

[a] It corresponds to the phonon mode polarization determined by Di Salvo [48].

## 7.1 Exciton condensation driving the periodic lattice distortion of $1T$-$TiSe_2$

C. Monney[1], C. Battaglia[1], H. Cercellier[2], H. Beck[1], P. Aebi[1],

[1] *Institut de Physique, Université de Fribourg, CH-1700 Fribourg, Switzerland*

[2] *Institut Néel, CNRS-UJF, BP 166, 38042 Grenoble, France*

Not submitted yet

We address the question of the lattice instability of $1T$-$TiSe_2$ in the framework of the exciton condensate phase. In a recent work, we already proposed this mechanism as the cause for the charge density wave phase of $1T$-$TiSe_2$. Here, in this model, we show that, at low temperature, condensed excitons formed by holes from the valence band and electrons from the conduction bands, influence the lattice through electron-lattice interaction. Calculations are made in a tight-binding formalism. It is found that at zero temperature, in the exciton condensate phase of $1T$-$TiSe_2$, this exciton density exerts a force on the lattice generating ionic displacements comparable to what is measured in experiment.

In a semimetallic or semiconducting system exhibiting a small (negative, respectively positive) gap, the Coulomb interaction, when poorly screened, leads to the formation of bound states of holes and electrons, called excitons. If their binding energy $E_B$ is bigger than the gap, they may condense at low temperature and drive the system into a new ground state. This new ground state, called the excitonic insulator phase [2, 3, 65], is then characterized by some wave vectors $\vec{w}_i$. If the latter are not vectors of the reciprocal lattice, they will generate a new periodicity in the electronic structure of the system, leading to the formation of a charge density wave phase (CDW).

$1T$-$TiSe_2$ belongs to the family of the transition metal dichalcogenides, a class of quasi-2D materials, famous for displaying a transition towards CDW phases [40]. $1T$-$TiSe_2$ is particular, as its commensurate 2x2x2 CDW phase cannot be explained by the usual mechanism of nesting [85]. It appears below $T_C \simeq 200$K and is characterized by three wave vector $\vec{w}_i$ $(i = 1, 2, 3)$ pointing from the maximum of the valence band at $\Gamma$ and to the minima of the conduction bands at the three symmetry equivalent $L$ points [48]. Among the proposed alternative mechanisms for the CDW figure a band Jahn-Teller effect [64] and the excitonic insulator phase. We already gave much support to the second scenario by adapting it to the particular case of $1T$-$TiSe_2$ [80] to generate photoemission intensity maps which compare very well with the experiment[87]. As explained above, in the excitonic picture the CDW phase is entirely due to an electronic mechanism. However, a weak periodic lattice distortion (PLD) accompanying the CDW has been measured by DiSalvo *et al.* [48], who inferred small ionic displacements $< 0.1$ Å. In our opinion, such small displacements, in comparison with the high spectral weight carried by the backfolded bands, indeed supports an electronic origin of the CDW [87].

In the exciton condensate framework, an important issue is to know whether such ionic displacements may appear as a consequence in the low temperature phase. To address this question, in this work we study the influence of an exciton condensate on the lattice.

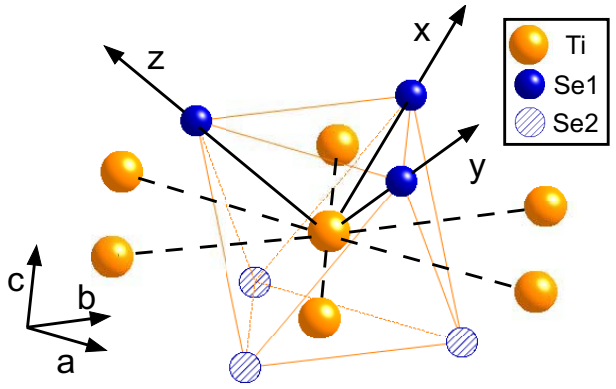


FIGURE 7.1: Atomic structure of $1T$-$TiSe_2$. The Se1 and Se2 atoms lie above and below, respectively, the Ti atom plane, forming an octahedral coordination (emphasized by the thin frame) with the center Ti atom. The orthonormal axis system points from the center Ti atom towards the neighbouring Se1 atoms. The crystallographic axes are also shown.

First, we derive the electron-phonon coupling in the framework of the tight-binding (TB) formalism. Focussing particularly on the valence and conduction electrons, we derive a formula relating the ionic displacements to the presence of an exciton condensate, the amplitude of which is the order parameter characterizing the low temperature phase. By fitting TB dispersions to those obtained from density functional theory band structure calculations, we obtain the transfer integrals specific to $1T$-$TiSe_2$. With other parameters from the literature, this allows us to apply our model to the case of $TiSe_2$ and calculate the amplitude of ionic displacements. Values similar to those obtained from experiment demonstrate that the exciton condensate phase, as a possible origin of the CDW phase of $1T$-$TiSe_2$, can also give account for the PLD.

The TB formalism for the electronic band structure and the coupling to the lattice described below is similar to that already developed by Yoshida and Motizuki [95]. $1T$-$TiSe_2$ consists of planes of Ti atoms forming a triangular lattice. Each of these Ti atoms is in octahedral coordination with its six neighbouring Se atoms. Then the crystals consists of a regular stacking of such Se-Ti-Se layers in the $c$ direction, so that one unit cell contains only one layer (in the $c$ direction). For the TB calculations of the present study, a cluster of atoms centered about one Ti atom will be considered. The (orthonormal) axis system is chosen so as to point towards the nearest neighbour Se atoms (in the same plane) from the Ti atom at origin. Fig. 7.1 displays partially such a cluster, with the axis system. In our calculations, for the Ti atoms, we include the five $3d$-orbitals of $xy$, $yz$, $xz$, $x^2-y^2$ and $3z^2-r^2$ symmetry and the three $4p$-orbitals for each of the two Se atoms, of $x$, $y$ and $z$ symmetry. In total we have 11 orbitals. The TB electronic Hamiltonian then reads

$$H_{el} = \sum_{ll'} \sum_{\mu\nu} \sum_{\alpha\beta} J_{\alpha\beta}(\vec{R}_l - \vec{R}_{l'} + \vec{\tau}_\mu - \vec{\tau}_\nu) \sum_{\vec{k}n} \mathrm{e}^{-i\vec{k}\cdot\vec{R}_l} T^*_{\alpha\mu,n}(\vec{k}) \mathrm{e}^{i\vec{k}\cdot\vec{R}_{l'}} T_{\beta\nu,n}(\vec{k}) c^\dagger_n(\vec{k}) c_n(\vec{k}). \tag{7.1}$$

Here $\vec{R}_l, \vec{R}_{l'}$ are vectors of the Bravais lattice and $\vec{\tau}_\mu, \vec{\tau}_\nu$ are the positions of the atoms labelled $\mu, \nu$ inside one unit cell. The indices $\alpha, \beta$ label the 11 orbitals and $n$ is the index of the bands in which the operators $c^\dagger_n$ create electrons. The transfer matrix

$J$, diagonalized by the eigenvectors $T$, consists here only of two center integrals for simplicity.

We now introduce ionic displacements of the form

$$\vec{u}_{l\mu} = \frac{1}{\sqrt{M_\mu}} \sum_{\vec{q}\lambda} \mathrm{e}^{i\vec{q}\cdot\vec{R}_l} \vec{e}(\mu, \vec{q}\lambda) Q(\vec{q}\lambda) = \sum_{\vec{q}\lambda} \mathrm{e}^{i\vec{q}\cdot\vec{R}_l} u_\mu(\vec{q}\lambda) \tag{7.2}$$

where $M_\mu$ is the mass of the ion labelled $\mu$, $\vec{e}$ a polarization vector and $Q$ the normal coordinate of the phonons. Here $u_\mu(\vec{q}\lambda)$ is the ionic displacement for the atom labelled $\mu$ and associated to a particular mode $\vec{q}\lambda$. Equation (7.2) provides us with a direct way to compute the amplitude of the displacement of each ion, once we get an expression for $Q$. This is our goal in the next paragraphs. Introducing the small ionic displacements $\vec{u}_{l\mu}$ in the argument of the transfer matrix $J$ in equation (7.1), we expand $J$ to first order in $\vec{u}_{l\mu}$ to deduce the electron-lattice interaction

$$H_{el-ph} = \sum_{nn'} \sum_{\vec{k}\vec{q}\lambda} g_{nn'}(\vec{k}, \vec{q}, \lambda) c_n^\dagger(\vec{k}) c_{n'}(\vec{k} - \vec{q}) Q(\vec{q}\lambda) \tag{7.3}$$

where the electron-lattice coupling constant

$$\begin{aligned} g_{nn'}(\vec{k}, \vec{q}, \lambda) = \sum_{\vec{\rho}} \sum_{\mu\nu} \sum_{\alpha\beta} T^*_{\alpha\mu,n}(\vec{k}) \frac{dJ_{\alpha\beta}}{d\vec{x}}\bigg|_{\vec{x}=\vec{\rho}+\vec{\tau}_\mu-\vec{\tau}_\nu} \\ \times T_{\beta\nu,n'}(\vec{k} - \vec{q}) \mathrm{e}^{-i\vec{k}\cdot\vec{\rho}} \cdot \left[ \vec{e}(\mu, \vec{q}\lambda) \mathrm{e}^{i\vec{q}\cdot\vec{\rho}} - \vec{e}(\nu, \vec{q}\lambda) \right], \end{aligned} \tag{7.4}$$

with $\vec{\rho} = \vec{R}_l - \vec{R}_{l'}$, involves the derivatives of the transfer matrix.

To evaluate the influence of excitons, we need now to recall results of our previous study on the exciton condensate phase of $TiSe_2$ [80]. In what follows, we focus on the influence of excitons created by holes in the valence and electrons in the three symmetry equivalent conduction bands. In that sense, the operators $a(\vec{k})$ and $b_i^\dagger(\vec{k})$ create holes with wave vector $\vec{k}$ in the valence band (at its maximum) and electrons with wave vector $\vec{k} + \vec{w}_i$ in the conduction band labelled $i$ (at its minimum) respectively. Thus the sum over the band indices $n, n'$ in equation (7.3) is restricted to terms mixing $a$ and $b$ operators only, so that

$$\begin{aligned} H_{el-ph} &= \sum_i \sum_{\vec{k}\vec{q}\lambda} Q(\vec{q}\lambda) g_{ab_i}(\vec{k}, \vec{q}, \lambda) a^\dagger(\vec{k}) b_i(\vec{k} - \vec{w}_i - \vec{q}) \\ &\quad + Q(\vec{q}\lambda) g_{b_i a}(\vec{k}, \vec{q}, \lambda) b_i^\dagger(\vec{k} - \vec{w}_i) a(\vec{k} - \vec{q}) \\ &= \sum_i \sum_{\vec{p}\lambda} Q(-\vec{w}_i\lambda) g_{ab_i}(\vec{p}, -\vec{w}_i, \lambda) a^\dagger(\vec{p}) b_i(\vec{p}) \\ &\quad + Q(\vec{w}_i\lambda) g_{b_i a}(\vec{p} + \vec{w}_i, \vec{w}_i, \lambda) b_i^\dagger(\vec{p}) a(\vec{p}). \end{aligned}$$

We considered only $\vec{q} = -\vec{w}_i$ in the term involving $g_{ab_i}$ and $\vec{q} = \vec{w}_i$ in that involving $g_{b_i a}$ (together with the substitution $\vec{p} = \vec{k} - \vec{w}_i$), restricting ourselves to the scattering between the extrema of the bands. The operators $b_i^\dagger a$ can be expanded in terms of the exciton creation operator $A^\dagger$

$$b_i^\dagger(\vec{k}) a(\vec{k}) = \sum_\lambda \phi^*_\lambda(\vec{k}) A^\dagger_\lambda(\vec{w}_i) \approx \phi^*_0(\vec{k}) A^\dagger_0(\vec{w}_i)$$

with the coefficients $\phi_\lambda$ being the hydrogen-like wavefunction for the exciton [80]. Here only the lowest lying excitonic state $\lambda = 0$ is kept. Then, averaging $\langle H_{el-ph} \rangle$ to lowest order over the electronic degrees of freedom yields the contribution of excitons to the phonon Hamilonian

$$\begin{aligned} H_{ph-x} &= \sum_i \sum_{\vec{p}\lambda} Q(-\vec{w}_i\lambda) g_{ab_i}(\vec{p}, -\vec{w}_i, \lambda) \phi_0(\vec{p}, \vec{w}_i) \xi_{0i} \\ &\quad + Q(\vec{w}_i\lambda) g_{b_i a}(\vec{p} + \vec{w}_i, \vec{w}_i, \lambda) \phi_0^*(\vec{p}, \vec{w}_i) \xi_{0i}^* \\ &= \sum_{i\lambda} Q(\vec{w}_i\lambda) \sum_{\vec{p}} \phi_0(\vec{p}, \vec{w}_i) \\ &\quad [g_{ab_i}(\vec{p}, \vec{w}_i, \lambda) \xi_{0i} + g_{b_i a}(\vec{p} + \vec{w}_i, \vec{w}_i, \lambda) \xi_{0i}^*] \\ &=: \sum_{i\lambda} Q(\vec{w}_i\lambda) P(\vec{w}_i\lambda) \end{aligned} \tag{7.5}$$

provided the temperature of the system is below the critical temperature of the transition, so that excitons may condense, resulting in a non-zero $\xi_{0i}^* := \langle A_0^\dagger(\vec{w}_i) \rangle$ [80]. We also used the inversion symmetry of the system to replace $-\vec{w}_i$ by $\vec{w}_i$. From this last equation, the equilibrium condition for the lattice in the presence of a condensate of exciton, $\partial(H_{ph,0} + H_{ph,x})/\partial Q(\vec{w}_i\lambda) = 0$, leads to an expression for the normal coordinate of the phonons $Q$ caused by the exciton condensate

$$Q(\vec{w}_i\lambda) = \frac{P(\vec{w}_i\lambda)}{\omega^2(\vec{w}_i\lambda)} \tag{7.6}$$

where $H_{ph,0} = (1/2) \sum_{i\lambda} \omega^2(\vec{w}_i\lambda) Q^*(\vec{w}_i\lambda) Q(\vec{w}_i\lambda)$ is the bare Hamiltonian of the lattice (in the absence of the exciton condensate). By using equation (7.2) we can relate it to the resulting ionic displacements.

Having now an analytical formula for the ionic displacements through equations (7.2), (7.4), (7.5), (7.6), we can look for the necessary numerical parameters for the final computation. We start with the transfer matrix $J_{\alpha\beta}$. According to Slater and Koster [115], its elements are computed as a combinations of direction cosines (directing the bonds joining two atoms) and transfer integrals (specific of the orbital types involved). In our case, these transfer integrals are determined by fitting a density functional theory (DFT) band structure. This first-principles band structure has been calculated using the full potential augmented plane wave plus local orbitals (APW+lo) method with the generalized gradient approximation in the parametrization of Perdew, Burke and Ernzerhof [116], in the local density approximation, as implemented in the WIEN2K software package [56]. The numerical details can be found in a footnote [b] are similar to those used in reference [93]. Parameters of the unit cell can be found in Tab. 7.1. In particular, the unit cell size parameters $a, b, c$ were fixed to the experimental values [47] but the reduced $z_{red}$ coordinate of Se atoms was determined by minimizing the forces on each atom. The resulting DFT band structure is plotted in Fig. 7.2. The goal of this DFT calculation here is not to be discussed in details but to offer a basis for the TB fit we perform for determining the transfer integrals. Such a detailed discussion may be found

[b] The APW+lo basis was expanded up to $R_{MT}K_{max} = 7$, with $R_{MT}$ the radius of the muffin tin sphere and $K_{max}$ the maximum length of the reciprocal lattice vector. Inside the muffin tin sphere, the $l$ expansion of the nonspherical potential and charge density is carried out up to $l_{max} = 10$. The number of $k$ points in the irreducible part of the Brillouin zone is 360. The maximum length of wave vector used for the Fourier expansion of the charge density is $12a_0^{-1}$ ($a_0$ is the Bohr radius).

TABLE 7.1: Reduced coordinates of $1T$-$TiSe_2$ in the trigonal symmetry with unit cell parameters: $a = b = 3.534$ Å, $c = 6.008$ Å, space groupe 164 ($P\bar{3}m1$)

| Atom | $x_{red}$ | $y_{red}$ | $z_{red}$ |
|---|---|---|---|
| Ti | 0 | 0 | 0 |
| Se | 1/3 | 2/3 | 0.265 |

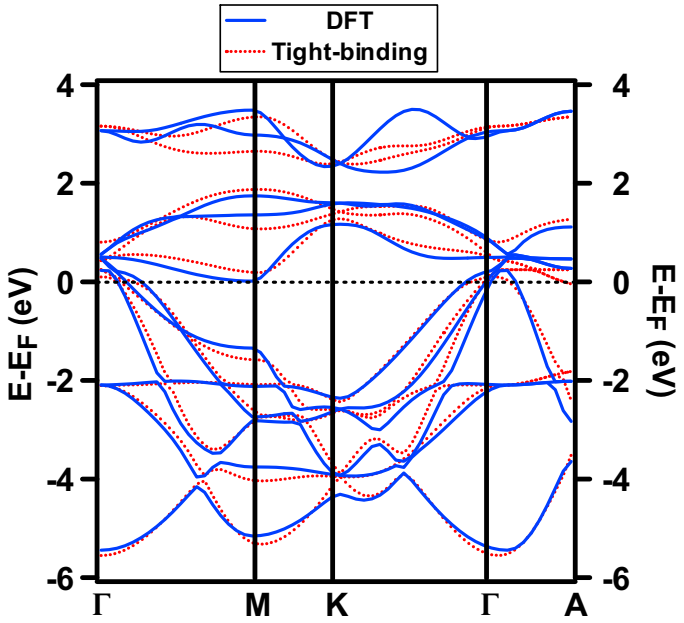


FIGURE 7.2: Comparison of the band structure of $1T$-$TiSe_2$ calculated with density functional theory and its fit within a TB approach.

in references [92, 93]. A least-square fit was used along the high symmetry directions $\Gamma MK\Gamma A$ on the DFT band structure and the transfer integrals obtained this way are summarized in Tab. 7.2. In our formulation, no overlap matrix was used to ensure orthogonality of the orbitals. However, this is implicitly included in the transfer matrix [117]. This TB parametrization allows us to build an effective Hamiltonian which can be diagonalized (at each $\vec{k}$ point) to provide us with the eigenvectors $T_{\alpha\mu,n}(\vec{k})$. Then the derivatives of the transfer matrix, appearing in the electron-lattice coupling $g_{nn'}(\vec{k},\vec{q},\lambda)$, imply derivatives of the direction cosines and derivatives of the transfer integrals. The latter are evaluated in the same way as Yoshida and Motizuki [95]. The derivative of the element $t(pd\sigma)$, for instance, is computed by $t'(pd\sigma) = t(pd\sigma)\alpha A(pd\sigma)/d$. The parameters $A$ have been calculated by Yoshida and Motizuki and are listed in Tab. 7.2. The adjustable parameter $\alpha$ is fixed to $\alpha = 2$ (it has a small influence on the final result). $d$ is the distance between the two atoms. According to Di Salvo *et al.* [48], the phonon polarization vectors $\vec{e}(\mu,\vec{q}\lambda)$ involved in the CDW are perpendicular to their respective $\vec{q}$ vector and lie in the $ab$ basal plane. This way, only the transverse phonon mode $\lambda_{tr}$ will be considered in the following calculations. At this point, we have all the ingredients necessary to evaluate the electron-lattice coupling $g_{nn'}(\vec{k},\vec{q},\lambda)$.

Now we would like to rewrite the expression of the $P$ function of equation (7.5) to replace the parameter $\xi_0$ (the average exciton creation operator) by the order parameter $\Delta$. $\Delta$, which describes the intensity of the exciton condensate in the low temperature phase,

TABLE 7.2: Transfer integrals for the $1T$-$TiSe_2$ structure, fitted from first-principles band structure.

| Transfer integral | Energy (eV) | Parameter $A^a$ |
|---|---|---|
| $t(pp\sigma)$ | 0.77 | -4.5 |
| $t(pp\pi)$ | -0.054 | -7.0 |
| $t(dd\sigma)$ | -0.35 | -2.0 |
| $t(dd\pi)$ | 0.0737 | -4.1 |
| $t(dd\delta)$ | -0.049 | -6.4 |
| $t(pd\sigma)$ | 1.3 | 0.8 |
| $t(pd\pi)$ | 0.70 | -2.7 |
| $t(pp\sigma)_2$ | 0.63 | -4.5 |
| $t(pp\pi)_2$ | -0.028 | -7.0 |
| $t(pp\sigma)_3$ | 0.61 | -4.5 |
| $t(pp\pi)_3$ | -0.096 | -7.0 |
| $\varepsilon_p = -2.00$ eV | $\varepsilon_{d\varepsilon} = 0.744$ eV | $\varepsilon_{d\gamma} = 1.20$ eV |

[a] Reference [95].

can be directly estimated from the experiment (see below). It obeys a gap equation similar to that of the BCS theory

$$\Delta(\vec{p}) = \sum_{\vec{q}} V_c(\vec{q})\phi_0(\vec{p}+\vec{q},\vec{w})\xi_0^*(\vec{w}_i)$$

involving the exciton wavefunction $\phi_0$ in the lowest energy state. $\phi_0$ is chosen to be an $s$-wave $\phi_0(\vec{r}) = 2\sqrt{\beta}\mathrm{e}^{-\beta|\vec{r}|}$ in real space, where $\beta$ is a variational parameter, determined by minizing the ground state energy in the presence of a screened Coulomb potential

$$V_c(\vec{r}) = \frac{1}{4\pi\epsilon_0}\frac{\mathrm{e}^{-r/l_s}}{r}. \tag{7.7}$$

The parameter $\beta$ is then a function of the screening length $l_s$ and the effective mass $m^*$ of the exciton (see for instance reference [118] for a detailed calculation). It is determined by minimization of the energy of independent excitons (and closely related to $l_s$). From the condition of having bound states (negative energy), we get the condition that $l_s \geq 1.65$ Å. This allows us also to replace $\xi_0$

$$\xi_{0i}^* = \frac{\Delta(\vec{p})}{\sum_{\vec{q}} V_c(\vec{q})\phi_0(\vec{p}+\vec{q})} \tag{7.8}$$

(here $V_c(\vec{q})$ is the Fourier transform of $V_c(\vec{r})$ and $\phi_0(\vec{q})$ the Fourier transform of $\phi_0(\vec{r})$) so that now, the $P$ function reads

$$P(\vec{w}_i\lambda_{tr}) = \sum_{\vec{p}} \Delta(\vec{p})\phi_0(\vec{p})\frac{[g_{ab_i}(\vec{p},\vec{w}_i,\lambda) + g_{b_ia}(\vec{p}+\vec{w}_i,\vec{w}_i,\lambda)]}{\sum_{\vec{q}} V_c(\vec{q})\phi_0(\vec{p}+\vec{q})}.$$

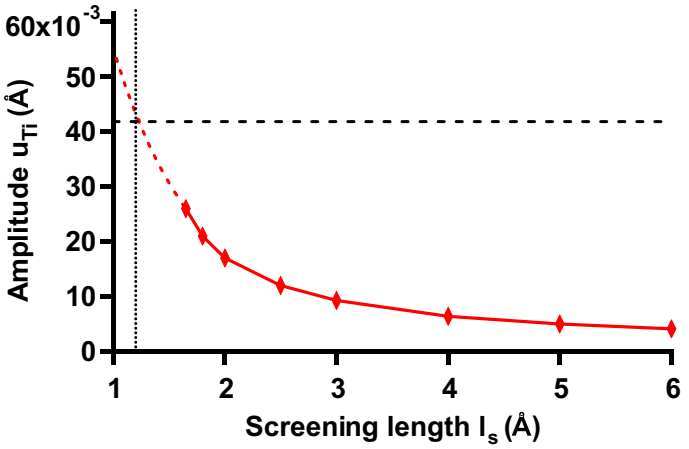


FIGURE 7.3: . Calculated amplitude of the Ti ionic displacement for a single $\vec{w}_i$, $u_{\mathrm{Ti}}(\vec{w}_i\lambda_{tr})$, in $1\,T$-$TiSe_2$ generated by the presence of an exciton condensate, as a function of the screening length $l_s$ (the diamonds show the calculated values). The vertical dotted line indicates the value at the calculated screening length $l_s = 1.2$ Å (see text). The horizontal dashed line indicates the experimental value.

In the end, the amplitude of the ionic displacement for a single $\vec{w}_i$ (and for transverse phonons) has the following form

$$u_\mu(\vec{w}_i\lambda_{tr}) = \frac{1}{\sqrt{M_\mu}}\frac{1}{\omega^2(\vec{w}_i\lambda_{tr})}\left|\sum_{\vec{p}}\frac{\Delta(\vec{p})\phi_0(\vec{p})\left[g_{ab_i}+g_{b_ia}\right]}{\sum_{\vec{q}}V_c(\vec{q})\phi_0(\vec{p}+\vec{q})}\right|. \tag{7.9}$$

In our recent temperature dependence study of the exciton condensate phase in $1\,T$-$TiSe_2$ [107], we evaluated the amplitude of the $\vec{k}$-independent order parameter at $T = 0$K to $\Delta_0 = 100$ meV. As a consequence, in the equation above, we take the value of the denominator in equation (7.8) for $\vec{p} = 0$, since $\xi_{0i}$ must be wave vector independent. For the transverse phonon frequency $\omega(\vec{w}_i\lambda_{tr})$, we decide to use the room temperature value of the lowest phonon at $L$ (located by the wave vectors $\vec{w}_i$). Indeed, this correponds to a situation where the excitons have a weak influence, being only present through fluctuations [80], so that $\omega(\vec{w}_i\lambda_{tr})$ represents a bare frequency with respect to excitonic effects. Wakabayashi *et al.* obtained a frequency $\omega(\vec{w}_i\lambda_{tr}) \cong 8.8$ THz at room temperature [119]. This is consistent with the x-ray diffraction study of Holt *et al.* [49]. Moreover, in this study, Holt *et al.* showed that the lowest phonon at $L$ is subject to softening when the temperature decreases towards $T_c$, which also motivates our choice.

Now all the necessary quantities are known to compute the amplitude of the ionic displacements (7.9), except the screening length $l_s$. This is an important element as it appears in the Coulomb potential $V_c$ and in the parameter $\beta$ of the exciton wavefunction $\phi_0$ (see above). We thus calculated the amplitude of the ionic displacements for Ti atoms and for a single-$\vec{w}_i$, $u_{\mathrm{Ti}}(\vec{w}_i\lambda_{tr})$, as a function of the screening length $l_s$. Fig. 7.3 summarizes our numerical results. As expected, one sees immediately a strong dependence of $u_{\mathrm{Ti}}(\vec{w}_i\lambda_{tr})$ on $l_s$. This behaviour can be traced back mainly to the factor $\beta^{-3}$ appearing in the exciton wavefunction $\phi_0(\vec{q})$ in the numerator of equation (7.9), since $\beta$ is an increasing function of $l_s$. Di Salvo *et al.* inferred a displacement (also for a single-$\vec{w}_i$) of about $u_{\mathrm{Ti}}^{\mathrm{exp}}(\vec{w}_i\lambda_{tr}) = 0.04$ Å from neutron diffraction experiments [48]. Our calculations underestimate slightly this value, as for the lowest screening length available here, $l_s = 1.7$ Å, $u_{\mathrm{Ti}}^{\mathrm{theo}}(\vec{w}_i\lambda_{tr}) = 0.03$ Å. However, this is a substantial result,

in view of the approximations used in this work. An estimate of the screening length in $TiSe_2$ can be derived with the Thomas-Fermi theory of screening applied to a free electron gas [104]. Using the electron density deduced by Li *et al.*, $n_{el} = 7.1 \cdot 10^{-20}$ $cm^{-3}$ [97], we get $l_s = 1.2$ Å, which is smaller than the lower limit allowed in Fig. 7.3. As explained above, this curve is limited in the low $l_s$ range, since no bound state exists in this regime for the crude variational model we used to obtain a wavefunction for the exciton. Bypassing this limitation leads to the ionic displacements $u_{\mathrm{Ti}}^{\mathrm{theo}}(\vec{w}_i\lambda_{tr}) = 0.04$ Å, for $l_s = 1.2$ Å, which are identical to what is observed (within the accuracy of the present calculations).

In conclusion, we adressed the question of the appearance of a periodic lattice distortion in $1T$-$TiSe_2$. We proposed exciton condensation as a purely electronic mechanism responsible for the CDW phase in this material. In this work, we elaborate in a tight-binding formalism a formula for estimating the ionic displacements produced by the presence of this exciton condensate through the electron phonon coupling. By fitting a first-principles electronic band structure with an electronic tight-binding Hamiltonian, we obtain transfer integrals which we use together with parameters obtained from the literature. The amplitude of the ionic displacements obtained as a function of the screening length of the system are of the same order of magnitude than what is experimentally found. This is thus the first explanation of the PLD observed in $1T$-$TiSe_2$, as a *consequence* of the exciton condensate phase which we proposed as a *purely electronic* origin of its CDW. This significant result gives thereby more strength to this scenario for $TiSe_2$.

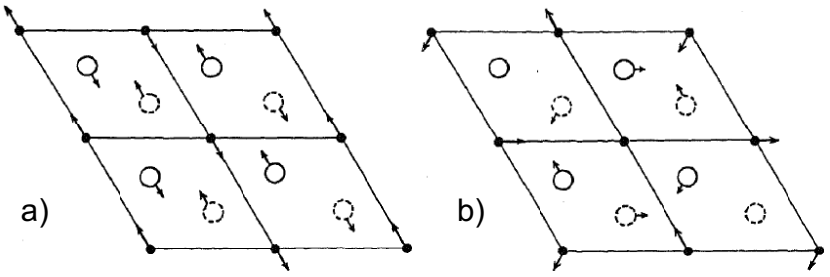


FIGURE 7.4: The PLD of $1T$-$TiSe_2$ from reference [61]. (a) Single-$q$ and (b) triple-$q$ structures. Filled circles represent Ti ions and open circles Se ions (sitting above and below the Ti plane).

## 7.2 Comment to "Exciton condensation driving the periodic lattice distortion of $1T$-$TiSe_2$"

The goal of this calculation was to investigate whether the presence of an exciton condensate in the CDW phase could produce ionic displacements with a reasonable amplitude. Surprisingly, despite the approximations we used, the value we obtain is not only within the right order of magnitude, but also close to the experimental one ($u_{\mathrm{Ti}}^{\mathrm{exp}}(\vec{w}_i\lambda_{tr}) = 0.04$ Å), since $u_{\mathrm{Ti}}^{\mathrm{theo}}(\vec{w}_i\lambda_{tr}) = 0.03$ Å at the limit screening length of $l_s = 1.65$ Å.

In our tight-binding calculations, we have made the natural choice of considering atomic orbitals related to the bands close to $E_F$. This results in 5 $d$-orbitals for Ti atoms and 3 $p$-orbitals for each Se atoms, involving a total of 11 orbitals. Concerning the fit to the DFT calculation in Fig. 7.2, it is then necessary to use bands ranging from -6 eV to 4 eV, where all these Ti3$d-$ and Se4$p$-bands disperse (fortunately they are well separated from the other bands). We also restricted ourselves to the $\Gamma MK\Gamma A$ $k$-path to avoid too many constrains on the fitting procedure. We obtained a good agreement between the tight-binding and the DFT dispersions, exhibiting in average discrepancies of about $\sim 200$ meV.

At this point, one may ask whether the three dimensional structure of the CDW can be explained within the model. In fact, this question has been already answered by Suzuki *et al.* [61]. Assuming a transverse polarization of the phonon mode implied in the CDW, as it is experimentally observed[c] [48], it is a direct consequence of the general equation for the ionic displacements 7.2. Indeed, if only one electron pocket, located at $\vec{w}_1$, is involved in the electron-hole pairing, according to equation 7.9 only the phonon mode $\vec{w}_1$ will couple to the exciton condensate. From equation 7.2, we know that the ionic displacements will develop in the direction transverse to $\vec{w}_1$ and in the $a-b$ plane, modulated by the Bravais lattice vectors $\vec{R}_l$. This results in the so-called single-$q$ mode, depicted in Fig. 7.4 (a) [61]. However, as we know from our model, three electron pockets at $\vec{w}_i$ ($i = 1, 2, 3$) are participating to the exciton condensate, generating ionic displacements which are a combination of three single-$q$ modes, called the triple-$q$ mode. This CDW structure is depicted in Fig. 7.4 (b). This figure shows one particular plane of the $TiSe_2$ structure, where the low temperature unit cell is clearly doubled along both directions of the $a-b$ plane. A third modulation happens in the $c-$direction, doubling also the corresponding lattice parameter.

[c] We do not have a theoretical proof of that. This is probably due to the particular symmetry of the phonon mode involved in the softening at the CDW transition [49].

The code used for these computations, as well as the technical details, are given in the appendix A.3.

## 7.3 An alternative way of calculating the exciton-lattice coupling

In section 7.1, the operators $b_i^\dagger a$ have been expanded in terms of the exciton creation operator $A^\dagger$, so that the exciton wave function appeared in the exciton-phonon Hamiltonian $H_{ph-x} = \langle H_{el-ph} \rangle$. This exciton wave function, which is unknown, has been chosen of a $s-$wave form, defined by a variational parameter $\beta$ depending notably on the screening length $l_s$. This method of calculating the atomic displacement $u_{\mathrm{Ti}}$ has therefore the drawback to rely on the exciton wave function, which is not well known, and depends on the screening length.

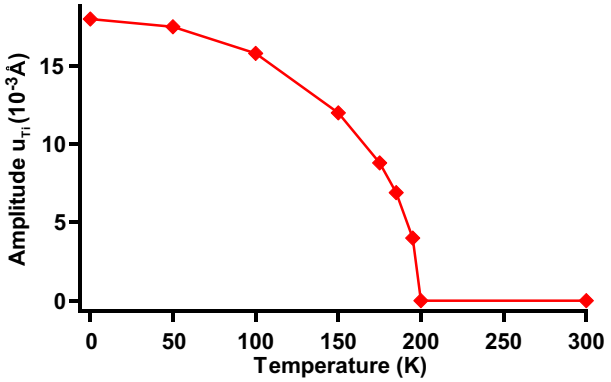


FIGURE 7.5: Amplitude of the ionic displacement of Ti atoms as a function of temperature, calculated on the basis of the anomalous Green's function.

As an alternative to this method, we propose now to use the anomalous Green's function, since $\langle b_i^\dagger a \rangle = -iF_i^\dagger(t=0)$. Generalizing it to its finite temperature form, $F_i^\dagger(\tau = 0)$ allows us to reuse our calculations of section 5.5 and in particular equation 5.5, since $\langle b_i^\dagger(\vec{p}) a(\vec{p}) \rangle = -F_i^\dagger(\vec{p}, \tau = 0)$. Using the fact that $F_i^\dagger(\vec{p}, \tau = 0) = F_i(\vec{p}, \tau = 0)$, we can rewrite equation 7.5 like

$$\begin{aligned} H_{ph-x} &= -\sum_{i\lambda} Q(\vec{w}_i\lambda) \sum_{\vec{p}} F_i(\vec{p}, \tau = 0) \left[ g_{ab_i}(\vec{p}, \vec{w}_i, \lambda) + g_{b_i a}(\vec{p} + \vec{w}_i, \vec{w}_i, \lambda) \right] \\ &= -\sum_{i\lambda} Q(\vec{w}_i\lambda) P(\vec{w}_i\lambda_{tr}, T). \end{aligned}$$

The resulting $P$ function acquires a temperature dependence through the anomalous Green's function $F_i$. The order parameter, which appears in the numerator of $F_i$ and in the poles of $F_i$, exhibits also a certain temperature dependence.

By choosing an order parameter of the form $\Delta(T) = \Delta_0 \sqrt{1 - (T/T_c)^2}$ with $\Delta_0 = 100$ meV and $T_c = 200$K, we obtained the results shown in Fig. 7.5 with this alternative method. We see that $u_{\mathrm{Ti}}(T)$ mimics the temperature dependence of $\Delta(T)$. At zero temperature, it reaches the value of $u_{\mathrm{Ti}}(T = 0\mathrm{K}) = 0.018$ Å, which is about half the experimentally observed value, $u_{\mathrm{Ti}}^{\mathrm{exp}}(\vec{w}_i\lambda_{tr}) = 0.04$ Å. Moreover, although this approach is different than that of section 7.1, this result is very similar to that previously obtained.

This is very satisfactory, as it gives us much reliance in our general tight-binding model of the exciton-phonon coupling.

# Chapter 8

# Conclusions and perspectives

## 8.1 Conclusions

This thesis has been devoted to the study of one material, $1T$-$TiSe_2$. Despite its simple layered structure, involving only two different atomic species, this system turns out to be the playground of very interesting collective phenomena. The onset of the CDW phase at low temperature has been explained in terms of an exciton condensate phase, theoretically modelled like a BCS condensate. A dramatic band renormalization developing at very low temperature was identified and qualitatively explained within this model. Finally, the response of the underlying lattice to the electron density modulation produced by the exciton condensate was calculated and shown to be quantitatively in good agreement with the observed PLD.

As it can be guessed in these short highlights, this thesis is the result of a close interplay between experiment and theory. The simple electronic band structure of $1T$-$TiSe_2$ around the Fermi level made it possible to build for this situation a model, being at the same time minimal and realistic. Of course, this model does not capture all the details observed in the photoemission measurements, but it offers a very good qualitative agreement between calculated and measured photoemission intensity maps. It has also lead to a deeper understanding of the phenomena occurring in $1T$-$TiSe_2$, like the resistivity or the origin of the PLD.

## 8.2 Perspectives

### 8.2.1 Time-resolved experiments

Although this thesis gives much support with the help of photoemission to the exciton condensate phase as the origin of the CDW phase in $1T$-$TiSe_2$, a direct evidence of the existence of the exciton condensate is still lacking. Indeed, the backfolded bands appearing in photoemission intensity maps are a consequence of the exciton condensation, as well as the peak in the resistivity or the PLD. It is unfortunately unlikely that conventional photoemission could bring a direct evidence.

However, time-resolved experiments could bring a new insight into this problem. Indeed, relaxation of electrons and phonons in solids after a short optical excitation (produced generally by laser pulses) occurs on different time scales, namely about $\sim 10$ fs and $\gtrsim 100$ fs respectively. This allows to disentangle their contribution, for instance in optical [120] or in photoemission spectra [121, 122]. In the case of the exciton condensate phase, the CDW, involving only electronic degrees of freedom, should disappear and possibly reappear before the lattice had time to react, that is, without affecting the PLD.

### 8.2.2 Sample quality

Another issue about $1T$-$TiSe_2$ concerns the quality of the sample. First of all, as discussed in section 5.4, the uncontrolled excess of Ti atoms in the crystal translates directly into a shift of the conduction bands. STM images of $1T$-$TiSe_2$ indicate that this Ti excess is distributed inhomogeneously over the surface, in domains of a typical size of $\sim 10$ nm. Photoemission of such a surface certainly results in a incoherent addition of spectra coming from domains with different dopings. This could be an explanation for the rather wide peaks we observe in our spectra (see for instance the energy distribution curves of Fig. 5.6 (a)). X-ray diffraction analysis of our samples also points towards a possibly high mosaicity of the crystal. Therefore improving the quality of the crystals with respect to doping and mosaicity could lead to spectra with substantially narrower peaks, allowing for a better resolution in the electronic structure.

### 8.2.3 Exciton-mediated superconductivity

In this work, we have studied the pure compound $1T$-$TiSe_2$. As mentioned in the overview of section 3.3.1, $1T$-$TiSe_2$ can be easily intercalated with foreign atoms due to its Van der Waals gap, opening a new dimension in the phase diagram. The copper intercalated system, $Cu_x$-$TiSe_2$, has already been much investigated, since its phase diagram exhibits a CDW phase together with superconductivity at low copper contents (see Fig. 3.5) [47]. The nature of the interplay between the CDW phase and superconductivity still remains a mystery, as well as the potential role played by the excitons in superconductivity. In that sense, the possibility of an exciton-mediated superconductivity has already been addressed in the existing literature [89, 123, 124]. Based on our deep understanding of the pure compound, a systematic investigation of $Cu_x$-$TiSe_2$ with photoemission can be a possible extension of the present work. Both the suppression of the exciton condensate phase with doping and the appearance of superconductivity would be very interesting to study in that framework.

### 8.2.4 Extension of the mean-field theory

The exciton condensate model has been calculated at the mean-field level. However, experiment clearly shows that fluctuation effects above $T_c$ are strong. These effects cannot of course be captured by our model in the present state. Therefore, its development at a higher order in the perturbation theory to tackle the problem of fluctuation is a natural continuation of the present theory. Explaining the appearance of the phonon mode softening at $T_c$ would be also a possible objective.

### 8.2.5 Extension of the model

In the exciton condensate model adapted to the bandstructure of $1T$-$TiSe_2$, three symmetry equivalent electron pockets (at $L$) have been considered for obtaining a minimal model, as explained in section 4.3. However, as it can be seen in the photoemission intensity map of Fig. 4.7 for instance, at low temperature, a second valence band (a spin-orbit split version of the topmost one) also participates to the backfolding at $L$. Including this second valence band in the model will certainly correct this discrepancy. It may also improve other weaknesses of the model, like the underestimation of the intensity transferred from the original bands to the backfolded ones (see section 4.4 for such a discussion). The resulting calculations will become heavier, involving a new coupling parameter, which will be a second order parameter.

# Appendix A

# Source codes used for numerical computations

## A.1 Chemical potential in the exciton condensate phase

In this section, we show details of the numerical routine used to compute the chemical potential shift resulting from a change of the order parameter in the exciton condensate phase. In section 4.7.3, we derived formula 4.42 to compute the electronic density $n$ of such a phase. It turns out that the electronic density is a function of the order parameter, the temperature and the chemical potential $n(\Delta, T, \mu)$.

The procedure used to determine this chemical potential shift is a simple one. First we compute the normal phase (room temperature) electronic density $n_0 = n(\Delta = 0\,\text{meV}, 300\,\text{K}, \mu = 0)$, which is our reference. Then, for a given order parameter $\Delta_1$ and for a given temperature $T_1$, we compute the corresponding electronic density $n(\Delta_1, T_1, \mu)$ and change $\mu$ until we recover the reference value $n_0 = n(\Delta_1, T_1, \mu_1)$. This determines $\mu_1$.

Practically, the integration is replaced by a sum, since the renormalized dispersions $\Omega_\alpha(\vec{k})$ are complicated and time-consuming formula. By discretizing the reciprocal space in $k_x, k_y, k_z$ directions, we have then a good control of the computational effort. The conversion of a one-dimensional integral into a summation is done according to

$$\int f(x)dx \simeq \sum_i f(x_i)\Delta x_i = \sum_i f(x_i)\frac{L}{N},$$

where $L$ is the size of the interval which is divided in $N$ steps for integration.

The C++ code of this routine is listed below. The resulting density is printed to the output line, in $10^{24}$ cm$^{-3}$.

```
1  //------------------------------------------------------------------------

   #include"Poles.h"
   #include<iostream>
   #include<fstream>
6  #include<stdlib.h>
   #include<math.h>
```

```
#include<time.h>

using namespace std;
double FDdistrib(double,double,double);

//------------------------------------------------------------------------

// temperature, screening length, value of order parameter
// checkintegrand : if 1, the integrand (fct of kx,ky,kz) is printed into
// IntegrandData.txt at kz value for kx,ky running over values defined in code

int main(int argc,char* argv[])
{
// input parameters:
// order parameter value
double ordparvalue=atof(argv[1]);
// temperature
double temp=atof(argv[2]);
// chemical potential
double chempot=atof(argv[3]);
// band energy cutoff
double energycutoff=atof(argv[4]);


double kx,ky,kz;
int nkx,nky,nkz;
int i,j,k;

double poles[4];
double valweights[4];
double condweights[4];

double coeff;
double sumRTTot=0.;
double resultRTTot=0.;
double sumLTTot=0.;
double resultLTTot=0.;
double sumRTVal = 0.;
double sumRTCond = 0.;
double sumLTVal=0.;
double sumLTCond=0.;
double resultRTVal = 0.;
double resultRTCond = 0.;
double resultLTVal=0.;
double resultLTCond=0.;
time_t start,end;
double kxrange,kyrange,kzrange;
double valueLTTot=0.;
double valueLTVal=0.;
double valueLTCond=0.;

long double time1,time2,elsapsedtime;


//load bands parameters from file
setglobalvars();

// number of k-points for reciprocal space discretization
nkx=20;
nky=20;
nkz=10;
kxrange=1.0;
kyrange=1.0;
kzrange=1.04;

start=time(NULL);

for(i=0;i<nkx+1;i++){
  for(j=0;j<nky+1;j++){
    for(k=0;k<nkz+1;k++){
      kx=-kxrange/2.+kxrange/nkx*i;
```

```
      ky=-kyrange/2.+kyrange/nky*j;
      kz=-0.52+kzrange/nkz*k;

        // renormalized band dispersions
        poles[0]=pole1(kx,ky,kz,ordparvalue);
        poles[1]=pole2(kx,ky,kz,ordparvalue);
        poles[2]=pole3(kx,ky,kz,ordparvalue);
        poles[3]=pole4(kx,ky,kz,ordparvalue);

        // load spectral weights at Gamma and L into the arrays
        specweightval(kx,ky,kz,poles,valweights);
        specweightcond(kx,ky,kz,poles,condweights,ordparvalue);

        // normal phase total electron density
        if(real(ea(kx,ky,kz))>energycutoff){
        sumRTTot = sumRTTot + FDdistrib(real(ea(kx,ky,kz)),temp,chempot) +
FDdistrib(real(eb1(kx,ky,kz)),temp,chempot)*3./2.;
        }
        else{
        sumRTTot = sumRTTot + FDdistrib(real(eb1(kx,ky,kz)),temp,chempot)*3./2.;
        }

        // CDW free hole density
      valueLTVal = valueLTVal + valweights[0]*FDdistrib(-poles[0],temp,-chempot)
+ valweights[1]*FDdistrib(poles[1],temp,chempot);
        valueLTVal = valueLTVal + valweights[2]*FDdistrib(poles[2],temp,chempot) +
valweights[3]*FDdistrib(poles[3],temp,chempot);//situation at Gamma (valence)


        // CDW free electron density
        valueLTCond = valueLTCond + 3./2.*(condweights[0]*FDdistrib(-
poles[0],temp,-chempot) + condweights[1]*FDdistrib(poles[1],temp,chempot));
        valueLTCond = valueLTCond +
3./2.*(condweights[2]*FDdistrib(poles[2],temp,chempot) +
condweights[3]*FDdistrib(poles[3],temp,chempot));//at L (conduction)

        // CDW electron density at Gamma
        if(poles[0]>energycutoff){
        valueLTTot = valueLTTot + valweights[0]*FDdistrib(poles[0],temp,chempot) +
valweights[1]*FDdistrib(poles[1],temp,chempot);
        valueLTTot = valueLTTot + valweights[2]*FDdistrib(poles[2],temp,chempot) +
valweights[3]*FDdistrib(poles[3],temp,chempot);//situation at Gamma (valence)
        }
        else{
        valueLTTot = valueLTTot + valweights[1]*FDdistrib(poles[1],temp,chempot);
        valueLTTot = valueLTTot + valweights[2]*FDdistrib(poles[2],temp,chempot) +
valweights[3]*FDdistrib(poles[3],temp,chempot);
              }

        // CDW electron density at L

        if(poles[0]>energycutoff){
        valueLTTot = valueLTTot +
3./2.*(condweights[0]*FDdistrib(poles[0],temp,chempot) +
condweights[1]*FDdistrib(poles[1],temp,chempot));
        valueLTTot = valueLTTot +
3./2.*(condweights[2]*FDdistrib(poles[2],temp,chempot) +
condweights[3]*FDdistrib(poles[3],temp,chempot));//at L (conduction)
        }
        else{
        valueLTTot = valueLTTot +
3./2.*(condweights[1]*FDdistrib(poles[1],temp,chempot));
        valueLTTot = valueLTTot +
3./2.*(condweights[2]*FDdistrib(poles[2],temp,chempot) +
condweights[3]*FDdistrib(poles[3],temp,chempot));
        }

        // normal phase hole density at Gamma
```

```
            sumRTVal = sumRTVal + FDdistrib(-real(ea(kx,ky,kz)),temp,-chempot);
151         // normal phase electron density at L
            sumRTCond = sumRTCond + FDdistrib(real(eb1(kx,ky,kz)),temp,chempot)*3./2.;

            sumLTTot = sumLTTot + valueLTTot;
            valueLTTot=0.;
156
            sumLTVal=sumLTVal+valueLTVal;
            valueLTVal=0.;

            sumLTCond=sumLTCond+valueLTCond;
161         valueLTCond=0.;
            }
      }
   }

166 // coefficient for conversion of the 3D integral into a sum
   coeff = 1./(4.*pow(M_PI,3))*kxrange/nkx*kyrange/nky*kzrange/nkz;
   // 4*pi^3 comes from the DOS definition (continuous form)
   // kxrange/nkx correspond to Delta kx_i,i.e the step in sum, ie discretized
   // version of infinitesimal element
171
   resultRTVal = sumRTVal*coeff;
   resultRTCond = sumRTCond*coeff;
   resultRTTot = sumRTTot*coeff;
   resultLTVal = sumLTVal*coeff;
176 resultLTCond = sumLTCond*coeff;
   resultLTTot = sumLTTot*coeff;


   end=time(NULL);
181
   // print to standard output the bands parameters used in this calculation
   printglobalvars();

   printf("after %.1f seconds\n",difftime(end,start));
186 printf("at temperature %.1f K with chemical potential %f and order parameter
   %f,\n",temp,chempot,ordparvalue);
   printf("(with an energy cutoff at %f)\n\n",energycutoff);


191 printf("the normal free hole density is : %f\n",resultRTVal);
   printf("the normal free electron density is : %f\n\n",resultRTCond);

   printf("the normal electron density is : %f\n\n",resultRTTot);

196

   printf("the CDW free hole density is : %f (with %d
   errors)\n",resultLTVal);
   printf("the CDW free electron density is : %f (with %d
   errors)\n\n",resultLTCond);
201
   printf("the CDW electron density is (Gamma + L) : %f (with %d
   errors)\n\n",resultLTTot);

   //unit of the result
206 printf("(every density given in 10^24 cm^(-3))\n\n");

   return 0;
   }

211 //-------------------------------------------------------------------------

   double FDdistrib(double energy,double temp,double chempot)
   {
     double kB = 8.617 * pow(10.,-5);
216  double result = 1./(1.+exp((energy-chempot)/(kB*temp)));

     return result;
   }
```

```
221 //------------------------------------------------------------------------
```

In this code, the functions `specweightval` and `specweightcond` compute the spectral weights $P^v_\alpha(\vec{k})$ and $P^c_\alpha(\vec{k})$, respectively, of the four renormalized dispersions $\Omega_\alpha(\vec{k})$.

## A.2 Calculation of the order parameter of the exciton condensate phase

In this section, we describe the method used for computing the order parameter of the (three-dimensional) exciton condensate phase. The numerical results have been discussed in section 5.5. Computing the order parameter for a given temperature consists of solving the integral equation 5.6, which involves $\Delta$ on both side, in a non-trivial manner. This is done iteratively by feeding the right hand side integral with an order parameter value $\Delta_i$ which provides us with a new value $\Delta_{i+1}$. The procedure is repeated until convergence is reached, when the difference $\Delta_{i+1} - \Delta_i$ is small. Technically this leads to two difficulties: the right hand side integral and the iterative procedure. We will show the former first and the latter below.

The following listing shows the code used to compute the right part of equation 5.6, where a three-dimensional integration in wave vector over the first Brillouin zone has to be performed. For that purpose, we have chosen to use the deterministic algorithm called Cuhre using the Cuba library [125]. The shape of the Brillouin zone has been approximated by a cylinder of radius $\Gamma M$ and height $2\Gamma A$ to increase the symmetry of the integral and decrease its numerical cost. This has no serious consequence, since in the anomalous Green's function $F_1^\dagger$ the valence and conduction bands are centered around the same $\vec{k}-$point, which can be chosen to be at $\Gamma$ without any loss of generality, and are essentially non-zero in its neighbourhood.

The order parameter, for a given temperature $T$ and a given screening length $\lambda_s$, is given in $eV$.

```
//------------------------------------------------------------------------

#include<iostream>
#include<fstream>
#include<stdlib.h>
#include<math.h>
#include<time.h>
#include"Poles.h"
#include"/home/koitzsch/Cuba-1.5/cuba.h"
#include"AnomalousGF.cpp"


using namespace std;

double tempint;
double SLint;
double ordparint;
double muint;
double krangeint;
double kzrangeint;

//------------------------------------------------------------------------
double CoulombPotential(double qx,double qy,double qz,double screenlen)
{
  double eps0=8.8542*pow(10.,-12);
  double echarge=1.602*pow(10.,-19);

  //Coulomb potential in reciprocal space ; in eV and for q in Angstroem^-1
  return 1./eps0*echarge/(pow(qx,2)+pow(qy,2)+pow(qz,2)+pow(2.*M_PI/screenlen,2))
*pow(10.,10);
}
//------------------------------------------------------------------------
```

```
double intcart(double qx,double qy,double qz,double OrdParam,double px,double
py,double pz,double temp,double screenlen,double mu)
{
  double result=0;
  double polesarr[4];

  //poles of the Anomalous Green's function
  poles(qx,qy,qz,OrdParam,polesarr);

  //integrand in cartesian coordinates
  result =  -CoulombPotential(qx-px,qy-py,qz-pz,screenlen)
*AnomalousGF(polesarr,OrdParam,qx,qy,qz,temp,mu);

  return result;
}
//---------------------------------------------------------------------
static void Integrand(const int *ndim, const double xx[], const int *ncomp,
double ff[])
{
#define k xx[0]
#define th xx[1]
#define kz xx[2]
#define f ff[0]

  double kint=k*krangeint;
  double thint=th*M_PI*2.;
  double kzint=-kzrangeint+2.*kz*kzrangeint;

  //integrand in cylindrical coordinates
  f = kint*intcart(kint*cos(thint),kint*sin(thint),kzint,ordparint,0,0,0,
tempint,SLint,muint);
}
//-----------------------------------------------------------------------------
double OrderParam(double temp,double screenlen,double ordparvalue,double mu,
int nbint,double* error,int verbose,int* fail)
{
  double result;

  //read the band parameters from an external file
  setglobalvars();

  tempint=temp;
  SLint=screenlen;
  ordparint=ordparvalue;
  muint=mu;

  //radius of cylinder in Brillouin zone
  krangeint=1.04;
  //GA distance
  kzrangeint=0.522;

  int comp,nregions,neval;
  double integral[1],prob[1];

  double epsrel=1e-2;
  double epsabs=1e-12;
  int flags=4+verbose;
  int key=11;

  //3D integral with Cuhre method
  Cuhre(3,1,Integrand,epsrel,epsabs,flags,0,nbint,key,&nregions,&neval,fail,
integral,error,prob);

  //conversion of sum into a 3D integral
  result=integral[0]/pow(2.*M_PI,3);

  //normalization by range of integral (since Cuhre is integrating on hypercube)
  result=result*2.*M_PI*krangeint*kzrangeint*2.;

  return result;
}
```

```
104 //------------------------------------------------------------------------
```

In the function `intcart`, `AnomalousGF` refers to the sum over the residues of the anomalous Green's function $F_1^{\dagger}$, in equation 5.5. This part of the code is not shown here. It must be said however that a particular algorithm, described in reference [126], has been used for finding roots of the (polynomial) denominator of the Green's function 4.39.

The next listing shows our iteration procedure to solve the integral equation 5.6.

```
1
#include<iostream>
#include<fstream>
#include<stdlib.h>
#include<math.h>
6 #include"OrderParamCuhre.h"


using namespace std;

11 //------------------------------------------------------------------------
//function for writing band parameter in the output file
void writeglobalvars(double Emax,double Emin)
{
  ofstream BandsParams("bandsparams.txt");
16  char temp[20];

  BandsParams << "Emax    " << Emax << endl << "meffA    " << -0.23 << endl <<
"EZwidthA   " << 0.06 << endl <<  "Emin    " << Emin << endl << "meffaB     "  <<
 5.5 << endl <<   "meffbB    " << 2.2 << endl << "EZwidthB   " << 0.03 << endl;
21

  BandsParams.close();
}
//------------------------------------------------------------------------
int Loop(double screenlen,string basename,int nbint,double Emax,double Emin){
26  double ordparstart=0.1;//eV
  double newordpar=ordparstart;
  double oldordpar;
  double convergence,oldconv;
  //accuracy for the iteration on the order parameter at a given temperature
31  double convthresh0 = 0.0001;//eV
  double delta0=10.;
  double convthresh;

  double error=0.;
36  int verbose=0;
  int fail=0;

  char space[4] = "\t";

41  //output file
  char filename[30];
  sprintf(filename,"%s%dkEmax%.3fEmin%.3f.txt",nbint/1000,Emax,Emin);
  ofstream outfile(filename,ios::app);

46  if(!outfile)
    {
      printf("couldn't open file\n");
      return 0;
    }
51
  //input file: band parameters
  ifstream infile("bandsparams.txt");
  char buff[200];

56  outfile << "Bands parameters" << endl;
  outfile << "----------------" << endl << endl;
```

```
  if(infile){
    do{
      infile.getline(buff,sizeof(buff));
      outfile << buff << endl;
    }
    while(!infile.eof());
  }
  else
    outfile << "could not append band parameters" << endl;

  outfile << endl << endl;


  outfile << "Beginning iteration at " << ctime(&time1) << endl;
  outfile << "---------------------------------------" << endl<<endl;

  outfile << "Screening Length" << space << screenlen << endl;
  outfile << "Nb of calls" << space << nbint << endl;
  outfile << "Basic convergence threshold" << space << convthresh0 << endl << endl;

  //starting temperature in loop (defined in code)
  double temperature=10.;

  //loop on temperature
  int i,j,iteration;
  for(i=0;i<51;i++)
    {
      outfile << "Temperature" << space << temperature << endl;
      outfile << "-----------------------------------" << endl;

      oldordpar=newordpar;
      convergence=1.0;
      iteration=0;
      j=0;

      convthresh=convthresh0;

      //for a given temperature, this while-loop ensures the convergence of
        //the integral equation
      while(fabs(convergence) > convthresh || j < 2)
        {
          oldordpar=newordpar;
          //limit for breaking non-converged iterations
          if(iteration > 35)
            {
              printf("failed to converge\n");
              break;
            }
          if(oldordpar < 0.001 && j > 2)
            break;

          //compute the new order parameter using the old one
          newordpar=OrderParam(temperature,screenlen,oldordpar,mu,nbint,&error,
verbose,&fail);

          if(i==0)
            delta0=newordpar;

          oldconv = convergence;
          //difference between the previous order parameter and the new one
          //(used for testing convergence)
          convergence=oldordpar-newordpar;

          //the convergence criterium
          if(j>2 && convergence*oldconv<0)
            break;

          ordparstart=newordpar;
          if(ordparstart < 0.002)
            ordparstart=newordpar;
```

```
            //prints intermediairy steps of the convergence loop
            outfile << "Intermediary Order Param" << space << newordpar << endl;
            outfile << "with error " << error << " and fail " << fail << endl;
            outfile << "(SL" << space << screenlen << " A and mu" << space << mu
<< " eV)" << endl;
            outfile << "Time needed [s]" << space << difftime(time2,time1) << endl;

            iteration++;
            j++;
          }

        //prints converged order parameter for a given temperature
        outfile << "----------------------" << endl<<endl;
        outfile << "Converged Order Param at"<< space << temperature << " K"
<< space << newordpar << endl;
        outfile << "corresp. SL"<< space << screenlen << " A" << endl;
        outfile << "and corresp. mu"<< space << mu << " eV" << endl << endl << endl;

        //stops the temperature loop above Tc
        if(newordpar < 0.001)
          break;

        //increment of the loop temperature defined here
        temperature=temperature+10.;
      }

    infile.close();
    outfile.close();

    return 0;
}
//------------------------------------------------------------------------
int main(int argc,char* argv[])
{
    double screenlen=atof(argv[1]);
    string basename=argv[2];
    int nbint=atoi(argv[3]);

    double Emax,Emin,i,j;

    for(i=0;i<5;i++){
      for(j=0;j<5;j++){
        Emax=-0.04+(double) 0.02*i;
        Emin=-0.04+(double) 0.02*j;

        writeglobalvars(Emax,Emin);
        Loop(screenlen,basename,nbint,Emax,Emin);
      }
    }

}
//------------------------------------------------------------------------
```

## A.3 Calculation of the ionic displacements due to the exciton condensate

In this section, we describe technically the method used to compute the amplitude of the ionic displacements generated by the exciton-lattice coupling. This method is derived from the analytical formula presented in section 7.1. In particular, we will dissect equations 7.4 and 7.9.

Our approach is based on a tight-binding formalism, so that a finite cluster of Ti and Se atoms ($Natom$ in total) must be constructed around a central unit cell, which contains the reference atoms (1 Ti and 2 Se atoms). Then all the possible $Nbond$ bonds (up to a certain cutoff distance) between the reference atoms and the others must be listed as a function of the distance. For each type of atom (Ti, $Se_1$ and $Se_2$), a defined number of orbitals is taken into account, for a total of $BasisSize$ orbitals. For Se atoms we consider $p_x, p_y, p_z$ orbitals and for Ti atoms $d_{z^2}, d_{x^2-y^2}, d_{xy}, d_{xz}, d_{yz}$ orbitals. Then, the tight-binding Hamiltonian $J_{\alpha\beta,\mu\nu}(\vec{k})$ of equation B.4 can be easily constructed by using for each bond and orbital combination the transfer integral of Slater and Koster [115]. Diagonalizing this Hamiltonian and fitting the resulting band to the DFT calculations (using a least-square method) provide us with the transfer integrals $t(\alpha\mu\ \beta\nu\ \xi)$ corresponding to the DFT band structure of $1T$-$TiSe_2$.

The most difficult element to compute in the exciton induced ionic displacements of equation 7.9 is the exciton-lattice coupling function 7.4. This function requires especially the derivative of the two-center energy integrals $dJ_{\alpha\beta}/d\vec{x}$ and the eigenvectors $T_{\alpha\mu,n}(\vec{k})$ of the tight-binding Hamiltonian. The derivatives of the two-center energy integrals involve the derivatives of the transfer integrals $t(\alpha\mu\ \beta\nu\ \xi)$, which are evaluated according to the method of Yoshida and Motizuki [95], and the derivatives of the cosine directors, which are easy to calculate. The eigenvectors $T_{\alpha\mu,n}(\vec{k})$ are obtained during the diagonalization process of the tight-binding Hamiltonian (for each $\vec{k}$ vector!).

Going back to equation 7.9, the coupling constant must be multiplied by the order parameter (which is a parameter of the calculation) and by the exciton wave function (which is known for a $s-$type wave). The numerator of equation 7.9 is a sum over the wave vector $\vec{q}$, which is also $\vec{p}$-dependent. To simplify this aspect, we average this $\vec{p}$-dependence to obtain a constant value with respect to the wave vector. This approximation does not have a strong impact on the result.

Finally, the most time consuming operation is the sum over the wave vector $\vec{p}$ in equation 7.9. Using the symmetry of the trigonal unit cell of $1T$-$TiSe_2$, we can restrict ourselves to 1/6th of the Brillouin zone. Nonetheless, to ensure a good convergence, we need to sum over 20 $k$ points in each direction, resulting in a fine $k$ mesh of 8000 points.

The code used for these calculations has been written with the program Igor Pro [127] and is shown below.

```
function Pfunction (orderparam,screenlen,nbsteps)
        variable orderparam,screenlen, nbsteps

        wave wvector=root:wvec1


        variable echarge=1.6*10^(-19)
        variable epsilon=8.854*10^(-12)
```

```
variable meff=2*1/(1/0.23+1/2.2+1/0.23+1/5.5)*2
variable error=0

variable alpha=alphaFct(screenlen,meff,error)
if(error)
        print "error in alpha fct ; calculation aborted"
        return 1
endif

variable i,j,u,k        //iterators

String BIndexR, BIndexC,BAtomR,BAtomC, BOrbitalR,BOrbitalC
String FromString, ToString
variable From, To
variable m,n,l,d //direction cosines and distance

variable/C OverlapReturn
make/C/O/N=3 OverlapVect

Variable kx,ky,kz
wave a=root:a   //unit cell primitive vectors
wave b=root:b   //reciprocal lattice vectors
wave bint=root:bint    //reciprocal lattice zone for k-integration
NVar nkpt = root:nkpt     //number of k-points along k-path
NVar Nbond = root:Nbond   //number of bonds considered in cluster
NVar Natom = root:Natom   //number of atoms considerd in cluster
Nvar NMatrixElements = root:NmatrixElements //number of transfer integrals
NVar BasisSize = root:BasisSize  //number of orbitals in the TB
wave/T BasisAtom=root:BasisAtom  //list of atom names
wave/T BasisOrbital=root:BasisOrbital  //list of orbital names
wave BasisEnergy = root:BasisEnergy    //list of orbital energies
wave BasisDerivCoeff=root:BasisDerivCoeff  //A parameters for the transfer
                                  //integrals derivatives
wave/T FromAtom = root:FromAtom   //name list of the first atom per bond
wave/T ToAtom = root:ToAtom   //name list of the second atom per bond
wave dircos = root:dircos   //direction cosines of the bonds
wave dist = root:dist   //length of the bonds
wave distBrav = root:distBrav   //length of the bonds (in Bravais lattice
                                     // vector units)
make/D/O/N=3 rho
variable MassTo=1
variable MassFrom=1


variable TiMass = 47.88*1.66*10^(-27) * 10^(-20) / (1.602*10^(-19))
// mass of Ti atom (in J s^2/m^2)
variable SeMass = 78.96*1.66*10^(-27) * 10^(-20) / (1.602*10^(-19))
// mass of Se atom (in J s^2/m^2)
variable StarMass = TiMass + 2/9*SeMass  //weighted combined mass
Make/O/N=(BasisSize) W_eigenvalues
Make/O/N=(BasisSize,BasisSize) M_R_eigenVectors
make/D/O/N=1 M_product

Make/D/O/N=(BasisSize,BasisSize)/C HamiltonianO
Make/D/O/N=(BasisSize,BasisSize)/C HamiltonianS
Make/D/O/N=(BasisSize,BasisSize)/C GabMatrix=0
Make/D/O/N=(BasisSize,BasisSize)/C GbaMatrix=0
variable/C Gabvalue=0
variable/C Gbavalue=0
variable/C resMatrix=0
variable wavefct=0

make/D/O/N=3 unitvect,polvect1,polvect2
variable mu,nu

variable ki,kj,kk
variable kimax=nbsteps
variable kjmax=nbsteps
variable kkmax=nbsteps
variable nbkpts=nbsteps*nbsteps*nbsteps
```

```
        variable renorm
        variable weight=1

        //loops for k-integration over the irreducible unit cell
        for(ki=0;ki<=kimax;ki=ki+1)
        for(kj=0;kj<=kjmax;kj=kj+1)
        for(kk=0;kk<=kkmax;kk=kk+1)

                //components of the k-wave vector for the k-integration
                kx=bint[0][0]*(ki)/(kimax+1) + bint[1][0]*(kj)/(kjmax+1)
+ bint[2][0]*(kk)/(kkmax+1)
                ky=bint[0][1]*(ki)/(kimax+1) + bint[1][1]*(kj)/(kjmax+1)
+ bint[2][1]*(kk)/(kkmax+1)
                kz=bint[0][2]*(ki)/(kimax+1) + bint[1][2]*(kj)/(kjmax+1)
+ bint[2][2]*(kk)/(kkmax+1)

                //weights for k-points at the border of the integration zone
                weight=kweight(ki,kj,kk)

                //loops over the orbital types
                i=0
                do
                j=0
                do
                BAtomR=BasisAtom[i]
                BAtomC=BasisAtom[j]
                BOrbitalR=BasisOrbital[i]
                BOrbitalC=BasisOrbital[j]

                //loop over the bond list
                u=0
                do

                FromString=(FromAtom[u])[0,2]
                ToString=(ToAtom[u])[0,2]

                If(stringmatch(BAtomR,FromString))
                If(stringmatch(BAtomC,ToString))

                //identification of each atom implied in the bond and
                //attribution of its mass
                if(stringmatch(FromString,BasisAtom[0]))
                        mu=1
                        MassFrom=TiMass
                elseif(stringmatch(FromString,BasisAtom[5]))
                        mu=2
                        MassFrom=SeMass
                else
                        mu=3
                        MassFrom=SeMass
                endif
                if(stringmatch(ToString,BasisAtom[0]))
                        nu=1
                        MassTo=TiMass
                elseif(stringmatch(ToString,BasisAtom[5]))
                        nu=2
                        MassTo=SeMass
                else
                        nu=3
                        MassTo=SeMass
                endif

                //direction cosines
                l=dircos[u][0]
                m=dircos[u][1]
                n=dircos[u][2]
                d=dist[u][3]
                unitvect={l,m,n}

                //calculation of the directed bond (R_l   R_l )
```

```
                rho[0]=distBrav[u][0]*a[0][0]+distBrav[u][1]*a[1][0]
+distBrav[u][2]*a[2][0]
                rho[1]=distBrav[u][0]*a[0][1]+distBrav[u][1]*a[1][1]
+distBrav[u][2]*a[2][1]
                rho[2]=distBrav[u][0]*a[0][2]+distBrav[u][1]*a[1][2]
+distBrav[u][2]*a[2][2]

                //calculation of the two-center integral derivatives
                //for the electron-phonon couplings

                //transfer integral contribution
                OverlapReturn=OverlapS(BOrbitalR,BOrbitalC,l,m,n,d,"derivative")

                //direction cosine contribution
                OverlapCosDerivS(BOrbitalR,BOrbitalC,l,m,n,d,"orthogonal"
                                                    ,OverlapVect)

                //calculation of the transverse polarization vectors
                PolarizVector(polvect1,wvector,mu,0)
                PolarizVector(polvect2,wvector,nu,0)

                //calculation of electon-phonon coupling: g_ab and g_ba
                Gabvalue = 1/sqrt(MassFrom) * (OverlapReturn
* ScalarProd(unitvect,polvect1) + ScalarProd(OverlapVect,polvect1))
*Exp(cmplx(0,1)*(rho[0]*wvector[0]+rho[1]*wvector[1]+rho[2]*wvector[2]))
- 1/sqrt(MassTo) * (OverlapReturn * ScalarProd(unitvect,polvect2)
+ ScalarProd(OverlapVect,polvect2))
                Gbavalue = 1/sqrt(MassFrom) * (OverlapReturn
* ScalarProd(unitvect,polvect1) + ScalarProd(OverlapVect,polvect1))
*Exp(cmplx(0,1)*(rho[0]*wvector[0]+rho[1]*wvector[1]+rho[2]*wvector[2]))
- 1/sqrt(MassTo) * (OverlapReturn * ScalarProd(unitvect,polvect2)
+ ScalarProd(OverlapVect,polvect2))

                GabMatrix[i][j]=GabMatrix[i][j] + Gabvalue * Exp(-cmplx(0,1)
*(kx*rho[0]+ky*rho[1]+kz*rho[2]))
                GbaMatrix[i][j]=GbaMatrix[i][j] + Gabvalue * Exp(-cmplx(0,1)
*((kx+wvector[0])*rho[0]+(ky+wvector[1])*rho[1]+(kz+wvector[2])*rho[2]))

                endif
                endif


                If(stringmatch(BAtomR,FromString))
                        If(stringmatch(BAtomC,ToString))
                          l=dircos[u][0]
                                m=dircos[u][1]
                                n=dircos[u][2]
                                d=dist[u][3]

                                //calculation of the two-center integrals for
                //building the Hamiltonian to obtain their eigenvectors
                OverlapReturn=OverlapS(BOrbitalR,BOrbitalC,l,m,n,d,"orthogonal")

                                //building the Hamiltonians
                                HamiltonianO[i][j]=HamiltonianO[i][j]
+OverlapReturn*Exp(cmplx(0,1)*(kx*dist[u][0]+ky*dist[u][1]+kz*dist[u][2]))
                                HamiltonianS[i][j]=HamiltonianS[i][j]
+OverlapReturn*Exp(cmplx(0,1)*((kx+wvector[0])*dist[u][0]
+(ky+wvector[1])*dist[u][1]+(kz+wvector[2])*dist[u][2]))
                        endif
                endif

                u=u+1
                while(u<Nbond)
                //end of the bond loop

                j=j+1
                while(j<BasisSize)
                i=i+1
                while(i<BasisSize)
                //end of the orbital loops
```

```
223                  //calculation of the exciton wave function
                     wavefct = 4/sqrt(2*pi)*(alpha)^(3/2)*1/((kx^2+ky^2+kz^2)
+ alpha^2)^2

                     //calculation of the eigenvectors of the TB Hamiltonian
228                  MatrixEigenV/R/X/B=0 HamiltonianO
                     Make/O/N=(BasisSize) bandsort,bandkey
                     bandsort=real(W_eigenValues)
                     makeindex bandsort,bandkey
                     duplicate/O/R=[][bandkey[5],bandkey[5]] M_R_eigenVectors EVO5
233                  duplicate/O/R=[][bandkey[6],bandkey[6]] M_R_eigenVectors EVO6

                     MatrixEigenV/R/X/B=0 HamiltonianS
                     Make/O/N=(BasisSize) bandsort,bandkey
                     bandsort=real(W_eigenValues)
238                  makeindex bandsort,bandkey
                     duplicate/O/R=[][bandkey[5],bandkey[5]] M_R_eigenVectors EVS5
                     duplicate/O/R=[][bandkey[6],bandkey[6]] M_R_eigenVectors EVS6

                     //multiplication of the TB Hamiltonian with its eigenvectors
243                  duplicate/O EVO5 EVO5H
                     matrixtranspose/H EVO5H
                     matrixmultiply EVO5H,GabMatrix,EVS6

                     resMatrix = resMatrix + M_product*wavefct*weight
248
                     duplicate/O EVS6 EVS6H
                     matrixtranspose/H EVS6H
                     matrixtranspose GbaMatrix
                     matrixmultiply EVS6H,GbaMatrix,EVO5
253
                     resMatrix = resMatrix + M_product*wavefct*weight


                     GabMatrix=0
258                  GbaMatrix=0
                     HamiltonianO=0
                     HamiltonianS=0

                     knb=knb+1
263          endfor
             endfor
             endfor
             //end of the k-loop for k-integration

268          //multiplication by the order parameter and the inverse of the average
             //of the Coulomb potential times the exciton wave function
             renorm = orderparam/ExcDensity(screenlen,alpha,meff)
             resMatrix *=  renorm

273          //renormalization of the integral by the integration step (to ensure
             //conversion from sum to integral) for a trigonal unit cell
             resMatrix *= cos(pi/6)* sqrt(bint[0][0]^2+bint[0][1]^2+bint[0][2]^2)*
sqrt(bint[1][0]^2+bint[1][1]^2+bint[1][2]^2)*sqrt(bint[2][0]^2+bint[2][1]^2
+bint[2][2]^2)/((nbsteps+1)^3) * 6
278          //factor 6: to cover the whole BZ from the irreducible BZ


             variable phononfreq=1*10^12
             variable/C Qvalue = resMatrix/(phononfreq)^2
283          // P/w^2 value for a unit frequency in THz

             //print the atomic displacement of Ti atoms
             print "for a phonon frequency of 1 THz:"
             print " displ. for Ti  (Angstroems) real "
288  + num2str(real(Qvalue)*1/sqrt(StarMass)) + " and imag "
     + num2str(imag(Qvalue)*1/sqrt(StarMass))

     end
```

# Appendix B

# Electronic structure calculations

## B.1 A short introduction to LCAO

Originally proposed by Bloch [128], the LCAO method consists in expressing the wave function of an electron in a crystal as a linear combination of atomic orbitals located on the various atoms of the crystal. An atomic orbital centered on an atom at position $\vec{\tau}_\mu + \vec{R}_l$ can be written like $\phi_\alpha^{(\mu)}(\vec{r} - \vec{R}_l)$, where $\alpha$ represents the different quantum numbers and $\mu$ refers to the position $\vec{\tau}_\mu$ of the atom $\mu$ in the unit cell situated at the site $\vec{R}_l$ of the Bravais lattice. Then, a Bloch sum of these localized orbitals, namely

$$\varphi_{\alpha\vec{k}}^{(\mu)}(\vec{r}) = \sum_l \mathrm{e}^{i\vec{k}\cdot\vec{R}_l}\phi_\alpha^{(\mu)}(\vec{r} - \vec{R}_l), \tag{B.1}$$

describes a delocalized state, which respects the translational symmetry of the crystal. The sum here is performed over all the equivalent atomic positions in the crystal. Such a Bloch sum can be done for every type of orbitals of each inequivalent atom in the crystal. At this stage, the orbital wave functions $\phi_\alpha^{(\mu)}$ centered on different atoms are not orthogonal to each other (but this is the case for orbitals $\phi_\alpha^{(\mu)}$ sitting on the same atom). Then, the eigenstates of the Hamiltonian of our crystal $H$ may be written as a linear combination of different $\varphi_{\alpha\vec{k}}^{(\mu)}$, combining all the different orbitals $\alpha$ of all the different inequivalent atoms $\mu$.

The Hamiltonian of our crystal contains a kinetic part and a periodic potential $V$, which is approximately a summation of spherical potentials located on all the atoms of our crystal. Therefore, in the worst case, the matrix elements

$$\int d^3r \varphi_{\alpha\vec{k}}^{(\mu)}(\vec{r})V(\vec{r} - \vec{R}_{l''})\varphi_{\beta\vec{k}}^{(\nu)}(\vec{r}) \propto \int d^3r \phi_\alpha^{(\mu)}(\vec{r} - \vec{R}_l)V(\vec{r} - \vec{R}_{l''})\phi_\beta^{(\nu)}(\vec{r} - \vec{R}_{l'})$$

involve two wave functions and one potential centered at three different positions $\vec{R}_l$, $\vec{R}_{l'}$, $\vec{R}_{l''}$. Such integrals are called three-center integrals. It is now clear that performing a rigorous calculation with this LCAO method represents a desperate challenge.

To improve this situation, Slater and Koster proposed a few simplifications, reorientating slightly the LCAO method [115]. First of all, they appealed to the method of Loewdin [129], replacing therefore the wave functions $\phi_\alpha^{(\mu)}$ by orthogonal wave functions $\psi_\alpha^{(\mu)}$ in

the Bloch sums B.1, so that

$$\Psi^{(\mu)}_{\alpha\vec{k}}(\vec{r}) = \frac{1}{\sqrt{N}} \sum_l \mathrm{e}^{i\vec{k}\cdot\vec{R}_l} \psi^{(\mu)}_\alpha(\vec{r} - \vec{R}_l). \tag{B.2}$$

As mentionned above, the general wave function we are looking for is then a linear combination of such Bloch sums

$$\Psi_{\vec{k}}(\vec{r}) = \sum_{\alpha\mu} c_{\alpha\mu}(\vec{k}) \Psi^{(\mu)}_{\alpha\vec{k}}(\vec{r}), \tag{B.3}$$

whose coefficients $c_{\alpha\mu}(\vec{k})$ will be determined by solving the secular problem

$$\begin{aligned} H\Psi_{\vec{k}}(\vec{r}) &= E_{\vec{k}}\Psi_{\vec{k}}(\vec{r}) \\ \Leftrightarrow \quad \sum_{\alpha\mu} c_{\alpha\mu}(\vec{k}) H\Psi^{(\mu)}_{\alpha\vec{k}}(\vec{r}) &= \sum_{\alpha\mu} c_{\alpha\mu}(\vec{k}) E_{\vec{k}} \Psi^{(\mu)}_{\alpha\vec{k}}(\vec{r}) \end{aligned}$$

for each $\vec{k}$ point. The matrix elements between two Bloch sums, for the Hamiltonian $H$, look like

$$\begin{aligned} \frac{1}{N} \sum_{ll'} \mathrm{e}^{i\vec{k}\cdot(\vec{R}_{l'} - \vec{R}_l)} \int d^3r \; \psi^{(\mu)*}_\alpha(\vec{r} - \vec{R}_{l'}) H \quad \psi^{(\nu)}_\beta(\vec{r} - \vec{R}_l) \quad = \\ \sum_l \mathrm{e}^{i\vec{k}\cdot(\vec{R}_{l'} - \vec{R}_l)} \int d^3r \quad \psi^{(\mu)*}_\alpha(\vec{r} - \vec{R}_{l'}) \quad H\psi^{(\nu)}_\beta(\vec{r} - \vec{R}_l). \end{aligned}$$

One of the sums could be cancelled with the $1/N$ factor, because it effectively multiplies the whole by $N$ due to the translational symmetry of the Bravais lattice. Such matrix elements represent the interaction of orbitals located at a distance $|\vec{R}_l - \vec{R}_{l'}|$ apart. Due to the localized nature of the orbitals $\psi^{(\mu)}_\alpha$, it is reasonable to think that these matrix elements will become smaller as this distance increases. Therefore, a first simplification consists in truncating the sum over $\vec{R}_l$ so that only the nearest neighours are considered in the interaction.

A second simplification is not to keep all the atomic orbitals related to the atoms in the crystal, but to choose only those which are concerned by the energy scale of the calculation.

We have mentionned previously that up to three different positions $\vec{R}_l$ may be involved in the matrix elements, leading to three-center integrals. As a third simplification, one neglects such contributions and focus on two-center integrals. This means that in the interaction part of $H$ made of a sum of spherical potentials, we retain only sums including those potentials which are located on one of the two atoms in interaction. Therefore, these two-center integrals are similar to those found in a diatomic molecule, the vector $\rho := \vec{R}_l - \vec{R}_{l'}$ being the directed distance between the two atoms. It is then advantageous to decompose orbitals in $\pi$, $\sigma$ and $\delta$ symmetries (these symbols refer to the component of the angular momentum around $\rho$), depending on their nature and their orientation with respect to $\rho$. Due to symmetry reasons, only matrix elements involving orbitals of the same angular projection are different than zero.

This last consideration, together with the fact that only the nearest neighbours interactions are dominant, reduces considerably the amount of orbital combinations to be considered in the matrix element computations and thus an exhaustive counting is made

possible. Slater and Koster defined two-center energy integrals like (with a slightly different notation)

$$J_{\alpha\beta}(\vec{R}_l + \vec{\tau}_\mu - \vec{R}_{l'} - \vec{\tau}_\nu) = \int d^3r\ \psi_\alpha^{(\mu)*}(\vec{r} - \vec{R}_{l'}) H \psi_\beta^{(\nu)}(\vec{r} - \vec{R}_l).$$

For every combination of $s$, $p$ and $d$ orbitals, they calculated the decomposition of $J_{\alpha\beta}$ in terms of basic elements $t(\alpha\mu\ \beta\nu\ \xi)$, called the transfer integrals, weighted by the cosine directors $a, b, c$ of the vector $\rho$ to account for the orientation of the original orbitals. A transfer integral represents a matrix element between an orbital $\psi_\alpha^{(\mu)}$ and an orbital $\psi_\beta^{(\nu)}$ having a bond symmetry $\xi$ ($\xi = \sigma, \pi, \delta$). To illustrate this decomposition, we consider the case in which $\psi_\alpha^{(\mu)}$ is a $p_x$ wave function on an atom at position $\vec{r}_1$ and $\psi_\beta^{(\nu)}$ is a $p_y$ wave function on an atom at position $\vec{r}_2$. Then, their (two center) energy integral is $J_{\alpha\beta}(\vec{r}_1 - \vec{r}_2) = ab\ t(pp\sigma) - ab\ t(pp\pi)$ [115]. We see that this energy integral for $p$-type orbitals decomposes into the bond symmetries $\sigma$ and $\pi$, so that two parameters $t(pp\sigma)$ and $t(pp\pi)$ should be really calculated. These parameters will be also used for other $p-p$ energy integrals. One should realize that the transfer integrals $t(\alpha\mu\ \beta\nu\ \xi)$ are functions of the distance between atoms, so that for nearest neighbours and for second-nearest neighbours for example, they are different and should be distinguished. This is usually indicated by a subscript, like $t(pp\sigma)_1$, $t(pp\sigma)_2$.

With these two-center energy integrals, a Hamiltonian can be built in second quantization on the basis of the LCAO wave functions $\Psi_{\vec{k}}(\vec{r})$ by converting the coefficients $c_{\alpha\mu}(\vec{k})$ appearing in equation B.3 into fermionic operators

$$\begin{aligned} H &= \sum_{\vec{k}} \sum_{\alpha\beta} \sum_{\mu\nu} \sum_{ll'} \mathrm{e}^{i\vec{k}\cdot(\vec{R}_{l'} - \vec{R}_l)} \int d^3r\ \psi_\alpha^{(\mu)*}(\vec{r} - \vec{R}_{l'}) H \psi_\beta^{(\nu)}(\vec{r} - \vec{R}_l)\ c_{\alpha\mu}^\dagger(\vec{k}) c_{\beta\nu}(\vec{k}) \\ &= \sum_{\vec{k}} \sum_{\alpha\beta} \sum_{\mu\nu} \underbrace{\sum_{ll'} \mathrm{e}^{i\vec{k}\cdot(\vec{R}_{l'} - \vec{R}_l)} J_{\alpha\beta}(\vec{R}_l + \vec{\tau}_\mu - \vec{R}_{l'} - \vec{\tau}_\nu)}_{=J_{\alpha\beta,\mu\nu}(\vec{k})}\ c_{\alpha\mu}^\dagger(\vec{k}) c_{\beta\nu}(\vec{k}) \end{aligned} \tag{B.4}$$

(we appealed to the translation symmetry of the system to cancel one sum over $\vec{k}\,'$ due to $\vec{k} = \vec{k}\,'$). For every $\vec{k}$, the matrix $J_{\alpha\beta,\mu\nu}(\vec{k})$, called the transfer matrix, can be diagonalized into the matrix $\varepsilon_{nn'}(\vec{k})\delta_{n,n'} \equiv \varepsilon_n(\vec{k})$ by the eigenvector $T_{\alpha\mu,n}(\vec{k})$ leading to

$$\begin{aligned} H &= \sum_{n\vec{k}} \varepsilon_n(\vec{k}) \sum_{\alpha\beta} \sum_{\mu\nu} T_{\alpha\mu,n}^*(\vec{k}) c_{\alpha\mu}^\dagger(\vec{k}) T_{\beta\nu,n}(\vec{k}) c_{\beta\nu}(\vec{k}) \\ &= \sum_{n\vec{k}} \varepsilon_n(\vec{k}) c_n^\dagger(\vec{k}) c_n(\vec{k}). \end{aligned}$$

Here new fermionic operators have been defined $c_n(\vec{k}) = \sum_{\beta\nu} T_{\beta\nu,n}(\vec{k}) c_{\beta\nu}(\vec{k})$ for the diagonal matrix $\varepsilon_n(\vec{k})$. We immediately recognize the band dispersions $\varepsilon_n(\vec{k})$, labelled by the band index[a] $n$.

Finally, with this last discussion, we see that a finite and relatively small amount of transfer integrals $t(\alpha\mu\ \beta\nu\ \xi)$ is necessary for a tight-binding calculation. For the particular case of the near-$E_F$ band structure of $1T$-$TiSe_2$, the three $p$-orbitals of the

[a]This band index $n$ has the same size than the total number of orbitals in the system $\alpha\mu$, ensuring that each atomic orbital converts into a band after the LCAO.

two inequivalent Se atoms and the five $d$-orbitals of the Ti atoms should be considered. This results in 11 different Bloch sums $\Psi^{(\mu)}_{\alpha\vec{k}}$ (here $\mu = \mathrm{Se}_1, \mathrm{Se}_2, \mathrm{Ti}$ and $\alpha = p_x, p_y, p_z, d_{xy}, d_{xz}, d_{yz}, d_{x^2-y^2}, d_{3z^2-r^2}$). The LCAO wave function B.3 is then a linear combination of these 11 Bloch sums, giving rise to a $(11 \times 11)$ matrix $\langle \Psi_{\vec{k}}(\vec{r})|H|\Psi_{\vec{k}}(\vec{r})\rangle$. Considering only the nearest neighbour interactions, the energy integrals involved in this matrix can be decomposed into seven transfer integrals: $t(pp\sigma)$, $t(pp\pi)$, $t(dd\sigma)$, $t(dd\pi)$, $t(dd\delta)$, $t(pd\sigma)$ and $t(pd\pi)$. Three more terms are needed, $\varepsilon_p, \varepsilon_{d\epsilon}, \varepsilon_{d\gamma}$, which appear in the diagonal elements of the matrix $J_{\alpha\alpha}(0)$. They represent the energy of the atomic levels (the $d$ atomic level is separated in two to take into account the crystal field splitting). This makes a total of 14 parameters needed to compute this near-$E_F$ band structure and brings us to the fourth simplification of Slater and Koster. As computing directly these 14 parameters is complicated and demands an exact knowledge of the atomic orbitals, this LCAO method can be used in a different way. The LCAO band structure can be fitted to a band structure measured or calculated with an *ab initio* method, so that these 14 parameters are used like fitting parameters. This is what we will do in section 7.1 for the case of $1T$-$TiSe_2$.

## B.2 Principles of DFT

In the previous section, we have emphasized that the LCAO method could be used to produce a trial band structure, which should be fitted on another band structure, for instance calculated with an *ab initio* method. This would permit to obtain the transfer integrals $t(n\mu\ n'\nu\ \alpha)$ for every type of molecular bonding involved in the system investigated. In this section, we will shortly describe an *ab initio* method, the DFT, which will be used to compute the reference band structure needed to obtain the transfer integrals for $1T$-$TiSe_2$. We follow the introduction to DFT of Cottenier [130].

First of all, DFT focusses on the electronic degrees of freedom and does not consider any movement of the nuclei in the lattice, relying on the Born-Oppenheimer approximation. In other words, the underlying lattice is reduced to a given source of positive charge, working like an external potential $V_{ext}$. The Hamiltonian of the electron gas in this lattice potential is then

$$H = T + V + V_{ext},$$

where $T$ is the the kinetic energy of the electrons and $V$ represents the electron-electron interactions. This is in general a very difficult problem to solve, specific to the lattice potential $V_{ext}$.

DFT is based on a seminal work of Hohenberg and Kohn, where it is proven that there is a one-to-one correspondence between the ground state density $\rho(\vec{r})$ of the many-body system and $V_{ext}$ (in the Hamiltonian above, the $T + V$ is general to any system) [131]. It implies that all observable quantities can be retrieved from the density only, so that they can be written as functionals of the density. In other words, the wave function of the whole electronic system, containing $3N$ variables, can be replaced by the electronic density, which is a function of only 3 variables!

As a consequence, the total energy can be written as a functional of the electronic density

$$E[\rho] = \langle\Psi|H|\Psi\rangle = \underbrace{\langle\Psi|T+V|\Psi\rangle}_{=F_{HK}[\rho]} + \int d^3r\ \rho(\vec{r})V_{ext}. \tag{B.5}$$

Knowing the ground state density $\rho$, the contribution of $V_{ext}$ to the ground state energy can be easily computed. However, an explicit formula for the Hohenberg-Kohn functional $F_{HK}$, which is universal for any electron gas, is not known.

We now turn to the Kohn-Sham equations, which propose an approximate way of determining $F_{HK}$ [132]. By comparing equation B.5 with that of the Hartree-Fock approximation, a formulation of $F_{HK}$ is obtained

$$F_{HK}[\rho] = T_0[\rho] + V_H[\rho] + \underbrace{V_x[\rho] + V_c[\rho]}_{V_{xc}[\rho]}.$$

Here $T_0$ is a functional for the kinetic energy of a non-interacting electron gas, $V_H$ stands for the Hartree contribution, $V_x$ is the (exchange) Fock contribution and $V_c$ is the correlation functional, which contains all the contributions beyond the Hartree-Fock approach and tuhs all the difficulties. Replacing this Hohenberg-Kohn functional in the functional energy B.5 leads to

$$E[\rho] = T_0[\rho] + V_H[\rho] + V_{xc}[\rho] + V_{ext}[\rho].$$

The idea of the DFT is now to interpret this equation as the energy functional of a *non-interacting* electron gas, subject to the potential of the lattice $V_{ext}$ and to the exchange and correlation potential $V_{xc}$. The corresponding Kohn-Sham Hamiltonian is then

$$H_{KS} = T_0 + V_H + V_{xc} + V_{ext} = -\frac{\hbar^2}{2m_e}\nabla^2 + \frac{e^2}{4\pi\epsilon_0}\int d^3r'\ \frac{\rho(\vec{r}\,')}{|\vec{r}-\vec{r}\,'|} + \frac{\delta V_{xc}[\rho]}{\delta\rho} + V_{ext}.$$

The exact ground state density $\rho(\vec{r}) = \sum_i |\phi_i(\vec{r})|^2$ is obtained after that the $N$ single-particle wave functions $\phi_i$ have been calculated from the eigenvalue equations

$$H_{KS}\phi_i = \varepsilon_i\phi_i. \tag{B.6}$$

These single-particle wave functions $\phi_i$ are determined from potentials appearing in a non-interacting Schroedinger-like equation. This is the great advantage of the DFT. However, there are two major drawbacks.

1. All the difficulties of the correlation energy in the interacting electron gas are hidden in the potential $V_{xc}$. No exact form of this potential is known. One solution is to use the LDA. In this approximation, the complicated $V_{xc}$ is replaced by that of an homogeneous electron gas (which can be calculated exactly) and is made position dependent. This potential is local, since its value at a particular position is a function of the electronic density at that position only. LDA is then an approximation to the exact DFT described above.

2. The second problem is more technical. The single-particle wave functions $\phi_i$ are solution of equation B.6, where the potentials appearing in $H_{KS}$ depend on the electronic density which is a function of all the $\phi_i$. This is therefore a *self-consistent* problem, which is solved in practice iteratively until convergence is reached.

There are many programs implementing this DFT method within the LDA. For our purposes, we have chosen the Wien2k package [56]. In practice, the numerical solutions to the Kohn-Sham Hamiltonian B.6 are expanded in a finite set of basis functions. In the Wien2k program, the unit cell of the crystal is divided into non-overlapping muffin-tin spheres centered on the atoms and an interstitial region. In the interstitial region, the basis functions are plane-waves, but in the muffin-tin sphere, where the proximity of the nucleus may induce large oscillations of the wave function, a linear combination of spherical harmonics is used. Matching these two different sets of basis functions at the boundary between the muffin tin spheres and the interstitial region ensures a well-behaved solution to the Kohn-Sham problem. More technical details can be found in reference [130] and in the manual of the Wien2k program [56].

# Appendix C

# Investigation of the near-surface atomic structure of $Na_1CoO_2$

In this appendix, we present both a new material, $Na_xCoO_2$, and a photoemission diffraction technique, XPD. The reasons for separating this discussion from the rest of the thesis are not only that this work has nothing to do with the exciton condensate phase and $1T$-$TiSe_2$, but also that it came to a dead end.

## C.1 Introduction to the x-ray photoelectron diffraction technique

In this section, we introduce the XPD technique, which is devoted to the determination of the atomic structure of crystals near their surface, due to the limited mean free path of the photoelectrons. It relies on the diffraction process of the outgoing photoelectron, which can be described by a conventional scattering theory.

For presenting a simplified theory, we follow the description of reference [134] and we consider the case of a single scattering event for plane waves [133]. In that case, the

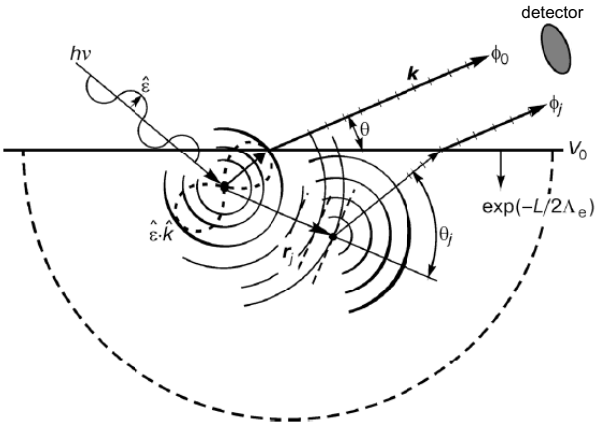


FIGURE C.1: Schematic picture of a single-scattering event for the photoelectron diffraction process (based on reference [133]).

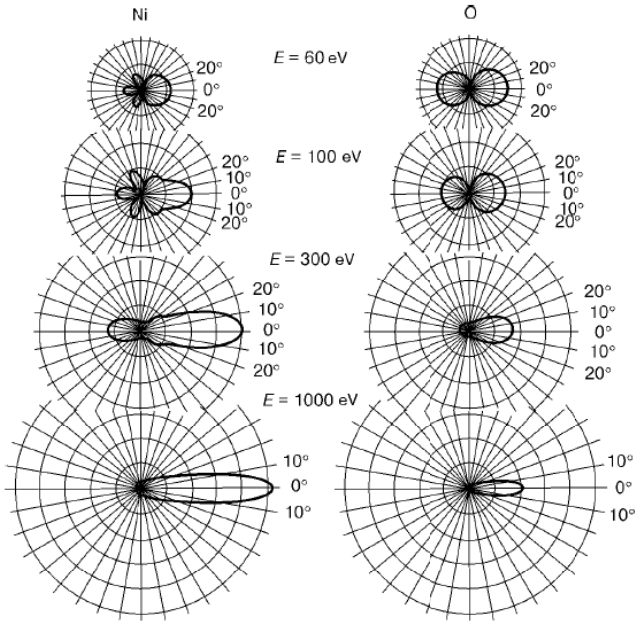


FIGURE C.2: Angular distribution of the electron scattering amplitude $|f_j(\theta_j)|$ on Ni and O atomic chains for different electron kinetic energies. The angle $\theta = 0^\circ$ corresponds to the direction of the nearest neighbour (from reference [136]).

photoemission intensity $I(\vec{k})$ reaching the detector under a direction given by the wave vector $\vec{k}$ is the result of the interference of the unscattered photoelectron wave function $\phi_0$ with the wave functions $\phi_j$ of the photoelectron scattered on atoms at position $\vec{r}_j$

$$I(\vec{k}) \propto |\phi_0 + \sum_j \phi_j|^2. \tag{C.1}$$

For the case of electrons in an initial $s$-state, this formula can be elaborated to

$$I(\vec{k}) \propto \left| (\vec{\varepsilon} \cdot \hat{\vec{k}}) + \sum_j \left( \frac{\vec{\varepsilon} \cdot \hat{\vec{r}}_j}{r_j} \right) |f_j(\theta_j)| \mathrm{e}^{i[kr_j(1-\cos\theta_j)+\varphi_j(\theta_j)]} \right|^2 \tag{C.2}$$

(here no temperature and no inelastic scattering effects are taken into account) [135]. The corresponding situation is schematized in Fig. C.1. The incident light of energy $h\nu$ and polarization $\vec{\varepsilon}$excites electrons through photoemission, whose dipole matrix element is proportional to $\vec{\varepsilon} \cdot \hat{\vec{k}}$ for the unscattered wave and to $\vec{\varepsilon} \cdot \hat{\vec{r}}_j$ for the scattered one. The complex factor $f_j(\theta_j) = |f_j(\theta_j)| \exp[i\varphi_j(\theta_j)]$, where $\theta_j$ is the angle at which the scattered photoelectron escapes, contains the information on the atomic scattering of the initial electron wave $\phi_0$.

Van Hove *et al.* have calculated the angular distribution of the electron scattering amplitude $|f_j(\theta_j)|$ on Ni and O atoms for different electron kinetic energies [136]. Their results are shown in Fig. C.1. At higher kinetic energies, approximatively for $E_{kin} > 500$ eV, the electron scattering amplitude is focussed towards the nearest neighbour. This phenomenon, called *forward focussing*, is essential to the XPD technique, since it ensures that the spots of highest intensities corresponds to nearest neighbour directions in the

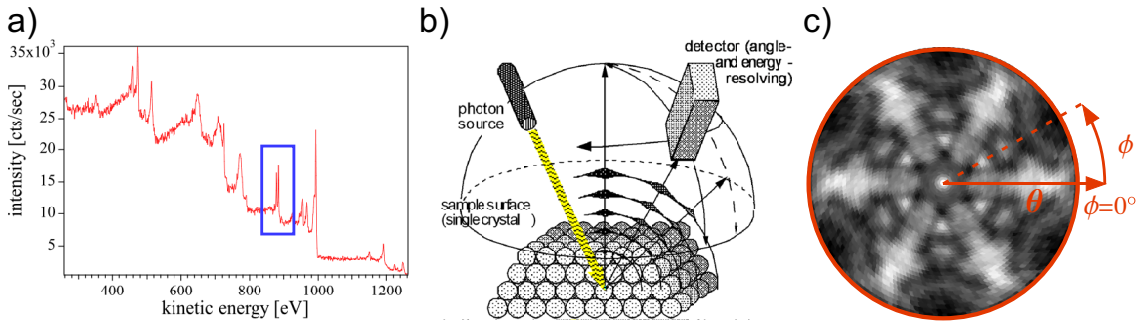


FIGURE C.3: A typical XPD procedure. (a) XPS spectrum from $Na_1CoO_2$, using a Mg K$\alpha$ anode ($h\nu = 1253.6$ eV). The Co2$p$ peak is highlighted. (b) Schematic view of a photoemission intensity measurement on the full hemisphere above the sample. (c) XPD diffractogram of $Na_1CoO_2$ taken at the binding energy of the Co2$p$ core-level.

near-surface atomic structure of the probed system. As a consequence, the photoemission intensity pattern reflects the geometry of the local environment of the photoelectron emitter [a].

Due to the necessity of having photoelectrons with high kinetic energies, the XPD technique, as indicated by its name, is usually performed using an X-ray tube as the light source for photoemission. Conventional x-ray tubes typically deliver light at energies of 1200 eV to 1500 eV (see section 2.2), so that core electrons, which are dispersionless states, are mainly probed.

A standard procedure for an XPD measurement is shown in Fig. C.3. First an XPS spectrum is recorded, which displays distinct peaks for the different core electrons of each atom species in the studied sample. Graph C.3 (a) shows a typical XPS spectrum for $Na_1CoO_2$ obtained with a Mg K$\alpha$ anode ($h\nu = 1253.6$ eV). Each of these peaks can be attributed to a particular core-level of a given atom using XPS data tables (see for instance reference [139]). Therefore, selecting the binding energy of a particular peak on the XPS spectrum permits to selecting a particular type of emitter for XPD. The photoemission intensity at this binding energy is then recorded as a function of the polar and azimuthal angles $\theta$ and $\phi$, as shown in Fig. C.3 (b). The measured intensity pattern is then projected stereographically, giving rise to a XPD diffractogram like that of in Fig. C.3 (c). This diffractogram has been taken at the binding energy of the Co2$p$ core-level, reflecting therefore the local environment of Co atoms near the surface of the crystal.

[a] However, when multiple scattering events are also considered in the diffraction process, the interpretation of the photoemission intensity pattern becomes more difficult, since forward focussing are weakened and new intensity features appear [137, 138].

## C.2 Strong surface effects revealed in $Na_xCoO_2$ by x-ray photoelectron diffraction

C. Monney[1], L. Despont[1], C. Battaglia[1], H. Cercellier[1], M. G. Garnier[1], K. Conder[2], E. Pomjakushina[2,3], J. Mesot[3] and P. Aebi[1],

[1] *Institut de Physique, Université de Neuchâtel, CH-2000 Neuchâtel, Switzerland*

[2] *Laboratory for Developments and Methods, PSI, 5232 Villigen, Switzerland*

[3] *Laboratory for Neutron Scattering, ETHZ & PSI, 5232 Villigen, Switzerland*

Unpublished

X-ray photoelectron diffraction measurements have been performed on $Na_xCoO_2$ with "$x_{bulk} \cong 1$" ($\alpha$-phase) at room temperature to study the atomic structure near the surface. Data are compared with single scattering simulations based on the $P6_3/mmc$ and the $R\bar{3}m$ unit cells which are bulk atomic structures proposed in the literature for different dopings $x$. We are able to discard the $R\bar{3}m$ symmetry and to validate the $P6_3/mmc$ symmetry for surface unit cells. This is in contradiction with bulk measurements, revealing a drastic change in the surface structure. Moreover, further analysis suggests a Na doping at the surface of $x_{surf} \cong 0.8$.

The recent discovery of superconductivity in hydrated sodium doped cobaltates $Na_{0.35}CoO_2 \cdot 1.3H_2O$ at the critical temperature $T_C \simeq 5$K triggered a great interest on this compound [140]. Detailed transport measurments of Foo *et al.*[141] allowed to draw a rich phase diagram as a function of sodium content $x$. To get a deeper understanding of $Na_xCoO_2$ and its peculiars properties, bandstructure calculations were performed within the local density approximation (LDA) [142]. Many angle-resolved photoemission spectroscopy (ARPES) experiments were done at different dopings to map its electronic structure [143, 144, 145] but discrepancies concerning the Fermi surface reveal a fundamental problem in our understanding of the $Na_xCoO_2$ bandstructure. It is mainly attributed to three possible reasons : strong electronic correlations [146, 147], localisation by Na atom disorder [148] or surface effects. Therefore, different theoretical approaches to this problem were carried out, in particular to take into account strong correlations. However, this issue is today still under discussion. Moreover, the highly Na doping dependent sequence of phases rises the interesting question of the effect of Na atoms. In that sense, several experimental and theoretical studies [149, 150] address a possible order among Na atoms which are situated in the Van der Waals (VdW) gaps between $CoO_2$ layer (see Fig. 1).

In this work, we address experimentally the question of surface effects for the first time, using x-ray photoelectron diffraction (XPD). This issue is of great importance since in ARPES experiments measured photoelectrons are coming from the top atomic layers and consequently calculations based on atomic structures determined by bulk sensitive methods may fail to reproduce photoemission data. Recently, Liebsch and Ishida pointed out that electronic correlations do not explain the Fermi surface discrepancies and that more experimental work should be dedicated to the geometrical aspect of $Na_xCoO_2$ [153].

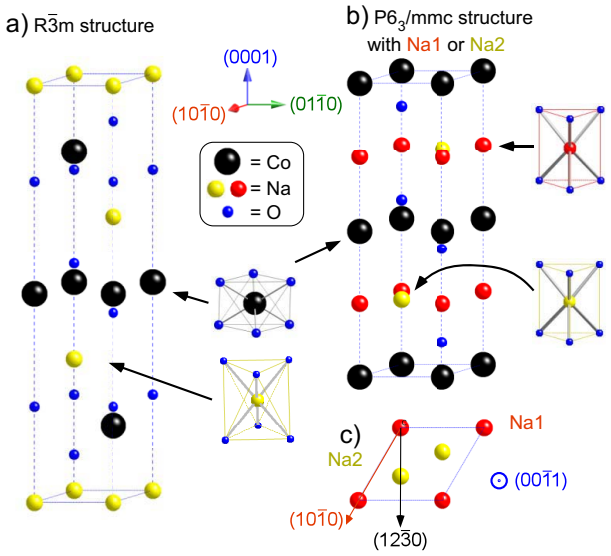


FIGURE C.4: (a) R$\bar{3}$m (with cell parameters $a = 2.889$ Å and $c = 15.600$ Å for $a \parallel (10\bar{1}0)$ and $c \parallel (0001)$) and (b) P6$_3$/mmc (with cell parameters $a = 2.883$ Å and $c = 10.492$ Å for $a \parallel (10\bar{1}0)$ and $c \parallel (0001)$) unit cells taken from ref.[151, 152] and used for SSC simulations. Atomic coordinations of Co, O and Na are shown next to their corresponding unit cell. (c) Below the P6$_3$/mmc unit cell figures a (0001) view of the Na1 and Na2 sites.

To date, the possibility that surface atomic layers suffer from drastic deviation from bulk symmetry or relaxation has not been explored. Moreover, the high mobility of Na atoms in the VdW gap strengthens this doubt, since cleavage of samples for ARPES could lead to uncontrolled desorption of Na atoms. Indeed, extensive x-ray and neutron diffraction studies determined the $Na_xCoO_2$ unit cell as a function of doping and revealed a strong dependence [151, 152, 154]. However, as previously indicated, the link with ARPES experiments, which are surface sensitive, is not straightforward. Therefore, we report XPD measurements on $Na_xCoO_2$ at $x_{bulk} \cong 1$ in the $\alpha-$phase and therefore of R$\bar{3}$m symmetry in the bulk, (for details of the different thermodynamic phases of $Na_xCoO_2$ see Ref.[151]) to provide structural information more appropriate to ARPES. We find that among unit cells proposed at high Na doping, we can discard the R$\bar{3}$m structure at the surface and we identify the P6$_3$/mmc structure (proposed for bulk crystals in the $\gamma$-phase) for near-surface atomic layers by comparing our XPD data with single scattering cluster (SSC) simulations. Consequently, we give evidence for strong surface effects. Furthermore, in the P6$_3$/mmc unit cell, Na atoms can occupy two inequivalent sites. A detailed analysis allows us to estimate the occupancy ratio of these two sites, from which, with help of results of Huang *et al.* [152], we infer in comparison with bulk measurements a Na concentration at surface of about $x_{surface} \cong 0.8 < x_{bulk}$.

Polycrystalline $Na_xCoO_2$ was prepared by a solid state reaction. Starting materials of $Na_2CO_3$ and $Co_3O_4$ with 99.99% purity were mixed and ground followed by heat treatment at 700-900 $^\circ$C in air, during at least 70h with several intermediate grindings. Phase purity of the compound was checked with conventional x-ray diffractometer (SIEMENS D500). The resulting powder was hydrostatically pressed in the form of rods (8 mm in diameter and 60 mm in length). The rods were subsequently sintered at 950 $^\circ$C during 20h. The crystal growth was carried out using optical floating zone furnace (FZ-T-10000-H-IV-VP-PC, Crystal System Corp., Japan) with four 300W halogen lamps as a

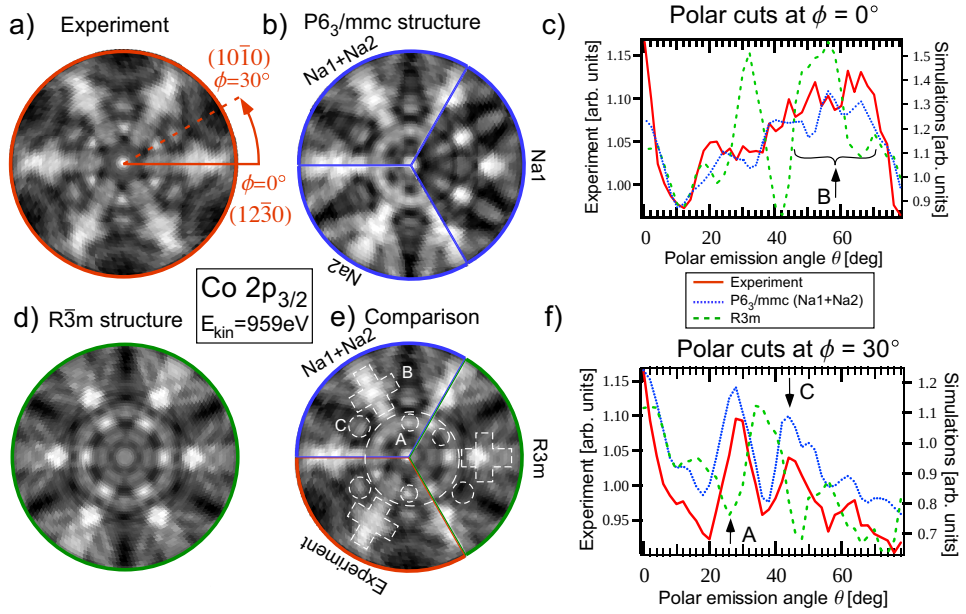


FIGURE C.5: Experimental and simulated data for Co2p$_{3/2}$ emission at $E_{kin}$ = 959 eV. (a) XPD measurements. (b) P6$_3$/mmc based SSC simulations for Na1, Na2 and Na1+Na2 (with the optimized ratio of 1:4) sites. (d) R$\bar{3}$m based SSC simulation. (e) Comparison between experiment and simulations. (c) and (f) display polar cuts along $\phi = 0^\circ$ and $\phi = 30^\circ$ respectively.

heat source. The growing conditions were the following: growth rate was 2 mm/h, both rods (feeding and seeding rod) were rotated at about 20 rpm in opposite directions to secure the liquid homogeneity, 7.5 bar pressure of argon with 20% of oxygen was applied during growing. The Na content was precisely determined to be $x_{bulk} = 0.98(1)$ by the energy dispersive x-ray method. After growth, samples were transferred *ex situ* to a modified Vacuum Generators ESCALAB Mk II photoelectron spectrometer, where they were cleaved parallel to the (0001) plane in a pressure of the order of $10^{-10}$ mbar and at room temperature. The XPD measurement system comprises a hemispherical energy analyzer with a three-channel detector, an x-ray photon source with two possible energies (1253.6 eV for Mg K$\alpha$ and 1740.0 eV for Si K$\alpha$) and a computer-controlled two-axis goniometer capable of rotating the photoelectron emission angle over the full hemisphere above the sample [155]. Briefly, after selecting a core-level emission line of a particular atom species in the x-ray photoemission spectrum, its intensity variation is recorded as a function of emission angle and stereographically projected (the resulting map is called diffractogram). For photoelectron kinetic energies approximatively above 500 eV, the photoelectron leaving the emitter is strongly focused in the direction of neighbouring atoms due to highly anisotropic angular distribution of its scattering amplitude [156]. This phenomenon is called a forward-focusing. The heavier the scattering atom, the stronger the forward-focusing. Moreover, at this kinetic energy photoelectrons have a mean free path of about 20Å. This allows us to retrieve geometrical information about the local real space environnement of selected atom species near the surface of samples. In the case of $Na_1CoO_2$, we used the Co $2p_{3/2}$ peak located at kinetic energy $E_{kin}$ = 959 eV, the O 1$s$ at $E_{kin}$ = 1211 eV and the Na Auger KLL peak at $E_{kin}$ = 993 eV as emission for XPD. The Co and O lines were excited by the SiK$\alpha$ anode and the Na line by the MgK$\alpha$ anode. The corresponding intensity maps were taken over the full hemispherical range up to polar angle $\theta = 78^\circ$. Afterwards a smooth polar angle dependent

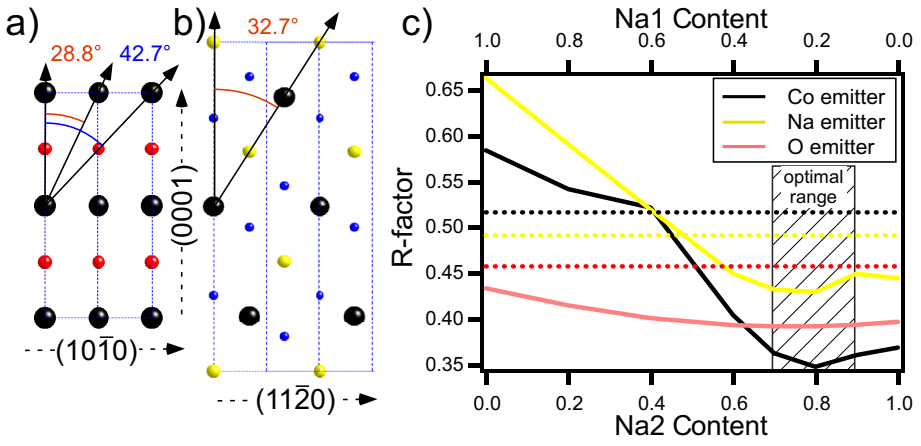


FIGURE C.6: Atomic planes displaying Co-Co interlayer directions for the (a) $P6_3/mmc$ unit cell and (b) $R\bar{3}m$ unit cell. (c) R-factor results for the incoherent addition of $P6_3/mmc$ structure as a function of Na1 and Na2 sites occupancy (continuous lines) and the $R\bar{3}m$ structure (dashed lines, only one possible Na site).

background was substracted from both measured and calculated diffractogram in order to simplify comparison. An R-factor analysis can be carried out to obtain a quantitative value for the agreement between measured and simulated diffractograms[157].

Sodium doped cobaltate is composed of $CoO_2$ layers where Co, forming a triangular lattice, is in octahedral coordination with O (see Fig. C.4). Na dopants sit in between two such layers and have a strong influence on unit cell structures and parameters. According to recent x-ray and neutron diffraction studies [151, 152, 154], Na atoms have either prismatic or octahedral coordination with neighboring O atoms and unit cells contain 1, 2 or 3 layers of $CoO_2$. These two criteria permit to elaborate a detailed classification. In our case, we focused on the structures determined near optimal doping $x = 1$, i.e. the $R\bar{3}m$ and the $P6_3/mmc$ symmetries, which have respectively three $CoO_2$ layers with Na in octahedral coordination for a total height of about 15.6 Å and two $CoO_2$ layers with Na in prismatic coordination for a total height of about 10.5 Å. These are depicted in Fig. C.4. Besides, the $P6_3/mmc$ unit cell allows two inequivalent sites for Na atoms ($2b$ and $2d$ Wyckoff positions) labelled Na1 and Na2 whose occupation ratio depends strongly on the doping [152]. One main difference between the $P6_3/mmc$ and the $R\bar{3}m$ symmetries is the stacking sequence of Co atoms in different layers. For the case of $P6_3/mmc$, in two adjacent layers, Co atoms sit exactly below each other, while in $R\bar{3}m$ they have a $ABCABC$ stacking sequence. For our SSC simulations, we used these two structures with a Na content fixed at $x = 1$. We built atomic clusters with Na termination (the diffractograms show a weak sensitivity to surface termination) and emitters were introduced down to 15 Å below the cluster surface.

Figure C.5 shows the diffractograms for $Co2p_{3/2}$ emission at $E_{kin} = 959$ eV. The experiment (Fig. C.5(a)) exhibits a six-fold symmetry (and has been symmetrized this way to improve statistics) and shows intensity structures mainly along the $\phi = 0\,^\circ$ and $\phi = 30\,^\circ$ directions (high atomic density planes). These azimuthal directions correspond to the (12$\bar{3}$0) and the (10$\bar{1}$0) direction respectively (Fig. C.4(c)). In Fig. C.5(b) three SSC simulations are placed in the same diffractogram. They all stem from the $P6_3/mmc$ unit cell, but with Na atoms at different positions, specified by their label (for each one $x = 1$). In particular, the part labelled Na1+Na2 results from an incoherent addition of

Na1 and Na2 diffractograms in the optimized ratio 1 to 4. The corresponding procedure is described below. The SSC diffractogram of the R$\bar{3}$m unit cell is shown in Fig. C.5(d). All these simulations present originally a three-fold symmetry (due to the octahedral and prismatic coordination of the emitters) and have been two-fold symmetrized to recover the experimental symmetry, expressing this way a multidomain structure in $Na_1CoO_2$ or a surface termination at different heights of the unit cell. To help comparison, experiment and the Na1+Na2 simulation have been reported in Fig. C.5(e). In this figure, it is evident that the Na1+Na2 simulation reproduces well the experimental features. In particular the six strong forward focusing maxima (labelled A) at low polar angles (inside the white dashed circle) appearing at $\phi = 30^\circ$ and at $\theta \cong 28^\circ$ are more intense than the blurry spot at $\phi = 0^\circ$, while the R$\bar{3}$m symmetry gives a totally incorrect behaviour. In fact, these forward focusings are absent for the R$\bar{3}$m diffractogram. Their origin can be traced back in the $P6_3/mmc$ unit cell to a Co-Co interlayer diffraction along the $(10\bar{1}0)$ direction (Fig. C.6 (a)), which is absent in the R$\bar{3}$m unit cell due to the different $CoO_2$ layer stacking (see Fig. C.6 (b)). At higher polar angles, the cross-like features ($\theta = 40 - 70^\circ$, labelled B) in the experiment is again better reproduced in the Na1+Na2 simulation while visually incomplete in the R$\bar{3}$m simulation. Finally, the double spot at $\phi = 30^\circ$ ($\theta \simeq 44^\circ$, labelled C) in the experiment (small white dashed circle) is not reproduced by the R$\bar{3}$m whereas it is in the Na1+Na2 simulation. Its origin is also due to Co-Co interlayer diffraction present only in the $P6_3/mmc$ structure (Fig. C.6 (a) and (b)). At high polar angles between two $(12\bar{3}0)$ directions, simulations fail to render a curved blurry structure of the experiment. This may be due to some surface interferences since it appears at high $\theta$. The polar cuts in Fig. C.5(c) and Fig. C.5(f) give a more precise view of these comparisons and strengthen the previous conclusions (intensity features are indicated by arrows and labels). They give a strong support in favour of the $P6_3/mmc$ stucture too. An R-factor analysis has been performed for Co emission diffractograms with the two different unit cells (Fig. C.6(c)). For the case of the $P6_3/mmc$ symmetry (continuous line), diffractograms steming from structures with Na atoms at different positions (Na1 or Na2 sites) have been mixed (always satisfying $x = 1$). This addition of intensities corresponds to an incoherent sum in the sense that this cannot lead to events like the interference of photoelectrons diffracted by different types of Na atoms. This choice is reasonable, since a configuration with two adjacent Na atoms sitting in the Na1 and Na2 positions in the same layer is energetically unfavorable, for Na ions would be too close from each other [158], weakening thus the possibility of interference. This R-factor analysis confirms our previous visual approach since for a Na2 content of 0.8 (Na1= 0.2) the $P6_3/mmc$ symmetry produces an R-factor which is about 35% smaller than the R$\bar{3}$m symmetry does (Fig. C.6 (c)).

A similar analysis has been applied to diffractograms with Na (KLL Auger line, $E_{kin} =$ 993 eV) and O (O1s line, $E_{kin} = 1211$ eV) emission. Fig. C.7 (a) and (b) shows the experiments and Fig. C.7(c) and d) their corresponding simulations displayed in a similar manner on Fig. C.5. The differences for Na diffractograms are less clear-cut than for Co. Both R$\bar{3}$m and $P6_3/mmc$ structures produce valuable simulations. For instance, intensity structures marked by the rectangular (A') and the triangle (B') are better reproduced by the $P6_3/mmc$ and the R$\bar{3}$m unit cells respectively. This fact can be understood through the difference in the stacking sequence of Co atoms (see Fig. C.4). Except for Na atoms at the Na1 position (which is the minority at the optimal R-factor), the coordination of Na and O atoms with respect to neighbouring Co atoms (the strongest diffuser) displays a triangular symmetry with two possible orientations so that when applying a two-fold symmetry (multidomain structure or termination effect),

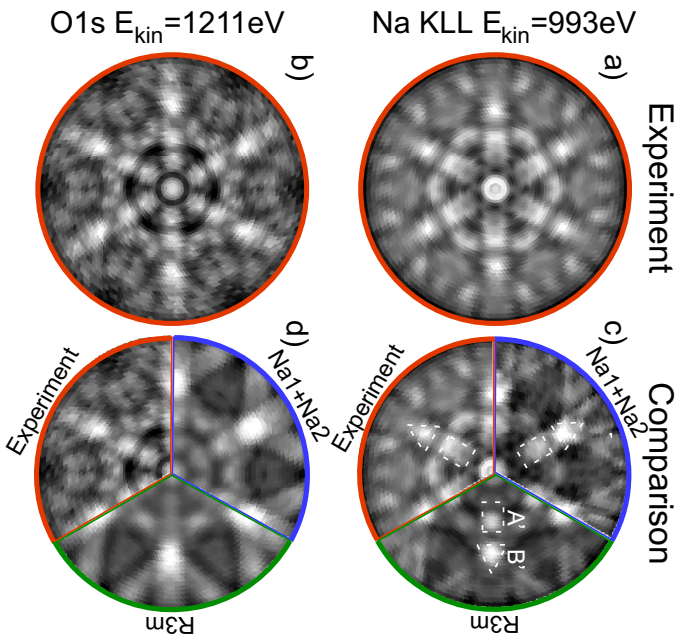


FIGURE C.7: Experimental and simulated data for Na Auger KLL emission at $E_{kin}$ = 993 eV and for O1s emission at $E_{kin}$ = 1211 eV. (a) XPD measurements for Na. (b) Comparison between experiment and simulations for Na (Na1+Na2 structure built with the optimized ratio of 1:4). (c) XPD measurements for O. (d) Comparison between experiment and simulations for O (Na1+Na2 structure built with the optimized ratio of 1:4).

these become equivalent, inducing therefore comparable diffractograms. In the case of Co atoms, there is a clear difference, as one cas see on Fig. C.6 (a) and (b). We must resort to polar cuts which support the $P6_3/mmc$ structure due to better agreement in peak position and shape (not shown here). Again, the R-factor analysis confirms this conclusion, however less clearly than for the Co case (Fig. C.6 (c)).

Huang *et al.*[152] have measured the bulk occupancy of the two types of Na sites in the $P6_3/mmc$ unit cell for samples with different Na content. They find that at $x = 1$ only Na2 sites are occupied (i.e. Na2=1 and Na1=0). In our case, all the R-factor curves of Fig. C.6(c) have their minima at Na2$\simeq$ 0.8 and Na1$\simeq$ 0.2, that is an occupation ratio Na1:Na2 $\simeq$ 1/4. From data of Huang *et al.* such an occupatio ratio is realised only at $x \simeq 0.8$, which suggests that in our samples, Na content at surface is $x_{surf} \simeq 0.8$.

In conclusion, we report the first surface structure measurements of $Na_xCoO_2$ samples in the $\alpha-$phase at $x_{bulk} = 0.98$, using XPD. By comparing our data with SSC simulations we can clearly identify the $P6_3/mmc$ unit cell, in contradiction to bulk measurements which identify the $R\bar{3}m$ unit cell (at $x \cong 1$ and in the $\alpha-$phase) [151, 159]. Based on bulk studies of Huang *et al.*[152], we infer a Na content near the surface of $x_{surf} \cong 0.8 < x_{bulk} \cong 1$ to explain the Na1 to Na2 sites occupation ratio of about 1/4. The presence of Na atoms at different positions give support to the disorder scenario of Singh and Kasinathan [148]. Furthermore, to recover the six-fold symmetry of measured diffractograms, we had to symmetrize two-fold our simulations. Hence there are different domains in $Na_1CoO_2$ samples in which $P6_3/mmc$ unit cells have different orientations (60 $^\circ$ apart) in (0001) planes. Finally, in this work, we show that for the case of $Na_1CoO_2$

surface effects cannot be neglected.

We are grateful to our workshop and electric engineering team for skillful technical assistance. This project has been supported by the Fonds National Suisse pour la Recherche Scientifique through Div. II and MaNEP.

## C.3 Quality of the crystal: an impasse

In this study, we identified the structure at the surface of $Na_1CoO_2$ samples, which turns out to be different than what is predicted by the bulk measurements in references [151, 159]. This interesting result has been spoiled by an unexpected deterioration of the sample.

$Na_xCoO_2$ crystals are known to be very sensitive to moisture, particularly those having $x > 0.7$. If they are not stored in a moisture-free environment, a white precipitate builds up on their surface, resulting probably from the reaction of Na ions with water to form NaOH [160]. $Na_xCoO_2$ exhibits a rich phase diagram as a function of the sodium doping $x$ [141], related to many different atomic structures [151, 152, 154]. Therefore, a gradual desorption of sodium atoms in the vicinity of the surface may lead to the appearance of a diversity of atomic structures in the near surface region of the sample. In that sense, STM measurements recently carried out on $Na_xCoO_2$ with $x = 0.84$ revealed a cleaved surface showing many different Na ordered patterns, pointing towards a surface with a reduced Na concentration, $x \cong 0.42$ [161].

In our XPD study of $Na_1CoO_2$, we determined that the unit cell near the surface was essentially of the $P6_3/mmc$ space group, with a certain mixing of the two inequivalent sodium sites, $Na_1$ and $Na_2$. Based on the existing literature, we realized that this structure was different than that identified for such crystals by bulk sensitive methods, supporting therefore the idea that strong surface effects were at play in this system. At that moment, we decided to perform x-ray diffraction measurements on samples from the same batch to confirm this hypothesis. These measurements revealed a mixture of many different phases in the bulk, which were probably a consequence of the unstability of the samples, as well as their bad quality.

In the next months, a special effort was invested to improve the quality of the samples, without much success. We finally decided to drop this project.

# *Acknowledgements*

Je tiens tout d'abord à témoigner ma profonde reconnaissance à Philipp Aebi pour m'avoir donné l'opportunité d'effectuer ce travail de thèse dans son groupe. J'ai particulièrement apprécié sa confiance en mon travail, qui m'a permis de présenter ces résultats à de nombreuses conférences, ainsi que ses précieux conseils, qui m'ont guidé efficacement tout au long de ce travail, en me laissant toutefois une liberté essentielle à mon épanouissement.

I would like also to thank Felix Baumberger (who came especially from St. Andrews for my defense), Manfred Sigrist and Hans Beck, who all accepted to be member of the jury of my thesis and read it carefully. I thank them for their corrections too.

Durant l'élaboration de cette thèse, j'ai eu la chance de renouer avec la théorie et ai eu beaucoup de plaisir à développer cet aspect-là en parallèle de la photoémission. Cette chance, je la dois à Hans Beck, qui a investi beaucoup de son temps libre pour m'accompagner dans le monde passionnant des excitons, et je l'en remercie vivement.

Je veux aussi exprimer ici toute ma gratitude aux anciencs membres du groupe de spectroscopie qui m'ont initié à la photoémission. Je pense à Florian Clerc, avec qui j'ai fait mes premiers pas dans ce monde. Je le remercie pour sa bonne humeur et sa patience. C'est aussi lui qui m'a introduit à la théorie de la condensation des excitons. J'ai découvert la technique de l'XPD grâce à Laurent Despont. Et peut-être aussi une certaine dépendance à la caféine ... Je me remémore ces excellents moments passés dans le labo ESCA en sa compagnie (sur un petit air de musique ...) et je le remercie pour ces souvenirs. J'ai aussi eu la chance de travailler étroitement avec un scientifique experimenté en la personne d'Hervé Cercellier, qui a rédigé le premier article sur les excitons et a ainsi préparé le terrain pour la suite de nos travaux. Je le remercie pour cette collaboration fructueuse et pour les bons moments passés ensemble. A Neuchâtel, j'ai partagé mon bureau pendant plus de trois années avec Corsin Battaglia, ce qui nous a permis non seulement de mener de nombreux débats scientifiques sur toutes sortes de sujets, mais aussi de développer une réelle amitié, notamment sur le lac (tourmenté parfois) de Neuchâtel. Je le remercie pour tout cela et notamment pour m'avoir fait découvrir la voile.

Parmi les membres actuels du groupe, j'aimerais exprimer en particulier ma reconnaissance à Gunnar Garnier, non seulement pour tout le savoir qu'il m'a transmis dans le laboratoire, son domaine de prédilection, mais aussi pour les soupers et les excursions qu'il a organisés et qui contribuent grandement à l'excellente ambiance du groupe. Je remercie aussi Clément Didiot et Eike Schwier, pour leur bonne humeur et leurs intentions particulières ... Je mentionne ici aussi les nouvelles arrivées, Miryam Garcia Fernandez et Zuzana Vydrova, et leur souhaite beaucoup de plaisir avec la photoémission, spécialement à Zuzana Vydrova qui reprendra le flambeau excitonique.

J'aimerais aussi remercier les membres des ateliers mécaniques et électroniques de l'institut de physique de Neuchâtel, pour leur compétence et leur disponibilité irréprochables. Ce fut un réel plaisir que d'interagir avec eux. Je suis reconnaissant aussi aux membres du secrétariat de l'institut de physique pour leur aide efficace face à toutes sortes de complications administratives et pour leurs généreux sourires.

Finalement, je tiens à souligner ici ma profonde gratitude envers ma famille, qui a toujours été à mes côtés durant ce travail de thèse, dans les moments agréables comme dans les moments difficiles. Cette réussite, c'est en partie à elle que je la dois.

# Curriculum vitae

## Personal details

| | |
|---|---|
| Family name | Monney |
| First name | Claude |
| Date of birth | December 23, 1980 |
| Place of birth | Billens, Switzerland |
| Citizen of | St-Martin (FR), Switzerland |
| Marital status | Single |

## Education

| | |
|---|---|
| 2005-2009 | Ph.D. in physics: "Exciton condensation in $1T$-$TiSe_2$: a photoemission study and its theoretical model" Research group of Prof. Philipp Aebi, Université de Neuchâtel |
| 2005 | Diploma thesis: "Phases solides anisotropes dans les systèmes à effet Hall quantique" Research group of Prof. Cristiane de Morais Smith, University of Fribourg and University of Utrecht (the Netherlands) |
| 2000 - 2005 | Studies in Physics- Mathematics, University of Fribourg |
| 1996 - 2000 | High school graduation in Fribourg, Collège Ste-Croix Baccalauréat et maturité fédérale, type B (latin, english) |

## List of Publications

- **Temperature dependence of the excitonic insulator phase model in $1T$-$TiSe_2$** C. Monney, H. Cercellier, C. Battaglia, E.F. Schwier, C. Didiot, M.G. Garnier, H. Beck, P. Aebi *Physica B*, DOI:/10.1016/j.physb.2009.07.047 (2009).

- **Elementary structural building blocks encountered in silicon surface reconstructions**
  C. Battaglia, K. Gaal-Nagy, C. Monney, C. Didiot, E.F. Schwier, M.G. Garnier, G. Onida, P. Aebi *J. Phys. Condens. Matter* **21**, 013001 (2009).

- **New Structural Model for the Si$(331)-(12\times 1)$ Surface Reconstruction**
  C. Battaglia, K. Gaal-Nagy, C. Monney, C. Didiot, E.F. Schwier, M.G. Garnier, G. Onida, P. Aebi *Phys. Rev. Lett.* **102**, 066102 (2009).

- **Spontaneous exciton condensation in 1$T$-$TiSe_2$: BCS-like approach**
  C. Monney, H. Cercellier, F. Clerc, C. Battaglia, E.F. Schwier, C. Didiot, M.G. Garnier, H. Beck, P. Aebi, H. Berger, L. Forro, *Phys. Rev. B* **79**, 045116 (2009).

- **Unveiling new systematics in self-assembly of atomic chains on Si**(111)
  C. Battaglia, H. Cercelier, C. Monney, L. Despont, M. G. Garnier, P. Aebi, *J. Phys. Conf. Ser.* **100**, 052078 (2008).

- **A new structural model for the Si$(331)-(12\times 1)$ reconstruction**
  C. Battaglia, K. Gaal-Nagy, C. Monney, C. Didiot, E. F. Schwier, M. G. Garnier, G. Onida, P. Aebi, *arXiv:* 0807.3875 (2008).

- **Evidence for an excitonic insulator phase in 1$T$-$TiSe_2$**
  H. Cercellier, C. Monney, F. Clerc, C. Battaglia, L. Despont, M. G. Garnier, H. Beck, L. Patthey, H. Berger and P. Aebi, *Phys. Rev. Lett.* **99**, 146403 (2007).

- **Fermi surface of layered compounds and bulk charge density wave systems**
  F. Clerc, C. Battaglia, C. Monney, H. Berger, L. Despont, M. G. Garnier, P. Aebi, *J. Phys. Condens. Matter* **19**, 355002 (2007).

- **Non-uniform doping across the Fermi surface of $NbS_2$ intercalates**
  C. Battaglia, H. Cercellier, L. Despont, C. Monney, M. Prester, H. Berger, L. Forró, M. G. Garnier, P. Aebi, *Eur. Phys. J. B* **57**, 385 (2007).

- **Stabilization of silicon honeycomb chains by trivalent adsorbates**
  C. Battaglia, H. Cercellier, C. Monney, M.G. Garnier, P. Aebi, *Eur. Phys. Lett.* **77**, 36003 (2007).

- **Lattice-distortion-enhanced electron-phonon coupling and Fermi surface nesting in 1$T$-$TaS_2$**
  F. Clerc, C. Battaglia, M. Bovet, L. Despont, C. Monney, H. Cercellier, M. G. Garnier, H. Berger, L. Forr, P. Aebi, *Phys. Rev. B* **74**, 155114 (2006).

# Bibliography


[1] K. Siegbahn, C. Nordling, R. Fahlman, R. Nordberg, K. Hamrin, J. Hedman, G. Johansson, R. Bergmark, S.-E. Karlsson, I. Lindgren, and B. Lindberg. ESCA, Atomic, Molecular and Solid State Structure Studies by Means of Electron Spectroscopy. *Nova Acta Regiae Soc. Sci. Upsaliensis*, 20:Ser. IV, 1967.

[2] D. Jérome, T.M. Rice, and W. Kohn. Excitonic Insulator. *Phys. Rev.*, 158:462, 1967.

[3] L.V. Keldysh and Y.V. Kopaev. Possible instability of the semimetallic state toward Coulomb interaction. *Soviet Phys. Solid State*, 6:2219, 1965.

[4] A. Damascelli. Probing the Electronic Structure of Complex System by ARPES. *Physica Scripta*, T109:61, 2004.

[5] S. Huefner. *Photoelectron Spectroscopy.* Springer-Verlag, 1995.

[6] S.D. Kevan. *Angle Resolved Photoemission, Theory and Current Applications.* Elsevier Science, 1992.

[7] G.D. Mahan. Theory of Photoemission in Simple Metals. *Phys. Rev. B*, 11:4334, 1970.

[8] H. Hertz. Ueber einen Einfluss des ultravioletten Lichtes auf die electrische Entladung. *Ann. Physik*, 31:983, 1887.

[9] A. Einstein. Ueber einen die Erzeugung und Verwandlung des Lichtes betreffenden heuristischen Gesichtspunkt. *Ann. Physik*, 322:132, 1905.

[10] J.B. Pendry. Theory of photoemission. *Surf. Sci.*, 57:679, 1975.

[11] P. Feibelman and D. Eastman. Photoemission spectroscopy - Correspondence between quantum theory and experimental phenomenology. *Phys. Rev. B*, 10:4932, 1974.

[12] C. Caroli, D. Lederer-Rozenblatt, B. Roulet, and D. Saint-James. Inelastic Effects in Photoemission: Microscopic Formulation and Qualitative Discussion. *Phys. Rev. B*, 8:4552, 1973.

[13] L. Plucinski, J. Minar, B.C. Sell, J. Braun, H. Ebert, C.M. Schneider, and C.S. Fadley. Band mapping in higher-energy x-ray photoemission: Phonon effects and comparison to one-step theory. *Phys. Rev. B*, 78:035108, 2008.

[14] S. de Jong, Y. Huang, R. Huisman, F. Massee, S. Thirupathaiah, M. Gorgoi, F. Schaefers, R. Follath, J.B. Goedkoop, and M.S. Golden. High-resolution, hard x-ray photoemission investigation of $BaFe_2As_2$: Moderate influence of the surface and evidence for a low degree of Fe $3d$As $4p$ hybridization of electronic states near the Fermi energy. *Phys. Rev. B*, 79:115125, 2009.

[15] T. Togashi, T. Kanai, T. Sekikawa, S. Watanabe, C. Chen, C. Zhang, Z. Xu, and J. Wang. Generation of vacuum-ultraviolet light by an optically contacted, prism-coupled $KBe_2BO_3F_2$ crystal. *Opt. Lett.*, 28:254, 2003.

[16] J.D. Koralek, J.F. Douglas, N.C. Plumb, J.D. Griffith, S.T. Cundiff, H.C. Kapteyn, M.M Murnane, and D.S. Dessau. Experimental setup for low-energy laser-based angle resolved photoemission spectroscopy. *Rev. Sci. Instrum.*, 78:053905, 2007.

[17] M. Hengsberger. *Unusual Aspects of Surface Electronic Structure studied with Photoelectron Spectroscopy.* Thesis, Université de Neuchâtel, 2000.

[18] P. Aebi, J. Osterwalder, R. Fasel, D. Naumovic, and L. Schlapbach. Fermi-surface mapping with photoelectrons at UV energies. *Surf. Sci.*, 917:307, 1994.

[19] E. Krasovskii. Augmented-plane-wave approach to scattering of Bloch electrons by an interface. *Phys. Rev. B*, 70:245322, 2004.

[20] E. Krasovskii, V. Strocov, N. Barrett, H. Berger, W. Schattke, and R. Claessen. Band mapping in the one-step photoemission theory: Multi-Bloch-wave structure of final states and interference effects. *Phys. Rev. B*, 75:045432, 2007.

[21] V. Strocov. Intrinsic Accuracy in 3-dimensional photoemission band mapping. *Journal of Electron Spectroscopy and related phenomena*, 65:130, 2003.

[22] G.D. Mahan. *Many Body Physics.* Plenum, 1981.

[23] D. Baeriswyl and N. Macris. *Méthode à N corps en matière condensée.* Troisième cycle de la physique, 2000.

[24] A.L. Fetter and J.D. Walecka. *Quantum theory of many-particle systems.* Dover Publication, 1971.

[25] A. Hofmann, X.Y. Cui, J. Schaefer, S. Meyer, P. Hoepfner, C. Blumenstein, M. Paul, L. Patthey, E. Rotenberg, J. Buenemann, F. Gebhard, T. Ohm, W. Weber, and R. Claessen. Renormalization of bulk magnetic electron states at high binding energies. *Phys. Rev. Lett.*, 102:187204, 2009.

[26] F. Schmitt, W.S. Lee, D.-H. Lu, W. Meevasana, E. Motoyama, M. Greven, and Z.-X. Shen. Analysis of the spectral function of NdCeCuO4 obtained by angle-resolved photoemission spectroscopy. *Phys. Rev. B*, 78:100505R, 2008.

[27] M. Klein, D. Zur, D. Menzel, J. Schoenes, K. Doll, J. Roeder, and F. Reinert. Evidence for itineracy in the anticipated Kondo insulator FeSi: a quantitative determination of the band renormalization. *Phys. Rev. Lett.*, 101:046406, 2008.

[28] C. Weber, K. Haule, and G. Kotliar. Optical weights and waterfalls in doped charge-transfer insulators: A local density approximation and dynamical mean-field theory study of $La_{2-x}Sr_xCuO_4$. *Phys. Rev. B*, 78:134519, 2008.

[29] B. Kyung, S.S. Kancharla, D. Sénéchal, A.-M.S. Tremblay, M. Civelli, and G. Kotliar. Pseudogap induced by short-range spin correlations in a doped Mott insulator. *Phys. Rev. B*, 73:165114, 2006.

[30] R.E. Peierls. *Quantum Theory of Solids*. Oxford University Press, 1955.

[31] F. Clerc. *Photoemission from transition metal dichalcogenides, Quasi-two dimensional systems with charge density waves*. Thesis, Université de Neuchâtel, 2006.

[32] J. Schaefer, E. Rotenberg, S. D. Kevan, P. Blaha, R. Claessen, and R. E. Thorne. High-Temperature Symmetry Breaking in the Electronic Band Structure of the Quasi-One-Dimensional Solid $NbSe_3$. *Phys. Rev. Lett.*, 87:196403, 2001.

[33] J. Voit, L. Perfetti, F. Zwick, H. Berger, G. Margaritondo, G. Gruener, H. Hoechst, and M. Grioni. Electronic Structure of Solids with Competing Periodic Potentials. *Science*, 290:501, 2000.

[34] V. Brouet, W. L. Yang, X. J. Zhou, Z. Hussain, N. Ru, K. Y. Shin, I. R. Fisher, and Z. X. Shen. Fermi Surface Reconstruction in the CDW State of $CeTe_3$ Observed by Photoemission. *Phys. Rev. Lett.*, 93:126405, 2004.

[35] F. Clerc, C. Battaglia, C. Monney, H. Berger, L. Despont, M. G. Garnier, and P. Aebi. Fermi surface of layered compounds and bulk charge density wave systems. *J. Phys. C.*, 19:355002, 2007.

[36] C. Battaglia, H. Cercellier, F. Clerc, L. Despont, M.G. Garnier, C. Koitzsch, P. Aebi, H. Berger, L. Forró, and C. Ambrosch-Draxl. Fermi-surface-induced lattice distortion in NbTe2. *Phys. Rev. B*, 72:195114, 2005.

[37] D. S. Inosov, V. B. Zabolotnyy, D. V. Evtushinsky, A. A. Kordyuk, B. Buechner, R. Follath, H. Berger, and S. V. Borisenko. Fermi surface nesting in several transition metal dichalcogenides. *New J. Phys.*, 10:125027, 2008.

[38] M.D. Johannes and I.I. Mazin. Fermi surface nesting and the origin of Charge Density Wave in metals. *Phys. Rev. B*, 77:165135, 2008.

[39] J.A. Wilson and A.D. Yoffe. The transition metal dichalcogenides discussion and interpretation of the observed optical, electrical and structural properties. *Adv. Phys.*, 18:193, 1969.

[40] J.A. Wilson, F.J. Di Salvo, and J. Mahajan. Charge-density waves and superlattices in the metallic layered transition metal dichalcogenides. *Adv. Phys.*, 24:117, 1975.

[41] Y. Aiura, H. Bando, R. Kitagawa, S. Maruyama, Y. Nishihara, K. Horiba, M. Oshima, O. Shiino, and M. Nakatake. Electronic structure of layered $1T$-$TaSe_2$ in commensurate charge-density-wave phase studied by angle-resolved photoemission spectroscopy. *Phys. Rev. B*, 68:073408, 2003.

[42] P. Fazekas and E. Tosatti. Charge carrier localization in pure and doped $1T$-$TaS_2$. *Physica B+C*, 99:183, 1980.

[43] F. Clerc, M. Bovet, H. Berger, L. Despont, C. Koitzsch, M. G. Garnier, and P. Aebi. CDW in $1T$-$TaS_2$: An angle-resolved photoemission study. *Physica B*, 351:245, 2004.

[44] F. Clerc, C. Battaglia, M. Bovet, L. Despont, C. Monney, H. Cercellier, M. G. Garnier, and P. Aebi. Lattice-distortion-enhanced electron-phonon coupling and Fermi surface nesting in 1$T$-$TaS_2$. *Phys. Rev. B*, 74:115114, 2006.

[45] S.V. Borisenko, A.A. Kordyuk, A.N. Yaresko, V.B. Zabolotnyy, D.S. Inosov, R. Schuster, B. Buechner, R. Weber, R. Follath, L. Patthey, and H. Berger. Pseudogap and Charge Density Waves in Two Dimensions. *Phys. Rev. Lett.*, 100:196402, 2008.

[46] K.E. Wagner, E. Morosan, Y.S. Hor, J. Tao, Y. Zhu, T. Sanders, T.M. McQueen, H.W. Zandbergen, A.J. Williams, D.V. West, , and R.J. Cava. Tuning the charge density wave and superconductivity in $Cu_xTaS_2$. *Phys. Rev. B*, 78:104520, 2008.

[47] E. Morosan, H.W. Zandbergen, B.S. Dennis, J.W.G. Bos, Y. Onose, T. Klimczuk, A.P. Ramirez, N.P. Ong, and R.J. Cava. Superconductivity in $Cu_xTiSe_2$. *Nature Physics*, 2:544, 2006.

[48] F.J. Di Salvo, D.E. Moncton, and J.V. Waszczak. Electronic properties and superlattice formation in the semimetal $TiSe_2$. *Phys. Rev. B*, 14:4321, 1976.

[49] M. Holt, P. Zschack, H. Hong, M.Y. Chou, and T.-C. Chiang. X-Ray Studies of Phonon Softening in $TiSe_2$. *Phys. Rev. Lett.*, 86:3799, 2001.

[50] N.V. Baranov, K. Inoue, V.I. Maksimov, A.S. Ovchinnikov, V.G. Pleschov, A. Podlesnyak, A.N. Titov, and N.V. Toporova. Ni intercalation in titanium diselenide: effect on the lattice, specific heat and magnetic properties. *J. Phys.: Condens. Matter*, 16:9243, 2004.

[51] X. Y. Cui, H. Negishi, S. G. Titova, K. Shimada, A. Ohnishi, M. Higashiguchi, Y. Miura, S. Hino, A. M. Jahir, A. Titov, H. Bidadi, S. Negishi, H. Namatame, M. Taniguchi, and M. Sasaki. Direct evidence of band modification and suppression of superstructure in $TiSe_2$ upon Fe intercalation: An angle-resolved photoemission study. *Phys. Rev. B*, 73:085111, 2006.

[52] N.V. Baranov, V.I. Maksimov, J. Mesot, V.G. Pleschov, A. Podlesnyak, V. Pomjakushin, and N.V. Selezneva. Possible reappearance of the charge density wave transition in $M_xTiSe_2$ compounds intercalated with 3d metals. *J. Phys.: Condens. Matter*, 19:016005, 2007.

[53] S.E. Stoltz, H.I. Starnberg, and L.J. Holleboom. Rb deposition on $TiSe_2$ and $TiTe_2$ at 100 K and at room temperature studied by photoelectron spectroscopy. *Phys. Rev. B*, 71:125403, 2005.

[54] A.N. Titov and A.V. Dolgoshein. Phase Diagrams of Intercalation Materials with Polaron-Type Carrier Localization. *Phys. Solid State*, 42:434, 2000.

[55] F.J. Di Salvo and J.V. Waszczak. Transport properties and the phase transition in $Ti_{1-x}M_xSe_2$ ($M$ =Ta or V). *Phys. Rev. B*, 17:3801, 1978.

[56] P. Blaha, K. Schwarz, G.K.H. Madsen, D. Kavasnicka, and J. Luitz. *WIEN2K, an Augmented Plane Wave Plus Local Orbitals Program for Calculating Crystal Properties*. Technische Universität, Wien, Austria, 2001.

[57] Th. Pillo, J. Hayoz, H. Berger, F. Levy, L. Schlapbach, and P. Aebi. Photoemission of bands above the Fermi level: The excitonic insulator phase transition in 1$T$-$TiSe_2$. *Phys. Rev. B*, 61:16213, 2000.

[58] O. Anderson, R. Manzke, and M. Skibowski. Three-Dimensional and Relativistic Effects in Layered $1T$-$TiSe_2$. *Phys. Rev. Lett.*, 55:2188, 1985.

[59] T.E. Kidd, T. Miller, M.Y. Chou, and T.-C. Chiang. Electron-Hole Coupling and the Charge Density Wave Transition in $TiSe_2$. *Phys. Rev. Lett.*, 88:226402, 2002.

[60] K. Rossnagel, L. Kipp, and M. Skibowski. Charge-density-wave phase transition in $1T$-$TiSe_2$: Excitonic insulator versus band-type Jahn-Teller mechanism. *Phys. Rev. B*, 65:235101, 2002.

[61] N. Suzuki, A. Yamamoto, and K. Motizuki. Microscopic Theory of the CDW State of $1T$-$TiSe_2$. *J. Phys. Soc. Jpn.*, 54:4668, 1975.

[62] J. Rasch, T. Stemmler, B. Mueller, L. Dudy, and R. Manzke. $1T$-$TiSe_2$: Semimetal or Semiconductor? *Phys. Rev. Lett.*, 101:237602, 2008.

[63] R.M. White and G. Lucovsky. Suppression of Antiferroelectricity in $TiSe_2$ by Excess Carrier. *Nuovo Cimento Soc. Ital. Fis. B*, B38:280, 1977.

[64] H.P. Hughes. Structural distortion in $TiSe_2$ and related materials — a possible Jahn-Teller effect? *J.Phys. C: Solid State Phys.*, 10:L319, 1977.

[65] N.F. Mott. The transition of the Metallic State. *Phil. Mag.*, 6:287, 1961.

[66] R.S. Knox. Theory of excitons. *Solid State Phys. Suppl.*, 5:100, 1963.

[67] J. Zittartz. Anisotropy Effects in the Excitonic Insulator. *Phys. Rev.*, 162:752, 1967.

[68] J. Zittartz. Theory of the Excitonic Insulator in the Presence of Normal Impurities. *Phys. Rev.*, 164:575, 1967.

[69] C. Klingshirn. *Semiconductor optics*. Springer, 2007.

[70] S.A. Moskalenko and D.W. Snoke. *Condensation of Excitons and Biexcitons and Coherent Nonlinear Optics with Excitons*. Cambridge University Press, 2000.

[71] J. Bardeen, L.N. Cooper, and J.R. Schrieffer. Theory of Superconductivity. *Phys. Rev.*, 108:1175, 1957.

[72] A.V. Balatsky, W.S. Lee, and Z.X. Shen. Bogoliubov angle, particle-hole mixture, and angle-resolved photoemission spectroscopy in superconductors. *Phys. Rev. B*, 79:020505(R), 2009.

[73] R.W. Morse and H.V. Bohm. Superconducting Energy Gap from Ultrasonic Attenuation Measurements. *Phys. Rev.*, 108:1094, 1957.

[74] M.J. Rice and Y.N. Gartstein. The excitonic ground state of the half-filled Peierls insulator. *J. Phys.: Condens. Matter*, 17:4615, 2005.

[75] J.A. Wilson, F.J. Di Salvo, and S. Mahajan. Charge-density waves and superlattices in the metallic layered transition metal dichalcogenides. *Adv. Phys.*, 24:117, 1975.

[76] D. Malterre, M. Grioni, and Y. Baer. Recent developments in high-energy spectroscopies of Kondo systems. *Adv. Phys.*, 45:299, 1996.

[77] W. Kohn. Excitonic Phases. *Phys. Rev. Lett.*, 19:439, 1967.

[78] B.I. Halperin and T.M. Rice. Possible Anomalies at a Semimetal-Semiconductor Transition. *Rev. Mod. Phys.*, 40:755, 1968.

[79] F.X. Bronold and H. Fehske. Possibility of an excitonic insulator at the semiconductor-semimetal transition. *Phys. Rev. B*, 74:165107, 2006.

[80] C. Monney, H. Cercellier, F. Clerc, C. Battaglia, E.F. Schwier, C. Didiot, M. G. Garnier, H. Beck, P. Aebi, H. Berger, L. Forro, and L. Patthey. Spontaneous exciton condensation in $1T$-$TiSe_2$: BCS-like approach. *Phys. Rev. B*, 79:045116, 2009.

[81] J.A. Wilson, A.S. Barker, F.J. Di Salvo, and J.A. Ditzenberger. Infrared properties of the semimetal $TiSe_2$. *Phys. Rev. B*, 18:2866, 1978.

[82] C. Didiot, Y. Fagot-Revurat, S. Pons, B. Kierren, C. Chatelain, and D. Malterre. Reconstruction-induced multiple gaps in the weak coupling limit: The surface bands of Au(111) vicinal surfaces. *Phys. Rev. B*, 74:081404R, 2006.

[83] M.-H. Whangboo and E. Canadell. Analogies between the Concepts of Molecular Chemistry and Solid-State Physics concerning the Structural Instabilities. Electronic Origin of the Structural Modulations in Layered Transition-Metal Dichalcogenides. *J. Am. Chem. Soc.*, 114:9587, 1992.

[84] A. Spijkerman, J.L. de Boer, A. Meetsma, G.A. Wiegers, and S. van Smaalen. X-ray crystal-structure refinement of the nearly commensurate phase of $1T$-$TaS_2$ in $(3+2)$-dimensional superspace. *Phys. Rev. B*, 56:13757, 1997.

[85] A. Zunger and A.J. Freeman. Band structure and lattice instability of $TiSe_2$. *Phys. Rev. B*, 17:1839, 1978.

[86] B. Sipos, A. F. Kusmartseva, H. Berger, L. Forro, and E. Tutis. *to be published.*

[87] H. Cercellier, C. Monney, F. Clerc, C. Battaglia, L. Despont, M.G. Garnier, H. Beck, P. Aebi, L. Patthey, H. Berger, and L. Forró. Evidence for an Excitonic Insulator Phase in $1T$-$TiSe_2$. *Phys. Rev. Lett.*, 99:146403, 2007.

[88] P. Wachter, B. Bucher, and J. Malar. Possibility of a superfluid phase in a bose condensed excitonic state. *Phys. Rev. B*, 69:094502, 2004.

[89] V.S. Babichenko and M.N. Kiselev. Superconductivity in systems with excitonic instability. *J. Moscow Phys. Soc.*, 2:311, 1992.

[90] A. Caillé, Y. Lepine, M.H. Jericho, and A.M. Simpson. Thermal expansion, ultrasonic velocity, and attenuation measurements in $TiS_2$, $TiSe_2$ and $TiS_{0.5}Se_{1.5}$. *Phys. Rev. B*, 28:5454, 1983.

[91] K.C. Woo, F.C. Brown, W.L. McMillan, R.J. Miller, M.J. Schaffman, and M.P. Sears. Superlattice formation in titanium diselenide. *Phys. Rev. B*, 14:3242, 1976.

[92] C.M. Fang, R.A. de Groot, and C. Haas. Bulk and surface electronic structure of $1T$-$TiS_2$ and $1T$-$TiSe_2$. *Phys. Rev. B*, 56:4455, 1997.

[93] R.A. Jishi and H.M. Alyahyaei. Electronic structure of superconducting copper intercalated transition metal dichalcogenides: First-principles calculations. *Phys. Rev. B*, 78:144516, 2008.

[94] T. Kusawake, Y. Takahashi, M.Y. Wey, and K. Ohshima. X-ray structure analysis and electron density distributions of the layered compounds $Cu_xTiS_2$. *J.Phys.C.M.*, 13:9913, 2001.

[95] Y. Yoshida and K. Motizuki. Electron Lattice Interaction and Lattice Instability of $1T$-$TiSe_2$. *J. Phys. Soc. Jpn.*, 49:898, 1980.

[96] K. Rossnagel and N.V. Smith. Spin-orbit splitting, Fermi surface topology, and charge-density-wave gapping in $2H$-$TaSe_2$. *Phys. Rev. B*, 76:073102, 2007.

[97] G. Li, W.Z. Hu, D. Qian, D. Hsieh, M.Z. Hasan, E. Morosan, R.J. Cava, and N.L. Wang. Semimetal to Semimetal Charge Density Wave Transition in $1T$-$TiSe_2$. *Phys. Rev. Lett.*, 99:027404, 2007.

[98] K. Motizuki. *Structural Phase Transitions in Layered Transition Metal Compounds*. D. Reidel Publishing Company, Motizuki.

[99] L. Fang, Y. Wang, P.Y. Zou, L. Tang, Z. Xu, H. Chen, C. Dong, L. Shan, and H.H. Wen. Fabrication and superconductivity of $Na_xTaS_2$ crystals. *Phys. Rev. B*, 72:014534, 2005.

[100] C. Monney, H. Cercellier, C. Battaglia, E.F. Schwier, C. Didiot, M. G. Garnier, H. Beck, and P. Aebi. Temperature dependence of the excitonic insulator phase model in $1T$-$TiSe_2$. *accepted for publication in Physica B*, 2009.

[101] V.J. Emery and S.A. Kivelson. Importance of phase fluctuations in superconductors with small superfluid density. *Nature*, 374:434, 1995.

[102] D. Ihle, M. Pfafferott, E. Burovski, F.X. Bronold, and H. Fehske. Bound state formation and the nature of the excitonic insulator phase in the extended Falicov-Kimball model. *Phys. Rev. B*, 78:193103, 2009.

[103] P. Ebert, M. Heinrich, M. Simon, C. Domke, K. Urban, C. K. Shih, M. B. Webb, and M. G. Lagally. Thermal formation of Zn-dopant-vacancy defect complexes on InP(110) surfaces. *Phys. Rev. B*, 53:4580, 1996.

[104] N.W. Ashcroft and N.D. Mermin. *Solid State Physics*. Brooks and Cole, 1976.

[105] M. Tinkham. *Introduction to superconductivity*. Dover publication, New-York, 1996.

[106] L. Perfetti, T.A. Gloor, F. Mila, H. Berger, and M. Grioni. Unexpected periodicity in the quasi-two-dimensional Mott insulator $1T$-$TaS_2$ revealed by angle-resolved photoemission. *Phys. Rev. B*, 71:153101, 2005.

[107] C. Monney, H. Cercellier, E.F. Schwier, C. Battaglia, N. Mariotti, C. Didiot, M.G. Garnier, J. Marcus, H. Beck, and P. Aebi. Temperature dependence of the exciton condensate phase of $1T$-$TiSe_2$. *submitted to PRB*, 2009.

[108] T. Yoshida, X. J. Zhou, T. Sasagawa, W. L. Yang, P. V. Bogdanov, A. Lanzara, T. Mizokawa Z. Hussai and, A. Fujimori, H. Eisaki, Z.-X. Shen, T. Kakeshita, and S. Uchida. Metallic Behavior of Lightly Doped $La_{2-x}Sr_xCuO_4$ with a Fermi Surface Forming an Arc. *Phys. Rev. Lett.*, 91:027001, 2003.

[109] T. Yoshida, X.J. Zhou, D.H. Lu, S. Komiya, Y. Ando, H. Eisaki, T. Kakeshita, S. Uchida, Z. Hussain, Z.-X. Shen, and A. Fujimori. Low-energy electronic structure of the high-Tc cuprates $La_{2-x}Sr_xCuO_4$f studied by angle-resolved photoemission spectroscopy. *J. Phys.: Condens. Matter*, 19:125209, 2007.

[110] C. Jacoboni, C. Canali, G. Ottaviani, and A.A. Quaranta. A review of some charge transport properties of silicon. *Solid State Electron.*, 20:77, 1977.

[111] H.P. Myers. *Introductory Solid State Physics.* CRC Press, 1997.

[112] S.W. Koch, M. Kira, G. Khitrova, and H.M. Gibbs. Semiconductor excitons in new light. *Nature Materials*, 5:523, 2006.

[113] T.M. Rice. The Electron-Hole Liquid in Semiconductors: Theoretical Aspects. *Solid State Phys.*, 32:1, 1977.

[114] J.C Hensel, T.G. Philips, and G.A. Thomas. The Electron-Hole Liquid in Semiconductors: Experimental Aspects. *Solid State Phys.*, 32:1, 1977.

[115] J.C. Slater and J.F. Koster. Simplified LCAO Method for the Periodic Potential Problem. *Phys. Rev.*, 94:1498, 1954.

[116] J.P. Perdew, K. Burke, and M. E Ernzerhof. Generalized Gradient Approximation Made Simple. *Phys. Rev. Lett.*, 77:3865, 1996.

[117] W.A. Harrison. *Electronic Structure and the Properties of Solids.* Freeman, San Francisco, 1980.

[118] S. Flügge. *Practical Quantum Mechanics.* Springer Verlag, 1971.

[119] N. Wakabayashi, H.G. Smith, K.C. Woo, and F.C. Brown. Phonons and charge density waves in $1T$-$TiSe_2$. *Solid State Comm.*, 1978:923, 2005.

[120] J. Demsar, L. Forró, H. Berger, and D. Mihailovic. Femtosecond snapshots of gap-forming charge-density-wave correlations in quasi-two-dimensional dichalcogenides $1T$-$TaS_2$ and $2H$-$TaSe_2$. *Phys. Rev. B*, 66:041101(R), 2002.

[121] L. Perfetti, P.A. Loukakos, M. Lisowski, U. Bovensiepen, H. Berger, S. Biermann, P.S. Cornaglia, A. Georges, and M. Wolf. Time Evolution of the Electronic Structure of $1T$-$TaS_2$ through the Insulator-Metal Transition. *Phys. Rev. Lett.*, 97:067402, 2006.

[122] W.S. Fann, R. Storz, H.W.K. Tom, and J. Bokor. Electron thermalization in gold. *Phys. Rev. B*, 46:13592(R), 1992.

[123] V.S. Babichenko and M.N. Kiselev. On the excitonic mechanism of superconductivity. *Physica C*, 209:133, 1993.

[124] E.G. Batyev. Superconducting state of an excitonic insulator. *Mod. Phys. Lett. B*, 22:1703, 2008.

[125] T. Hahn. CUBA — a library for multidimensional numerical integration. *Comput. Phys. Commun.*, 78:168, 2005.

[126] M.A. Jenkins. Algorithm 493 zeros of a real polynomial (c2). *ACM Transactions on Mathematical Software*, 1:178, 1975.

[127] WaveMetrics. IGOR Pro 6.05, 2009. http://www.wavemetrics.com/.

[128] F. Bloch. Ueber die Quantenmechanik der Elektronen in Kristallgittern. *Z. Physik*, 52:555, 1928.

[129] P.-O. Loewdin. On the Non-Orthogonality Problem Connected with the Use of Atomic Wave Functions in the Theory of Molecules and Crystals. *J. Chem. Phys.*, 18:365, 1950.

[130] S. Cottenier. *Density Functional Theory and the family of (L)APW-methods: a step-by-step introduction.* Instituut voor Kern- en Stralingfiysica, K.U. Leuven, Belgium, 2002.

[131] P. Hohenberg and W. Kohn. Inhomogeneous Electron Gas. *Phys. Rev.*, 136:B864, 1964.

[132] W. Kohn and L.J. Sham. Self-Consistent Equations Including Exchange and Correlation Effects. *Phys. Rev.*, 140:A1133, 1965.

[133] C.S. Fadley. Diffraction and holography with photoelectrons and Auger electrons: some new directions. *Surf. Sci. Rep.*, 19:231, 1993.

[134] E.V. Shalaeva and M.V. Kuznetsov. X-ray photoelectron diffraction. Possibilities of surface structural analysis. *J. Struct. Chem.*, 44:465, 2003.

[135] C.S. Fadley. Angle-resolved x-ray photoelectron spectroscopy. *Prog. Surf. Sci.*, 16:275, 1984.

[136] M.-L. Xu, J.J. Barton, and M.A. Van Hove. Electron scattering by atomic chains: Multiple-scattering effects. *Phys. Rev. B*, 39:8275, 1989.

[137] L. Despont, D. Naumovic, F. Clerc, C. Koitzsch, M.G. Garnier, F.J Garcia de Abajo, M.A. van Hove, and P. Aebi. X-ray photoelectron diffraction study of Cu(111): Multiple scattering investigation. *Surf. Sci.*, 600:380, 2006.

[138] L. Despont, F. Clerc, M.G. Garnier, H. Berger, L. Forró, and P. Aebi. Multiple scattering investigation of the $1T$-$TaS_2$ surface termination. *Eur. Phys. J. B*, 52:421, 2006.

[139] J.F. Moulder, W.F. Stickle, P.E. Sobol, and K.D. Bomben. *Handbook of X-ray Photoelectron Spectroscopy.* Perkin-Elmer, Eden Prairie, 1992.

[140] K. Takada, H. Sakurai, E. Takayama-Muromachi, F. Izumi, R.A. Dilanian, and T. Sasaki. Superconductivity in two-dimensional $CoO_2$ layers. *Nature (London)*, 422:53, 2003.

[141] M.L. Foo, Y. Wang, S. Watauchi, H. W. Zandbergen, T. He, R. J. Cava, and N. P. Ong. Charge Ordering, Commensurability, and Metallicity in the Phase Diagram of the Layered $Na_xCoO_2$. *Phys. Rev. Lett.*, 92:247001, 2004.

[142] D.J. Singh. Electronic structure of $NaCo_2O_4$. *Phys. Rev. B*, 61:13397, 2000.

[143] D. Qian, L. Wray, D. Hsieh, L. Viciu, R. J. Cava, J. L. Luo, D. Wu, N. L. Wang, and M. Z. Hasan. Complete $d$-Band Dispersion Relation in Sodium Cobaltates. *Phys. Rev. Lett.*, 97, 2006.

[144] D. Qian, D. Hsieh, L. Wray, A. Fedorov, D. Wu, J. L. Luo, N. L. Wang, L. Viciu, R. J. Cava, and M. Z. Hasan. Low-lying quasiparticle states and hidden collective charge instabilities in parent cobaltates superconductors ($Na_xCoO_2$). *Phys. Rev. Lett.*, 96:216405, 2006.

[145] H.-B. Yang, Z.-H. Pan, A. K. P. Sekharan, T. Sato, S. Souma, T. Takahashi, R. Jin, B. C. Sales, D. Mandrus, A. V. Fedorov, Z. Wang, and H. Ding. Fermi Surface Evolution and Luttinger Theorem in $Na_xCoO_2$: A Systematic Photoemission Study. *Phys. Rev. Lett.*, 95:146401, 2005.

[146] P. Zhang, W. Luo, M.L. Cohen, and S.G. Louie. Fermi Surface of $Na_xCoO_2$. *Phys. Rev. Lett.*, 93:236402, 2004.

[147] C.A. Marianetti and G. Kotliar. Na-Induced Correlations in $Na_xCoO_2$. *Phys. Rev. Lett.*, 98:176405, 2007.

[148] D.J. Singh and Deepa Kasinathan. Destruction of the small Fermi surfaces in $Na_xCoO_2$ by Na disorder. *Phys. Rev. Lett.*, 97:016404, 2006.

[149] H.W. Zandbergen, M. Foo, Q. Xu, V. Kumar, and R.J. Cava. Sodium ion ordering in $Na_xCoO_2$: Electron diffraction study. *Phys. Rev. B*, 70:024101, 2004.

[150] P. Zhang, R.B. Capaz, M.L. Cohen, and S.G. Louie. Theory of sodium ordering in $Na_xCoO_2$. *Phys. Rev. B*, 71:153102, 2005.

[151] L. Viciu, J. W. G. Bos, H. W. Zandbergen, Q. Huang, M. L. Foo, S. Ishiwata, A. P. Ramirez, M. Lee, N. P. Ong, and R. J. Cava. Crystal structure and elementary properties of $Na_xCoO_2$ ($x = 0.32, 0.51, 0.6, 0.75$ and 0.92) in the three-layer $NaCoO_2$ family. *Phys. Rev. B*, 73:174104, 2006.

[152] Q. Huang, M.L. Foo, R.A. Pascal, J.W. Lynn, B.H. Toby, Tao He, H.W. Zandbergen, and R.J. Cava. Coupling between electronic and structural degrees of freedom in triangular lattice conductor $Na_xCoO_2$. *Phys. Rev. B*, 70:184110, 2004.

[153] A. Liebsch and H. Ishida. Coulomb correlation do not fill the $e'_g$ hole pockets in $Na_{0.3}CoO_2$. *arXiv:condmat/0705.3627v1*, 2007.

[154] Y.G. Shi, H.X. Yang, H. Huang, X. Liu, and J.Q. Li. Superconductivity, charge ordering, and structural properties of $\alpha-$ and $\beta-Na_xCoO_2 \cdot y(H_2O,D_2O)$. *Phys. Rev. B*, 73:094505, 2006.

[155] D. Naumovic, A. Stuck, T. Greber, J. Osterwalder, and L. Schlapbach. Full-hemispherical photoelectron-diffraction data from Cu(001): Energy dependence and comparison with single-scattering-cluster simulations. *Phys. Rev. B*, 47:7462, 1993.

[156] C. S. Fadley. *Synchrotron Radiation Research: Advances in Surface Science.* Plenum, 1990.

[157] R. Fasel, P. Aebi, J. Osterwalder, and L. Schlapbach. Local structure of $c(2\times2)$-Na on Al(001): Experimental evidence of the coexistence of intermixing and on-surface adsorption. *Phys. Rev. B*, 50:14516, 1994.

[158] M. Onoda and T. Ikeda. Modulated and unmodulated structures, and the transport mechanisms in the triangular lattice system $Na_xCoO_2$ with $x \cong 0.48$, 0.58 and 0.65. *J. Phys.: Condens. Matter*, 19:186213, 2007.

[159] G. Lang, J. Bobroff, H. Alloul, P. Mendels, N. Blanchard, and G. Collin. Evidence of a single nonmagnetic $Co^{3+}$ state in the $Na_1CoO_2$ cobaltate. *Phys. Rev. B*, 72:094404, 2005.

[160] G.J. Shu, A. Prodi, S.Y. Chu, Y.S. Lee, H.S. Sheu, and F.C. Chou. Searching for stable Na-ordered phases in single-crystal samples of $\gamma{-}Na_xCoO_2$. *Phys. Rev. B*, 76:184115, 2007.

[161] W.W. Pai, S.H. Huang, Y.S. Menga, Y.C. Chao, C.H. Lin, H.L. Liu, and F.C. Chou. Sodium Trimer Ordering on a $Na_xCoO_2$ surface. *Phys. Rev. Lett.*, 100:206404, 2008.